PhD Thesis

Multi-wavelength study of Gamma-Ray Bursts emission

PhD Student: **Ana Virginia Penacchioni**

Supervisor: Prof. Remo Ruffini

Co-Supervisor: Dr. Carlo Luciano Bianco

Università degli Studi di Roma La Sapienza

Université de Nice Sofia Antipolis

Rome, September 2013

Acknowledgements

I would like to thank all the people who helped me during these three years of PhD.

In the first place, I would like to thank Prof. Ruffini for his support, and all the effort he has put day by day to help me become known in the scientific community, through the numerous meetings he made me attend and the people he introduced me to. I thank him also for taking into account my opinions and for his enthusiasm on my research.

I am very grateful to Carlo, for always trying to help me and answering my innumerable technical questions, apart from being such a good officemate.

I thank all the Erasmus students from my cycle: Sheyse, Bernardo, Vineeth, Vincenzo, Philipp, Christine, Andrey, Alberto and Parikshit, for all the good times we spent together, most of all our first September in Nice, which I will never forget.

I want to thank all my colleagues from Rome: Jorge, Charly, Diego, Giovanni, Damien, Micol, Andrea, Jonas, Yu, Yuanbin, Maxime, Bruno, Luca, Riccardo, Narek, Fernanda, Cristina, Marco and Kuantay; I enjoyed very much working with you during these years and having a lot of discussions on different topics.

I am very grateful to Prof. Amati and Prof. Della Valle, with whom I shared a lot of dinners and discussions and who gave me some advice which was very useful for my work.

Finally, I want to give thanks to my family, specially my parents, because without them all this would have not been possible to achieve.

Thank you!

Acronyms

ASI = Italian Space Agency
BAT = Burst Alert Telescope
BATSE = Burst And Transient Source Experiment
BB = Blackbody
BGO = Bismuth Germanate
BH = Black Hole
CGRO = Compton Gamma-Ray Observatory
COMPTEL = Imaging Compton Telescope
EGRET = Energetic Gamma Ray Experiment Telescope
ESA = European Space Agency
GBM = Gamma-ray Burst Monitor
GCN= Gamma-ray Coordination Network GLAST = Gamma-ray Large Area Space Telescope
GRB = Gamma-Ray Burst
HPGSPC = High Pressure Gas Scintillation Proportional Counter
ICG = Induced Gravitational Collapse
INa = Sodium Iodide
LAD = Large Area Detector
LAT = Large Area Telescope
LOFT = Large Observatory for X-ray Timing
LECS = Low Energy Concentrator Spectrometer
MECS = Medium Energy Concentrator Spectrometer
NIVR = Netherlands Agency for Aerospace Programmes
OSSE = Oriented Scintillation Spectrometer Experiment
PDS = Phoswich Detector System
PL = Power-law
ROTSE = Robotic Optical Transient Search Experiment
SDD = Silicon Drift Detector
SN = Supernova
ToO= Target of Opportunity
UVOT = Ultraviolet/Optical Telescope
VLA = Very Large Area (telescope)
WD = White Dwarf WFC = Wide Field Camera
WFM = Wide Field Monitor
XRT = X-Ray Telescope

Contents

1 The discovery of GRBs **5**
- 1.1 The 10^3 models . . . 6
- 1.2 The BATSE era . . . 6
- 1.3 The BeppoSAX era . . . 11
  - 1.3.1 Discovery of the afterglow . . . 14
- 1.4 The "Standard" Fireball model . . . 18
  - 1.4.1 Compactness Problem . . . 19
- 1.5 The Swift era . . . 21
- 1.6 The Fermi era . . . 23

2 The Fireshell Model **27**
- 2.1 Description of the Fireshell Model . . . 27
- 2.2 Long, short and disguised GRBs . . . 28
- 2.3 The physics of GRBs after the transparency . . . 31
- 2.4 Modified spectrum . . . 31
- 2.5 EQuiTemporal Surfaces (EQTS) . . . 32
- 2.6 Afterglow simulation . . . 33

3 Disguised and short GRBs vs. long GRBs **39**
- 3.1 Short GRBs: the case of GRB 090227B . . . 40
  - 3.1.1 Spectral Analysis . . . 40
  - 3.1.2 Analysis within the Fireshell model . . . 41
  - 3.1.3 Conclusions . . . 42
- 3.2 Disguised short GRBs: the case of GRB 090510 . . . 43
  - 3.2.1 Analysis in the Fireshell model . . . 44
  - 3.2.2 Conclusions . . . 44

4 GRB - SN association **69**
- 4.1 Spectroscopic evidence for GRBs and SNe . . . 69
  - 4.1.1 GRB 980425 and SN 1998bw . . . 70
  - 4.1.2 GRB 030329 and SN 2003dh . . . 71
  - 4.1.3 GRB 031203 and SN 2003lw . . . 71
  - 4.1.4 GRB 060218 and SN 2006aj . . . 73
  - 4.1.5 GRB 100316D and SN 2010bh . . . 73
- 4.2 Supporting evidence of the GRB-SN connection . . . 73
- 4.3 GRB-SN connection within the Fireshell model . . . 75
  - 4.3.1 GRB 090618: Observations . . . 76
  - 4.3.2 Data analysis . . . 77

4.3.3 Analysis of the first episode . . . 82
4.3.4 Conclusions . . . 83
4.3.5 GRB 101023: Observations . . . 84
4.3.6 Redshift determination . . . 86
4.3.7 Data analysis . . . 88
4.3.8 Analysis of the first episode: radius of the emitting region 91
4.3.9 Conclusions . . . 91

5 The induced gravitational collapse model 125
5.1 Introduction . . . 125
5.2 The IGC model . . . 125
5.3 GRB 110709B in the IGC scenario . . . 126
5.3.1 Data analysis . . . 129
5.3.2 Cosmological redshift estimation . . . 131
5.3.3 Radius of the emitting region . . . 133
5.3.4 Episode 2 in the Fireshell model . . . 134
5.3.5 Nature of the progenitor . . . 135
5.4 Conclusions . . . 139

6 The scaling law for GRBs 155
6.1 The sample . . . 155
6.2 Data analysis . . . 157
6.3 Conclusions . . . 157

7 Future prospects 165
7.1 Observational predictions . . . 165
7.1.1 Predictions of a SN . . . 165
7.1.2 Conclusions . . . 168
7.2 The LOFT mission . . . 168
7.2.1 LOFT payload . . . 169
7.2.2 Science Objectives . . . 171
7.3 GRB science with LOFT . . . 172

Appendix 179

Introduction

The phenomena of Gamma-ray bursts (GRBs) have been a mystery for many physicists and astrophysicists since their discovery. As has happened with many of the major discoveries in the human history, they were discovered by chance. Currently, significant progress are made in their classification in equivalent classes and on their progenitors.

The Vela satellites, a group of American satellites designed to monitor against nuclear testing in the atmosphere, detected in 1967 anomalous gamma-ray signals while they monitored the Earth and the sky. The information was classified. Moreover, they did not know where this emissions came from. Similar observations were performed in the following years, with the same results. After some time, they reached the conclusion that the emissions were not coming neither from the Earth nor the Moon, so they had to be events of outside the Solar system.

In 1973, the discovery was announced at the Meeting of the American Association for the Advancement of Science (AAAS), in S. Francisco (Gursky & Ruffini 1975; Strong 1975) and a new era started: the GRB era. Many efforts have been made in order to go further in the understanding of these intriguing phenomena, which occurred at an average of one per day. Not knowing the distance, their energy was totally unknown. Many space missions were launched and thousands of theories were elaborated to try to explain their nature (Ruffini 2001). Among them, there is the one of Tibault Damour and Remo Ruffini (Damour & Ruffini 1975), which is based on the mass-energy formula of black holes. This model can naturally explain the energetics up to 10^{54-55} erg. They proposed that the progenitor was the electromagnetic energy of a BH creating a vacuum polarization process and generating an $e^{\pm}$ plasma by vacuum polarization processes in the Kerr-Newman geometry (for a recent review see Ruffini et al. (2010b)).

In the meanwhile, new space missions were developed, which brought very important results. The Compton Gamma-ray Observatory (CGRO), launched in 1991, observed more than 1000 bursts. Thanks to it, it was known that the GRBs distribution in the sky is isotropic, so they could originate either very near inside the galaxy or they could be extragalactic events. With the excellent performance of *BeppoSaX*, a satellite launched in 1996, more achievements were made. The first afterglow in X-rays, corresponding to GRB 970228, was discovered and located in the sky. The on-ground observatories were alerted and the coordinates of the burst distributed among them, enabling the observation and follow-up of the optical afterglow. This, in turn, enabled to calculate the cosmological redshift, eliminating any doubt about their nature: they were events of extragalactic origin and their energy was up to 10×10^{54} erg, as predicted

in Damour & Ruffini (1975) and now requested by the cosmological nature of GRBs. From the thousands of models proposed, just a handful survived. Ruffini and collaborators returned to this paradigm and developed since a quite detailed model about the creation and evolution of GRBs in the 90's, called the Fireshell model.

In the XXI century, two important satellites were launched, which are still operative and detect an average of two GRBs per day. They are *Swift* and *Fermi*.

Nowadays, a lot of improvements have been made with respect to the 70's, but we still cannot reach a complete understanding of GRBs; their progenitors and the exact physical processes that take place during their emission are still a matter of debate. Of the many theoretical models proposed, only a few survived after the observational evidence by the first satellite missions. The Fireshell model is one of these.

In this thesis, after a historical introduction and the explanation of some theoretical models developed on GRBs, I present the work I have done as a member of Professor Ruffini's group at Sapienza University in Rome.

During my three years of PhD, many GRBs have been analyzed within the Fireshell model, which has been further developed thanks to our results. Apart form the standard classification into short and long, we created a new class of GRBs: the disguised short.

However, the truly unexpected new understanding has come from the relation of the Supernova (SN) event to the GRBs. Furthermore, we found some similarities between some long GRBs, with which we created a sub-class. To explain the physical processes that take place during the formation of this kind of GRBs, we worked out a new model called the Induced Gravitational Collapse (IGC). The model explains the emission of some long GRBs as originating in a binary system. It comes out naturally from the model that these GRBs are associated to a SN, which we can corroborate by the optical emission occurring days after the burst. The model enables us to make predictions about the SN occurrence as well, so as to alert the optical observations from a very early time.

I also present some of the most recent results regarding the IGC model, concentrating in the case of GRB 130427A. This was a very luminous GRB, and was detected by almost all the operating detectors. We predict the occurrence of an optical SN emission ~ 13 days before its actual appearance on the ground of the identification of our novel features in the GRB prompt emission phase.

The new scenario speaks for the first time of a multi body interaction of gravitationally collapsed objects. The IGC paradigm represents an authentic collapse-matrix (C-matrix): from the occurrence of an SN originating in the detonation of a CO-core in a tightly bound binary system with a companion NS (the *in-state*), it leads to the formation of a BH and a newly-born NS (the *out-state*).

Finally, I describe one of the new possible space missions dedicated (among other topics) to the study of GRBs: the Large Observatory for X-ray Timing (LOFT). Some simulations that indicate how the light curves of some GRBs would have looked like if detected by LOFT will be shown, as well as the difference in their spectra with respect to what is achieved with the current missions.

"Few people are capable of expressing with equanimity opinions which differ from the prejudices of their social environment. Most people are even incapable of forming such opinions."
Albert Einstein

Chapter 1

The discovery of GRBs

About once a day, an intriguing phenomenon occurs: the sky is suddenly lit up by an intense flash of gamma rays. For a few seconds, this mysterious burst outshines every other electromagnetic source in the known Universe. They are hundreds of times brighter than a typical Supernova (SN) and a million trillion times brighter than the Sun. They are called Gamma-Ray Bursts (GRBs). We know today that they last from a fraction of a second up to a few minutes, and they have an extragalactic origin, that is why they are randomly and isotropically distributed in the sky. The human eye is not able to detect gamma rays, and they cannot penetrate the atmosphere. The only way to get some information about them is through the orbiting satellites. Many models have arisen to try to explain the nature of this sources, but the truth is that they are so complex that none of them has yet been able to explain them completely.

The 5 August 1963, during the Cold War, the United States, the United Kingdom and the Soviet Union signed the "Nuclear Test-Ban Treaty". This treaty prohibited all kind of nuclear-weapons tests in the atmosphere, in outer space and underwater, except those conducted underground. It aimed to create worldwide public concern over the danger posed by atmospheric radioactive fallout produced by the aboveground testing of nuclear weapons, and to diminish their rapid proliferation.

To assure that there were no violations of this treaty, in October of 1963 the United States launched the first of the twelve '*Vela*' satellites (from the Spanish verb 'velar', to watch). The satellites were launched and operated in pairs with two identical satellites on opposite sides of a circular orbit 250.000 kilometers in diameter (about a 4 day orbit) so that no part of the Earth was shielded from direct observation. The Vela satellites carried X-ray, gamma-ray, and neutron detectors as a basic instrumentation complement. They also carried a variety of optical and electromagnetic pulse (EMP) detectors as well as instruments designed to monitor the space environment.

On July 2, 1967, at 14:19 UTC, the Vela 3 and Vela 4 satellites detected a flash of gamma radiation unlike any known nuclear weapons signature. Uncertain what had happened but not considering the matter particularly urgent, the team at the Los Alamos Scientific Laboratory, led by Ray Klebesadel, filed the data away for investigation. By analyzing the different arrival times of the bursts as detected by different satellites, the team was able to deduce the sky positions of sixteen bursts with sufficient accuracy to rule out a terrestrial or

solar origin. They concluded that the gamma-ray events were "of cosmic origin". The discovery was declassified in 1973 and published as an Astrophysical Journal article entitled "Observations of Gamma-Ray Bursts of Cosmic Origin" (Klebesadel et al. 1973). A few days later it was announced at the Meeting of the American Association for the Advancement of Science (AAAS), in S. Francisco. This alerted the astronomical community to the existence of GRBs, now recognized as the most violent events in the universe [1].

1.1 The 10^3 models

The number of theories grew exponentially but without any clear conclusion. Among these theories there were Soon after the announcement of the discovery of GRBs, many satellite missions (e.g., the Russian satellites Venera 11, Venera 12, Prognoz 6, Prognoz 9, Konus, Granat, and the American Pioneer-Venus Orbiter and solar Maximum Mission) which included instrumentation devoted to the detection of GRBs were performed, but a very small progress in understanding the GRB origin was obtained. The localizations were very coarse and no counterpart at longer wavelengths was found. Many theoretical models on GRB progenitors were worked out, with the largest consensus being obtained by the models which assumed that GRBs originate in galactic disk NS (see the review by Costa & Frontera (2011)). A partial list of the models is shown in Fig.1.1 (Ruffini 2001). Some other theories related the GRB phenomenon to the Hawking radiation process. Damour & Ruffini (1975) proposed to explain the energy source of GRBs in terms of an $e^- - e^-$ plasma, which was created in the process of vacuum polarization during the formation of a Kerr-Newman black hole. The energetics to be expected according to their model was $10^{54} - 10^{55}$ erg for a 10 $M_\odot$ BH (see Table 1 of that paper). At the time nothing was known about the energetics of the GRBs, their distances being unknown. They did not explained any further details of the model, waiting for new observational evidence (for further details see Chapter 2).

1.2 The BATSE era: short and long GRBs and the homogeneity of their distribution in the sky

The origin of GRBs remained unknown until 25 years after their discovery. On 5 April 1991, NASA launched the Compton Gamma-Ray Observatory (CGRO), shown in Fig.1.2 (Murdin 2000; Gehrels et al. 1993). It was a space observatory that detected light from 20 keV to 30 GeV, the second 'Great Observatory" launched by NASA, after the Hubble Space Telescope. It carried four instruments onboard:

[1] GRBs are named according to the date in which they were detected. For example, a GRB detected on 05 April 2003 is called GRB 030405. If more than one GRB is detected in the same day, they are differentiated by capital letters, like 030405A, 030405B, etc.

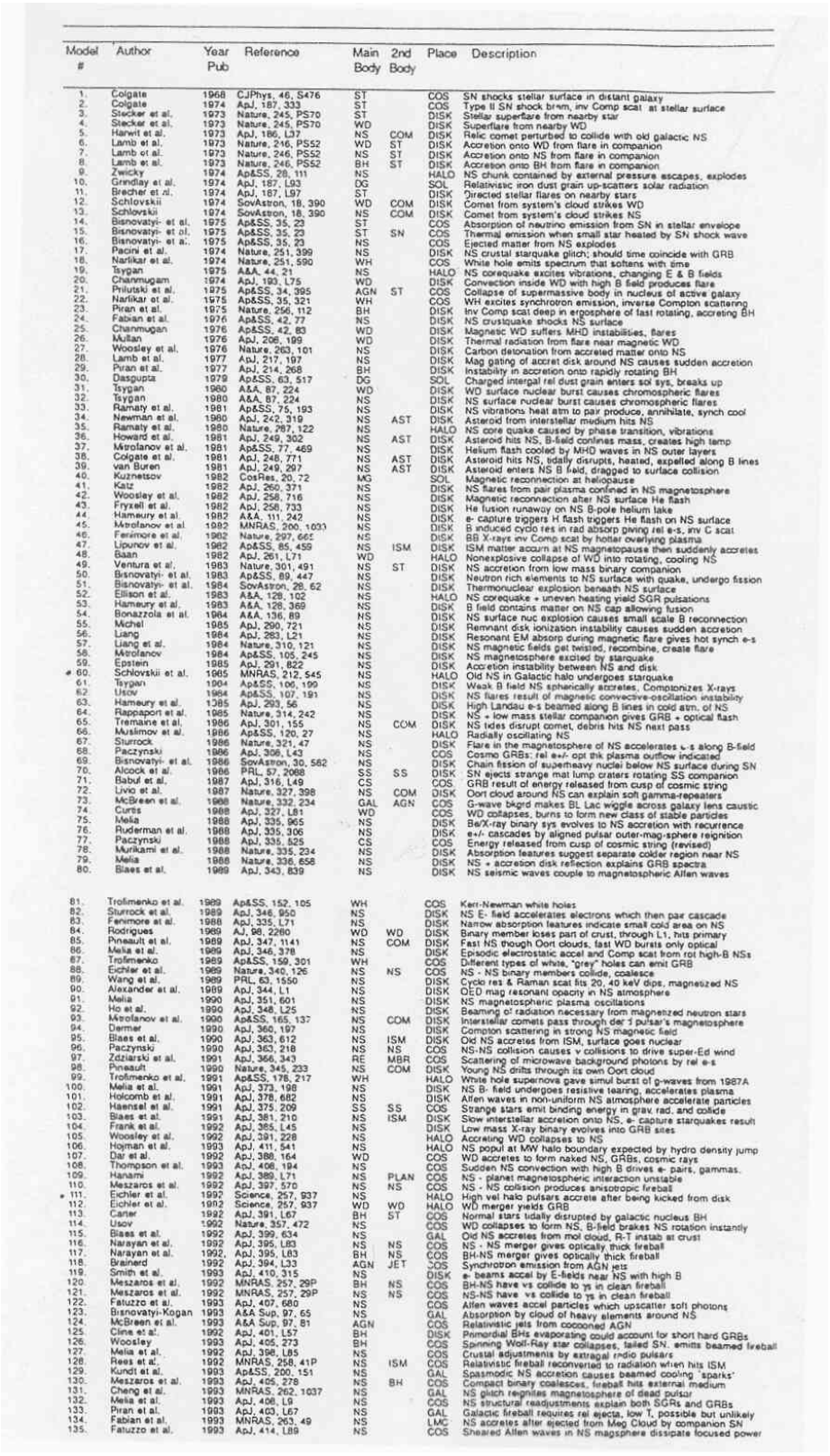

Model #	Author	Year Pub	Reference	Main Body	2nd Body	Place	Description
1.	Colgate	1968	CJPhys, 46, S476	ST		COS	SN shocks stellar surface in distant galaxy
2.	Colgate	1974	ApJ, 187, 333	ST		COS	Type II SN shock brkm, inv Comp scat at stellar surface
3.	Stecker et al.	1973	Nature, 245, PS70	ST		DISK	Stellar superflare from nearby star
4.	Stecker et al.	1973	Nature, 245, PS70	WD		DISK	Superflare from nearby WD
5.	Harwit et al.	1973	ApJ, 186, L37	NS	COM	DISK	Relic comet perturbed to collide with old galactic NS
6.	Lamb et al.	1973	Nature, 246, PS52	WD	ST	DISK	Accretion onto WD from flare in companion
7.	Lamb et al.	1973	Nature, 246, PS52	NS	ST	DISK	Accretion onto NS from flare in companion
8.	Lamb et al.	1973	Nature, 246, PS52	BH	ST	DISK	Accretion onto BH from flare in companion
9.	Zwicky	1974	Ap&SS, 28, 111	NS		HALO	NS chunk contained by external pressure escapes, explodes
10.	Grindlay et al.	1974	ApJ, 187, L93	DG		SOL	Relativistic iron dust grain up-scatters solar radiation
11.	Brecher et al.	1974	ApJ, 187, L97	ST		DISK	Directed stellar flares on nearby stars
12.	Schlovskii	1974	SovAstron, 18, 390	WD	COM	DISK	Comet from system's cloud strikes WD
13.	Schlovskii	1974	SovAstron, 18, 390	NS	COM	DISK	Comet from system's cloud strikes NS
14.	Bisnovatyi- et al.	1975	Ap&SS, 35, 23	ST		COS	Absorption of neutrino emission from SN in stellar envelope
15.	Bisnovatyi- et al.	1975	Ap&SS, 35, 23	ST	SN	COS	Thermal emission when small star heated by SN shock wave
16.	Bisnovatyi- et al.	1975	Ap&SS, 35, 23	NS		COS	Ejected matter from NS explodes
17.	Pacini et al.	1974	Nature, 251, 399	NS		DISK	NS crustal starquake glitch; should time coincide with GRB
18.	Narlikar et al.	1974	Nature, 251, 590	WH		COS	White hole emits spectrum that softens with time
19.	Tsygan	1975	A&A, 44, 21	NS		HALO	NS corequake excites vibrations, changing E & B fields
20.	Chanmugam	1974	ApJ, 193, L75	WD		DISK	Convection inside WD with high B field produces flare
21.	Prilutski et al.	1975	Ap&SS, 34, 395	AGN	ST	COS	Collapse of supermassive body in nucleus of active galaxy
22.	Narlikar et al.	1975	Ap&SS, 35, 321	WH		COS	WH excites synchrotron emission, inverse Compton scattering
23.	Piran et al.	1975	Nature, 256, 112	BH		DISK	Inv Comp scat deep in ergosphere of fast rotating, accreting BH
24.	Fabian et al.	1976	Ap&SS, 42, 77	NS		DISK	NS crustquake shocks NS surface
25.	Chanmugan	1976	Ap&SS, 42, 83	WD		DISK	Magnetic WD suffers MHD instabilities, flares
26.	Mullan	1976	ApJ, 206, 199	WD		DISK	Thermal radiation from flare near magnetic WD
27.	Woosley et al.	1976	Nature, 263, 101	NS		DISK	Carbon detonation from accreted matter onto NS
28.	Lamb et al.	1977	ApJ, 217, 197	NS		DISK	Mag gating of accret disk around NS causes sudden accretion
29.	Piran et al.	1977	ApJ, 214, 268	BH		DISK	Instability in accretion onto rapidly rotating BH
30.	Dasgupta	1979	Ap&SS, 63, 517	DG		SOL	Charged intergal rel dust grain enters sol sys, breaks up
31.	Tsygan	1980	A&A, 87, 224	WD		DISK	WD surface nuclear burst causes chromospheric flares
32.	Tsygan	1980	A&A, 87, 224	NS		DISK	NS surface nuclear burst causes chromospheric flares
33.	Ramaty et al.	1981	Ap&SS, 75, 193	NS		DISK	NS vibrations heat atm to pair produce, annihilate, synch cool
34.	Newman et al.	1980	ApJ, 242, 318	NS	AST	DISK	Asteroid from interstellar medium hits NS
35.	Ramaty et al.	1980	Nature, 287, 122	NS		HALO	NS core quake caused by phase transition, vibrations
36.	Howard et al.	1981	ApJ, 249, 302	NS	AST	DISK	Asteroid hits NS, B-field confines mass, creates high temp
37.	Mitrofanov et al.	1981	Ap&SS, 77, 469	NS		DISK	Helium flash cooled by MHD waves in NS outer layers
38.	Colgate et al.	1981	ApJ, 248, 771	NS	AST	DISK	Asteroid hits NS, tidally disrupts, heated, expelled along B lines
39.	van Buren	1981	ApJ, 249, 297	NS	AST	DISK	Asteroid enters NS B field, dragged to surface collision
40.	Kuznetsov	1982	CosRes, 20, 72	MG		SOL	Magnetic reconnection at heliopause
41.	Katz	1982	ApJ, 260, 371	NS		DISK	NS flares from pair plasma confined in NS magnetosphere
42.	Woosley et al.	1982	ApJ, 258, 716	NS		DISK	Magnetic reconnection after NS surface He flash
43.	Fryxell et al.	1982	ApJ, 258, 733	NS		DISK	He fusion runaway on NS B-pole helium lake
44.	Hameury et al.	1982	A&A, 111, 242	NS		DISK	e- capture triggers H flash triggers He flash on NS surface
45.	Mitrofanov et al.	1982	MNRAS, 200, 1033	NS		DISK	B induced cyclo res in rad absorp plwing rel e-s, inv C scat
46.	Fenimore et al.	1982	Nature, 297, 665	NS		DISK	BB X-rays inv Comp scat by hotter overlying plasma
47.	Lipunov et al.	1982	Ap&SS, 85, 459	NS	ISM	DISK	ISM matter accum at NS magnetopause then suddenly accretes
48.	Baan	1982	ApJ, 261, L71	WD		HALO	Nonexplosive collapse of WD into rotating, cooling NS
49.	Ventura et al.	1983	Nature, 301, 491	NS	ST	DISK	NS accretion from low mass binary companion
50.	Bisnovatyi- et al.	1983	Ap&SS, 89, 447	NS		DISK	Neutron rich elements to NS surface with quake, undergo fission
51.	Bisnovatyi- et al.	1984	SovAstron, 28, 62	NS		DISK	Thermonuclear explosion beneath NS surface
52.	Ellison et al.	1983	A&A, 128, 102	NS		HALO	NS corequake + uneven heating yield SGR pulsations
53.	Hameury et al.	1983	A&A, 128, 369	NS		DISK	B field contains matter on NS cap allowing fusion
54.	Bonazzola et al.	1984	A&A, 136, 89	NS		DISK	NS surface nuc explosion causes small scale B reconnection
55.	Michel	1985	ApJ, 290, 721	NS		DISK	Remnant disk ionization instability causes sudden accretion
56.	Liang	1984	ApJ, 283, L21	NS		DISK	Resonant EM absorp during magnetic flare gives hot synch e-s
57.	Liang et al.	1984	Nature, 310, 121	NS		DISK	NS magnetic fields get twisted, recombine, create flare
58.	Mitrofanov	1984	Ap&SS, 105, 245	NS		DISK	NS magnetosphere excited by starquake
59.	Epstein	1985	ApJ, 291, 822	NS		DISK	Accretion instability between NS and disk
* 60.	Schlovskii et al.	1985	MNRAS, 212, 545	NS		HALO	Old NS in Galactic halo undergoes starquake
61.	Tsygan	1984	Ap&SS, 106, 199	NS		DISK	Weak B field NS spherically accretes, Comptonizes X-rays
62.	Usov	1984	Ap&SS, 107, 191	NS		DISK	NS flares result of magnetic convective-oscillation instability
63.	Hameury et al.	1985	ApJ, 293, 56	NS		DISK	High Landau e-s beamed along B lines in cold atm. of NS
64.	Rappaport et al.	1985	Nature, 314, 242	NS		DISK	NS + low mass stellar companion gives GRB + optical flash
65.	Tremaine et al.	1986	ApJ, 301, 155	NS	COM	DISK	NS tides disrupt comet, debris hits NS next pass
66.	Muslimov et al.	1986	Ap&SS, 120, 27	NS		HALO	Radially oscillating NS
67.	Sturrock	1986	Nature, 321, 47	NS		DISK	Flare in the magnetosphere of NS accelerates e-s along B-field
68.	Paczynski	1986	ApJ, 308, L43	NS		COS	Cosmo GRBs: rel e+/- opt thk plasma outflow indicated
69.	Bisnovatyi- et al.	1986	SovAstron, 30, 562	NS		DISK	Chain fission of superheavy nuclei below NS surface during SN
70.	Alcock et al.	1986	PRL, 57, 2088	SS	SS	DISK	SN ejects strange mat lump craters rotating SS companion
71.	Babul et al.	1987	ApJ, 316, L49	CS		COS	GRB result of energy released from cusp of cosmic string
72.	Livio et al.	1987	Nature, 327, 398	NS	COM	DISK	Oort cloud around NS can explain soft gamma-repeaters
73.	McBreen et al.	1988	Nature, 332, 234	GAL	AGN	COS	G-wave bkgrd makes BL Lac wiggle across galaxy lens caustic
74.	Curtis	1988	ApJ, 327, L81	WD		COS	WD collapses, burns to form new class of stable particles
75.	Melia	1988	ApJ, 335, 965	NS		DISK	Be/X-ray binary sys evolves to NS accretion with recurrence
76.	Ruderman et al.	1988	ApJ, 335, 306	NS		DISK	e+/- cascades by aligned pulsar outer-mag-sphere reignition
77.	Paczynski	1988	ApJ, 335, 525	CS		COS	Energy released from cusp of cosmic string (revised)
78.	Murikami et al.	1988	Nature, 335, 234	NS		DISK	Absorption features suggest separate colder region near NS
79.	Melia	1988	Nature, 336, 658	NS		DISK	NS + accretion disk reflexion explains GRB spectra
80.	Blaes et al.	1989	ApJ, 343, 839	NS		DISK	NS seismic waves couple to magnetospheric Alfen waves
81.	Trofimenko et al.	1989	Ap&SS, 152, 105	WH		COS	Kerr-Newman white holes
82.	Sturrock et al.	1989	ApJ, 346, 950	NS		DISK	NS E- field accelerates electrons which then pair cascade
83.	Fenimore et al.	1988	ApJ, 335, L71	NS		DISK	Narrow absorption features indicate small cold area on NS
84.	Rodrigues	1989	AJ, 98, 2260	WD	WD	DISK	Binary member loses part of crust, through L1, hits primary
85.	Pneault et al.	1989	ApJ, 347, 1141	NS	COM	DISK	Fast NS though Oort clouds, fast WD bursts only optical
86.	Melia et al.	1989	ApJ, 346, 378	NS		DISK	Episodic electrostatic accel and Comp scat from rot high-B NSs
87.	Trofimenko	1989	Ap&SS, 159, 301	WH		COS	Different types of white, "grey" holes can emit GRB
88.	Eichler et al.	1989	Nature, 340, 126	NS	NS	COS	NS - NS binary members collide, coalesce
89.	Wang et al.	1989	PRL, 63, 1550	NS		DISK	Cyclo res & Raman scat fits 20, 40 keV dips, magnetized NS
90.	Alexander et al.	1989	ApJ, 344, L1	NS		DISK	QED mag resonant opacity in NS atmosphere
91.	Melia	1990	ApJ, 351, 601	NS		DISK	NS magnetospheric plasma oscillations
92.	Ho et al.	1990	ApJ, 348, L25	NS		DISK	Beaming of radiation necessary from magnetized neutron stars
93.	Mirofanov et al.	1990	Ap&SS, 165, 137	NS	COM	DISK	Interstellar comets pass through der 1 pulsar's magnetosphere
94.	Dermer	1990	ApJ, 360, 197	NS		DISK	Compton scattering in strong NS magnetic field
95.	Blaes et al.	1990	ApJ, 363, 612	NS	ISM	DISK	Old NS accretes from ISM, surface goes nuclear
96.	Paczynski	1990	ApJ, 363, 218	NS	NS	COS	NS-NS collision causes ν collisions to drive super-Ed wind
97.	Zdziarski et al.	1991	ApJ, 366, 343	RE	MBR	COS	Scattering of microwave background photons by rel e-s
98.	Pneault	1990	Nature, 345, 233	NS	COM	DISK	Young NS drifts through its own Oort cloud
99.	Trofimenko et al.	1991	Ap&SS, 178, 217	WH		HALO	White hole supernovs gave simul burst of g-waves from 1987A
100.	Melia et al.	1991	ApJ, 373, 198	NS		DISK	NS B- field undergoes resistive tearing, accelerates plasma
101.	Holcomb et al.	1991	ApJ, 378, 682	NS		DISK	Alfen waves in non-uniform NS atmosphere accelerate particles
102.	Haensel et al.	1991	ApJ, 375, 209	SS	SS	COS	Strange stars emit binding energy in grav. rad. and collide
103.	Blaes et al.	1991	ApJ, 381, 210	NS	ISM	DISK	Slow interstellar accretion onto NS, e- capture starquakes result
104.	Frank et al.	1992	ApJ, 385, L45	NS		DISK	Low mass X-ray binary evolves into GRB sites
105.	Woosley et al.	1992	ApJ, 391, 228	NS		HALO	Accreting WD collapses to NS
106.	Hojman et al.	1993	ApJ, 411, 541	NS		HALO	NS popul at MW halo boundary expected by hydro density jump
107.	Dar et al.	1992	ApJ, 388, 164	WD		COS	WD accretes to form naked NS, GRBs, cosmic rays
108.	Thompson et al.	1993	ApJ, 408, 194	NS		COS	Sudden NS convection with high B drives e- pairs, gammas.
109.	Hanami	1992	ApJ, 389, L71	NS	PLAN	COS	NS - planet magnetospheric interaction unstable
110.	Meszaros et al.	1992	ApJ, 397, 570	NS	NS	COS	NS - NS collision produces anisotropic fireball
* 111.	Eichler et al.	1992	Science, 257, 937	NS		HALO	High vel halo pulsars accrete after being kicked from disk
112.	Eichler et al.	1992	Science, 257, 937	WD	WD	HALO	WD merger yields GRB
113.	Carter	1992	ApJ, 391, L67	BH	ST	COS	Normal stars tidally disrupted by galactic nucleus BH
114.	Usov	1992	Nature, 357, 472	NS		COS	WD collapses to form NS, B-field brakes NS rotation instantly
115.	Blaes et al.	1992	ApJ, 399, 634	NS		GAL	Old NS accretes from mol cloud, R-T instab at crust
116.	Narayan et al.	1992	ApJ, 395, L83	NS	NS	COS	NS - NS merger gives optically thick fireball
117.	Narayan et al.	1992,	ApJ, 395, L83	BH	NS	COS	BH-NS merger gives optically thick fireball
118.	Brainerd	1992	ApJ, 394, L33	AGN	JET	COS	Synchrotron emission from AGN jets
119.	Smith et al.	1993	ApJ, 410, 315	NS		DISK	e- beams accel by E-fields near NS with high B
120.	Meszaros et al.	1992	MNRAS, 257, 29P	BH	NS	COS	BH-NS have νs collide to γs in clean fireball
121.	Meszaros et al.	1992	MNRAS, 257, 29P	NS	NS	COS	NS-NS have νs collide to γs in clean fireball
122.	Fatuzzo et al.	1993	ApJ, 407, 680	NS		COS	Alfen waves accel particles which upscatter soft photons
123.	Bisnovatyi-Kogan	1993	A&A Sup, 97, 65	NS		GAL	Absorption by cloud of heavy elements around NS
124.	McBreen et al.	1993	A&A Sup, 97, 81	AGN		COS	Relativistic jets from cocooned AGN
125.	Cline et al.	1992	ApJ, 401, L57	BH		DISK	Primordial BHs evaporating could account for short hard GRBs
126.	Woosley	1993	ApJ, 405, 273	BH		COS	Spinning Wolf-Ray star collapses, failed SN, emits beamed fireball
127.	Melia et al.	1992	ApJ, 398, L85	NS		COS	Crustal adjustments by astragal radio pulsars
128.	Rees et al.	1992	MNRAS, 258, 41P	NS	ISM	COS	Relativistic fireball reconverted to radiation when hits ISM
129.	Kundt et al.	1993	Ap&SS, 200, 151	NS		GAL	Spasmodic NS accretion causes beamed cooling 'sparks'
130.	Meszaros et al.	1993	ApJ, 405, 278	NS	BH	COS	Compact binary coalesces, fireball hits external medium
131.	Cheng et al.	1993	MNRAS, 262, 1037	NS		GAL	NS glitch reignites magnetosphere of dead pulsar
132.	Melia et al.	1993	ApJ, 408, L9	NS		COS	NS structural readjustments explain both SGRs and GRBs
133.	Piran et al.	1993	ApJ, 403, L67	NS		GAL	Galactic fireball requires rel ejecta, low T, possible but unlikely
134.	Fabian et al.	1993	MNRAS, 263, 49	NS		LMC	NS accretes after ejected from Meg Cloud by companion SN
135.	Fatuzzo et al.	1993	ApJ, 414, L89	NS		COS	Sheared Alfen waves in NS magsphere dissipate focused power

Figure 1.1: Partial list of theories (135 of the thousands that were created) after the declassification of the observations made by the Vela satellites. Taken from Ruffini (2001) with kind permission.

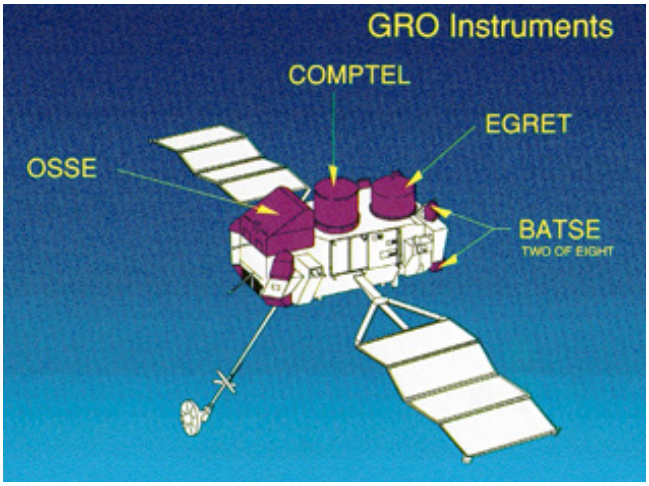

Figure 1.2: Compton satellite and its four instruments, which covered the electromagnetic spectrum from 20 keV to 30 GeV: BATSE, OSSE, COMPTEL and EGRET.

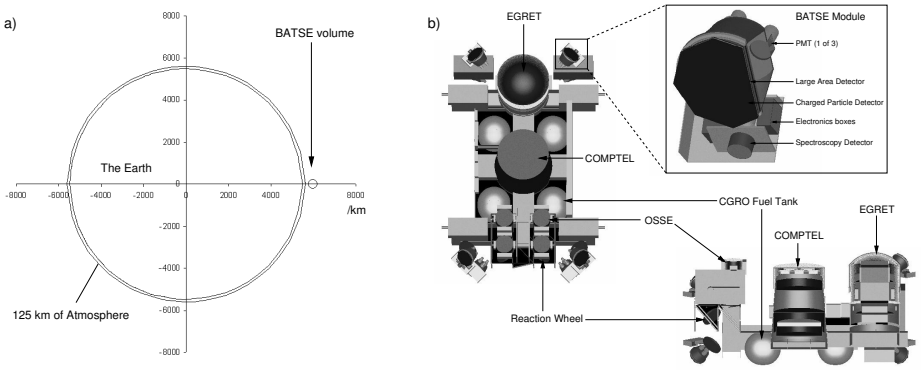

Figure 1.3: a) Relative scale of the Earth, its atmosphere (up to 125 km) and the virtual BATSE volume. b) Detailed structural, geometrical and material infomation for BATSE, EGRET, COMPTEL, OSSE and the CGRO spacecraft. Cut-aways of the BATSE module (top right) and the whole CGRO (bottom right) show the internal detail. Taken from Willis et al. (2005).

BATSE

The Burst and Transient Source Experiment (BATSE) (Fishman 1988) was an all sky monitor that looked for GRBs in the range (20 - $\geq$ 600 keV). It consisted of eight identical detector modules, one at each of the satellite's corners (see Fig.1.3). Each module consisted of both a NaI(Tl) Large Area Detector (LAD) covering the 20 keV to $\sim$2 MeV range (Paciesas et al. 1989), 50.48 cm diameter by 1.27 cm thick, and a 12.7 cm diameter by 7.62 cm thick NaI Spectroscopy Detector (SD), which extended the upper energy range to 8 MeV, all surrounded by a plastic scintillator in active anti-coincidence to reject the large background rates due to cosmic rays and trapped radiation. Sudden increases in the LAD rates triggered a high-speed data storage mode, the details of the burst being read out to telemetry later. Bursts were typically detected at rates of roughly one per day.

OSSE

The Oriented Scintillation Spectrometer Experiment (OSSE) (Johnson et al. 1989; Kurfess et al. 1989), detected gamma rays entering the field of view of any of the four detector modules, which could be pointed individually, and were effective in the (0.05- 10 MeV) range (Share et al. 1992). Each detector had a central scintillation spectrometer crystal of NaI(Tl), optically coupled at the rear to a CsI(Na) crystal of similar diameter, viewed by seven photomultiplier tubes. Thus the CsI backing crystal acted as an active anticoincidence shield, vetoing events from the rear (Strickman et al. 1992, 1990). During a gamma-ray source observation, one detector would take observations of the source, while the other would slew slightly off source to measure the background levels (Battersby et al. 1993).

COMPTEL

The Imaging Compton Telescope (COMPTEL) (Diehl 1988; Ryan 1989; Schoenfelder 1991) worked in the (0.75 - 30 MeV) energy range and determined the angle of arrival of photons to within a degree and the energy to within five percent. It had a field of view of 1 sr. For cosmic gamma-ray events, the experiment required two nearly simultaneous interactions, in a set of front and rear scintillators. Gamma rays would Compton scatter in a forward detector module, where the interaction energy E_1, given to the recoil electron was measured, while the Compton scattered photon would then be caught in one of a second layer of scintillators to the rear, where its total energy, E_2, would be measured. From these two energies, E_1 and E_2, the Compton scattering angle θ can be determined, along with the total energy of the incident photon, $E_1 + E_2$. The vector $\mathbf{V}$ connecting the two interaction points determined a direction to the sky, and the angle θ about this direction defined a cone about $\mathbf{V}$ on which the source of the photon must lie, and a corresponding "event circle" on the sky (Kippen et al. 1995).

EGRET

The Energetic Gamma Ray Experiment Telescope (EGRET) worked in the range 2 MeV - 30 GeV (Nolan et al. 1992; Hartman et al. 1992). It mea-

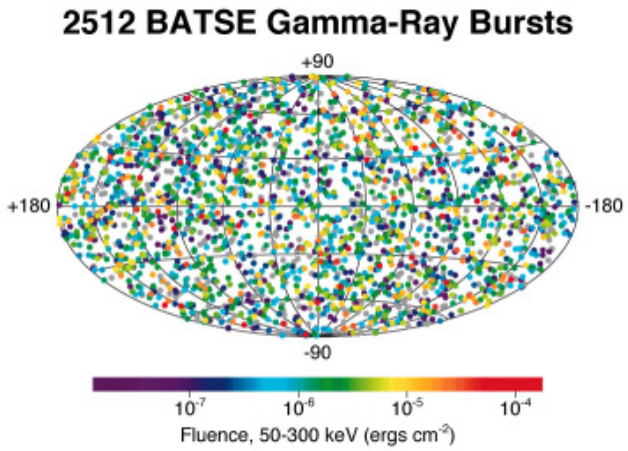

Figure 1.4: GRBs located by the BATSE detectors. Sky coordinates are galactic latitude and longitude. The color of each GRB corresponds to the indicated fluence of the burst. The source distribution is isotropic, and there is no concentration in the galactic plane, indicating an extragalactic origin. Credit: CGRO BATSE Team.

sured positions to a fraction of a degree and photon energy to within 15 %. It operated on the principle of electron-positron pair production from high energy photons interacting in the detector. The tracks of the high-energy electron and positron created were measured within the detector volume,and the axis of the **V** of the two emerging particles projected to the sky. Finally, their total energy was measured in a large calorimeter scintillation detector at the rear of the instrument.

BATSE was the most important instrument of CGRO, because it provided detailed observations of the temporal and spectral characteristics of large samples of GRBs (Fishman et al. 1991b,a), and it was the first experiment to provide rapid notifications of the coarse location of many of them. The observed isotropic sky distribution (Meegan et al. 1992; Briggs et al. 1993; Fishman & Meegan 1995) together with the intensity distribution (Brock et al. 1992) of the more than 2000 GRBs observed with BATSE during its 9 years of operation, showed with high significance that the sources had to be either at cosmological distances or very close to the solar system so as not to feel the galactic anisotropic distribution (Gehrels et al. 1994). Their origin was unlike that of any known Galactic distribution and they were not associated with any known extragalactic objects or regions. The final BATSE sky distribution of GRBs is shown in Fig. 1.4.

The BATSE data also revealed that although there is a great variety of structure in individual bursts, there were at least two types of events: short GRBs with duration 0.03 - 3 s and long GRBs with duration 7 - 400s (Yu et al. 2000; Horváth 2002). Examples of both are shown in Fig. 1.5. The morphology of the light curves is very varied, being no two identical light curves for different GRBs. The number of GRBs as a function of their duration is plotted in Fig.

1.6.

Using BATSE results, Band et al. (1993) found that the best description of the time averaged photon spectrum of a GRB (Hanlon et al. 1995), from 20 keV up to a few MeV, was the following function, which later became known as the **Band Function**:

$$N(E) = A \begin{cases} \left(\frac{E}{100keV}\right)^{\alpha} exp(-E/E_0) & \text{if } (\alpha-\beta)E_0 \geq E; \\ \left[\frac{(\alpha-\beta)E_0}{100keV}\right]^{\alpha-\beta} exp(\beta-\alpha)\left(\frac{E}{100keV}\right)^{\beta} & \text{if } (\beta-\alpha)E_0 \leq E. \end{cases} \quad (1.1)$$

Here α and β are the power-law low energy (below E_0) and high energy (above E_0) photon indices, respectively, and A is the normalization parameter. The values of these parameters change from one GRB to another (Preece 2000), with typical values of $\alpha = -1$, $\beta = -2.3$ and $E_0 = 150$ keV. This function shows a maximum (Mallozzi et al. 1995) at photon energy $E_p = E_0(2+\alpha)$ if $\beta < -2$ (see Fig.1.7).

CGRO operated in low Earth orbit (LEO) for over 9 years until it was deorbited in June 2000.

1.3 The BeppoSAX era: the cosmological nature of GRBs

Now we know that to find a distant source, an arcsecond location is needed to select the source of interest from the many faint objects that crowd the field. Fortunately, there is a long lived component associated with most GRBs, which involves material ejected at high velocity. This material will interact with the ambient medium, and the resultant heated material will radiate energy for a period of time following the burst. This is the afterglow.

So the key to the identification of GRBs was to measure a rough, few-arcminute location quickly enough so that telescopes with much better (arcsecond) resolution could manage to image the faint, rapidly fading afterglow. The Dutch-Italian satellite BeppoSAX (see Fig.1.8) played a crucial role in this matter, because it was the first X-ray mission capable of simultaneously observing targets over more than 3 decades of energy (from 0.1 to 300 keV) with a relatively large area, good energy resolution and imaging capabilities. It was a major program of the Italian Space Agency (ASI) with the participation of the Netherlands Agency for Aerospace Programmes (NIVR).

BeppoSAX was named in honour of the Italian physicist Giuseppe "Beppo" Occhialini. SAX stands for "Satellite per Astronomia a raggi X" or "Satellite for X-ray Astronomy". It contained five science instruments:

- a Low Energy Concentrator Spectrometer (LECS),
- three Medium Energy Concentrator Spectrometers (MECS),
- a High Pressure Gas Scintillation Proportional Counter (HPGSPC),
- a Phoswich Detector System (PDS), and
- two Wide Field Cameras (WFC).

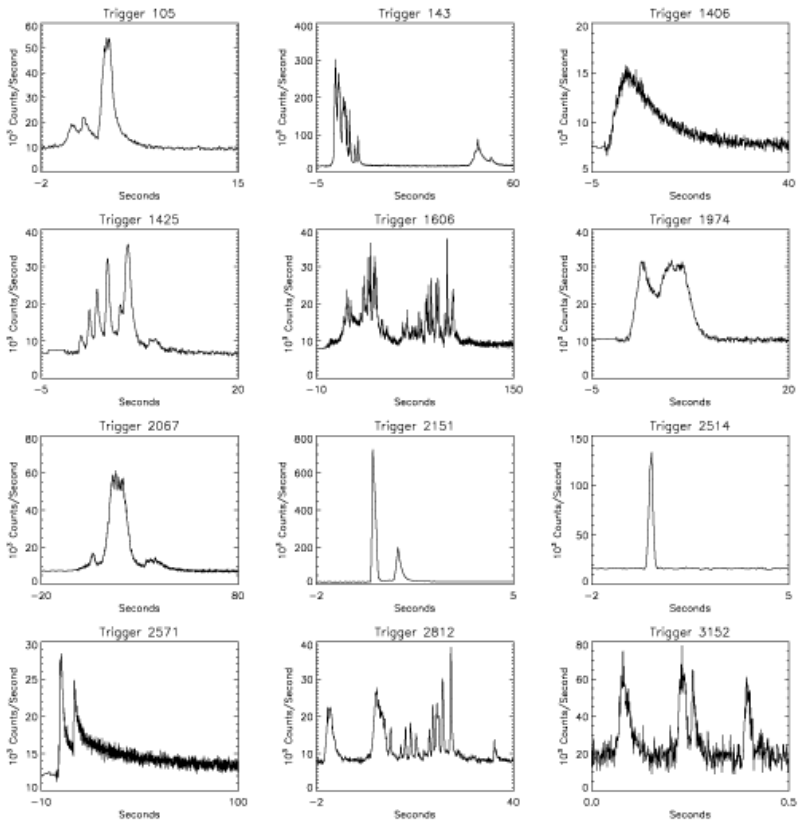

Figure 1.5: Light curves of 9 GRBs detected by BATSE. No two gamma-ray burst light curves are identical, with large variation observed in almost every property: the duration of observable emission can vary from milliseconds to tens of minutes, there can be a single peak or several individual subpulses, and individual peaks can be symmetric or with fast brightening and very slow fading. The light curves of some events have extremely chaotic and complicated profiles with almost no discernible patterns.

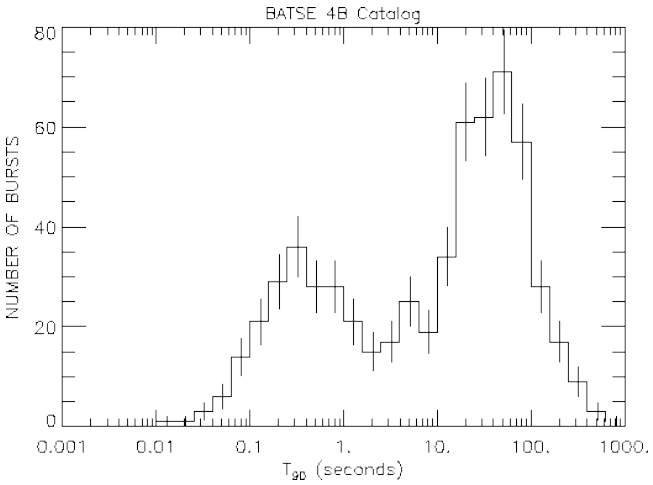

Figure 1.6: Distribution of the T_{90} for the GRBs detected by BATSE. Although the boundary between the distributions is broad, two distinct groups are clear (short and long GRBs).

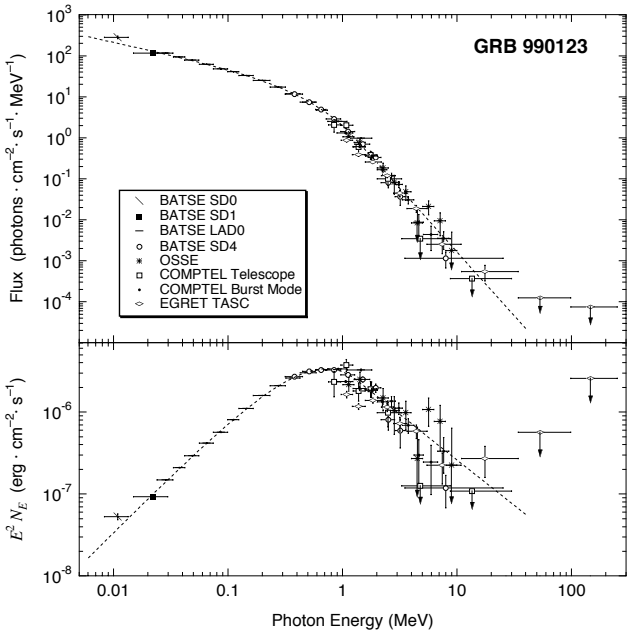

Figure 1.7: An example of GRB photon spectrum. It shows the deconvolved spectra of GRB 990123 from the CGRO detectors, shown both as photon ux N_E and in $E^2 N_E = \nu f_\nu$ units. The spectra have been rebinned into wider bins for clarity. GRB 990123 was also promptly detected and further localized with Beppo-SaX. Taken from Briggs et al. (1999).

The first four instruments (called Narrow Field Instruments or NFI) pointed to the same direction, and allowed observations of an object in a broad energy band (0.1 - 300) keV. The LECS and MECS had imaging capability, whereas the high-energy narrow field instruments were non-imaging.

The MECS contained three identical gas scintillation proportional counters operating in the 1.3 to 10 keV range. On 6 May 1997, one of the three identical MECS units was lost when a fault developed in the High Voltage power supply.

The LECS was similar to the MECS units, expect that it had a thinner window that allowed photons with lower energies (down to 0.1 keV) to pass through and operated in a "driftless" mode which is necessary to detect the lowest energy X-rays.

The HPGSPC was also a gas scintillation proportional counter, operating at a high pressure (5 atm). High pressure equals high density, and dense photon-stopping material allowed detection of photons from 4 up to 120 keV.

The PDS was a crystal (NaI/CsI) scintillator detector capable of absorbing photons up to 300 keV. The spectral resolution of the PDS was rather modest when compared to the gas detectors, but the low background counting rate resulting from the low inclination orbit (3.9°) and good background rejection capabilities made the PDS one of the most sensitive high-energy instruments flown.

The WFC contained two coded aperture cameras operating in the (2 - 30) keV range and each covering a region of 40 x 40 degrees (20 by 20 degrees full width at half maximum) on the sky. The WFC were complemented by the shielding of PDS which had a (nearly) all-sky view in the (100 - 600) keV band, ideal for detecting GRBs (see Fig.1.9).

In theory, after a GRB was seen in the PDS, the position was refined first with the WFC. However, due to the many spikes in the PDS, in practice a GRB was found using the WFC, often corroborated by a BATSE-signal. The position up to arcminute precision (depending on the signal to noise ratio of the burst) was found using the deconvoluted WFC-image. The coordinates were speedily sent out as an International Astronomical Union (IAU) and GCN circular. After this, immediate follow-up observations with the NFI and optical observatories around the world allowed accurate positioning of the GRB and detailed observations of the X-ray, optical and radio afterglow.

1.3.1 Discovery of the afterglow

On 28 February 1997, a turning point occurred in the GRB field: the italian scientists responsible for the gamma-ray burst detector onboard the satellite, i.e., E. Costa, CNR, F. Frontera, University of Ferrara, Costa et al. (1997)) and the whole team of BeppoSaX, were able to reschedule the satellite observations and point the BeppoSAX narrow field X-ray telescopes in only 8 hours at the gamma-ray burst source, using the BeppoSAX arc-minute X-ray location of GRB 970228. They detected the afterglow in X-rays and communicated the position to the optical telescopes, which detected the optical afterglow 21 hours after the burst (Djorgovski et al. 1999). This was also the first time that a GRB had been detected from Earth. A second follow-up with BeppoSAX was performed with narrow field instruments after about 3 days (see Fig.1.10). Paradijs and collaborators (van Paradijs et al. 1997) measured the location with arc second accuracy, enabling the identification of a host galaxy (see Fig.1.11)

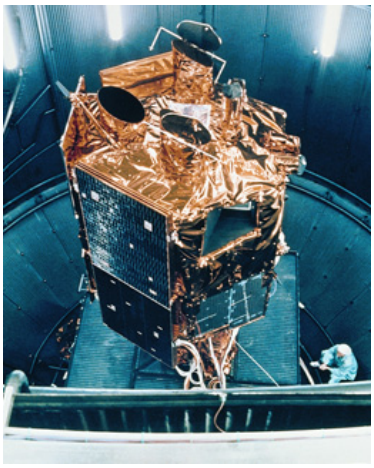

Figure 1.8: The BeppoSaX satellite.

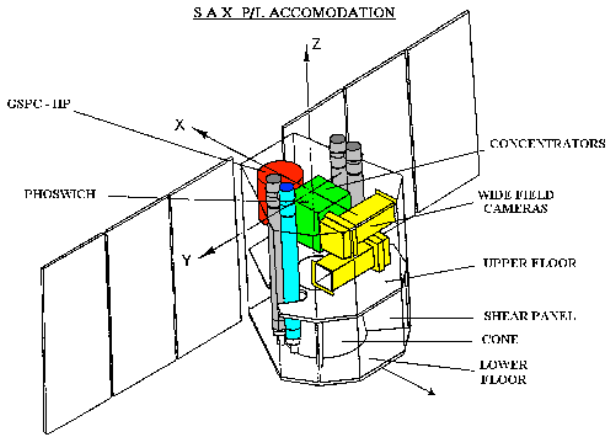

Figure 1.9: The BeppoSaX payload

and the first redshift measurement for a GRB, of $z = 0.695$. This corresponds to about 8.1 billion light years, providing robust evidence that GRBs occur at cosmological distances, well beyond the Milky Way.

This was the first of a series of successive discoveries. On May 8, 1997 GRB 970508 was detected by the WFC on GRBM trigger. The afterglow was detected by the NFIs. On May 11, when the optical afterglow was still relatively bright, the CalTech/NRAO group observed with the Keck Low Resolution Imaging Spectrograph. Various absorption lines were identified, some at $z = 0.835$, some at $z = 0.767$. The immediate consequence was to fix the scale of the energetic. From the distance it was derived an energy that, assuming an isotropic energy emission, resulted to be $E_{iso} = (0.61 \pm 0.13) \times 10^{52}$ erg. Three months later, using the VLA telescope, a radio afterglow was discovered from GRB 970508 by Frail and Kulkarni (Frail et al. 1997). On December 14, 1997 the redshift of another BeppoSaX GRB was determined: $z = 3.42$, from GRB 971214. The corresponding energetics was $E_{iso} = (2.45 \pm 0.28) \times 10^{53}$ erg. On 23 January 1999, Beppo-SaX detected GRB 990123. The Robotic Optical Transient Search Experiment (ROTSE) detected a simultaneous optical flash, making it the brightest optical GRB so far. It peaked at eighth magnitude and lasted about 15 minutes. The host galaxy[2] lied at a redshift of $z = 1.6$ (see Fig.1.12).

In other words, the observations by Beppo-SaX led to the determination of a much more accurate position for these sources in the sky, which allowed in turn, for the first time, their optical and radio identification. The optical identification has led to the determination of their cosmological distances and to their paramount energetic requirements, in some cases $\geq 10^{54}$ erg. Practically the totality of the existing theories were at once wiped out, not being able to fit stringent energy requirements imposed by the observations. It became clear instead that the energetics presented by Damour & Ruffini (1975) was indeed correct and their work represented one of the handful models still viable.

Much of the research following BeppoSAX has concentrated on GRB afterglows, a highlight of which was the successful prediction of the general X-ray and optical behavior of GRB 970228 (Meszaros & Rees 1997). Since then more than 40 afterglows have been studied in detail, and a number of interesting developments have occurred. A prompt optical flash (also predicted by theory) was found in one burst; X-ray lines believed to be from Iron and other metals have been reported from a number of bursts; and a new variety of softer bursts dubbed "X-ray flashes" has been identified, which are very similar to classical GRB but have a softer spectrum. Other work has concentrated on identifying the progenitors of GRB. Many of the afterglows identified by Beppo-SAX (all belonging to the class of 'long' bursts) have been shown to be associated with massive young stars, and in some cases a peculiar supernova ("hypernova") may be associated (Woosley & Weaver 1982; Paczyński 1998).

[2]Locating the host galaxy is not the only way to determine the redshift of a GRB. If the spectra of the afterglow show emission or absorption lines, the redshift can be derived from the energy of the lines. Observing quickly so as to collect enough photons is very important to get a decent spectrum. So a rapid, autonomous response by space and ground-based telescopes is crucial in detecting GRBs and learning about their true nature.

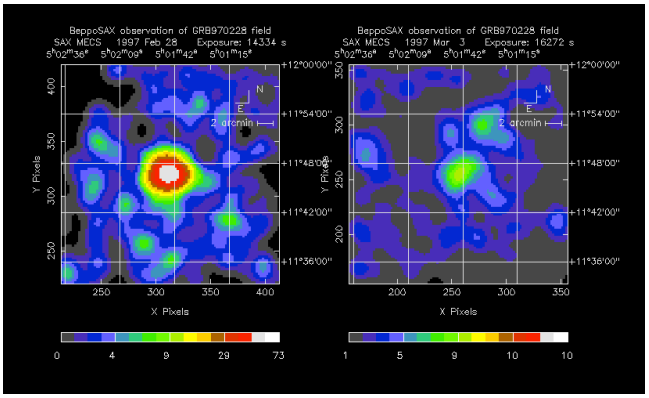

Figure 1.10: The fading X-ray afterglow of GRB 970228 as imaged by BeppoSAX. An X-ray source never seen before was discovered and localized with an accuracy of one hundred of a degree (left). The source is actually in the constellation of Orion. A second follow-up has been performed with narrow field instruments after about 3 days. This second observation has shown a strong drop, about 20 times lower, in the source flux (left).

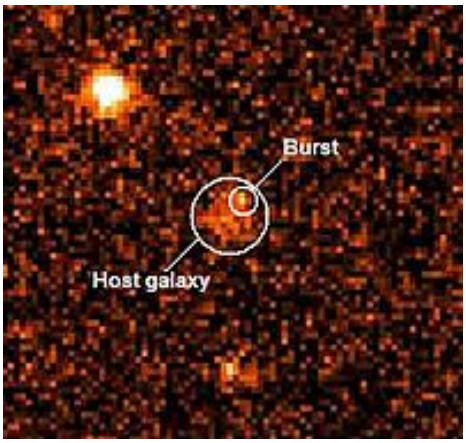

Figure 1.11: Optical afterglow of GRB 970228 as seen by the Hubble Space Telescope.

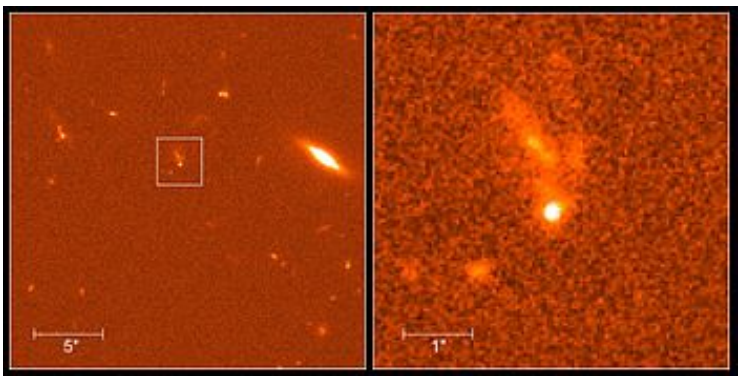

Figure 1.12: Optical afterglow of GRB 990123 (the bright dot within the white square and in the enlarged cutout) on January 23, 1999. The object above it with the finger-like filaments is its originating galaxy. This galaxy seems to be distorted by a collision with another galaxy. Source: http://imgsrc.hubblesite.org/hu/db/1999/09/images/a/formats/print.jpg

1.4 The "Standard" Fireball model

A generic scheme of a cosmological GRB model appeared in the last decades (Piran 1999), known as the "*Fireball Model*" (see Fig.1.13). This model was proposed by Goodman (Goodman 1986) and Paczynski (Paczynski 1986). It predicted the observed X-ray, optical and radio counterparts. A "fireball" is a large concentration of energy (radiation) in a small region of space in which there are relatively few baryons. According to this scheme the observed γ-rays are emitted when an ultrarelativistic energy flow is converted to radiation. Possible forms of the energy flow are kinetic energy of ultrarelativistic particles or electromagnetic Poynting flux. A great amount of energy is suddenly released in a compact volume. As a result, a fraction of this energy is converted into neutrinos and gravitational waves, while a smaller fraction goes into a high temperature fireball (kT $\geq$ MeV) consisting of $e^{\pm}$, γ-rays and baryons. This leads to the prompt emission, of energy around several 10^{53} erg and a few seconds of duration. This amount of energy is generally observed as non-thermal γ-rays, which indicates that this energy is converted to radiation in an optically thin region.

The photon luminosity inferred from the observed energies and timescales is many orders of magnitude larger than the Eddington luminosity

$$L_E = 4\pi G M m_p c/\sigma_T = 1.25 \times 10^{38}(M/M_\odot) erg/s,$$

above which radiation exceeds self-gravity, so the fireball will expand at relativistic velocities. However, the ultimate expansion velocity depends on the baryon load of the fireball. If there are too many baryons, the expansion will be sub-relativistic. The sudden release of a large quantity of gamma-ray photons into a compact region can lead to an opaque photon-lepton fireball through the production of electron-positron pairs. The term "fireball" thus refers to an opaque radiation plasma whose initial energy is significantly greater than its rest mass.

The spectrum of the prompt emission would be expected to be a blackbody (Paczynski 1986; Goodman 1986; Shemi & Piran 1990). However, the observed γ-ray spectrum is generally non-thermal. In addition, the expansion would lead to a conversion of internal energy to kinetic energy of expansion, so even after the fireball becomes optically thin, it would be highly inefficient, most of the energy being in the kinetic energy of the associated protons, rather than in photons. It has been suggested that the energy conversion occurs either due to the interaction with an external medium, like the ISM (Rees & Meszaros 1992), or due to internal processes, such as internal shocks and collisions within the flow (Narayan et al. 1992; Rees & Meszaros 1994; Paczynski & Xu 1994). These shocks can be expected to accelerate particles via the Fermi process to ultra-relativistic energies (Blandford & Eichler 1987; Achterberg et al. 2001; Ellison & Double 2002; Lemoine & Pelletier 2003; Sokolov et al. 2006) and the relativistic electron component can produce non-thermal radiation via the Synchrotron and Inverse Compton (IC) processes. Sari & Piran (1997) show that the external shock scenario is quite unlikely, unless the energy flow is confined to an extremely narrow beam, or else the process is highly inefficient. The only alternative is that the burst is produced by internal shocks. Such internal shocks have the advantage that they reproduce some of the more complicated light curves (Sari & Piran 1997; Kobayashi et al. 1997; Panaitescu & Mészáros 1999). The γ-ray emission of GRB from internal shocks radiating via a synchrotron and/or IC mechanism reproduces the general features of the γ-ray observations. There remain, however, questions concerning the low energy spectral slopes for some bursts.

The "inner engine" that produces the relativistic energy flow is hidden from direct observations. However, the observed temporal structure reflects directly its activity. This model requires a compact internal engine that produces a wind - a long energy flow (long compared to the size of the 'engine' itself) - rather than an explosive engine that produces a fireball whose size is comparable to the size of the engine. Not all the energy of the relativistic shell can be converted to radiation (or even to thermal energy) by internal shocks (Beloborodov 2003; Berezhiani et al. 2003; Berezinsky et al. 2005). The remaining kinetic energy will most likely dissipate via external shocks that will produce an "afterglow" in different wavelengths (Band et al. 2004). At present there is no agreement on the nature of the 'engine' - even though binary neutron star mergers (Berger et al. 2005) are a promising candidate. All that can be said with some certainty is that whatever drives a GRB must satisfy the following general features: It produces an extremely relativistic energy flow containing 10^{51} - 10^{52} erg. The flow is highly variable as most bursts have a variable temporal structure and it should last for the duration of the burst (typically a few dozen seconds). It may continue at a lower level on a time scale of a day or so (Berger et al. 2003). Finally, it should be a rare event occurring about once per million years in a galaxy. The rate is of course higher and the energy is lower if there is a significant beaming of the gamma-ray emission. In any case the overall GRB emission in γ-rays is $\approx 10^{52}$ erg $/10^{6}$ years/galaxy (Piran 1999).

1.4.1 Compactness Problem

Consider a typical burst with an observed fluence F. For a source emitting isotropically at a distance D this fluence corresponds to a total energy release

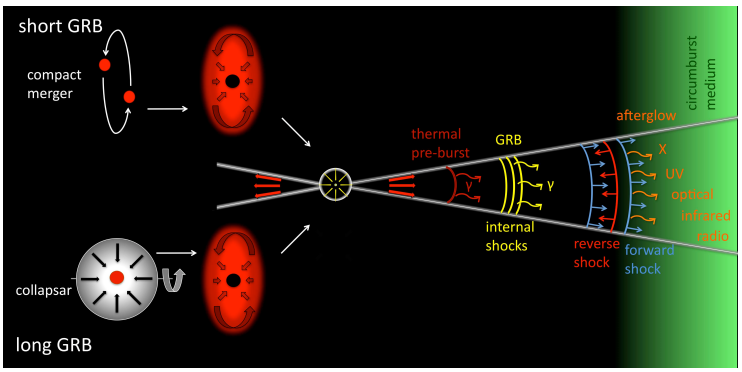

Figure 1.13: Scheme of the fireball model.

of

$$E = 4\pi D^2 F = 10^{50} erg \left(\frac{D}{3000 Mpc}\right)^2 \left(\frac{F}{10^{-7} erg/cm^2}\right). \tag{1.2}$$

The rapid temporal variability on a time scale $\delta T \approx 10$ msec implies that the sources are compact with a size $R_i \leq c\delta T \approx 3000$ km. The observed spectrum contains a large fraction of high energy γ-ray photons. These photons (with energy E_1) could interact with lower energy photons (with energy E_2) and produce $e^{\pm}$ pairs via $\gamma\gamma \rightarrow e^+e-$ if $(E_1E_2)^{1/2} > m_e c^2$. Denote by f_p the fraction of photon pairs that satisfy this condition. The average optical depth for this process is

$$\tau_{\gamma\gamma} = \frac{f_p \sigma_T F D^2}{R_i^2 m_e c^2}, \tag{1.3}$$

which is very large. Even if there are no pairs to begin with, they will form rapidly and Compton scatter lower energy photons, resulting in a huge optical depth for all photons. However, the observed non-thermal spectrum indicates that the source must be optically thin.

The solution to this so-called compactness problem comes from the invocation of relativistic expansion of the radiating material (Bloom 2011). If the material is expanding at a rate close to the speed of light, then two effects work to diminish the true optical depth greatly. First, relativistic motion leads to extreme Doppler shifts of the intrinsic spectrum; a photon observed at tens of MeV might have been generated in the source at much less than a few keV. Thus, at the source, the number of photon pairs satisfying the pair-production energy threshold is greatly reduced. Second, a relativistically expanding source that is emitting can be much larger than the observed variability timescale would suggest. The first effect reduces the inferred τ by roughly $\Gamma^{2\beta}$, where β is the Band spectral index after the peak. The second effect arises because the emitter closely lags behind the light it just emitted, so the arrival time of successive pulses is bunched up for the distant observer. A pulse emitted over a time $\delta t'$ (as viewed by someone traveling outward with the explosion) appears to last just $\delta t = \delta t'/(2\Gamma^2)$. Since the effective τ is reduced by $\Gamma^{2\beta-2}/2$, an optically thin GRB ($\tau < 1$) requires $\Gamma \gg 1$. This implies that the material producing the GRB must be moving at relativistic velocities.

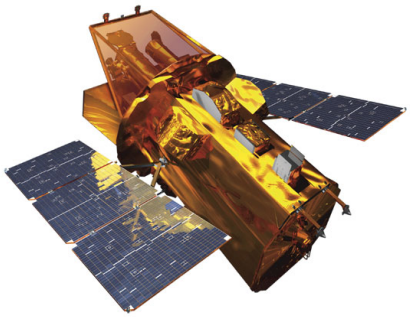

Figure 1.14: The Swift satellite.

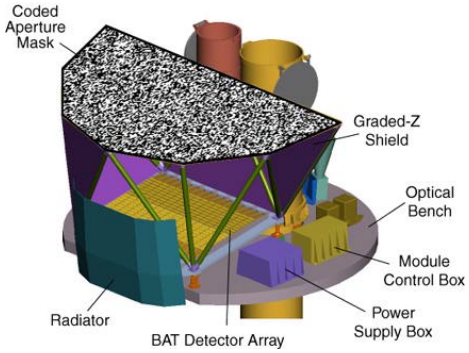

Figure 1.15: The *Swift*-BAT detector array.

1.5 The Swift era

On 20 November 2004, the Swift satellite was launched (see Fig.1.14). It is managed by the NASA Goddard Space Flight Center, and was developed by an international consortium from the United States, United Kingdom, and Italy. It has been designed to detect GRBs in the gamma-ray, X-ray, ultraviolet and optical bands. It has three instruments onboard:

BAT

The Burst Alert Telescope (BAT) (Barthelmy et al. 2005) is a highly sensitive, large FOV instrument designed to provide critical GRB triggers and 4-arcmin positions. It is a coded aperture imaging instrument with a 1.4 steradian field-of-view (half coded). It calculates an initial position with an accuracy of 1 to 4 arc-minutes within 15 seconds, decides whether the burst merits a spacecraft slew and, if so, sends the position to the spacecraft (see Fig.1.15). The energy range is 15-150 keV for imaging with a non-coded response up to 500 keV.

XRT

The X-Ray Telescope (XRT) (Burrows et al. 2004) takes images and performs spectral analysis of the GRB afterglow. This provides a more precise location of the GRB, with a typical error circle of approximately 2 arcseconds radius.

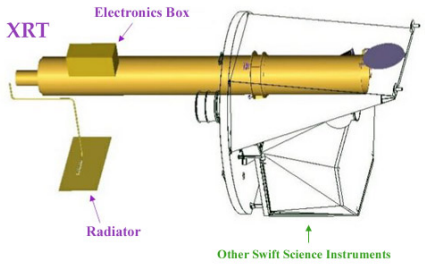

Figure 1.16: The *Swift*-XRT detector.

Figure 1.17: The *Swift*-UVOT detector.

It is also used to perform long-term monitoring of GRB afterglow light-curves for days to weeks after the event, depending on the brightness of the afterglow. The XRT uses a Wolter Type I X-ray telescope with 12 nested mirrors, focused onto a single MOS charge-coupled device (CCD). It works in the range $0.3 - 10$ keV (see Fig.1.16).

UVOT

The Ultraviolet/Optical Telescope (UVOT) (Roming et al. 2005) detects the optical afterglow once Swift has slewed towards a GRB. Co-aligned with the XRT, it provides a sub-arcsecond position, as well as optical and UV photometry through lenticular filters and low-resolution spectra (170650 nm) through the use of its optical and UV grisms (Mason et al. 2004). The UVOT is also used to provide long-term follow-ups of GRB afterglow light curves (see Fig.1.17). Since UVOT has photon counting detectors, which are able to retain individual photon positions and timing information, it operates in a mode more similar to typical x-ray telescopes than to typical optical telescopes.

The Swift mission has four key scientific objectives:
- To determine the origin of GRBs,
- To use GRBs to expand the understanding of the young universe. GRBs seem

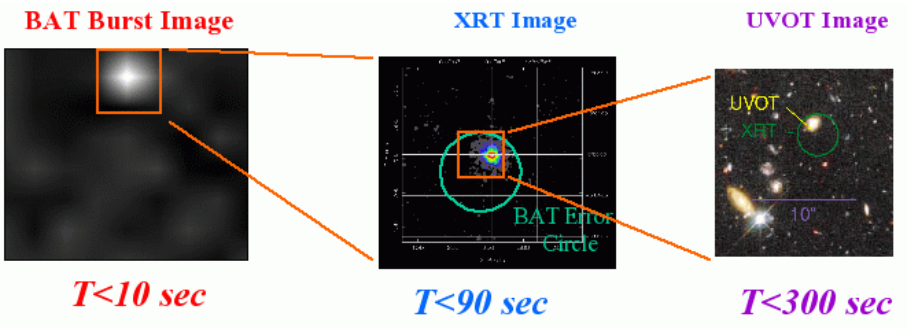

Figure 1.18: *Swift* response. The BAT triggers on a GRB and calculates its position to $\sim$ 3 arcmin. The spacecraft autonomously slews to GRB position in 20-70 seconds. The XRT determines the position to within $\sim$ 3 arcsec. The UVOT images the field and transmits a finding chart to ground.

to take place at "cosmological distances" of many millions or billions of light-years, which means they can be used to probe the distant, and therefore young, cosmos.
- To conduct an all-sky survey which will be more sensitive than any previous one, and will add significantly to scientific knowledge of astronomical X-ray sources.
- To serve as a general purpose gamma-ray/X-ray/optical observatory platform, performing rapid "target of opportunity" (ToO) observations of many transient astrophysical phenomena, such as supernovae.

Fig.1.18 shows how the three instruments complement each other to give a quick response. The BAT detects elevated gamma-ray emission from a large portion of the sky. After this initial detection, *Swift* slews rapidly and autonomously, re-pointing itself to bring the detected burst into the field of view of the sensitive narrow field instruments (XRT and UVOT), which then observe the afterglow. *Swift* provides spectra and multi-wavelength light curves for the duration of the afterglow and, where possible, distance determinations. This will help enable the most comprehensive study of GRBs and their host galaxies to date.

1.6 The Fermi era

The Fermi Gamma-ray Space Telescope, formerly referred to as the Gamma-ray Large Area Space Telescope (GLAST) (Michelson 2008; Meegan 2008), is a space observatory being used to perform gamma-ray astronomy observations from low Earth orbit (see Fig. 1.19). Fermi was launched on 11 June 2008 at 16:05 GMT aboard a Delta II 7920-H rocket. The mission is a joint venture of NASA, the United States Department of Energy, and government agencies in France, Germany, Italy, Japan, and Sweden.

Fermi includes two scientific instruments, the Large Area Telescope (LAT) (Cohen-Tanugi 2008) and the Gamma-ray Burst Monitor (GBM) (Meegan et al. 2009; Bhat et al. 2009). The LAT is an imaging gamma-ray detector (a pair-conversion instrument) which detects photons with energy in the range (30 MeV

Figure 1.19: The Fermi satellite.

- 300 GeV), with a field of view of about 20% of the sky; it may be thought of as a sequel to the EGRET instrument on the Compton gamma ray observatory. The GBM consists of 14 scintillation detectors, twelve sodium iodide (INa) crystals for the 8 keV to 1 MeV range and two bismuth germanate (BGO) crystals with sensitivity from 150 keV to 30 MeV, and can detect GRBs in that energy range across all the sky not occluded by the Earth (see Fig.1.20).

General Dynamics Advanced Information Systems (formerly Spectrum Astro and now Orbital Sciences) in Gilbert, Arizona designed and built the spacecraft that carries the instruments. It travels in a low, circular orbit with a period of about 95 minutes. Its normal mode of operation maintains its orientation so that the instruments will look away from the earth, with a "rocking" motion to equalize the coverage of the sky. The view of the instruments will sweep out across most of the sky about 16 times per day. The spacecraft can also maintain an orientation that points to a chosen target. Data from the instruments are available to the public through the Fermi Science Support Center website[3]. Software for analyzing the data is also available.

The main objectives of the mission are:

-Explore the most extreme environments in the Universe, where nature harnesses energies far beyond anything possible on Earth.

-Search for signs of new laws of physics and what composes the mysterious Dark Matter.

-Explain how black holes accelerate immense jets of material to nearly light speed.

-Help crack the mysteries of GRBs.

-Answer long-standing questions across a broad range of topics, including solar flares, pulsars and the origin of cosmic rays.

[3]http://fermi.gsfc.nasa.gov/ssc/

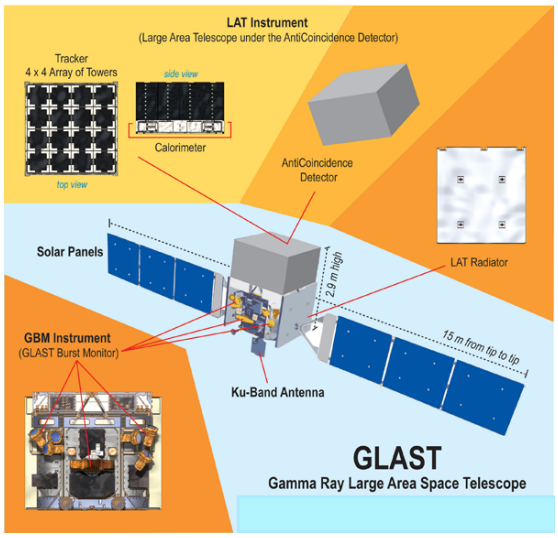

Figure 1.20: The Fermi Gamma-Ray Space telescope (formerly known as GLAST) instruments. The Large Area Telescope (LAT) measures high-energy photons via detection of electron-positron pairs produced in tungsten sheets inside the direction-sensitive tracker towers. The energy of the pairs is measured in the calorimeter unit under the tracker. The GBM consists of 14 scintillation detectors, twelve sodium iodide (INa) crystals for the 8 keV to 1 MeV range and two bismuth germanate (BGO) crystals with sensitivity from 150 keV to 30 MeV, and can detect GRBs in that energy range across all the sky not occluded by the Earth. Taken from Winstein & Zurek (2009).

"Only two things are infinite, the
universe and human stupidity, and
I'm not sure about the former."
Albert Einstein

Chapter 2

The Fireshell Model

2.1 Description of the Fireshell Model

Thanks to the observations by the *Fermi* and *Swift* satellites, it turned out that the standard classification of GRBs as "long" and "short" is misleading, or at least incomplete, and needs to be revised. We here describe an alternative theoretical model, the *Fireshell Model*, which divides GRBs in three classes: the *long*, *genuine short* and *disguised short* GRBs. This classification is based on the intrinsic properties of the bursts, as the CBM density, the amount of energy emitted in each phase and other quantities that will be described below.

The Fireshell Model assumes a progenitor that approaches asymptotically the formation of a Kerr-Newmann black hole and gravitationally collapses to it. In the end a GRB is produced, but the initial conditions and therefore the outcome is different from the Fireball Model. While the core of the progenitor is collapsing and the outer shells are expanding, an electric field E is created in between. The distribution of the charges in the inner and outer shells makes the star act as a capacitor (Preparata et al. 1998). This field grows until it reaches its critical value, given by $E_c = m^2c^3/\hbar e$. At this point, a quantum phenomenon called vacuum polarization occurs, leading to the formation of electron-positron ($e^+ - e^-$) pairs at expenses of the gravitational energy. The $e^+ - e^-$ plasma is optically thick and has a total energy $E_{tot}^{e^\pm}$ in the range $10^{49} - 10^{54}$ erg. Some of the pairs will annihilate to form photons.

On a timescale of $\sim 10^{-12}$ s it reaches thermal equilibrium and then it accelerates due to its internal radiation pressure, expanding in a region of low baryonic contamination because the environment has been cleared by the gravitational collapse of the central black hole. The Lorentz Gamma factor increases with radius and the dynamics can be described by the energy conservation and the condition of adiabatic expansion:

$$T^{0\nu}_{,\nu} = 0 \tag{2.1}$$

$$\frac{\epsilon_0}{\epsilon} = \left(\frac{V}{V_0}\right)^\Gamma = \left(\frac{V'\gamma}{V'_0\gamma_0}\right)^\Gamma . \tag{2.2}$$

Here $T^{\mu\nu}$ is the energy-momentum tensor of the $e^+ - e^-$ plasma, assumed to be a perfect fluid; ϵ is its internal energy density, V and V' are the volumes in

the co-moving and laboratory frames, respectively, and Γ is the thermal index. The quantities with and without the subscript $\circ$ are measured at two different times during the expansion.

Outside this region there is the baryonic remnant of the progenitor star. Its existence is guaranteed by the charge neutrality condition of the system: the collapsing core has the opposite charge of the remnant and the system as a whole is clearly neutral. As the fireshell moves out, it catches this baryonic remnant, whose distribution is assumed to be in a shell of thickness Δ, at a distance such that the system has not yet reached the transparency. At the moment when the baryons are engulfed by the fireshell the Γ factor suddenly drops. The collision is fully inelastic. The baryons of the shell are described by the *baryon load* parameter $B = M_B c^2/E_{tot}^{e^\pm}$, where M_B is the baryon mass and $E_{tot}^{e^\pm}$ is the initial energy of the plasma inside the fireshell. This is a dimensionless parameter.

The still optically thick fireshell now composed by electrons, positrons, baryons and protons in thermodynamical equilibrium self accelerates again up to relativistic velocities. The Lorentz γ factor increases again with radius until the transparency point is reached (at this point it reaches the asymptotic value $\gamma_{asym} = 1/B$). A flash of radiation is then emitted, known as the "Proper-GRB" (P-GRB) (Ruffini et al. 2001b). The amount of energy radiated in the P-GRB is only a fraction of the initial energy $E_{tot}^{e^\pm}$. The remaining energy is stored in the kinetic energy of the now optically thin baryonic and leptonic matter fireshell that expands ballistically and starts to slow down due to the inelastic collisions with the Circumburst Medium (CBM). the Lorentz γ factor will decrease with radius. This interaction gives rise to the extended afterglow, a multi-wavelength emission. The dynamical equations are the same as previously, but we need to add the conservation of the baryon number:

$$\frac{n_B^\circ}{n_B} = \frac{V}{V_0} = \frac{V'\gamma}{V_0\gamma_0} \tag{2.3}$$

Fig. 2.1 shows the evolution of the Lorentz γ factor as a function of the external radius (Ruffini et al. 2001c, 2003b).

2.2 Long, short and disguised GRBs: the role of the P-GRB and the afterglow

Within the Fireshell scenario we can discriminate between long and short bursts by the amount of energy emitted in the first phase with respect to the second one. This difference is determined by the B parameter. When $3 \times 10^{-4} \leq B \leq 10^{-2}$ we have a long burst and the extended afterglow phase is energetically predominant. When $B \leq 10^{-5}$ the P-GRB phase is predominant and we observe a short burst. B must be $\leq 10^{-2}$, otherwise there will be no relativistic expansion. There is another class, the "disguised short" GRBs. They appear like short bursts because they are characterized by a first, short, hard episode and a following deflated tail, but this last part, which coincides with the peak of the extended afterglow, is actually energetically predominant. This is due to the very low density of the CBM ($\sim 10^{-3}$ part/cm^3), compatible with galactic halos. Some GRBs belonging to this class are GRB 970228, GRB 060614, GRB

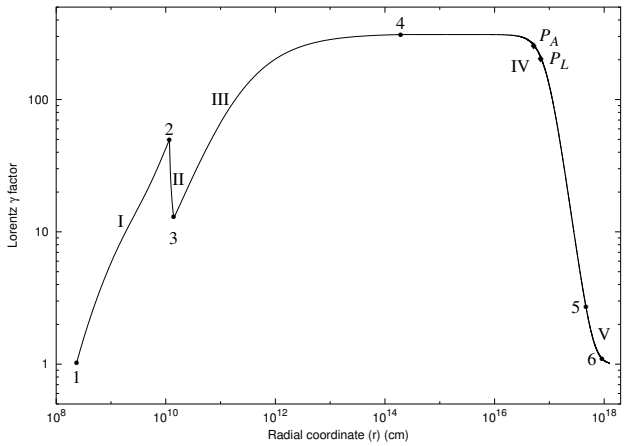

Figure 2.1: Lorentz gamma factor as a function of the external radius. Taken from Ruffini et al. (2001c).

071227 and GRB 050509B. The sole extended afterglow part of these GRBs follows the Amati relation, while the P-GRB part does not.

After the transparency point is reached, the contribution of the rate equation starts to be important. The rate equation describes the annihilation of $e^{\pm}$ pairs and is given by

$$\frac{\partial}{\partial t}N_e^{\pm} = -N_e^{\pm}\frac{1}{V'}\frac{\partial V'}{\partial t} + \sigma\bar{\nu}\frac{1}{\gamma^2}\left(N_{e^{\pm}}^2(T) - N_{e^{\pm}}^2\right), \tag{2.4}$$

where $N_{e^{\pm}}$ is the number of $e^{\pm}$ pairs and $N_{e^{\pm}}(T)$ is the number of $e^{\pm}$ in thermal equilibrium at temperature T.

The characteristic inhomogeneities of the CBM can be estimated by fitting the X-ray luminosity of the source and imposing the fully radiative condition in the collision between the ultrarelativistic baryonic shell and and the clouds of the Interstellar Medium (ISM). The complete solution is developed in Bianco & Ruffini (2004, 2005a,b), together with the analytic expression of the Surfaces of Equal arrival Time (EQTS) of the photons at the detector.

We therefore define a "canonical" GRB light curve with two sharply different components: the P-GRB and the extended afterglow. The afterglow presents three different regimes: a rising part, a peak and a decaying tail. What is usually called "Prompt emission" in the literature mixes the P-GRB with the rising part and the peak of the extended afterglow (Ruffini et al. 2003a). It is appropriate to stress that in the emission of the P-GRB there are two different contributions: one corresponding to the emission of the photons due to the reaching of the transparency condition, and the second originating from the interaction of the protons and electrons with the CBM. Therefore, a spectral energy distribution with a thermal component and a non-thermal one should be expected to occur.

Fig. 2.2 (first panel) shows the evolution of the radius at transparency as a function of B, for four different values of $E_{tot}^{e^{\pm}}$ in the interval $(10^{49} - 10^{55})$ erg. If we solve the rate equation we can evaluate the evolution of the temperature during the fireshell expansion, all the way up to the transparency condition. The

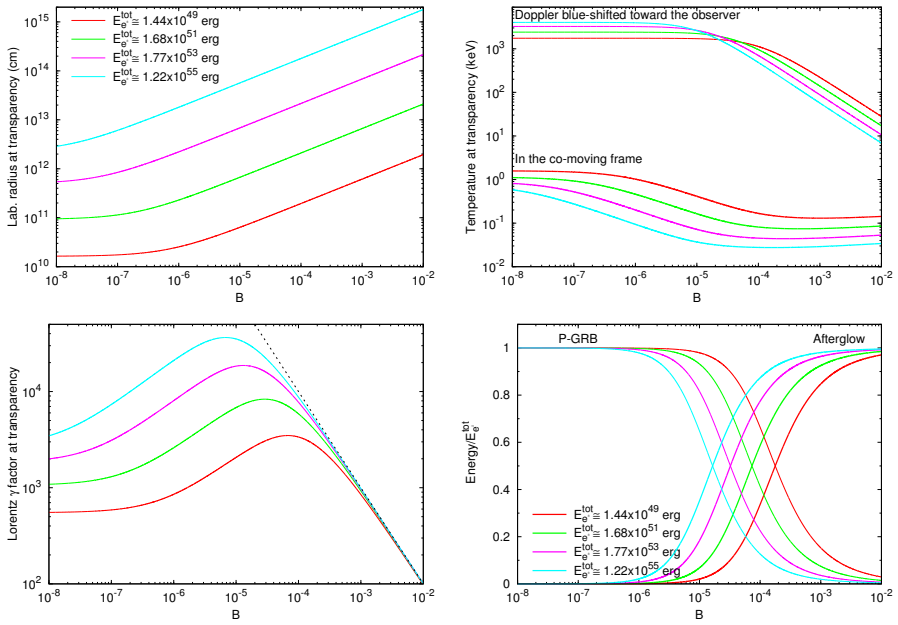

Figure 2.2: Laboratory radius (left upper panel) and fireshell temperature (right upper panel) in the co-moving and observer frame at the transparency emission; Lorentz Gamma factor at the transparency (left lower panel) and energy radiated in the P-GRB and in the afterglow in units of $E_{tot}^{e^\pm}$ as a function of the baryon load B, for 4 different values of $E_{tot}^{e^\pm}$ (right lower panel).

second panel of Fig. 2.2 shows the fireshell temperature T at the transparency point (i.e. the temperature of the P-GRB radiation) as a function of the baryon load B. Both the value in the co-moving frame $T_\circ^{com}$ and the one Doppler blue-shifted toward the observer $T_\circ^{obs} = (1+\beta_\circ)\gamma_\circ T_\circ^{com}$ are plotted, where $\beta_\circ$ is the fireshell speed at the transparency point in units of c. The third panel of Fig. 2.2 shows the value of the Lorentz γ factor as a function of B. The fourth panel shows the total energy radiated at the transparency point in the P-GRB and the one converted into baryonic and leptonic kinetic energy and later emitted in the extended afterglow. The plot is drawn for the same four different values of $E_{tot}^{e^\pm}$ of the other panels. We see that for $B \leq 10^{-5}$ the total energy emitted in the P-GRB is always larger than the one emitted in the extended afterglow. In the limit $B \to 0$ it gives rise to a genuine short GRB. On the other hand, for $3 \times 10^{-4} \leq B < 10^{-2}$ the total energy emitted in the P-GRB is always smaller than the one emitted in the extended afterglow. If it is not below the instrumental threshold and if $n_{CBM} \sim 1$ particle/cm^3, the P-GRB can be observed in this case as a small pulse preceding the main GRB event (which coincides with the peak of the extended afterglow), i.e. as a GRB precursor. Therefore, we can define the P-GRB as the precursor emitted when the fireshell becomes transparent (Ruffini et al. 2009, 2003a, 2001b, 2008a; Bernardini et al. 2007; Bianco et al. 2008a,b).

2.3 The physics of GRBs after the transparency

The dynamics of the optically thin fireshell of baryonic matter propagating in the CBM can be obtained from the conservation of energy and momentum (Bianco & Ruffini 2005b).

$$dE_{int} = (\gamma - 1) dM_{CBM} c^2, \tag{2.5}$$

$$d\gamma = -\frac{\gamma^2 - 1}{M} dM_{CBM}, \tag{2.6}$$

$$dM = \frac{1 - \epsilon}{c^2} dE_{int} + dM_{CBM}, \tag{2.7}$$

and

$$dM_{CBM} = 4\pi m_p n_{CBM} r^2 dr. \tag{2.8}$$

Here γ is the Lorentz gamma factor, E_{int} is the internal energy, M is the mass-energy, n_{CBM} is the CBM number density, m_p is the proton mass, ϵ is the emitted fraction of the energy developed in the collision with the CBM and M_{CBM} is the amount of CBM mass swept up within the radius r: $M_{CBM} = m_p n_{CBM} \frac{4}{3}\pi(r^3 - r_0^3)$, where r_0 is the starting radius of the shock front.

When using these conservation laws within the Fireshell scenario, the exact solution of the equations of motion of the fireshell is adopted, contrary to the standard model, in which an ultra relativistic approximation is used. Therefore, the Lorentz gamma factor takes the form

$$\gamma^2 = \frac{\gamma_0^2 + 2\gamma_0 (M_{CBM}/M_B) + (M_{CBM}/M_B)^2}{1 + 2\gamma_0 (M_{CBM}/M_B) + (M_{CBM}/M_B)^2} \tag{2.9}$$

in the adiabatic regime ($\epsilon = 0$) and

$$\gamma = \frac{1 + (M_{CBM}/M_B)(1 + \gamma_0^{-1})[1 + (1/2)(M_{CBM}/M_B)]}{\gamma_0^{-1} + (M_{CBM}/M_B)(1 + \gamma_0^{-1})[1 + (1/2)(M_{CBM}/M_B)]} \tag{2.10}$$

in the fully radiative regime ($\epsilon = 1$).

2.4 Modified spectrum

The radiation viewed in the co-moving frame of the accelerated baryonic matter is assumed to have a thermal spectrum and to be produced by the interaction of the CBM with the front of the expanding optically thin fireshell (Ruffini et al. 2004). However, the shape of the final instantaneous spectrum in the laboratory frame is non-thermal (Bernardini et al. 2005). In fact, as explained in Ruffini et al. (2004), the temperature of the fireshell is evolving with the co-moving time and, therefore, each single instantaneous spectrum is the result of an integration of hundreds of thermal spectra with different temperatures over the corresponding *EQuiTemporal Surfaces* (EQTS), which we will explain below. This calculation produces a non thermal instantaneous spectrum in the observer frame (Bernardini et al. 2005). Another distinguishing feature of the GRB spectra which is also present in these instantaneous spectra is the hard to soft transition during the evolution of the event (Bernardini et al. 2005;

Piran 1999; Frontera et al. 2000; Ghirlanda et al. 2002). In fact the peak of the energy distributions E_p shifts monotonically to softer frequencies with time (Bernardini et al. 2005). This feature explains the change in the power-law (PL) low energy spectral index α (Band et al. 1993) which at the beginning of the prompt emission of the burst ($t_{ad} = 2$ s) is $\alpha = 0.75$, and progressively decreases for later times. In this way the link between E_p and α identified in Crider et al. (1997) is explicitly shown.

The time-integrated observed GRB spectra show a clear power-law behavior. Within a different framework (see e.g. Pozdnyakov et al. (1983)), it has been argued that it is possible to obtain such PL spectra from a convolution of many non-PL instantaneous spectra monotonically evolving in time. This result was recalled and applied to GRBs assuming for the instantaneous spectra a thermal shape with a temperature changing with time (Blinnikov et al. 1999). The integration of such energy distributions over the observation time gives a typical PL shape possibly consistent with GRB spectra.

In the Fireshell model, the instantaneous spectrum is not a BB. Each instantaneous spectrum is obtained by an integration over the corresponding EQTS: it is itself a convolution, weighted by appropriate Lorentz and Doppler factors, of thousands of thermal spectra with variable temperature. Therefore, the time-integrated spectra are not plain convolutions of thermal spectra: they are convolutions of convolutions of thermal spectra (Ruffini et al. 2004; Bernardini et al. 2005). The modified BB spectrum is therefore characterized by a different asymptotic PL index in the low-energy region with respect to the thermal one (Patricelli et al. 2012). This index is represented by a free parameter α, so that the pure thermal spectrum corresponds to the case $\alpha = 0$:

$$\frac{dN_\gamma}{dV d\epsilon} = \left(\frac{8\pi}{h^3 c^3}\right)\left(\frac{\epsilon}{k_B T}\right)^{\alpha} \frac{\epsilon^2}{exp\left(\frac{\epsilon}{k_b T}\right) - 1}. \tag{2.11}$$

2.5 EQuiTemporal Surfaces (EQTS)

In general, besides Eqs.(2.5), (2.6), (2.7), and (2.8), one more equation is needed to express the dependence of ϵ with the radial coordinate. However, we assume it is constant.

For the case of a spherically symmetric expansion, the EQTS are surfaces of revolution around the line of sight (Bianco & Ruffini 2005b). Their general expression in the form $\vartheta = \vartheta(r)$, corresponding to an arrival time t_a[1] of the photons at the detector, can be obtained from

$$ct_a = ct(r) - rcos\vartheta + r^*, \tag{2.12}$$

where r^* is the initial size of the expanding source, ϑ is the angle between the radial expansion velocity of a point on its surface and the line of sight, and $t = t(r)$ is its equation of motion, expressed in the laboratory frame, obtained by the integration of the Eqs.(2.5), (2.6), (2.7) and (2.8). From the definition of the Lorentz gamma factor, $\gamma^2 = 1 - (dr/cdt)^2$, we have

[1]The arrival time is defined as $\Delta t_a = \Delta t - \frac{r(\Delta t)}{c} = \Delta t\left(1 - \frac{v}{c}\right)$. The difference between the emission time Δt and the arrival time is just due to a Doppler contraction and does not involve any Lorentz transformation.

$$ct(r) = \int_0^r [1 - \gamma^{-2}(r')]^{-1/2} dr, \tag{2.13}$$

where $\gamma(r)$ comes from the integration of Eqs.(2.5), (2.6), (2.7) and (2.8).

As mentioned in section 2.3, the dynamics of the system in the adiabatic case ($\epsilon = 0$) is given by Eq. (2.9). If we perform an exact analytic integration of $ct(r)$ using Eq. (2.9), we obtain the exact analytic solution:

$$t(r) = \left(\gamma_0 - \frac{m_i^0}{M_B}\right) \frac{r - r_0}{c\sqrt{\gamma_0^2 - 1}} + \frac{m_i^0}{4M_B r_0^3} \frac{r^4 - r_0^4}{c\sqrt{\gamma_0^2 - 1}} + t_0. \tag{2.14}$$

Here t_0 is the value of the time t at the beginning of the afterglow phase and $m_i^0 = (4/3)\pi m_p n_{ISM} r_0^3$.

The analytic expression of the EQTS in the adiabatic regime can be then obtained substituting this expression for $t(r)$ in Eq.(2.12). We obtain

$$cos\vartheta = \frac{m_i^0}{4M_B\sqrt{\gamma_0^2 - 1}} \left[\left(\frac{r}{r_0}\right)^3 - \frac{r_0}{r}\right] + \frac{ct_0}{r} - \frac{ct_a}{r} + \frac{r^*}{r} - \frac{\gamma_0 - (m_i^0/M_B)}{\sqrt{\gamma_0^2 - 1}} \left(\frac{r_0}{r} - 1\right). \tag{2.15}$$

In the case of a fully radiative regime ($\epsilon = 1$) the dynamics of the system is given by Eq.(2.10), and if we perform an exact analytic integration of $ct(r)$ using Eq.(2.10) we obtain

$$\begin{aligned} t(r) =& \frac{M_b - m_i^0}{2c\sqrt{C}}(r - r_0) + \frac{m_i^0 r_0}{8c\sqrt{C}} \left[\left(\frac{r}{r_0}\right)^4 - 1\right] + \frac{r_0\sqrt{C}}{12cm_i^0 A^2} ln \left[\frac{[A + (r/r_0)]^3 (A^3 + 1)}{[A^3 + (r/r_0)^3](A + 1)^3}\right] + \\ &+ t_0 + \frac{r_0\sqrt{3C}}{6cm_i^0 A^2} \left[arctan\frac{2(r/r_0) - A}{a\sqrt{3}} - arctan\frac{2 - A}{a\sqrt{3}}\right], \end{aligned} \tag{2.16}$$

where $A = [(M_B - m_i^0)/m_i^0]^1/3$ and $C = M_B^2(\gamma_0 - 1)/(\gamma_0 + 1)$.

The analytic expression for the EQTS in the fully radiative regime is obtained substituting this expression in Eq.(2.12):

$$\begin{aligned} cos\vartheta =& \frac{M_b - m_i^0}{2r\sqrt{C}}(r - r_0) + \frac{m_i^0 r_0}{8r\sqrt{C}} \left[\left(\frac{r}{r_0}\right)^4 - 1\right] + \frac{r_0\sqrt{C}}{12rm_i^0 A^2} ln \left[\frac{[A + (r/r_0)]^3 (A^3 + 1)}{[A^3 + (r/r_0)^3](A + 1)^3}\right] + \\ &+ \frac{ct_0}{r} - \frac{ct_a}{r} + \frac{r^*}{r} + \frac{r_0\sqrt{3C}}{6rm_i^0 A^2} \left[arctan\frac{2(r/r_0) - A}{a\sqrt{3}} - arctan\frac{2 - A}{a\sqrt{3}}\right]. \end{aligned} \tag{2.17}$$

Fig.2.3 shows the EQTS in both the adiabatic and fully radiative regimes, for selected values of the arrival time.

2.6 Simulation of the light curve and spectrum of a GRB afterglow within the Fireshell model

The majority of the works in the current literature have addressed the analysis of the prompt emission as originating from various combinations of synchrotron

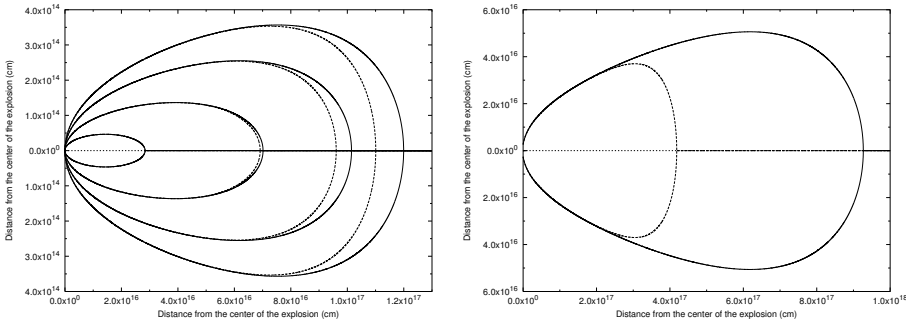

Figure 2.3: Comparison between EQTSs in the adiabatic regime (solid lines) and in the fully radiative regime (dashed lines). The left plot shows the EQTSs for $t_a = 5$s, $t_a = 15$s, $t_a = 30$s, and $t_a = 45$s, respectively, from the inner to the outer one. The right plot shows the EQTS at an arrival time of 2 days. Taken from Bianco & Ruffini (2005b).

and inverse Compton processes (Piran 2004). It appears clear, however, that this interpretation is not satisfactory (Ghirlanda et al. 2003; Kumar & McMahon 2008; Piran et al. 2009). Furthermore, in the description of an ultrarelativistic collision between protons and electrons and the CBM new collective processes of ultrarelativistic plasma physics occur, not yet fully explored and understood.

We have adopted a very pragmatic approach in the Fireshell model by making full use of the knowledge of the equations of motion, of all the EQTS formulations and of the correct relativistic transformations between the co-moving frame of the fireshell and the observer frame. In this respect, we have adopted a fundamental procedure: to make an ansatz on the spectral properties of emission of the collisions between the baryons and the CBM in the comoving frame, and then evaluate all the observational properties in the observer frame. In order to take into proper account the filamentary, clumpy and porosity structure of the CBM, we have introduced an additional parameter $\mathcal{R}$: the fireshell surface filling factor. It is defined as the ratio between the effective emitting area of the fireshell A_{eff} and its total visible area A_{vis} (Ruffini et al. 2002, 2004, 2005):

$$\mathcal{R} = \frac{A_{eff}}{A_{vis}}. \tag{2.18}$$

It must be emphasized that the fact that only a fraction $\mathcal{R}$ of the shell surface is emitting does not mean that only a fraction $\mathcal{R}$ of the total shell energy is emitted. We must in fact distinguish between an instantaneous interaction of the fireshell with a single filament and its overall interaction with all the filaments of the entire cloud giving rise to the spiky structure of the light curve. This global interaction is clearly the superposition of randomly distributed instantaneous events. The different filaments inside the cloud interact with different parts of the fireshell and the entire cloud reduces the kinetic energy of the entire fireshell. The key point is that, during the prompt emission, the cloud, typically with a mass of the order of $10^{-8}-10^{-11}M_{\odot}$, covers the entire visible area of the fireshell (typically with a radius between $10^{13} - 10^{15}$ cm). Consequently, at any given instant of time, each filament of the cloud covers only a small fraction of the fireshell surface. However, when we integrate over the cloud crossing time, the

coverage of the cloud as a whole is equal to unity (Patricelli et al. 2012).

To best reproduce the observational data within the Fireshell model, we need to determine the following five parameters: $E_{tot}^{e^\pm}$, B, n_{CBM} and $\mathcal{R}$. The procedure assumes a specific value of $E_{tot}^{e^\pm}$ and B. It is clear that $E_{tot}^{e^\pm}$ has to be larger or equal to the observed isotropic equivalent energy E_{iso} of the GRB. $E_{tot}^{e^\pm}$ can be actually quite larger than E_{iso} since, in many sources, we are limited by the threshold and the bandpass of the detectors. The value of B is determined by the ratio between the energetics of the P-GRB and of the extended afterglow, as well as by the time separation between the corresponding peaks (Ruffini et al. 2001b, 2008a; Aksenov et al. 2010).

The determination of the three remaining parameters depends on the detailed "fitting" of the shape of the extended afterglow light curves and spectra. In particular, the parameter $\mathcal{R}$ determines the effective temperature in the co-moving frame and the corresponding peak energy of the spectrum; α determines the low energy slope of the co-moving spectrum and n_{CBM} determines the temporal behavior of the light curve. It is found that the CBM is typically formed of "clumps" of width $\sim 10^{15} - 10^{16}$ cm and density contrast $10^{-1} \leq \delta n/n \leq 10$. Particularly important is the determination of the average value of n_{CBM}. Values of the order of $0.1-10$ particles/cm^3 have been found for GRBs exploding inside star forming region galaxies, while values of the order of 10^{-3} particles/cm^3 have been found for GRBs exploding in galactic halos (i.e. the "disguised" GRBs, see (Bernardini et al. 2007; Caito et al. 2009, 2010; de Barros et al. 2011)).

"Fitting" a GRB within the Fireshell model is much more complex than simply fitting the $N(E)$ spectrum with phenomenological analytic formulas for a finite temporal range of the data. It is a consistent picture, which has to "fit" the intrinsic parameters of the source, as well as its spectrum and its light curve temporal structure (Patricelli et al. 2012). Concerning the theoretical spectrum to be compared with the observational data, it is obtained by an averaging procedure of instantaneous spectra. In turn, each instantaneous spectrum is linked to the fit of the observed multiband light curves in the chosen time interval. Therefore, both the "fit" of the spectrum and of the observed multiband light curves have to be performed together and jointly optimized. Moreover, the parameters used in the numerical simulations are not independent. In fact, they have to be computed self-consistently through the entire dynamical evolution of the system and not separately at each time step. For each spike in the light curve the parameters of the corresponding CBM clumps must be computed, taking into proper account all the thousands of convolutions of co-moving spectra over each EQTS leading to the observed spectrum. It is clear then that since the EQTS encompass emission processes occurring at different co-moving times, weighted by their Lorentz and Doppler factors, the "fitting" of a single spike of the light curve is not only a function of the properties of the specific CBM clump but of the entire previous history of the source. Any step of the "fitting" process affects the entire following evolution and, viceversa, at any step a "fit" must be made consistently with all the previous and subsequent history: due to the non linearity of the system and to the EQTS, any change in the fit produces observable effects up to a much later time. This implies that the fitting process cannot proceed for successive temporal steps: the complete analysis must be applied to the entire GRB as a whole, to avoid possible systematic

error propagation from a temporal step to the following ones. This leads to an extremely complex trial and error procedure in the fitting of the data in which the uniqueness of the parameters defining the source are further and further narrowed down. Of course, we cannot expect the latest parts of the fit to be very accurate, since some of the basic hypotheses on the equations of motion, and the possible fragmentation of the shell (Dainotti et al. 2007) can affect the fitting procedure.

"The mind that opens to a new idea
never returns to its original size."
Albert Einstein

Chapter 3

Disguised and short GRBs vs. long GRBs

In recent years, after the launch of the *Swift* satellite (Gehrels et al. 2009), it appeared the possibility of the existence of a third class of GRBs, apart from the canonical long and short discovered by BATSE. This class presented hybrid properties between the ones belonging to the long and the short. They were called the Norris-Bonnell sources, or "Short GRBs with an extended emission", as indicated in the literature (Norris & Bonnell 2006). The prompt emission of these sources is characterized by an initial short spike-like emission that lasts a few seconds, followed by a prolonged softer extended emission that lasts up to hundreds of seconds. In parallel, the theoretical progress in the Fireshell model (Ruffini et al. 2001a,b,c) led to an alternative explanation of these sources as "disguised-short bursts" (Bernardini et al. 2007, 2008; Caito et al. 2009, 2010; de Barros et al. 2011). These are canonical long bursts exploding in halos of their host galaxies, with a mean CBM density of $n_{CBM} \approx 10^{-3}$ part cm^{-3}.

There is however a yet new class of GRBs theoretically predicted by the Fireshell model: the "genuine short" GRBs. These sources are characterized by a severely small value of the baryon load, $B \leq 10^{-5}$. The energy emitted in the P-GRB is predominant and their characteristic duration is shorter than a fraction of a second. This short bursts should have in the limit of $B \to 0$ no afterglow.

To summarize, the Fireshell model predicts the existence of three classes of bursts:

- **Canonical long GRBs**: these sources are characterized by a baryon load varying in the range $3 \times 10^{-4} \leq B \leq 10^{-2}$. They occur in a typical galactic CBM with an average density of $n_{CBM} \approx 1$ particle cm^{-3}. As a result, the extended afterglow is predominant with respect to the P-GRB.

- **Disguised short GRBs**: in these sources, the baryon load varies in the same range of the long bursts, but the CBM density is much lower ($n_{CBM} \approx 10^{-3}$ particles cm^{-3}). As a consequence, the extended afterglow is results in a "deflated" emission, exceeded in peak luminosity by the P-GRB. However, the integrated emission in the extended afterglow is much larger than the one of the P-GRB, as expected for long bursts. These

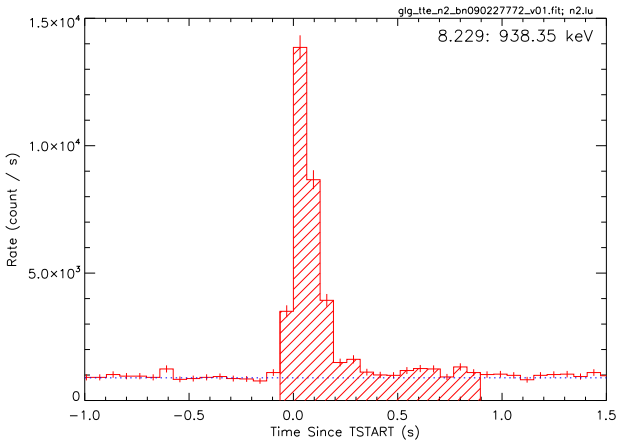

Figure 3.1: 64 ms time-binned NaI-n2 light curve of GRB 090227B.

sources have given the first evidence of GRBs originating from binary mergers of two NS and/or white dwarfs (WDs) in all possible combinations, that have spiraled out from their host galaxies into the halos.

- **Genuine short GRBs**: these GRBs occur in the limit of very low baryon load, $B \leq 10^{-5}$. The P-GRB emission is predominant with respect to the extended afterglow, which shrinks over the P-GRB. The thermalization of the $e^- - e^+$ plasma is reached in a very short timescale at the beginning of the expansion phase and the thermal equilibrium is implemented during the entire phase of the expansion (Aksenov et al. 2007). Therefore, the spectrum is expected to be characterized by a significant thermal-like emission. Since the baryon load is small but not zero, a non-thermal component originating from the extended afterglow is expected, in addition to the predominant role of the P-GRB.

3.1 Short GRBs: the case of GRB 090227B

We have started a search for the genuine short GRBs among the bursts detected by *Fermi*-GBM in its first three years of mission. We obtained a preliminary list of GRBs, which was reduced by requiring that no prominent X-rays and optical afterglows be observed. Among these sources we identified GRB 090227B (Muccino et al. 2013). The *Fermi*-GBM detector was triggered at 18:31:01.41 UT on February 27, 2009 (Guiriec 2009). The source was also detected by *Konus*-Wind (Golenetskii et al. 2009b). The light curve shows a single pulse of ~ 0.2 s of duration in the (20 keV - 10 MeV) energy band (see Fig. 3.1). No X-rays nor optical observations were reported, thus the redshift of the source is unknown.

3.1.1 Spectral Analysis

We performed a time integrated spectral analysis in the interval $(T_0 - 0.064, T_0 + 0.896)$, where T_0 is the GBM trigger time. We considered three spectral models:

Comptonization plus power-law (Comp+PL), Band+PL and BB+Band. We compared the models from a statistical point of view, but we found that the three models are viable.

We then focus on the spike at the beginning of the emission, which goes from $T_0 - 0.064$ s to $T_0 + 0.192$ s and that we called T_{spike}. We fit the same models mentioned above, but found again that they are statistically equivalent. Finally, we focused on the emission from $T_0 + 0.192$ s to $T_0 + 0.896$, which we called T_{tail}. This time we fit a Comptonization, a BB+PL and a PL model. In this case the best fit is given by the Comptonization model, so we rule out any thermal component.

Coming back to the first emission, and in view of the Fireshell scenario, we chose the BB+Band model to fit the data, because the three models are statistically equivalent but the BB+Band has also a physical sense. The emission of T_{spike} is interpreted as the P-GRB and its spectrum should be thermal, while the extended afterglow (interpreted as T_{tail}) should be non-thermal.

We then performed a time-resolved analysis, dividing the emission in 32 ms time intervals and fit them with a Blackbody plus a non thermal component, and with a Band model. The evidence for a thermal component is present just in the two first time intervals, while in the rest the Band model predominates.

3.1.2 Analysis within the Fireshell model

Since we do not know the redshift of the source, we cannot determine the isotropic energy of the burst, E_{iso} and that of the P-GRB, E_{P-GRB}. However, the ratio between them can be calculated as

$$\frac{E_{P-GRB}}{E_{tot}^{e^{\pm}}} = \frac{4\pi d_l^2 F_{BB} \Delta t_{BB}/(1+z)}{4\pi d_l^2 F_{tot} \Delta t_{tot}/(1+z)} = \frac{S_{BB}}{S_{tot}}, \tag{3.1}$$

where F_{BB} is the flux of the blackbody component of the P-GRB and F_{tot} is the total flux, d_l is the luminosity distance and $S = F\Delta t$ are the fluences. The observed energy ratio is $\frac{E_{P-GRB}}{E_{iso}} = (40.6 \pm 0.1)\%$. For this percentage of the P-GRB energy and from the Fireshell diagram (fourth panel in Fig.2.2), we obtain a value of the baryon load B for each value of the total energy. We then insert each of these couple of values in our numerical code and obtain one value of the P-GRB predicted temperature, kT_{blue}, which is related to the observed one by

$$\frac{kT_{blue}}{kT_{obs}} = 1 + z. \tag{3.2}$$

That way we obtain a value for the redshift for each couple of E_{tot} and B. To know which of the values is the correct one, we make use of the formula for the isotropic energy E_{iso}

$$E_{iso} = 4\pi d_l^2 \frac{S_{tot}}{(1+z)} \frac{\int_{E_{min}/(1+z)}^{E_{max}/(1+z)} EN(E)dE}{\int_8^{40000} EN(E)dE}. \tag{3.3}$$

Here, $N(E)$ is the photon spectrum of the burst and the integrals are due to the bolometric correction on S_{tot}. We tried the different values of z we had obtained until the value of E_{iso} coincided with the initial value of E_{tot} from

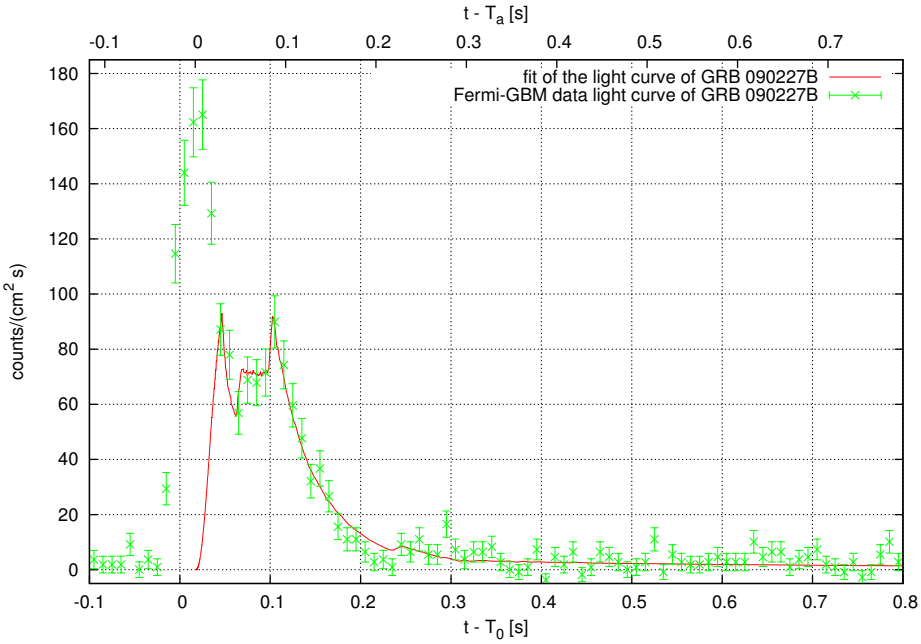

Figure 3.2: NaI-n2 simulated light curve of the extended afterglow of GRB 090227B. The zero of the x-axis corresponds to the trigger time T_0. We have started the simulation at $T_0 + 0.017$ s.

the Fireshell diagram. We obtained $z = 1.6 \pm 0.1$, $B = (4.13 \pm 0.05) \times 10^{-5}$ and $E_{iso} = (2.8 \pm 0.1) \times 10^{53}$ erg. We have performed the simulation of the light curve and spectrum of the extended afterglow (see Fig.3.2) by deriving the radial distribution of the CBM clouds (see Fig.3.3). The average density of the CBM is $n_{CBM} = (1.9 \pm 0.2) \times 10^{-5}$ particles cm^{-3}. This value is typical of galactic halos. The Lorentz factor at the transparency is $\Gamma = 1.44 \times 10^4$.

3.1.3 Conclusions

GRB 090227B is the first example of genuine short GRB. It is theoretically predicted by the Fireshell model, with a baryon load $B \leq 5 \times 10^{-5}$. Within the T_{90} and the T_{spike} all the considered models (BB+Band, Band+PL, Comptonization) are statistically equivalent, while in the T_{tail} the presence of a thermal component is ruled out. According to the Fireshell model, we interpret the emission in T_{spike} as the P-GRB and the emission in T_{tail} as the extended afterglow. The P-GRB emission is expected to have a thermal spectrum, with an additional non-thermal component due to the early onset of the afterglow. Although the three fitted models are viable from a statistical point of view, from an astrophysical point of view we chose the BB+Band model.

We have determined the cosmological redshift of the source $z = 1.6 \pm 0.1$, as well as the baryon load $B = (4.13 \pm 0.05) \times 10^{-5}$, its total energy $E_{tot} = (2.8 \pm 0.1) \times 10^{53}$ erg and its Lorentz Gamma factor at the transparency point $\Gamma = (1.44 \pm 0.01) \times 10^4$.

We conclude that the progenitor if this GRB must be a binary system formed

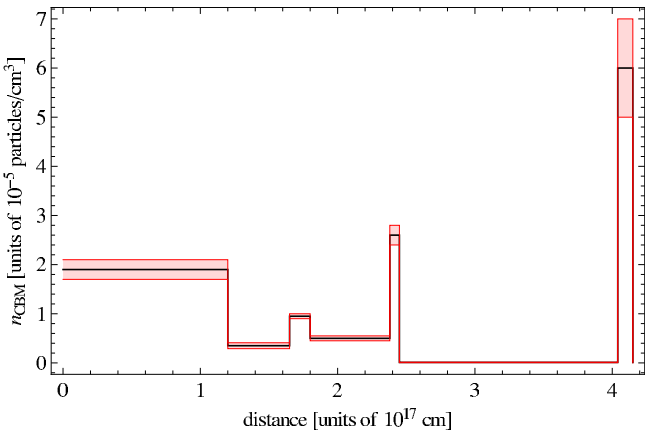

Figure 3.3: Radial CBM density distribution of GRB 090227B (black line) and its range of validity (red shaded region).

by two NS of the same mass, because of the following reasons:

- The very low average CBM density points to two compact objects in a binary system that have spiraled out in the halo of their host galaxy (Bernardini et al. 2007, 2008; Caito et al. 2009, 2010; de Barros et al. 2011).

-The large value of the isotropic energy and the very short timescale of emission point to a very compact object, as can be a binary NS system, with the total mass $m_1 + M2$ larger than the NS critical mass $M_{cr} = 2.67 M_\odot$. In the simplified case in which the masses are identical, and following the recent NS theory developed in Belvedere et al. (2012), we obtain $m_1 = m_2 = 1.34 M_\odot$ and $R_1 = R_2 = 12.24$ km.

-The very small value of the baryon load B is consistent with two NS that have a crust of ~ 0.47 km thick. The smaller the baryon load, the shorter the duration of the GRB.

Turning to the theoretical model with a general relativistic description of the gravitational collapse to a $10 M_\odot$ BH, we need a time resolution on the order of a fraction of ms in order to follow such a process. New space missions with a larger collecting area are required to prove with more accuracy the identification of a thermal component, as well as the best-fitting model.

3.2 Disguised short GRBs: the case of GRB 090510

Even if at the times of BATSE all GRBs were classified according to their duration into short and long, we have demonstrated that the classification is indeed much more complex. These sources originate from a variety of astrophysical scenarios and not from a simple one. We have defined three classes of GRBs: genuine short, disguised short and long. However, the class of disguised short is not homogeneous. It is composed by two sub-classes, according to the value of the CBM density. These are:

- **Disguised short by excess**: a sub-class composed of GRBs occurring

in a medium with a density much larger than the canonical one, e.g., $n_{CBM} \approx 10^3$ part cm^{-3}.

- **Disguised short by defect**: a sub-class composed of GRBs with a CBM density typical of galactic halo environments, $n_{CBM} \approx 10^{-3}$ part cm^{-3}.

GRB 090510 is a member of the first subclass. It is the first bright short hard GRB with an emission extending from the keV up to the GeV energy range. The CBM average spherically symmetric density is $n_{CBM} = (1.8 \pm 0.1) \times 10^3$ part cm^{-3}, one of the highest found in the Fireshell model. The Lorentz Gamma factor at the transparency is $\Gamma_{tr} \sim 700$. These high values may represent an important step toward the explanation of the GeV emission.

The *Fermi*-GBM detector triggered and located GRB 090510 at 00:22:59.97 UT on 2009 May 10 (Guiriec et al. 2009). The burst was also detected by the LAT detector (Ohno & Pelassa 2009), as well as by the *Swift* (Hoversten et al. 2009) and *AGILE* (Longo et al. 2009a) satellites, *Konus*-Wind (Golenetskii et al. 2009c) and *Suzaku*-WAM (Ohmori et al. 2009). The host galaxy was located by the VLT/FORS2 (Rau et al. 2009) at a redshift $z = 0.903 \pm 0.003$.

We took the data from the *Fermi*-GBM NaI-n6 (8-900 keV) and BGO-b1 (260 keV-40MeV) detectors, and the LAT data in the energy range (100 MeV-30 GeV). The light curve shows two different episodes, separated by a 0.5 s interval (see Fig.3.4). The first episode has a very small number of photons. However, we consider it in our analysis because it can play a crucial role in the identification of the P-GRB. We fit this episode with six different spectral models, i.e., PL, BB+PL, Band, Compt.,Band+BB and Compt.+BB. From these, according to a statistical analysis, the Compt. and BB+PL models are the best, but we adopted the BB+PL since it has a physical meaning. The BB observed temperature is $kT_{obs} = 34 \pm 7$ keV and the energy of the first episode is $E_1 = (2.2 \pm 0.3) \times 10^{51}$ erg.

For the second episode (from $T_0 + 0.4$ s to $T_0 + 1.024$ s), the model that best fits the data is Band+PL, even if we include the LAT data. The PL is observed up to 30 GeV and the total energy of the second episode is $E_2 = (1.08 \pm 0.06) \times 10^{53}$ erg.

3.2.1 Analysis in the Fireshell model

We identified the first episode, where the thermal component is not statistically excluded, with the P-GRB. We considered the second episode as the extended afterglow, and we simulated its light curve with our numerical code. We found a baryon load $B = (1.4 \pm 0.2) \times 10^{-3}$, a radius at the transparency $r = (6.5 \pm 0.9) \times 10^{13}$ cm, a Lorentz Gamma factor $\Gamma_{tr} = (6 \pm 1) \times 10^2$, a theoretically predicted P-GRB temperature $kT_{th} = 34 \pm 7$ keV and a P-GRB energy $E_{tr} = (2.9 \pm 0.5)\% E_{tot}$ (see Fig.3.5). The value of the P-GRB energy differs slightly from the observed one, since we expect some emission below the threshold between the small precursor and the main emission. Thus, E_1 is underestimated. Fig.3.6 shows the CBM particle density distribution as a function of the radius.

3.2.2 Conclusions

GRB 090510 is an example of disguised short burst by excess, as it occurs in an over dense medium with an average value of $< n_{CBM} > \approx 10^3$ particles

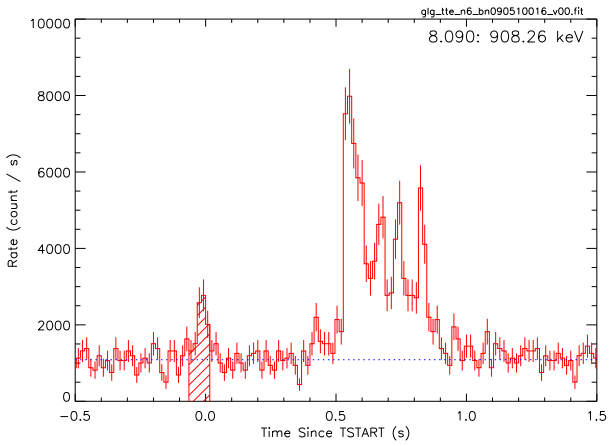

Figure 3.4: GRB 090510 16 ms time-binned NaI-n6 light curve, with the first episode evidenced.

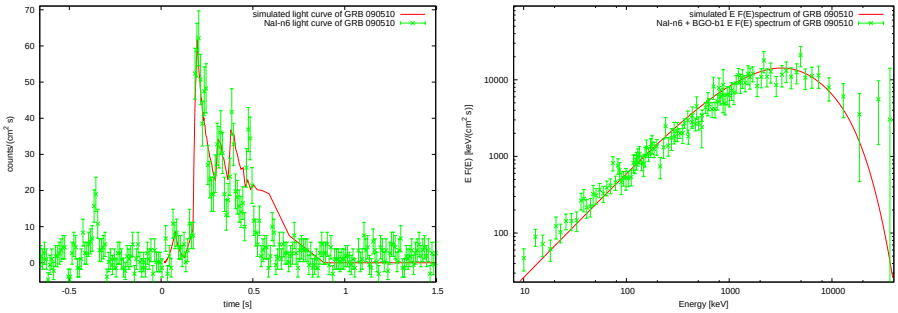

Figure 3.5: **Left**:simulated NaI-n6 light curve of the extended afterglow in the range 8-1000 keV. **Right**: simulated spectrum.

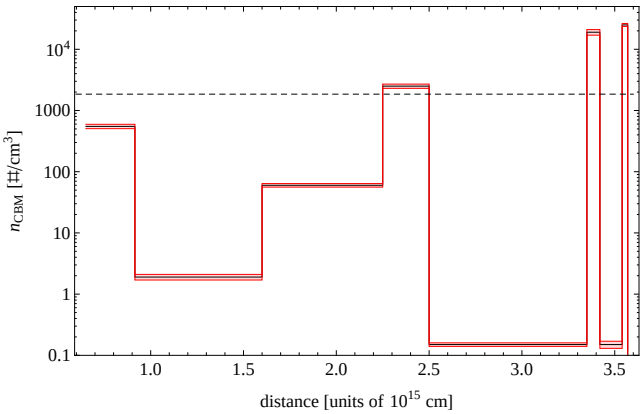

Figure 3.6: Radial CBM density distribution of GRB 090510 (red solid line) with its uncertainty (light red shaded region) and mean value (black dashed line).

cm^{-3}. The light curve presents two episodes. We identified the first one with the P-GRB and the second one with the extended afterglow within the Fireshell model. The quality of the data does not allow us to distinguish between BB+PL and Compt. models, but we adopted the BB+PL model since it has a physical meaning.

The joint effect of the high value of the Lorentz factor and the high density compresses the emission of the extended afterglow in time, making the light curve shorten in time and inflate in intensity with respect to the canonical one for disguised short bursts, and making it apparently closer to the one of genuine short bursts (Muccino et al. 2013). Another point to notice is that, with this extremely high value of the CBM density, the extended afterglow of GRB 090510 does not fulfill the Amati relation (Amati 2006a).

The Astrophysical Journal, 763:125 (16pp), 2013 February 1 doi:10.1088/0004-637X/763/2/125

GRB 090227B: THE MISSING LINK BETWEEN THE GENUINE SHORT AND LONG GAMMA-RAY BURSTS

M. Muccino[1,2], R. Ruffini[1,2,3], C. L. Bianco[1,2], L. Izzo[1,2], and A. V. Penacchioni[1,3]
[1] Dip. di Fisica and ICRA, Sapienza Università di Roma, Piazzale Aldo Moro 5, I-00185 Rome, Italy
[2] ICRANet, Piazza della Repubblica 10, I-65122 Pescara, Italy
[3] Universite de Nice Sophia Antipolis, Nice, CEDEX 2, Grand Chateau Parc Valrose, France
Received 2012 May 30; accepted 2012 November 4; published 2013 January 16

ABSTRACT

The time-resolved spectral analysis of GRB 090227B, made possible by the *Fermi*-GBM data, allows us to identify in this source the missing link between the genuine short and long gamma-ray bursts (GRBs). Within the Fireshell model of the GRBs we predict genuine short GRBs: bursts with the same inner engine of the long bursts but endowed with a severely low value of the baryon load, $B \lesssim 5 \times 10^{-5}$. A first energetically predominant emission occurs at the transparency of the e^+e^- plasma, the Proper-GRB (P-GRB), followed by a softer emission, the extended afterglow. The typical separation between the two emissions is expected to be of the order of 10^{-3}–10^{-2} s. We identify the P-GRB of GRB 090227B in the first 96 ms of emission, where a thermal component with the temperature $kT = (517 \pm 28)$ keV and a flux comparable with the non-thermal part of the spectrum is observed. This non-thermal component as well as the subsequent emission, where there is no evidence for a thermal spectrum, is identified with the extended afterglow. We deduce a theoretical cosmological redshift $z = 1.61 \pm 0.14$. We then derive the total energy $E^{\rm tot}_{e^+e^-} = (2.83 \pm 0.15) \times 10^{53}$ erg, the baryon load $B = (4.13 \pm 0.05) \times 10^{-5}$, the Lorentz Γ factor at transparency $\Gamma_{\rm tr} = (1.44 \pm 0.01) \times 10^4$, and the intrinsic duration $\Delta t' \sim 0.35$ s. We also determine the average density of the circumburst medium (CBM), $\langle n_{\rm CBM} \rangle = (1.90 \pm 0.20) \times 10^{-5}$ particles cm^{-3}. There is no evidence of beaming in the system. In view of the energetics and of the baryon load of the source, as well as of the low interstellar medium and of the intrinsic timescale of the signal, we identify the GRB progenitor as a binary neutron star. From the recent progress in the theory of neutron stars, we obtain masses of the stars $m_1 = m_2 = 1.34\, M_\odot$ and their corresponding radii $R_1 = R_2 = 12.24$ km and thickness of their crusts ∼0.47 km, consistent with the above values of the baryon load, of the energetics and of the time duration of the event.

Key words: gamma-ray burst: general – gamma-ray burst: individual (GRB 090227B)

Online-only material: color figures

1. INTRODUCTION

The understanding of gamma-ray bursts (GRBs) is among the most fascinating and profound conceptual problems of relativistic astrophysics. Observations at high energies from space missions, such as BATSE (Meegan et al. 1992), *Beppo-SAX* (Metzger et al. 1997), *Swift* Burst Alert Telescope (BAT; Gehrels et al. 2005), *AGILE* (Tavani et al. 2008), *Fermi* Gamma-Ray Burst Monitor (GBM; Meegan et al. 2009), and others have revealed that GRBs emit almost the energy equivalent to a solar mass in a few seconds of the time of the observer. This allows the observability of these sources over the entire visible universe.

The first systematic analysis on the large sample of GRBs observed by the BATSE instrument on board the *Compton Gamma-Ray Observer* satellite (Meegan et al. 1992) evidenced a bimodal temporal distribution in the T_{90} observed duration of prompt emission of GRBs. The "long" and "short" GRBs were defined as being longer or shorter than $T_{90} = 2$ s.

Another fundamental progress was achieved by *Beppo-SAX* with the discovery of a prolonged soft X-ray emission, the "afterglow" (Costa et al. 1997), following the traditional hard X-ray emission observed by BATSE, that was called the "prompt emission."

In recent years, the observations by the *Swift* satellite (Gehrels et al. 2005) evidenced the existence of a possible third class of burst, presenting hybrid properties between the short and the long ones: the Norris–Bonnell sources (Norris & Bonnell 2006). The prompt emission of these sources is characterized by an initial short spike-like emission lasting a few seconds, followed by a prolonged softer extended emission lasting up to some hundred seconds. They were initially indicated in the literature as "short GRBs with an extended emission."

In parallel, the theoretical progress in the Fireshell model of GRBs (see Ruffini et al. 2001a, 2001b, 2001c) has led to an alternative explanation of the Norris–Bonnell sources as "disguised short bursts" (Bernardini et al. 2007, 2008; Caito et al. 2009, 2010; de Barros et al. 2011): canonical long bursts exploding in halos of their host galaxies, with $\langle n_{\rm CBM} \rangle \approx 10^{-3}$ particles cm^{-3} (see Section 2.3).

The aim of this article, using the data obtained by the *Fermi*-GBM satellite (Meegan et al. 2009), is to probe the existence of a yet new class of GRBs which we define here as "genuine short GRBs," theoretically predicted by the Fireshell model (Ruffini et al. 2001b, 2002). This class of canonical GRBs is characterized by severely small values of the baryon load, $B \lesssim 10^{-5}$ (see Figure 1). The energy emitted in the Proper-GRB (P-GRB) is predominant and the characteristic duration is expected to be shorter than a fraction of a second (see Section 2.4).

We have started a search for these genuine short GRBs among the bursts detected by the *Fermi*-GBM instrument in its first three years of mission. The initial list of short GRBs was reduced requiring that no prominent X-rays and optical afterglows be observed. Among these bursts we have identified GRB 090227B. From its observed light curves, we have performed the spectral analysis of the source, and within the theory we have inferred its cosmological redshift, and all the

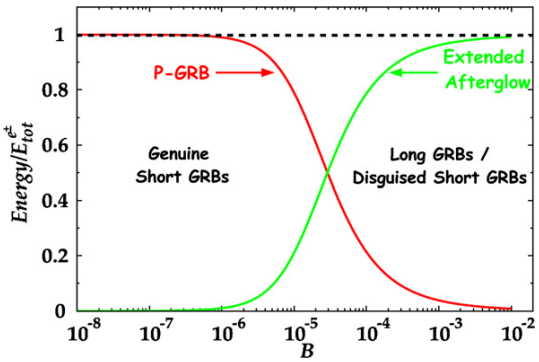

Figure 1. Energy emitted in the extended afterglow (solid green curve) and in the P-GRB (solid red curve) in units of $E^{\rm tot}_{e^+e^-} = 1.77 \times 10^{53}$ erg (dashed horizontal line), as functions of B. The crossing point, corresponding to the condition $E_{\rm P\text{-}GRB} \equiv 50\% E^{\rm tot}_{e^+e^-}$, marks the division between the genuine short and disguised short and long GRBs region.

(A color version of this figure is available in the online journal.)

basic parameters of the burst, as well as the isotropic energy, the Lorentz Γ factor at transparency, and the intrinsic duration.

In Section 2, we recall the relevant properties of the Fireshell model. In Section 3, we report the observation of GRB 090227B by the different satellites and the data analysis. In Section 4, we determine all the parameters characterizing GRB 090227B within the Fireshell scenario, including the redshift. In Section 5, we provide an estimation of the lower limit on the Lorentz Γ factor from the definition of opacity, finding the agreement with the theoretically determined Lorentz Γ factor. In the conclusions we show that GRB 090227B is the missing link between the genuine short and the long GRBs, with some common characteristics between the two classes. Further analysis of genuine short GRB with a yet smaller value of B should lead to P-GRB with a yet more pronounced thermal component. We identify the progenitor of GRB 090227B as a symmetric binary system of two neutron stars, each of $\sim$1.34 $M_\odot$.

2. THE FIRESHELL VERSUS THE FIREBALL MODEL AND THE ISSUE OF THE PHOTOSPHERIC EMISSION

Soon after the announcement of the discovery of GRBs (Strong et al. 1975), Damour & Ruffini (1975) proposed to explain the energy source of GRBs in terms of the e^+e^- pair plasma created in the process of vacuum polarization during the formation of a Kerr–Newman black hole. They mentioned that the energetics to be expected in this model is approximately 10^{54}–10^{55} erg for a 10 $M_\odot$ black hole. At the time nothing was known about the energetics of GRBs, their distance being unknown. They did not pursue further the details of the model pending additional observational evidence.

The idea of the role of an e^+e^- pair plasma as energy source of GRBs was proposed again and independently by Cavallo & Rees (1978). They proposed a sudden release of energy in a process of gravitational collapse leading to a large number of e^+e^- pairs, whose instantaneous annihilation would lead to a vast release of energy pushing on the circumburst medium (CBM): the concept of "fireball."

The concept of fireball was further examined by Goodman (1986), who quantified the dynamical effects of the expansion of the fireball computing the effect of the blueshift due to the bulk Lorentz Γ factor on the observed temperature. Shemi & Piran (1990) were among the first to compute the dynamics of such a fireball in presence of baryonic matter, described by the adimensional parameter $\eta = E_0/M_B c^2$, in which E_0 is the initial total energy of the fireball. They clearly pointed out that for large values of η, photons carry most of the energy of the fireball. In the opposite regime most of E_0 is converted in the kinetic energy of the baryons and only a small fraction is carried away by the photons at transparency. Further works were presented by Meszaros et al. (1993), Piran et al. (1993) and Katz (1994).

After the discovery by *Beppo-SAX* (Costa et al. 1997) of the cosmological nature of GRBs (van Paradijs et al. 1997), it became clear that the energetics presented by Damour & Ruffini (1975) was indeed correct and their work represented one of the handful GRB models still viable (Ruffini 2001). The return to the model led to a further step in the comprehension of GRBs (Ruffini et al. 1999, 2000) with the detailed analysis of the rate equation that accounts for the gradual annihilation of the pairs, in a relativistic expanding shell, during the entire optically thick acceleration phase of GRBs: the concept of "Fireshell."

The main differences between the fireball and the Fireshell scenarios are outlined in Bianco et al. (2006), while Aksenov et al. (2007) definitely proved that in an optically thick e^+e^- plasma the annihilation of the pairs does not occur instantaneously, as originally assumed by Cavallo and Rees. Instead, the optically thick e^+e^- plasma reaches the thermal equilibrium in a very short timescale, $\sim 10^{-12}$ s, and then dynamically expands following the approach in Ruffini et al. (1999, 2000).

In the meantime, the BATSE observations led to a phenomenological classification of GRBs, based on their observed duration, into "long" and "short" GRBs (Klebesadel 1992; Dezalay et al. 1992; Kouveliotou et al. 1993; Tavani 1998). Initially this fact was interpreted in terms of different progenitors for these two classes (see Blinnikov et al. 1984; Woosley 1993; Paczynski 1998).

In 2001 an interpretation within the Fireshell model was proposed to explain the differences between the short and the long GRBs. This interpretation was based on the baryon load B (inverse of η). In this picture, both long and short GRBs originate from the same basic machine, the dyadotorus, from an implosion leading to the formation of a Kerr–Newman black hole (Ruffini 2009). The long bursts correspond to GRBs with $B \gtrsim 3.0 \times 10^{-4}$ and the short ones to GRBs with $B \lesssim 10^{-5}$ (Figure 1). For $10^{-5} \lesssim B \lesssim 3.0 \times 10^{-4}$ it depends also on the value of the total energy of the pairs $E^{\rm tot}_{e^+e^-}$ (see Figure 2). The short bursts should have in the limit of $B \to 0$ no afterglow. This was followed in 2002 by a further theoretical work also evidencing the relevance of an additional parameter influencing the interpretation of the above classification: the average density of the environment CBM (Ruffini et al. 2002, 2004, 2005b). This led to the new concept of "disguised short" GRBs (Bernardini et al. 2007, 2008; Caito et al. 2009, 2010; de Barros et al. 2011).

Let us briefly discuss in more detail the Fireshell model. As we have noted, the GRBs originate from the process of vacuum polarization occurring in the formation of a black hole, resulting in pair creation (Damour & Ruffini 1975; Ruffini & Xue 2008; Ruffini et al. 2010). The formed e^+e^- plasma, with total energy $E^{\rm tot}_{e^+e^-}$, reaches the thermal equilibrium almost instantaneously (Aksenov et al. 2007). The annihilation of these pairs occurs gradually and it is confined in an expanding shell, called *Fireshell*, which self-accelerates up to ultrarelativistic velocities (Ruffini et al. 1999), and engulfs the baryonic matter (of mass M_B) left over in the process of collapse, which thermalizes with the pairs due to the large optical depth (Ruffini et al. 2000). The baryon load is measured by the dimensionless parameter

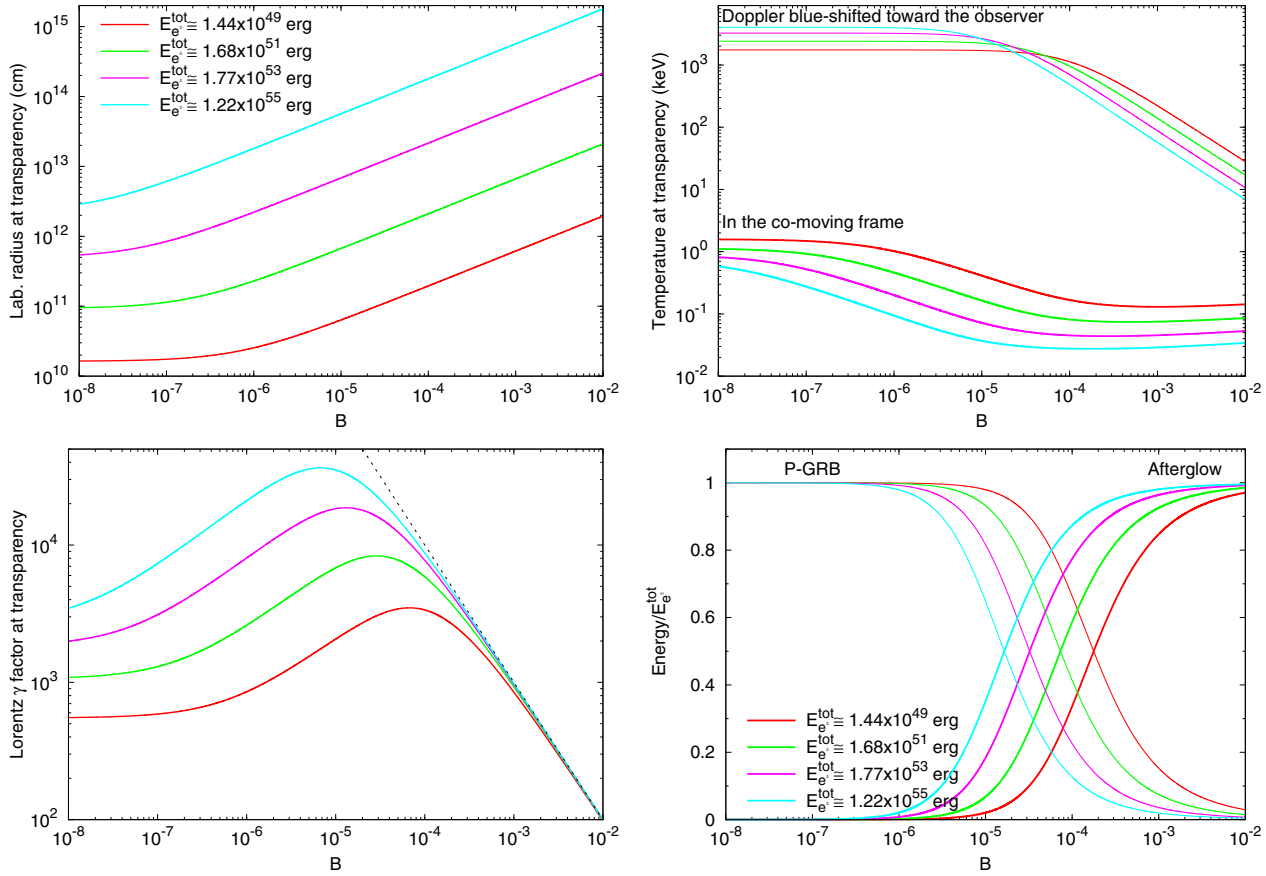

Figure 2. Main quantities of the Fireshell model at the transparency for selected values of $E^{\rm tot}_{e^+e^-}$: the radius in the laboratory frame, the comoving frame and blueshifted toward the observer temperatures of the plasma, the Lorentz Γ factor, and the fraction of energy radiated in the P-GRB and in the extended afterglow as functions of B. In these simulations a sudden transition between the optically thick adiabatic phase and the fully radiative condition at the transparency has been assumed.

(A color version of this figure is available in the online journal.)

$B = M_B c^2/E^{\rm tot}_{e^+e^-}$. The Fireshell continues to self-accelerate until it reaches the transparency condition and a first flash of radiation, the P-GRB, is emitted (Ruffini et al. 2001b). The radius at which the transparency occurs, the theoretical temperature, the Lorentz factor, as well as the amount of the energy emitted in the P-GRB are functions of $E^{\rm tot}_{e^+e^-}$ and B (see Figure 2).

In recent years a systematic analysis of the possible presence of a thermal component in the early phases of the prompt emission of GRBs has been performed using the earlier data from BATSE through the latest data from *Fermi* (Ryde 2004; Ryde & Pe'er 2009; Guiriec et al. 2011). The presence of episodes with a significant thermal component lasting typically from 20 to 50 s has been evidenced. In some specific cases the thermal component has been shown to vary with time following a broken power law (Ryde 2004; Ryde & Pe'er 2009). This problematic has led to the study of the so-called photospheric emission (Rees & Mészáros 2005; Pe'er et al. 2005, 2006; Lazzati & Begelman 2010). It has been pointed out (Ruffini et al. 2011; Izzo et al. 2012a, 2012b; Penacchioni et al. 2012) that a marked difference exists between these prolonged emissions occurring at $\Gamma \sim 1$ and the specific ones of the e^+e^- recombination occurring at ultrarelativistic regimes, $\Gamma > 10^2$, and lasting at most a few seconds. In the specific cases of GRB 970828 (Izzo et al. 2012a), GRB 090618 (Izzo et al. 2012b) and GRB 101023 (Penacchioni et al. 2012) the existence of these two components has been evidenced. The first component, at $\Gamma \sim 1$, has been associated with the Proto Black Hole, while the one at $\Gamma \geqslant 10^2$ has been identified with the P-GRB emission ($\Gamma = 495$, for GRB 090618, $\Gamma = 143$, for GRB 970828, and $\Gamma = 261$ for GRB 101023).

2.1. The Extended Afterglow Emission

After transparency, the residual expanding plasma of leptons and baryons interacts with the CBM and, due to these collisions, starts to slow down giving rise to a multi-wavelength emission: the extended afterglow. Assuming a fully radiative condition, the structures observed in the extended afterglow of a GRB are described by two quantities associated with the environment: the CBM density profile $n_{\rm CBM}$, which determines the temporal behavior of the light curve, and the Fireshell surface filling factor $\mathcal{R} = A_{\rm eff}/A_{\rm vis}$, in which $A_{\rm eff}$ is the effective emitting area of the Fireshell and $A_{\rm vis}$ its total visible area (Ruffini et al. 2002, 2005a). This second parameter takes into account the inhomogeneities in the CBM and its filamentary structure (Ruffini et al. 2004). The emission process of the collision between the baryons and the CBM has been assumed in the comoving frame of the shell as a modified blackbody spectrum

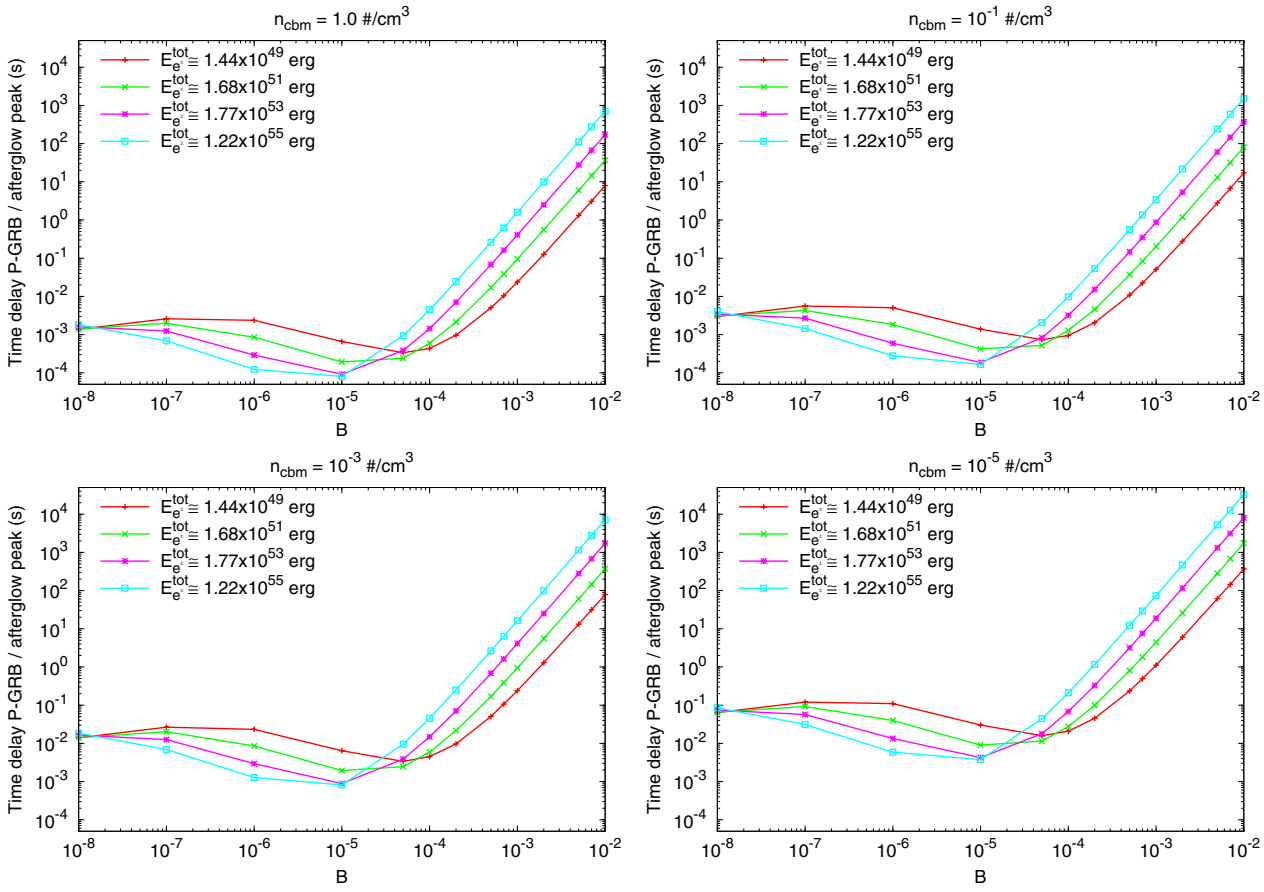

Figure 3. Plots of the arrival time separation Δt_a between the P-GRB and the peak of the extended afterglow as function of B for four different values of $E^{\rm tot}_{e^+e^-}$, measured in the source cosmological rest frame. This computation has been performed assuming four constant CBM density $n_{\rm CBM} = 1.0,\ 1.0 \times 10^{-1},\ 1.0 \times 10^{-3},\ 1.0 \times 10^{-5}$ particles cm^{-3}.

(A color version of this figure is available in the online journal.)

(Patricelli et al. 2012), given by

$$\frac{dN_\gamma}{dV d\epsilon} = \frac{8\pi}{h^3 c^3} \left(\frac{\epsilon}{kT}\right)^\alpha \frac{\epsilon^2}{\exp(\epsilon/kT) - 1}, \qquad (1)$$

where α is a phenomenological parameter. It is appropriate to clarify that this emission is different from the photospheric one due to the e^+e^- plasma annihilation, since it originates from the interactions between the baryons and the CBM in an optically thin regime.

The observed GRB non-thermal spectral shape is then produced by the convolution of a very large number of modified thermal spectra with different temperatures and different Lorentz and Doppler factors. This convolution is performed over the surfaces of constant arrival time for the photons at the detector (EQuiTemporal Surfaces, EQTS; Bianco & Ruffini 2005a, 2005b) encompassing the total observation time. The observed hard-to-soft spectral variation comes out naturally from the decrease with time of the comoving temperature and of the bulk Lorentz Γ factor. This effect is amplified by the curvature effect originated by the EQTS, which produces the observed time lag in the majority of the GRBs.

Assuming the spherical symmetry of the system, the isotropic energy emitted in the burst, $E_{\rm iso}$, is equal to the energy of the e^+e^- plasma, $E^{\rm tot}_{e^+e^-}$, and the GRB bolometric light curve is composed of the P-GRB and the extended afterglow. Their relative energetics and observed time separation are functions of the energy $E^{\rm tot}_{e^+e^-}$, of the baryon load B, and of the CBM density distribution $n_{\rm CBM}$ (see Figure 3). In particular, for decreasing B, the extended afterglow light curve "squeezes" itself on the P-GRB and the P-GRB peak luminosity increases (see Figure 4).

To reproduce the shape of the light curve for each CBM clump we must determine the filling factor $\mathcal{R}$, which determines the effective temperature in the comoving frame and the corresponding peak energy of the spectrum, and the CBM density $n_{\rm CBM}$, which determines the temporal behavior of the light curve. It is clear that, since the EQTS encompass emission processes occurring at different comoving times weighted by their Lorentz and Doppler factors, the fit of a single spike is not only a function of the properties of the specific CBM clump but of the entire previous history of the source. Due to the nonlinearity of the system and to the EQTS, any change in the simulation produces observable effects up to a much later time. This brings us to an extremely complex procedure by trial and error in the data simulation to reach the uniqueness.

It is appropriate to recall that in the Fireshell model the two phases, the one preceding the e^+e^- transparency and the following one, as well as their corresponding energetics, are directly linked by the Fireshell equations of motion (see

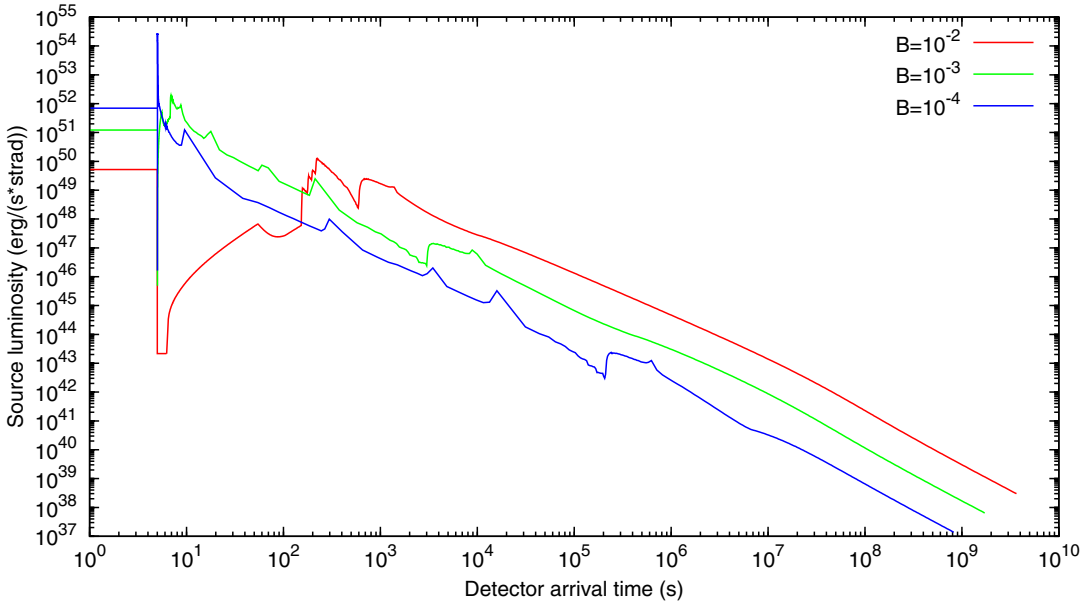

Figure 4. Dependence of the shape of the light curve on B. The computations have been performed assuming $E^{\rm tot}_{e^+e^-} = 4.83 \times 10^{53}$ erg, $\langle n_{\rm CBM}\rangle = 1.0$ particles cm^{-3}, three different values of the baryon load $B = 10^{-2}, 10^{-3}, 10^{-4}$ and the P-GRBs duration fixed, i.e., 5 s. For decreasing B, the extended afterglow light curve squeezes itself on the P-GRB and the peak becomes sharper and higher.
(A color version of this figure is available in the online journal.)

Figure 2). Consequently, their agreement with the data cannot be independently adjusted and optimized.

2.2. The Canonical Long GRBs

According to this theory, the canonical long GRBs are characterized by a baryon load varying in the range $3.0\times10^{-4} \lesssim B \leqslant 10^{-2}$ and they occur in a typical galactic CBM with an average density $\langle n_{\rm CBM}\rangle \approx 1$ particle cm^{-3}. As a result, the extended afterglow is predominant with respect to the P-GRB (see Figure 1).

2.3. The Disguised Short GRBs

After the observations by *Swift* of GRB 050509B (Gehrels et al. 2005), which was declared in the literature as the first short GRB with an extended emission ever observed, it has become clear that all such sources are actually disguised short GRBs (de Barros et al. 2011). It is conceivable and probable that a large fraction of the declared short duration GRBs in the BATSE catalog, observed before the discovery of the afterglow, are also members of this class. In the case of the disguised short GRBs, the baryon load varies in the same range of the long bursts, while the CBM density is of the order of 10^{-3} particles cm^{-3}. As a consequence, the extended afterglow results in a "deflated" emission that can be exceeded in peak luminosity by the P-GRB (Bernardini et al. 2007, 2008; Caito et al. 2009, 2010; de Barros et al. 2011). Indeed, the integrated emission in the extended afterglow is much larger than the one of the P-GRB (see Figure 1), as expected for long GRBs. With these understandings, long and disguised short GRBs are interpreted in terms of long GRBs exploding, respectively, in a typical galactic density or in a galactic halo density.

These sources have given the first evidence of GRBs originating from binary mergers, formed by two neutron stars and/or white dwarfs in all possible combinations, that have spiraled out from their host galaxies into the halos (Bernardini et al. 2007, 2008; Caito et al. 2009, 2010; de Barros et al. 2011). This interpretation has been supported by direct optical observations of GRBs located in the outskirt of the host galaxies (Sahu et al. 1997; van Paradijs et al. 1997; Bloom et al. 2006; Troja et al. 2008; Fong et al. 2010; Berger 2011; Kopač et al. 2012).

2.4. The Class of Genuine Short GRBs

The canonical genuine short GRBs occur in the limit of very low baryon load, e.g., $B \lesssim 10^{-5}$ with the P-GRB predominant with respect to the extended afterglow. For such small values of B the afterglow peak emission shrinks over the P-GRB and its flux is lower than that of the P-GRB (see Figure 4).

The thermalization of photon-pair plasma is reached in a very short timescale at the beginning of the expansion phase and the thermal equilibrium is implemented during the entire phase of the expansion (Aksenov et al. 2007), therefore the spectrum of these genuine short GRBs is expected to be characterized by a significant thermal-like emission. Since the baryon load is small but not zero, in addition to the predominant role of the P-GRB, a non-thermal component originating from the extended afterglow is expected.

3. OBSERVATIONS AND DATA ANALYSIS OF GRB 090227B

At 18:31:01.41 UT on 2009 February 27, the *Fermi*-GBM detector (Guiriec 2009) triggered and located the short and bright burst, GRB 090227B (trigger 257452263/090227772). The on-ground calculated location, using the GBM trigger data, was (R.A., Decl.) (J2000) = ($11^{\rm h}48^{\rm m}36^{\rm s}$, $32^\circ10'12''$), with an uncertainty of $1\overset{\circ}{.}77$ (statistical only). The angle from the *Fermi*-LAT boresight was 72°. The burst was also located by the Inter-Planetary Network (IPN; Golenetskii et al. 2009a) and detected by Konus/*Wind* (Golenetskii et al. 2009b), showing a single pulse with a duration of ∼0.2 s (20 keV–10 MeV). No X-rays

Table 1
The Time-integrated Spectral Analyses Performed Using BB+Band, Band+PL, and Compt+PL Models in the T_{90} and T_{spike} Time Intervals, and BB+PL, Compt, and PL in the T_{tail} Time Interval, in the Energy Range 8 keV–40 MeV

Int.	Model	kT (keV)	E_p (keV)	α	β	γ	F_{tot} (erg cm^{-2} s^{-1})	F_{BB}/F_{tot}	C-STAT/dof
T_{90}	BB+Band	397 ± 70	1942 ± 249	-0.60 ± 0.05	-2.90 ± 0.31		$(3.35 \pm 0.12) \times 10^{-5}$	0.22	286.84/240
	Band+PL		1835 ± 84	-0.35 ± 0.05	-3.46 ± 0.46	-1.47 ± 0.13	$(3.39 \pm 0.13) \times 10^{-5}$		287.73/240
	Compt+PL		1877 ± 72	-0.36 ± 0.05		-1.36 ± 0.05	$(3.44 \pm 0.13) \times 10^{-5}$		290.71/241
T_{spike}	BB+Band	515 ± 28	1072 ± 210	-0.40 ± 0.05	-2.32 ± 0.17		$(1.26 \pm 0.04) \times 10^{-4}$	0.69	266.17/240
	Band+PL		1879 ± 67	-0.33 ± 0.05	-3.61 ± 0.38	-1.35 ± 0.10	$(1.25 \pm 0.04) \times 10^{-4}$		266.32/240
	Compt+PL		1912 ± 58	-0.33 ± 0.05		-1.26 ± 0.07	$(1.26 \pm 0.04) \times 10^{-4}$		270.19/241
T_{tail}	BB+PL	36 ± 13				-1.44 ± 0.07	$(3.9 \pm 1.2) \times 10^{-6}$	*unc.*	293.85/242
	Compt		2703 ± 1760	-1.23 ± 0.09			$(2.03 \pm 0.79) \times 10^{-6}$		291.19/243
	PL					-1.44 ± 0.05	$(4.7 \pm 1.1) \times 10^{-6}$		296.07/244

Table 2
The C-STAT Improvement with the Addition of Extra Parameters in the T_{90}, T_{spike}, and T_{tail} Time Intervals (see Table 1)

Int.	Models	ΔC-STAT	Significance
T_{90}	BB+Band over Compt+PL	3.87	0.049
	Band+PL over Compt+PL	2.98	0.084
T_{spike}	BB+Band over Compt+PL	4.02	0.045
	Band+PL over Compt+PL	3.87	0.049
T_{tail}	BB+PL over PL	2.22	0.33
	BB+PL over Compt	2.66	0.10
	Compt over PL	4.88	0.027

and optical observations were reported on the GCN Circular Archive, thus the redshift of the source is unknown.

To obtain the *Fermi*-GBM light curves and the spectrum in the energy range 8 keV–40 MeV, we made use of the RMFIT program. For the spectral analysis, we have downloaded the TTE (Time-Tagged Events) files from the NASA Goddard Space Flight Center Web site[4], suitable for short or highly structured events. We used the light curves corresponding to the NaI-n2 (8–900 keV) and the BGO-b0 (250 keV–40 MeV) detectors. The 64 ms binned GBM light curves show one very bright spike with a short duration of 0.384 s, in the energy range 8 keV–40 MeV, and a faint tail lasting up to 0.9 s after the trigtime T_0 in the energy range 10 keV–1 MeV. After the subtraction of the background, we have proceeded with the time-integrated and time-resolved spectral analyses.

3.1. Time-integrated Spectral Analysis

We have performed a time-integrated spectral analysis in the time interval from $T_0 - 0.064$ s to $T_0 + 0.896$ s, which corresponds to the T_{90} duration of the burst. We have fitted the spectrum in this time interval considering the following models: Comptonization (Compt) plus power law (PL) and Band (Band et al. 1993) plus PL, as outlined e.g., in Guiriec et al. (2010), as well as a combination of Blackbody (BB) and Band. We have evaluated the significance values from the differences in the C-STAT, considered as χ^2 variables for the change in the number of the model parameters. In Table 2 we have compared the model with different numbers of degrees of freedom (dof). Within the T_{90} time interval, the BB+Band model improves the fit with respect to Compt+PL model at a significance level of 5%. The comparison between Band+PL and Compt+PL models is outside of such a confidence level (about 8%). The direct comparison between BB+Band and Band+PL models, which have the same number of dof (see Table 1), provides almost the same C-STAT values for BB+Band and Band+PL models (ΔC-STAT $\approx$ 0.89). This means that all the three models are viable. The results of the analysis are shown in Table 1 and Figure 5. For the BB+Band model, the ratio between the fluxes of the thermal component and the non-thermal one (NT) is $F_{BB}/F_{NT} \approx 0.22$. The BB component is important in the determination of the peak of the νF_ν spectrum and has an observed temperature $kT = (397 \pm 70)$ keV.

We have then focused our attention on the spike component, namely the time interval from $T_0 - 0.064$ s to $T_0 + 0.192$, which we indicate in the following as the T_{spike}. We have repeated the time-integrated analysis considering the same spectral models as the previous interval (see Table 1 and Figure 6). As reported in Table 2, within the T_{spike} time interval, both BB+Band and Band+PL models marginally improve the fits of the data with respect to Compt+PL model within a confidence level of 5%. Again, the C-STAT values of BB+Band and Band+PL models are almost the same (ΔC-STAT ≈ 0.15) and they are statically equivalent in the T_{spike}. For the BB+Band model, the observed temperature of the thermal component is $kT = (515 \pm 28)$ keV and the flux ratio between the BB component and the NT component increases up to $F_{BB}/F_{NT} \approx 0.69$.

We have performed a further analysis in the time interval from $T_0 + 0.192$ s to $T_0 + 0.896$ s, which we indicate as T_{tail}, by considering the BB+PL, Compt, and PL models (see Figure 7 and Table 1). The comparison in Table 2 shows that the best fit is the Compt model. The BB+PL model is less preferred. From the data analysis in the T_{tail} time interval, we can conclude that a thermal component is ruled out.

In view of the above, we have focused our attention on the fit of the data of the BB+Band model within the Fireshell scenario, which is equally probable from a mere statistical point of view, with the other two choices, namely Band+PL and Compt+PL. According to the Fireshell scenario (see Section 2.1), the emission within the T_{spike} time interval is related to the P-GRB and is expected to be thermal. In addition, the transition between the transparency emission of the P-GRB and the extended afterglow is not sharp. The time separation between the P-GRB and the peak of the extended afterglow depends on the energy of the e^+e^- plasma $E^{tot}_{e^+e^-}$, the baryon load B, and the CBM density n_{CBM} (see Figure 4). As shown in Figures 3 and 4, for decreasing values of B an early onset of the extended afterglow in the P-GRB spectrum occurs and thus an NT component in the T_{spike} is expected. As a further check, the theory of the Fireshell model

[4] ftp://legacy.gsfc.nasa.gov/fermi/data/gbm/bursts

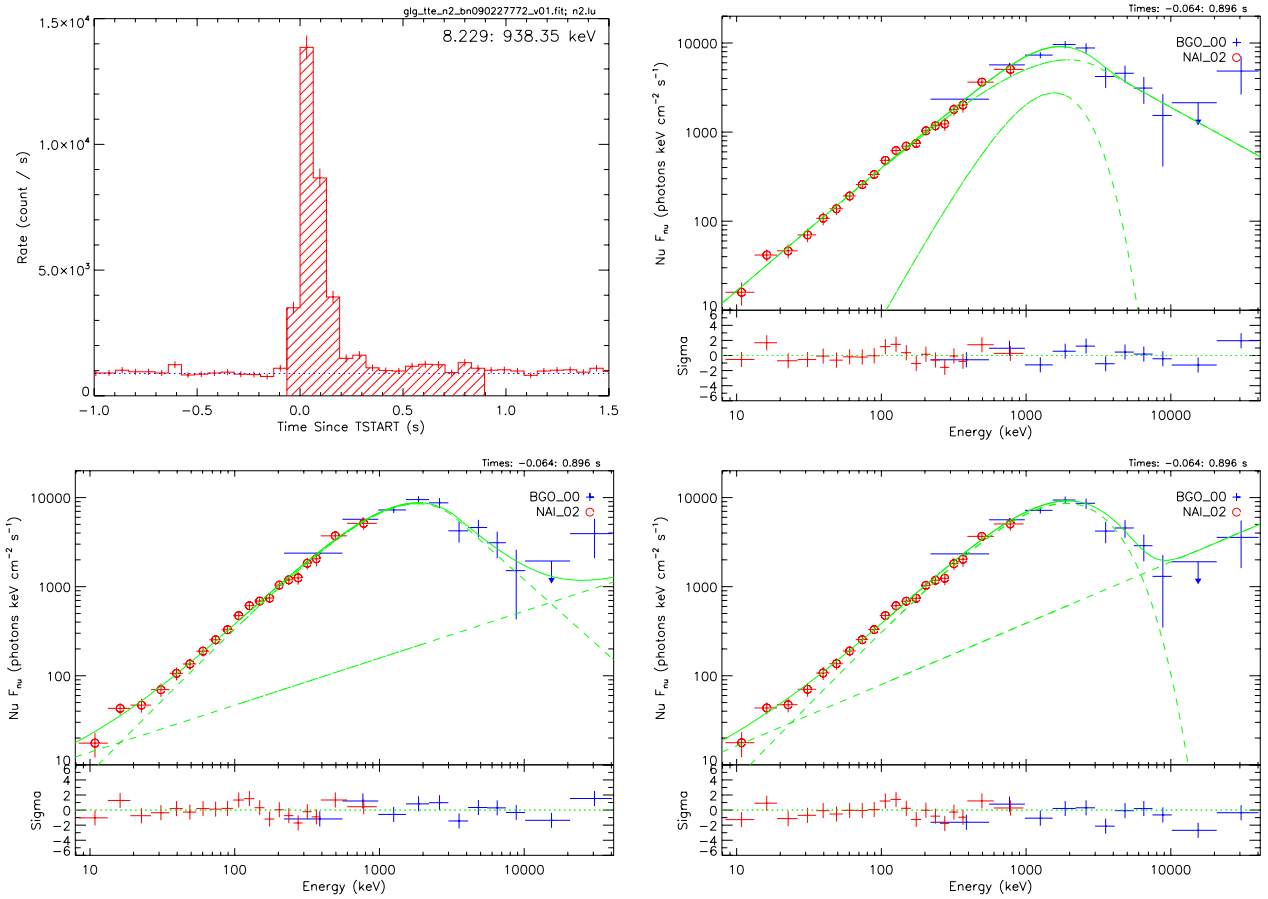

Figure 5. 64 ms time-binned NaI-n2 light curve (top left panel) and the NaI-n2+BGO-b0 νF_ν spectra (top right: BB+Band; bottom left: Band+PL; bottom right: Compt+PL) of GRB 090227B in the T_{90} time interval.

(A color version of this figure is available in the online journal.)

indeed predicts a thermal component due to the transparency of the e^+e^- plasma in the early part of the prompt emission of GRBs (see Section 2), while no thermal component is expected in the extended afterglow (see Section 2.1), as observed in the $T_{\rm tail}$ time interval.

Our theoretical interpretation is consistent with the observational data and the statistical analysis. From an astrophysical point of view, the BB+Band model is preferred over the other two models, and is statistically equivalent in view of the above theoretical considerations.

3.2. Time-resolved Spectral Analysis

We have performed a time-resolved spectral analysis on shorter selected time intervals of 32 ms in order to correctly identify the P-GRB, namely finding out in which time interval the thermal component exceeds or at least has a comparable flux with respect to the NT component due to the onset of the extended afterglow. In this way we can single out the contribution of the NT component in the spectrum of the P-GRB.

A time-resolved spectral analysis was performed by Guiriec et al. (2010) by selecting time intervals from 2 ms to 94 ms. In view of the low statistical content in some small time bins, the authors fitted the data by using simple Band functions. We have performed a time-resolved analysis on time intervals of 32 ms (see Figure 8) in order to optimize the statistical content in each time bin and to test the presence of BB plus an extra NT component. The results are summarized in Table 3, where we have compared the BB+NT with the single Band function.

In our analysis we have preferred the χ^2 statistic because of the high photon fluxes in the first five time intervals, $\gtrsim$100 photons (cm^2 s)$^{-1}$.

Within the first time-resolved interval the BB+PL model has a thermal flux (11.2 ± 3.4) times bigger than the PL flux; the fit with BB+Band provides $F_{\rm BB} = (0.50 \pm 0.26) F_{\rm NT}$, where the NT component is in this case the Band model. In the second and fourth intervals, the BB+Band model provides an improvement at a significance level of 5% in the fitting procedure with respect to the simple Band model (see Table 3, last column). In the third time interval as well as in the remaining time intervals up to $T_0 + 0.192$ s the Band spectral models provide better fits with respect to the BB+NT ones.

This is exactly what we expect from our theoretical understanding: from $T_0 - 0.032$ s to $T_0 + 0.096$ s we have found the edge of the P-GRB emission, in which the thermal components have fluxes higher than or comparable to the NT ones. The third interval corresponds to the peak emission of the extended afterglow (see Figure 11). The contribution of the extended afterglow in the remaining time intervals increases while the thermal flux noticeably decreases (see Table 3).

We have then explored the possibility of a further rebinning of the time interval $T_{\rm spike}$, taking advantage of the large statistical content of each time bin. We have plotted the NaI-n2 light

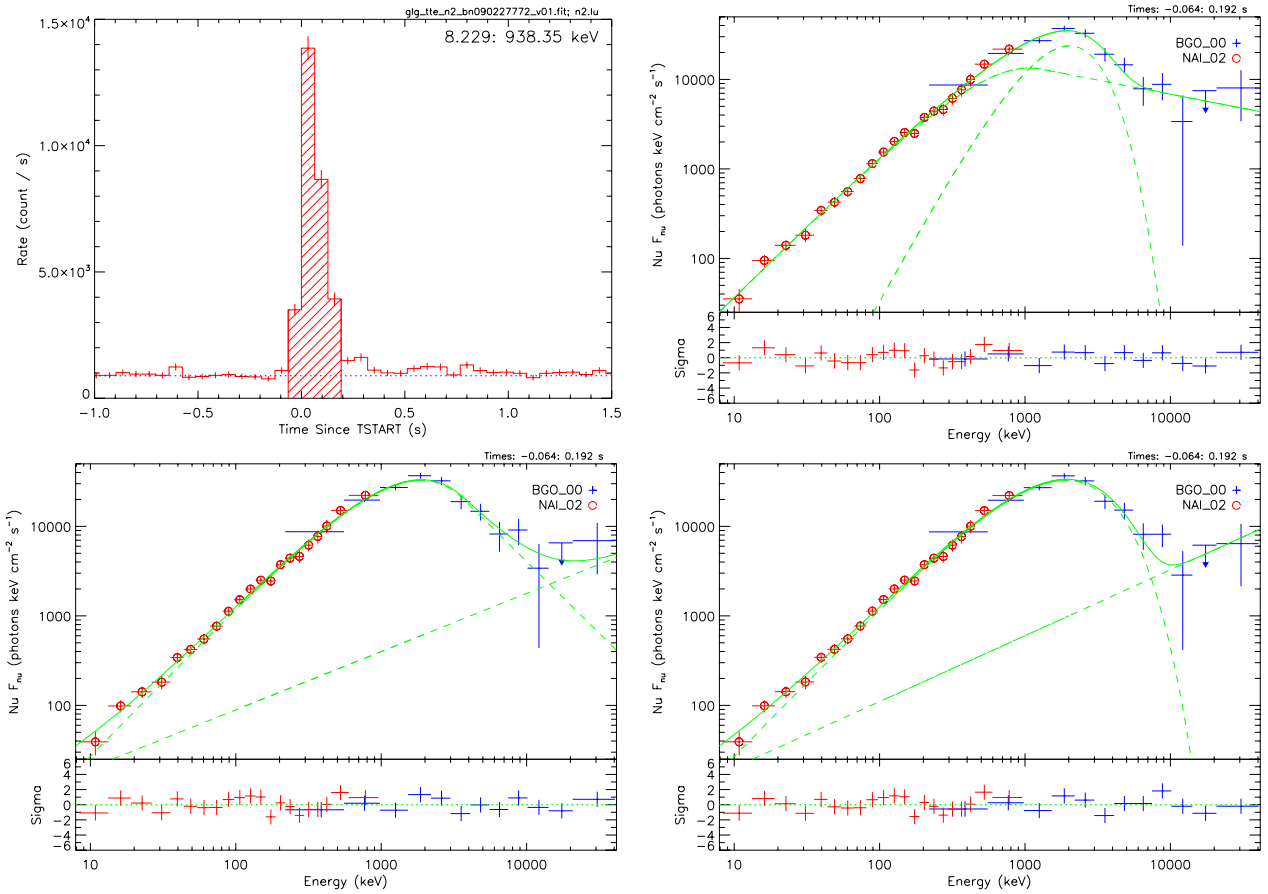

Figure 6. Same considerations as in Figure 5 in the $T_{\rm spike}$ time interval.
(A color version of this figure is available in the online journal.)

curve of GRB 090227B using time bins of 16 ms (see Figure 9, left panels). The rebinned light curves show two spike-like substructures. The duration of the first spike is 96 ms and it is clearly distinct from the second spike. In this time range the observed BB temperature is $kT = (517 \pm 28)$ keV (see Table 4) and the ratio between the fluxes of the thermal component and the non-thermal component is $F_{\rm BB}/F_{\rm NT} \approx 1.1$. Consequently, we have interpreted the first spike as the P-GRB and the second spike as part of the extended afterglow. Their spectra are shown in Figure 9 (right panels) and the results of the spectral analysis are summarized in Table 4.

4. ANALYSIS OF GRB 090227B IN THE FIRESHELL MODEL

The identification of the P-GRB is fundamental in order to determine the baryon load and the other physical quantities characterizing the plasma at the transparency point (see Figure 2). The determination of the cosmological redshift is crucial, which can be derived combining the observed fluxes and the spectral properties of the P-GRB and of the extended afterglow with the equation of motion of our theory. From the cosmological redshift we derive $E^{\rm tot}_{e^+e^-}$ and the relative energetics of the P-GRB and of the extended afterglow components (see Figure 2). Having so derived the baryon load B and the energy $E^{\rm tot}_{e^+e^-}$, we can constrain the total energy and simulate the canonical light curve of the GRBs with their characteristic pulses, modeled by a variable number density distribution of the CBM around the burst site.

4.1. Estimation of the Redshift of GRB 090227B

Having determined the redshift of the source, the analysis consists of equating $E^{\rm tot}_{e^+e^-} \equiv E_{\rm iso}$ (namely $E_{\rm iso}$ is a lower limit on $E^{\rm tot}_{e^+e^-}$) and inserting a value of the baryon load to complete the simulation. The right set of $E^{\rm tot}_{e^+e^-}$ and B is determined when the theoretical energy and temperature of the P-GRB match the observed ones of the thermal emission [namely $E_{\text{P-GRB}} \equiv E_{\rm BB}$ and $kT_{\rm obs} = kT_{\rm blue}/(1+z)$].

In the case of GRB 090227B, we have estimated the ratio $E_{\text{P-GRB}}/E^{\rm tot}_{e^+e^-}$ from the observed fluences:

$$\frac{E_{\text{P-GRB}}}{E^{\rm tot}_{e^+e^-}} = \frac{4\pi d_l^2 F_{\rm BB}\Delta t_{\rm BB}/(1+z)}{4\pi d_l^2 F_{\rm tot}\Delta t_{\rm tot}/(1+z)} = \frac{S_{\rm BB}}{S_{\rm tot}}, \qquad (2)$$

where d_l is the luminosity distance of the source and $S = F\Delta t$ are the fluences. The fluence of the BB component of the P-GRB (see Table 4, first interval) is $S_{\rm BB} = (1.54 \pm 0.45) \times 10^{-5}$ erg cm^{-2}. The total fluence of the burst is $S_{\rm tot} = (3.79 \pm 0.20) \times 10^{-5}$ erg cm^{-2} and has been evaluated in the time interval from $T_0 - 0.016$ s to $T_0 + 0.896$ s. This interval slightly differs from the T_{90} because of the new time boundaries defined after the rebinning of the light curve at resolution of 16 ms. Therefore the observed energy ratio is $E_{\text{P-GRB}}/E^{\rm tot}_{e^+e^-} = (40.67 \pm 0.12)\%$.

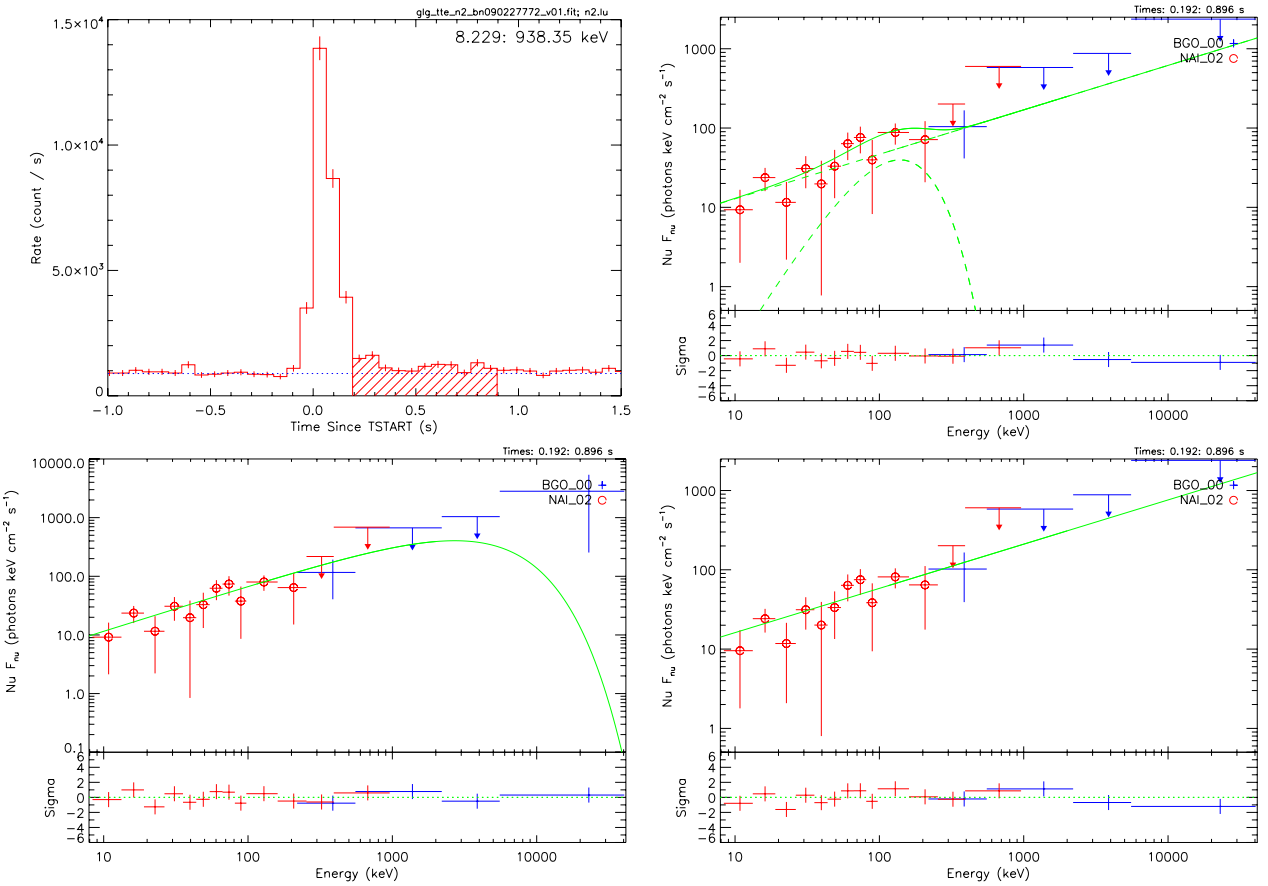

Figure 7. 64 ms time-binned NaI-n2 light curve (top left panel) and the NaI-n2+BGO-b0 νF_ν spectra (top right: BB+PL; bottom left: Compt; bottom right: PL) of GRB 090227B in the $T_{\rm tail}$ time interval.

(A color version of this figure is available in the online journal.)

As is clear from the bottom right diagram in Figure 2, for each value of this ratio we have a range of possible parameters B and $E^{\rm tot}_{e^+e^-}$. In turn, for each of their values we can determine the theoretical blueshifted toward the observer temperature $kT_{\rm blue}$ (see top right diagram in Figure 2). Correspondingly, for each couple of value of B and $E^{\rm tot}_{e^+e^-}$ we estimate the value of z by the ratio between $kT_{\rm blue}$ and the observed temperature of the P-GRB $kT_{\rm obs}$,

$$\frac{kT_{\rm blue}}{kT_{\rm obs}} = 1 + z. \quad (3)$$

In order to remove the degeneracy $[E^{\rm tot}_{e^+e^-}(z), B(z)]$, we have made use of the isotropic energy formula

$$E_{\rm iso} = 4\pi d_l^2 \frac{S_{\rm tot}}{(1+z)} \frac{\int_{E_{\rm min}/(1+z)}^{E_{\rm max}/(1+z)} EN(E)\,dE}{\int_8^{40000} EN(E)\,dE}, \quad (4)$$

in which $N(E)$ is the photon spectrum of the burst and the integrals are due to the bolometric correction on $S_{\rm tot}$. The correct value is the one for which the condition $E_{\rm iso} \equiv E^{\rm tot}_{e^+e^-}$ is satisfied.

We have found the equality at $z = 1.61 \pm 0.14$ for $B = (4.13 \pm 0.05) \times 10^{-5}$ and $E^{\rm tot}_{e^+e^-} = (2.83 \pm 0.15) \times 10^{53}$ erg. The complete quantities so determined are summarized in Table 5.

4.2. The Analysis of the Extended Afterglow and the Observed Spectrum of the P-GRB

As noted in Section 2, the arrival time separation between the P-GRB and the peak of the extended afterglow is a function of $E^{\rm tot}_{e^+e^-}$ and B and depends on the detailed profile of the CBM density. For $B \sim 4 \times 10^{-5}$ (see Figure 3), the time separation is $\sim 10^{-3}$–10^{-2} s in the source cosmological rest frame. In this light, there is an interface between the reaching of transparency of the P-GRB and the early part of the extended afterglow. This connection has already been introduced in the literature (Pe'er et al. 2012; Izzo et al. 2012b; Penacchioni et al. 2012).

From the determination of the initial values of the energy, $E^{\rm tot}_{e^+e^-} = 2.83 \times 10^{53}$ erg, of the baryon load, $B = 4.13 \times 10^{-5}$, and of the Lorentz factor $\Gamma_{\rm tr} = 1.44 \times 10^4$, we have simulated the light curve of the extended afterglow by deriving the radial distribution of the CBM clouds around the burst site (see Table 6 and Figure 10). In particular, each spike in Figure 10 corresponds to a CBM cloud. The error boxes on the number density on each cloud is defined as the maximum possible tolerance to ensure the agreement between the simulated light curve and the observed data. The average value of the CBM density is $\langle n \rangle = (1.90 \pm 0.20) \times 10^{-5}$ particles cm^{-3} with an average density contrast $\langle \delta n/n \rangle = 0.82 \pm 0.11$ (see also Table 5). These

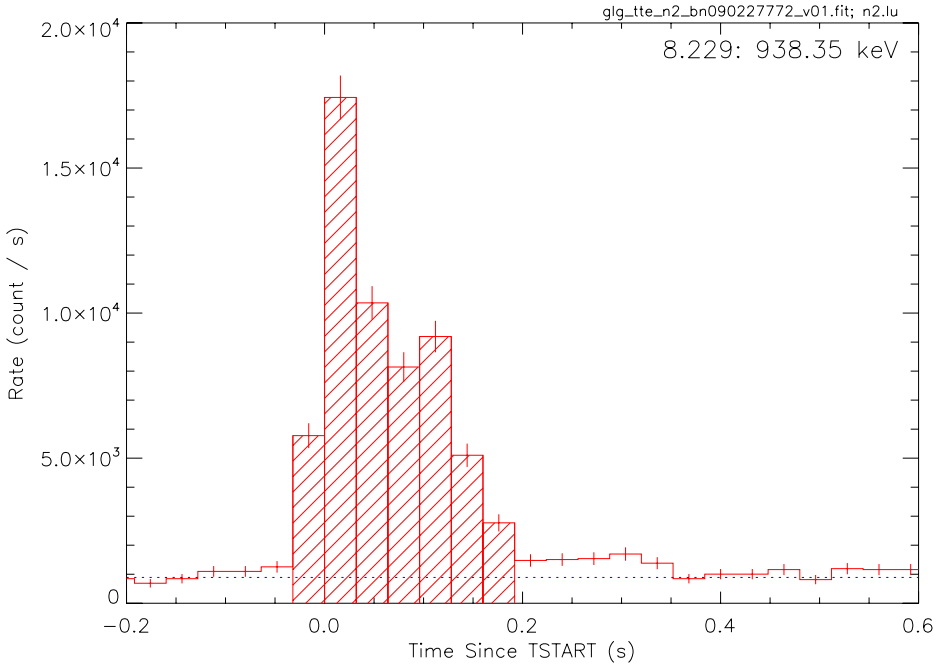

Figure 8. 32 ms time-binned NaI-n2 light curve of GRB 090227B in the time interval from $T_0 - 0.032$ s to $T_0 + 0.192$ s; each time bin corresponds to the time-resolved interval considered in Section 3.2.

(A color version of this figure is available in the online journal.)

Table 3
Time-resolved Analysis of GRB 090227B Performed Using BB+NT (NT = Band, PL) and a Single Band Model

Interval (s)	Models	kT (keV)	E_p (keV)	α	β	$F_{\rm tot} \times 10^{-5}$ (erg cm^{-2} s^{-1})	χ^2/dof	$F_{\rm BB}/F_{\rm NT}$	BB+Band over Band
	BB+PL	274 ± 17		-1.75 ± 0.29		7.03 ± 0.76	$196.85/241 = 0.82$	11.2 ± 3.4	
$-0.032 \rightarrow 0.000$	BB+Band	280 ± 66	1703 ± 407	-0.50 ± 0.25	unc	8.22 ± 0.99	$180.23/239 = 0.75$	0.50 ± 0.26	0.051
	Band		1493 ± 155	-0.21 ± 0.11	unc	8.13 ± 0.88	$186.17/241 = 0.77$		
	BB+PL	377 ± 12		-1.20 ± 0.03		62.2 ± 3.6	$308.97/241 = 1.28$	1.04 ± 0.11	
$0.000 \rightarrow 0.032$	BB+Band	571 ± 44	858 ± 214	0.15 ± 0.17	-2.45 ± 0.26	46.2 ± 2.3	$222.54/239 = 0.93$	1.41 ± 0.38	0.041
	Band		2140 ± 102	-0.10 ± 0.06	-5.3 ± 1.9	47.2 ± 2.1	$228.95/241 = 0.95$		
	BB+PL	437 ± 20		-1.21 ± 0.03		43.4 ± 3.1	$247.41/241 = 1.03$	1.00 ± 0.24	
$0.032 \rightarrow 0.064$	BB+Band	572 ± 65	1713 ± 1045	-0.42 ± 0.14	-1.77 ± 0.26	35.0 ± 2.6	$222.18/239 = 0.93$	0.55 ± 0.35	0.081
	Band		2439 ± 257	-0.29 ± 0.07	-2.64 ± 0.22	36.4 ± 2.6	$227.21/241 = 0.94$		
	BB+PL	329 ± 21		-1.41 ± 0.04		17.8 ± 1.9	$241.91/241 = 1.00$	0.92 ± 0.27	
$0.064 \rightarrow 0.096$	BB+Band	373 ± 34	435 ± 297	-0.48 ± 0.09	-1.70 ± 0.14	17.5 ± 1.9	$221.50/239 = 0.93$	0.85 ± 0.28	0.020
	Band		1586 ± 281	-0.48 ± 0.29	-2.23 ± 0.19	17.5 ± 2.0	$229.31/241 = 0.95$		
	BB+PL	124.9 ± 8.4		-1.27 ± 0.04		18.9 ± 0.23	$258.17/241 = 1.07$	0.21 ± 0.08	
$0.096 \rightarrow 0.128$	BB+Band	144 ± 84	454 ± 162	0.11 ± 0.30	-1.80 ± 0.17	16.1 ± 2.1	$226.61/239 = 0.95$	unc	0.061
	Band		622 ± 112	-0.11 ± 0.17	-1.99 ± 0.11	13.8 ± 1.8	$232.21/241 = 0.96$		
	BB+PL	35.5 ± 4.8		-1.52 ± 0.08		2.87 ± 0.95	$202.44/241 = 0.84$	0.13 ± 0.06	
$0.128 \rightarrow 0.160$	BB+Band	39.6 ± 6.8	unc	-1.2 ± 1.4	-1.54 ± 0.26	2.8 ± 1.2	$198.00/239 = 0.83$	0.14 ± 0.08	0.067
	Band		193 ± 124	-0.75 ± 0.40	-1.84 ± 0.18	2.55 ± 0.91	$203.40/241 = 0.84$		
	BB+PL	30.2 ± 7.7		-1.19 ± 0.10		5.7 ± 1.4	$237.82/241 = 0.99$	0.020 ± 0.019	
$0.160 \rightarrow 0.192$	BB+Band	22 ± 10	unc	unc	-1.25 ± 0.08	unc	$203.37/239 = 0.85$	unc	0.0045
	Band		unc	-0.7 ± 1.2	-1.40 ± 0.08	6.0 ± 1.4	$214.19/241 = 0.89$		

Notes. In the first column we have indicated the time bin; in the following five columns we have indicated the spectral models and their parameters. In the next three columns we have listed, respectively, the total flux, the χ^2, and the ratio between the thermal (where considered) and the non-thermal fluxes. The last column reports the significance in the addition of the BB with respect the sole Band model.

values are typical of the galactic halos environment. The filling factor varies in the range $9.1 \times 10^{-12} \leqslant \mathcal{R} \leqslant 1.5 \times 10^{-11}$, up to 2.38×10^{17} cm away from the burst site, and then drops to the value $\mathcal{R} = 1.0 \times 10^{-15}$. The value of the α parameter has been found to be -1.99 along the total duration of the GRB. In Figure 11 we show the NaI-n2 simulated light curve

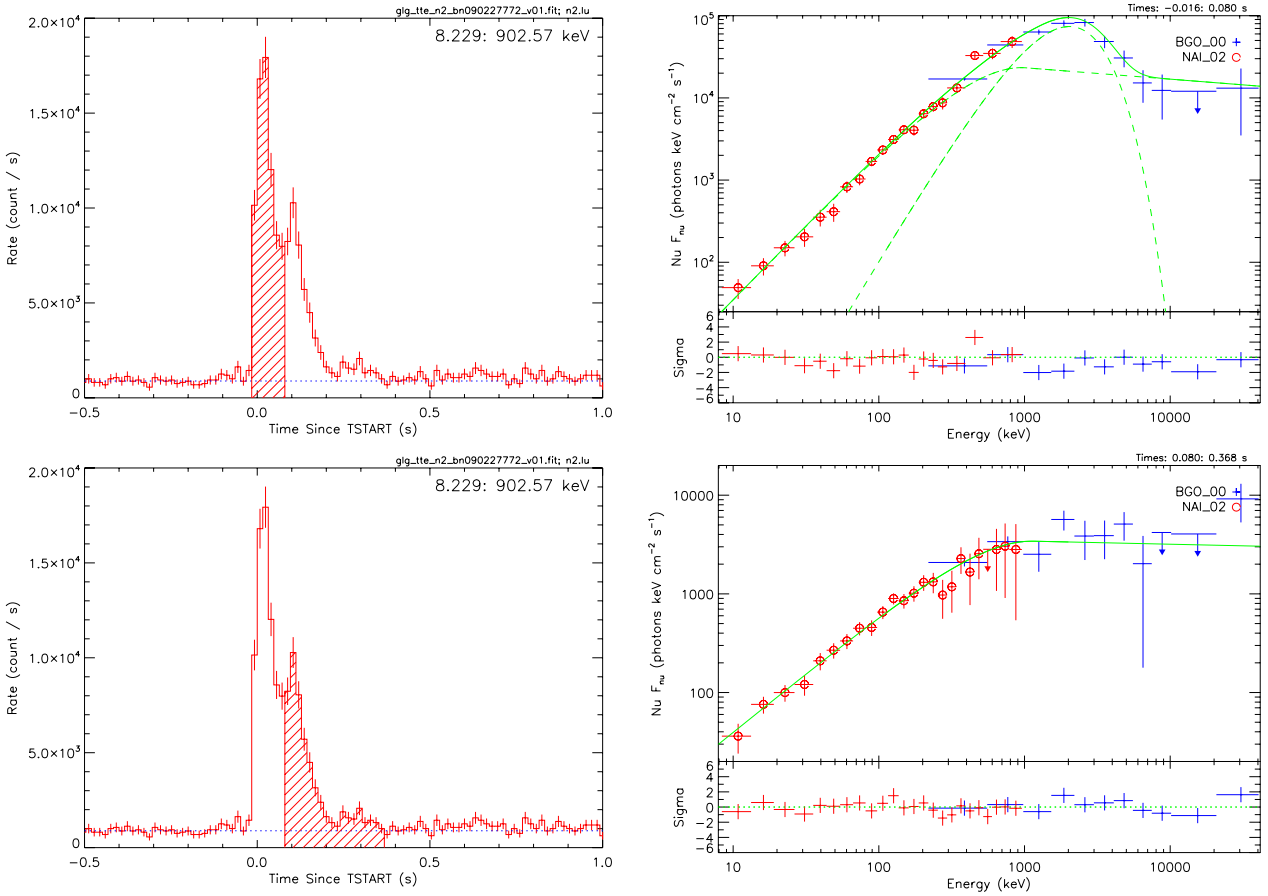

Figure 9. 16 ms time-binned NaI-n2 light curves of the P-GRB (left upper panel) and the extended afterglow (left lower panel) and their NaI-n2+BGO-b0 νF_ν spectra (on the right, the upper panel for the P-GRB and the lower one for the extended afterglow). The fit of the P-GRB is composed of a BB superimposed by a Band spectrum; the extended afterglow is well fitted by a simple Band function.

(A color version of this figure is available in the online journal.)

Table 4

The Results of the Spectral Analysis of the P-GRB (from $T_0 - 0.016$ s to $T_0 + 0.080$ s, Best-fit BB+Band Model) and the Extended Afterglow (from $T_0 + 0.080$ s to $T_0 + 0.368$ s, Best-fit Band Model) of GRB 090227B in the Energy Range 8 keV–40 MeV

	Model	kT (keV)	α	β	$E_{\rm peak}$ (keV)	$F_{\rm tot}$ (erg (cm^2 s)$^{-1}$)	$F_{\rm BB}$ (erg (cm^2 s)$^{-1}$)	C-STAT/dof
P-GRB	Band+BB	517 ± 28	-0.80 ± 0.05	-2.14 ± 0.17	952 ± 251	$(3.13 \pm 0.13) \times 10^{-4}$	$(1.61 \pm 0.47) \times 10^{-4}$	263.51/239
Ext. Aft.	Band		-0.79 ± 0.06	-2.01 ± 0.10	1048 ± 178	$(2.66 \pm 0.26) \times 10^{-5}$		276.50/241

Table 5

The Results of the Simulation of GRB 090227B in the Fireshell Model

Fireshell Parameter	Value
$E^{\rm tot}_{e^+e^-}$ (erg)	$(2.83 \pm 0.15) \times 10^{53}$
B	$(4.13 \pm 0.05) \times 10^{-5}$
$\Gamma_{\rm tr}$	$(1.44 \pm 0.01) \times 10^{4}$
$r_{\rm tr}$ (cm)	$(1.76 \pm 0.05) \times 10^{13}$
$kT_{\rm blue}$ (keV)	$(1.34 \pm 0.01) \times 10^{3}$
z	1.61 ± 0.14
$\langle n \rangle$ (particles cm^{-3})	$(1.90 \pm 0.20) \times 10^{-5}$
$\langle \delta n/n \rangle$	0.82 ± 0.11

(8–1000 keV) of GRB 090227B and in Figure 12 (left panel) we show the corresponding spectrum in the early ∼0.4 s of the emission, using the spectral model described by Equation (1) (Patricelli et al. 2012). The simulation of the extended afterglow starts $T_a - T_0 \sim 0.017$ s after the Trigtime T_0. After the submission of this manuscript, at the 13th *Marcel Grossmann* meeting Dr. G. Vianello suggested to extend our simulations from 1 MeV all the way to 40 MeV, since significant data are available from the BGO detector. Without changing the parameters used in the theoretical simulation of the NaI-n2 data, we have extended the simulation up to 40 MeV and we compared the results with the BGO-b0 data (see Figure 12, right panel). The theoretical simulation we performed, optimized on the NaI-n2 data alone, is perfectly consistent with the observed data all over the *entire* range of energies covered by the *Fermi*-GBM detector, both NaI and BGO.

We turn now to the emission of the early 96 ms. We have studied the interface between the P-GRB emission and the onset of the extended afterglow emission. In Figure 13 we have

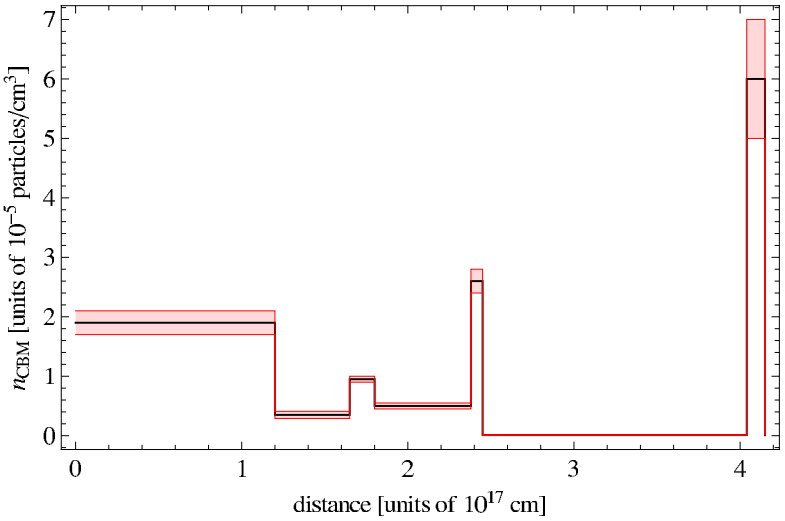

Figure 10. Radial CBM density distribution of GRB 090227B (black line) and its range of validity (red shaded region).
(A color version of this figure is available in the online journal.)

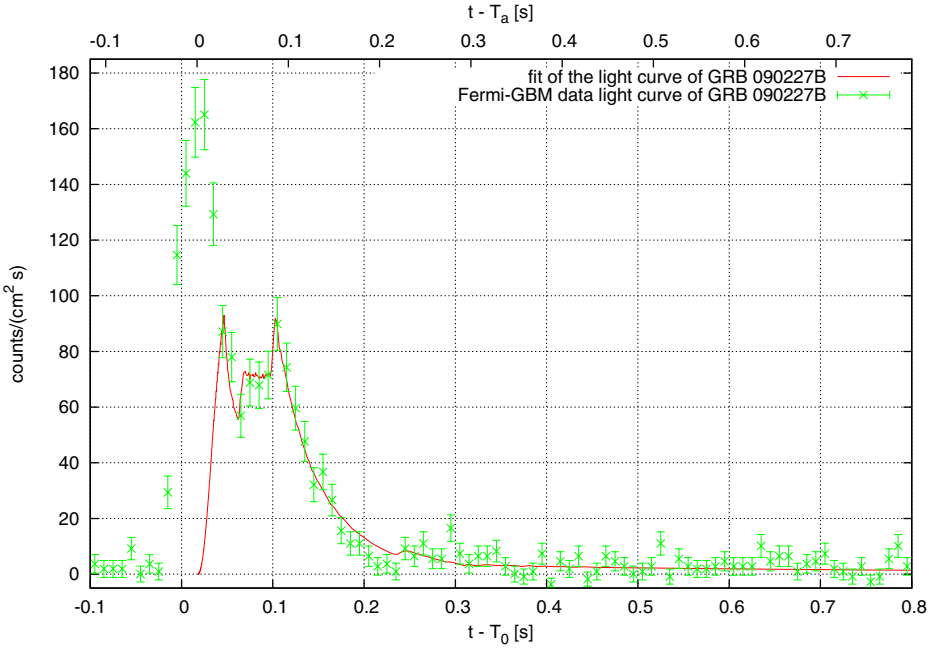

Figure 11. NaI-n2 simulated light curve of the extended-afterglow of GRB 090227B; each spike corresponds to the CBM density profile described in Table 6 and Figure 10. The zero of the lower x-axis corresponds to the trigtime T_0; the zero of the upper x-axis is the time from which we have started the simulation of the extended afterglow, T_a, namely 0.017 s after T_0.
(A color version of this figure is available in the online journal.)

plotted the thermal spectrum of the P-GRB and the Fireshell simulation (from T_0 + 0.015 s to T_0 + 0.080 s) of the early interaction of the extended afterglow. The sum of these two components is compared with the observed spectrum from the NaI-n2 detector in the energy range 8–1000 keV (see Figure 13, left panel). Then again, from the theoretical simulation in the energy range of the NaI-n2 data we have verified the consistency of the simulation extended up to 40 MeV with the observed data all over the range of energies covered by the *Fermi*-GBM detector, both NaI and BGO. The result is shown in Figure 13 (right panel).

5. CONSISTENCY WITH THE OPACITY DUE TO PAIR PRODUCTION

It is interesting to compare the Lorentz Γ factor theoretically determined from the P-GRB analysis with the lower limit coming from the opacity argument applied to the afterglow emission.

An estimate on this lower limit comes from the solution of the classical compactness problem for GRBs which arises from the combination of their large energy released, $\sim 10^{51}$ erg, the short variability timescale δt of a few milliseconds and

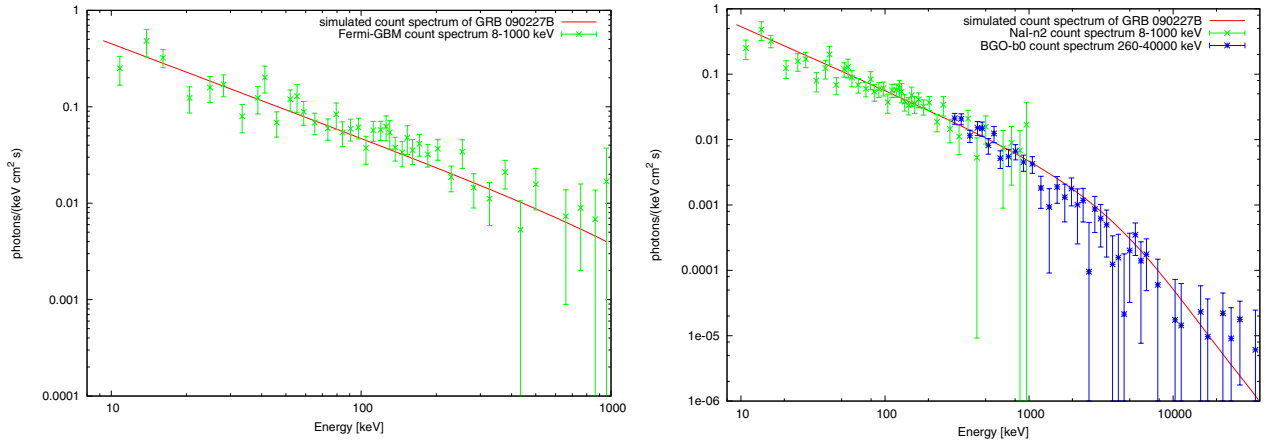

Figure 12. Left panel: the simulated photon number spectrum of the extended-afterglow of GRB 090227B (from $T_0 + 0.015$ s to $T_0 + 0.385$ s) in the energy band 8–1000 keV, compared to the NaI-n2 data in the same time interval. Right panel: the same simulated spectrum, with the same parameters, extended up to 40 MeV and compared to the NaI-n2 and the BGO-b0 data in the same time interval.

(A color version of this figure is available in the online journal.)

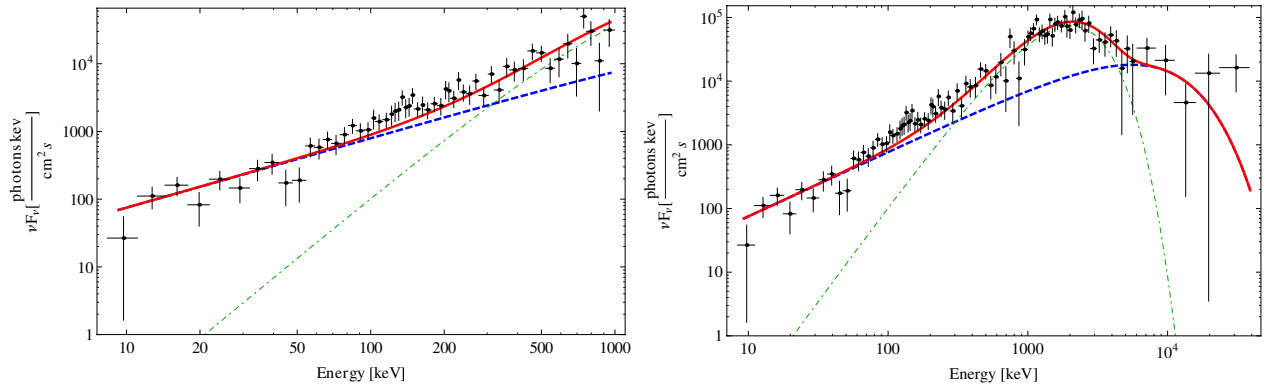

Figure 13. Left panel: the time-integrated (from $T_0+0.015$ s to $T_0+0.080$ s) Fireshell simulation in the energy band 8–1000 keV, dashed blue line, and the BB emission, dashed-dotted green line; the sum of the two components, the solid red line, is compared to the observed P-GRB emission. Right panel: the same considerations including the BGO data up to 40 MeV.

(A color version of this figure is available in the online journal.)

Table 6
The Density Mask of GRB 090227B

Cloud	Distance (cm)	$n_{\rm CBM}$ (cm^{-3})
1	1.76×10^{15}	$(1.9 \pm 0.2) \times 10^{-5}$
2	1.20×10^{17}	$(3.5 \pm 0.6) \times 10^{-6}$
3	1.65×10^{17}	$(9.5 \pm 0.5) \times 10^{-6}$
4	1.80×10^{17}	$(5.0 \pm 0.5) \times 10^{-6}$
5	2.38×10^{17}	$(2.6 \pm 0.2) \times 10^{-5}$
6	2.45×10^{17}	$(1.0 \pm 0.5) \times 10^{-7}$
7	4.04×10^{17}	$(6.0 \pm 1.0) \times 10^{-5}$

Notes. In the first column we report the number of CBM clouds, in the second their distance away from the black hole, and in the third the number density with the associated error box.

the observed hard non-thermal spectrum. Using the usual (Newtonian) causality limit on the size $R \leqslant c\delta t$ to estimate the density of photons, one finds that the optical depth for pair production at the source $\gamma\gamma \rightarrow e^+e^-$ would be $\sim 10^{15}$ (see Piran 1999). Such an optically thick source could not emit the observed non-thermal spectrum.

As Ruderman (1975) pointed out, relativistic effects can solve this problem. The causality limit of a source moving relativistically with Lorentz factor $\Gamma \gg 1$ toward us is $R \leqslant c\delta t/\Gamma^2$. Additionally, the observed photons have been blueshifted. At the source they have lower energy, by a factor $\approx 1/\Gamma$, which may be insufficient for pair production. Together this leads to a decrease in the estimated optical depth by a factor of $\Gamma^{2+2\beta}$ (Piran 2012), where β is the high energy spectral index of the photon number distribution. Thus, the average optical depth, up to a factor due to the cosmological effects, is

$$\tau_{\gamma\gamma} = \frac{f_p}{\Gamma^{2+2\beta}} \frac{\sigma_T S d_l^2}{c^2 \delta t^2 m_e c^2}, \quad (5)$$

where f_p is the fraction of photon pairs at the source that can effectively produce pairs, σ_T is the Thompson cross-section and S is the observed fluence. From the condition $\tau_{\gamma\gamma} < 1$, Equation (5) becomes

$$\Gamma > \left(\frac{f_p \sigma_T S d_l^2}{c^2 \delta t^2 m_e c^2} \right)^{\frac{1}{2+2\beta}}. \quad (6)$$

By setting δt equal to the minimum variability timescale observed for GRB 090227B, $\sim$2 ms (Guiriec et al. 2010), and

using the observed total fluence, $S_{\rm tot} = 3.79 \times 10^{-5}$ erg cm^{-2}, the high energy spectral index, $\beta = 2.90$, and the theoretically inferred redshift, $z = 1.61$, we obtain a lower limit $\Gamma > 594$.

The large quantitative difference between our theoretically estimated Lorentz factor from the P-GRB and the one derived from the opacity argument is not surprising in view of the very different approximations adopted. While the determination from the P-GRB consists of a precise analysis at the instant of transparency, the determination of the lower limit from the Equation (6) is based on an estimate taking a time-averaged value on the entire extended afterglow.

It is important, of course, that the precise value determined from the P-GRB does fulfill the inequality given in Equation (6).

6. CONCLUSIONS

The comprehension of this short GRB has been improved by analyzing the different spectra in the T_{90}, $T_{\rm spike}$, and $T_{\rm tail}$ time intervals. We have shown that within the T_{90} and the $T_{\rm spike}$ all the considered models (BB+Band, Band+PL, Compt+PL) are viable, while in the $T_{\rm tail}$ time interval the presence of a thermal component is ruled out. The result of the analysis in the $T_{\rm tail}$ time interval gives an additional correspondence between the Fireshell model (see Section 2.1) and the observational data. According to this picture, the emission within the $T_{\rm spike}$ time interval is related to the P-GRB, and it is expected to have a thermal spectrum with an additional extra NT component due to an early onset of the extended afterglow. In this time interval a BB with an additional Band component has been observed and we have shown that it is statistically equivalent to the Compt+PL and the Band+PL models. Our theoretical interpretation is consistent with the observational data and statistical analysis. From an astrophysical point of view, the BB+Band model is preferred over the Compt+PL and the Band+PL models, which has been described by a consistent theoretical model.

GRB 090227B is the missing link between the genuine short GRBs, with the baryon load $B \lesssim 5 \times 10^{-5}$ and theoretically predicted by the Fireshell model (Ruffini et al. 2001a, 2001b, 2001c), and the long bursts.

From the observations, GRB 090227B has an overall emission lasting ~0.9 s with a fluence of 3.79×10^{-5} erg cm^{-2} in the energy range 8 keV–40 MeV. In the absence of optical identification, no determination of its cosmological redshift and of its energetics was possible.

Thanks to the excellent data available from *Fermi*-GBM (Meegan et al. 2009), it has been possible to probe the comparison between the observation and the theoretical model. In this sense, we have then performed a more detailed spectral analysis on the timescale as short as 16 ms of the time interval $T_{\rm spike}$. As a result we have found a thermal emission in the early 96 ms which we have identified with the theoretically expected P-GRB component. The subsequent emission of the time interval $T_{\rm spike}$ has been interpreted as part the extended afterglow. Consequently, we have determined the cosmological redshift, $z = 1.61 \pm 0.14$, as well as the baryon load, $B = (4.13 \pm 0.05) \times 10^{-5}$, its energetics, $E^{\rm tot}_{e^+e^-} = (2.83 \pm 0.15) \times 10^{53}$ erg, and the extremely high Lorentz Γ factor at the transparency, $\Gamma_{\rm tr} = (1.44 \pm 0.01) \times 10^4$.

We are led to the conclusion (see also Rueda & Ruffini 2012) that the progenitor of this GRB is a binary neutron star, which, for simplicity, we assume to have the same mass, by the following considerations:

1. the very low average number density of the CBM, $\langle n_{\rm CBM} \rangle \sim 10^{-5}$ particles cm^{-3}; this fact points to two compact objects in a binary system that have spiraled out in the halo of their host galaxy (see Bernardini et al. 2007, 2008; Bianco et al. 2008; Caito et al. 2009, 2010; de Barros et al. 2011);
2. the large total energy, $E^{\rm tot}_{e^+e^-} = 2.83 \times 10^{53}$ erg, which we can indeed infer in view of the absence of beaming, and the very short timescale of emission point again to two neutron stars. We are led to a binary neutron star with a total mass $m_1 + m_2$ larger than the neutron star critical mass, $M_{\rm cr}$. In light of the recent neutron star theory in which all the fundamental interactions are taken into account (Belvedere et al. 2012), we obtain for simplicity in the case of equal neutron star masses, $m_1 = m_2 = 1.34\, M_\odot$, radii $R_1 = R_2 = 12.24$ km, where we have used the NL3 nuclear model parameters for which $M_{\rm cr} = 2.67\, M_\odot$;
3. the very small value of the baryon load, $B = 4.13 \times 10^{-5}$, is consistent with the above two neutron stars that have crusts ~0.47 km thick. The new theory of the neutron stars, developed in Belvedere et al. (2012), leads to the prediction of GRBs with still smaller baryon load and, consequently, shorter periods. We indeed infer an absolute upper limit on the energy emitted via gravitational waves, $\sim 9.6 \times 10^{52}$ erg (see Rueda & Ruffini 2012).

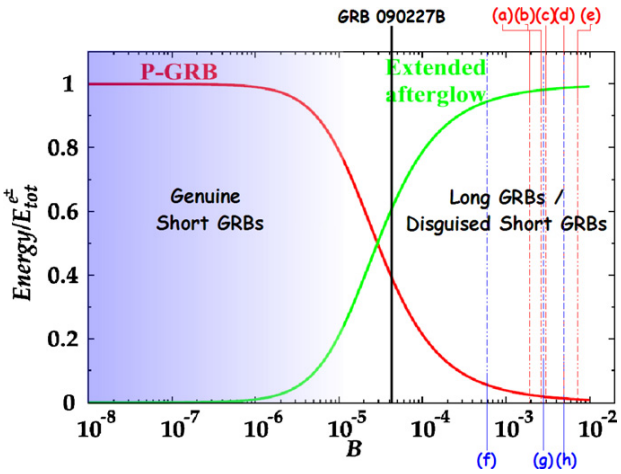

Figure 14. Energy emitted in the extended afterglow (green curve) and in the P-GRB (red curve) in units of the total energy $E^{\rm tot}_{e^+e^-} = 1.77 \times 10^{53}$ erg are plotted as functions of the B parameter. In the figure are also marked some values of the baryon load: in black GRB 090227B and in red and blue some values corresponding to, respectively, some long and disguised short GRBs we analyzed.

(A color version of this figure is available in the online journal.)

We can then generally conclude on the existence of three different possible structures of the canonical GRBs (see Figure 14 and Table 7):

1. long GRB with baryon load $3.0 \times 10^{-4} \lesssim B \leqslant 10^{-2}$, exploding in a CBM with average density of $\langle n_{\rm CBM} \rangle \approx 1$ particle cm^{-3}, typical of the inner galactic regions;
2. disguised short GRBs with the same baryon load as the previous class, but occurring in a CBM with $\langle n_{\rm CBM} \rangle \approx 10^{-3}$ particle cm^{-3}, typical of galactic halos (Bernardini et al. 2007, 2008; Bianco et al. 2008; Caito et al. 2009, 2010; de Barros et al. 2011);
3. genuine short GRBs which occur for $B \lesssim 10^{-5}$ with the P-GRB predominant with respect to the extended afterglow and exploding in a CBM with $\langle n_{\rm CBM} \rangle \approx 10^{-5}$ particle cm^{-3}, typical again of galactic halos, being GRB 090227B the first example.

Table 7
List of the Long and Disguised Short GRBs Labeled in Figure 14 compared with GRB 090227B

label	GRB	$E^{\rm tot}_{e^+e^-}$ (erg)	B	$\langle n_{\rm CBM}\rangle$ (cm^{-3})
(a)	090618	2.49×10^{53}	1.98×10^{-3}	1.0
(b)	080319B	1.32×10^{54}	2.50×10^{-3}	6.0
(c)	991216	4.83×10^{53}	3.00×10^{-3}	1.0
(d)	030329	2.12×10^{52}	4.80×10^{-3}	2.0
(e)	031203	1.85×10^{50}	7.40×10^{-3}	0.3
(f)	050509B	5.52×10^{48}	6.00×10^{-4}	1.0×10^{-3}
(g)	060614	2.94×10^{51}	2.80×10^{-3}	1.0×10^{-3}
(h)	970228	1.45×10^{54}	5.00×10^{-3}	9.5×10^{-4}
	090227B	2.83×10^{53}	4.13×10^{-5}	1.9×10^{-5}

Note. For each burst the total energy of the plasma, the baryon load, and the average CBM density are indicated.

Both classes of GRBs occurring in galactic halos originate from binary mergers.

Finally, if we turn to the theoretical model within a general relativistic description of the gravitational collapse to a 10 $M_\odot$ black hole (see e.g., Ruffini et al. 2003, 2005c and Figure 2 in Fraschetti et al. 2006), we find the necessity of time resolutions of the order of the fraction of a ms, possibly down to μs, in order to follow such a process. One would need new space missions larger collecting area to prove with great accuracy the identification of a thermal component. It is likely that an improved data acquisition with high signal to noise on shorter timescale would evidence more clearly the thermal component as well as distinguish more effectively different fitting procedure.

We are grateful to the anonymous referee for important remarks which have improved the presentation of our paper. We thank also Dr. Giacomo Vianello for the important suggestion of checking the extrapolation from 1 MeV up to 40 MeV of the simulated spectra, comparing them with the *Fermi*-BGO data: this has provided a further important check of the consistency of our theoretical model with the data all over the range of energies covered by the *Fermi*-GBM detector, both NaI and BGO. M.M. is especially grateful to Jorge A. Rueda and Gregory Vereshchagin for fruitful discussions about this work.

REFERENCES

Aksenov, A. G., Ruffini, R., & Vereshchagin, G. V. 2007, PhRvL, 99, 125003
Band, D., Matteson, J., Ford, L., et al. 1993, ApJ, 413, 281
Belvedere, R., Pugliese, D., Rueda, J. A., Ruffini, R., & Xue, S.-S. 2012, NuPhA, 883, 1
Berger, E. 2011, NewAR, 55, 1
Bernardini, M. G., Bianco, C. L., Caito, L., et al. 2007, A&A, 474, L13
Bernardini, M. G., Bianco, C. L., Caito, L., et al. 2008, in AIP Conf. Proc. 966, Relativistic Astrophysics, ed. C. L. Bianco & S. S. Xue (Melville, NY: AIP), 7
Bianco, C. L., Bernardini, M. G., Caito, L., et al. 2008, in AIP Conf. Proc. 966, Relativistic Astrophysics, ed. C. L. Bianco & S. S. Xue (Melville, NY: AIP), 12
Bianco, C. L., & Ruffini, R. 2005a, ApJL, 633, 13
Bianco, C. L., & Ruffini, R. 2005b, ApJL, 620, 23
Bianco, C. L., Ruffini, R., Vereshchagin, G. V., & Xue, S. 2006, JKPS, 49, 722
Blinnikov, S. I., Novikov, I. D., Perevodchikova, T. V., & Polnarev, A. G. 1984, SvAL, 10, 177
Bloom, J. S., Prochaska, J. X., Pooley, D., et al. 2006, ApJ, 638, 354
Caito, L., Amati, L., Bernardini, M. G., et al. 2010, A&A, 521, A80
Caito, L., Bernardini, M. G., Bianco, C. L., et al. 2009, A&A, 498, 501
Cavallo, G., & Rees, M. J. 1978, MNRAS, 183, 359
Costa, E., Frontera, F., Heise, J., et al. 1997, Natur, 387, 783
Damour, T., & Ruffini, R. 1975, PhRvL, 35, 463
de Barros, G., Amati, L., Bernardini, M. G., et al. 2011, A&A, 529, A130
Dezalay, J.-P., Barat, C., Talon, R., et al. 1992, in AIP Conf. Proc. 265, ed. W. S. Paciesas & G. J. Fishman (Melville, NY: AIP), 304
Fong, W., Berger, E., & Fox, D. B. 2010, ApJ, 708, 9
Fraschetti, F., Ruffini, R., Vitagliano, L., & Xue, S. S. 2006, NCimB, 121, 1477
Gehrels, N., Sarazin, C. L., O'Brien, P. T., et al. 2005, Natur, 437, 851
Golenetskii, S., Aptekar, R., Mazets, E., et al. 2009a, GCN, 8925, 1
Golenetskii, S., Aptekar, R., Mazets, E., et al. 2009b, GCN, 8926, 1
Goodman, J. 1986, ApJL, 308, 47
Guiriec, S. 2009, GCN, 8921, 1
Guiriec, S., Briggs, M. S., Connaugthon, V., et al. 2010, ApJ, 725, 225
Guiriec, S., Connaughton, V., Briggs, M. S., et al. 2011, ApJL, 727, 33
Izzo, L., Ruffini, R., Bianco, C. L., et al. 2012a, arXiv:1205.6651
Izzo, L., Ruffini, R., Penacchioni, A. V., et al. 2012b, A&A, 543, A10
Katz, J. I. 1994, ApJ, 422, 248
Klebesadel, R. W. 1992, in Gamma-Ray Bursts - Observations, Analyses and Theories, ed. C. Ho, R. I. Epstein, & E. E. Fenimore (Cambridge: Cambridge Univ. Press), 161
Kopač, D., D'Avanzo, P., Melandri, A., et al. 2012, MNRAS, 424, 2392
Kouveliotou, C., Meegan, C. A., Fishman, G. J., et al. 1993, ApJL, 413, 101
Lazzati, D., & Begelman, M. C. 2010, ApJ, 725, 1137
Meegan, C., Lichti, G., Bhat, P. N., et al. 2009, ApJ, 702, 791
Meegan, C. A., Fishman, G. J., Wilson, R. B., et al. 1992, Natur, 355, 143
Meszaros, P., Laguna, P., & Rees, M. J. 1993, ApJ, 415, 181
Metzger, M. R., Djorgovski, S. G., Kulkarni, S. R., et al. 1997, Natur, 387, 878
Norris, J. P., & Bonnell, J. T. 2006, ApJ, 643, 266
Paczynski, B. 1998, ApJL, 494, 45
Patricelli, B., Bernardini, M. G., Bianco, C. L., et al. 2012, ApJ, 756, 16
Pe'er, A., Mészáros, P., & Rees, M. J. 2005, ApJ, 635, 476
Pe'er, A., Mészáros, P., & Rees, M. J. 2006, ApJ, 642, 995
Pe'er, A., Zhang, B.-B., Ryde, F., et al. 2012, MNRAS, 420, 468
Penacchioni, A. V., Ruffini, R., Izzo, L., et al. 2012, A&A, 538, A58
Piran, T. 1999, Phys. Rep., 314, 575
Piran, T. 2012, in Twelfth Marcel Grossmann Meeting on General Relativity, ed. T. Damour, R. T. Jantzen, & R. Ruffini (Singapore: World Scientific), 269
Piran, T., Shemi, A., & Narayan, R. 1993, MNRAS, 263, 861
Rees, M. J., & Mészáros, P. 2005, ApJ, 628, 847
Ruderman, M. 1975, in Annals of the New York Academy of Sciences, Vol. 262, Seventh Texas Symposium on Relativistic Astrophysics, ed. P. G. Bergman, E. J. Fenyves, & L. Motz (New York: Wiley-Interscience), 164
Rueda, J. A., & Ruffini, R. 2012, ApJL, 758, 7
Ruffini, R. 2001, in Fluctuating Paths and Fields, ed. W. Janke, A. Pelster, H. J. Schmidt, & M. Bachmann (Singapore: World Scientific)
Ruffini, R. 2009, in The Kerr Spacetime, ed. D. L. Wiltshire, M. Visser, & S. Scott (Cambridge: Cambridge Univ. Press), 161
Ruffini, R., Bernardini, M. G., Bianco, C. L., et al. 2005a, in AIP Conf. Proc. 782, XIth Brazilian School of Cosmology and Gravitation, ed. M. Novello & S. E. Perez Bergliaffa (Melville, NY: AIP), 42
Ruffini, R., Bianco, C. L., Chardonnet, P., Fraschetti, F., & Xue, S. 2002, ApJL, 581, 19
Ruffini, R., Bianco, C. L., Fraschetti, F., Xue, S.-S., & Chardonnet, P. 2001a, ApJL, 555, 117
Ruffini, R., Bianco, C. L., Fraschetti, F., Xue, S.-S., & Chardonnet, P. 2001b, ApJL, 555, 113
Ruffini, R., Bianco, C. L., Fraschetti, F., Xue, S.-S., & Chardonnet, P. 2001c, ApJL, 555, 107
Ruffini, R., Bianco, C. L., Xue, S.-S., et al. 2004, IJMPD, 13, 843
Ruffini, R., Bianco, C. L., Xue, S.-S., et al. 2005b, IJMPD, 14, 97
Ruffini, R., Fraschetti, F., Vitagliano, L., & Xue, S.-S. 2005c, IJMPD, 14, 131
Ruffini, R., Izzo, L., Penacchioni, A. V., et al. 2011, Proceedings of the 2010 Texas Meeting, Heidelberg, Germany, PoS (Texas2010), 101
Ruffini, R., Salmonson, J. D., Wilson, J. R., & Xue, S. 2000, A&A, 359, 855
Ruffini, R., Salmonson, J. D., Wilson, J. R., & Xue, S.-S. 1999, A&A, 350, 334
Ruffini, R., Vereshchagin, G., & Xue, S.-S. 2010, PhR, 487, 1
Ruffini, R., Vitagliano, L., & Xue, S.-S. 2003, PhLB, 573, 33
Ruffini, R., & Xue, S.-S. 2008, in AIP Conf. Proc. 1059, 5th Sino-Italian Workshop on Relativistic Astrophysics, ed. D.-S. Lee & W. Lee (Melville, NY: AIP), 72

Ryde, F. 2004, ApJ, 614, 827
Ryde, F., & Pe'er, A. 2009, ApJ, 702, 1211
Sahu, K. C., Livio, M., Petro, L., et al. 1997, Natur, 387, 476
Shemi, A., & Piran, T. 1990, ApJL, 365, 55
Strong, I. B., Klebesadel, R. W., & Evans, W. D. 1975, in Annals of the New York Academy of Sciences, Vol. 262, Seventh Texas Symposium on Relativistic Astrophysics, ed. P. G. Bergman, E. J. Fenyves, & L. Motz (New York: Wiley-Interscience), 145
Tavani, M. 1998, ApJL, 497, 21
Tavani, M., Argan, A., Barbiellini, G., et al. 2008, in AIP Conf. Proc. 1000, Gamma-Ray Bursts 2007, ed. M. Galassi, D. Palmer, & E. Fenimore (Melville, NY: AIP), 523
Troja, E., King, A. R., O'Brien, P. T., Lyons, N., & Cusumano, G. 2008, MNRAS, 385, L10
van Paradijs, J., Groot, P. J., Galama, T., et al. 1997, Natur, 386, 686
Woosley, S. E. 1993, ApJ, 405, 273

The Astrophysical Journal, 772:62 (5pp), 2013 July 20 doi:10.1088/0004-637X/772/1/62

GRB 090510: A DISGUISED SHORT GAMMA-RAY BURST WITH THE HIGHEST LORENTZ FACTOR AND CIRCUMBURST MEDIUM

M. Muccino[1,2], R. Ruffini[1,2,3], C. L. Bianco[1,2], L. Izzo[1,2], A. V. Penacchioni[1,3], and G. B. Pisani[1,3]
[1] Dip. di Fisica and ICRA, Sapienza Università di Roma, Piazzale Aldo Moro 5, I-00185 Rome, Italy
[2] ICRANet, Piazza della Repubblica 10, I-65122 Pescara, Italy
[3] Universite de Nice Sophia Antipolis, Nice, CEDEX 2, Grand Chateau Parc Valrose, France
Received 2013 February 19; accepted 2013 May 7; published 2013 July 5

ABSTRACT

GRB 090510, observed by both *Fermi* and *AGILE* satellites, is the first bright short-hard gamma-ray burst (GRB) with an emission from the keV up to the GeV energy range. Within the Fireshell model, we interpret the faint precursor in the light curve as the emission at the transparency of the expanding e^+e^- plasma: the Proper-GRB. From the observed isotropic energy, we assume a total plasma energy $E^{\rm tot}_{e^+e^-} = (1.10 \pm 0.06) \times 10^{53}$ erg and derive a Baryon load $B = (1.45 \pm 0.28) \times 10^{-3}$ and a Lorentz factor at transparency $\Gamma_{\rm tr} = (6.7 \pm 1.6) \times 10^2$. The main emission ∼0.4 s after the initial spike is interpreted as the extended afterglow, due to the interaction of the ultrarelativistic baryons with the CircumBurst Medium (CBM). Using the condition of fully radiative regime, we infer a CBM average spherically symmetric density of $\langle n_{\rm CBM}\rangle = (1.85 \pm 0.14) \times 10^3$ particles cm^{-3}, one of the highest found in the Fireshell model. The value of the filling factor, $1.5 \times 10^{-10} \leqslant \mathcal{R} \leqslant 3.8 \times 10^{-8}$, leads to the estimate of filaments with densities $n_{\rm fil} = n_{\rm CBM}/\mathcal{R} \approx (10^6$–$10^{14})$ particles cm^{-3}. The sub-MeV and the MeV emissions are well reproduced. When compared to the canonical GRBs with $\langle n_{\rm CBM}\rangle \approx 1$ particles cm^{-3} and to the disguised short GRBs with $\langle n_{\rm CBM}\rangle \approx 10^{-3}$ particles cm^{-3}, the case of GRB 090510 leads to the existence of a new family of bursts exploding in an overdense galactic region with $\langle n_{\rm CBM}\rangle \approx 10^3$ particles cm^{-3}. The joint effect of the high $\Gamma_{\rm tr}$ and the high density compresses in time and "inflates" in intensity the extended afterglow, making it appear as a short burst, which we here define as a "disguised short GRB by excess." The determination of the above parameter values may represent an important step toward the explanation of the GeV emission.

Key words: gamma-ray burst: general – gamma-ray burst: individual (GRB 090510)

Online-only material: color figures

1. INTRODUCTION

In their earliest classification of the 4BATSE catalog (Meegan 1997), all gamma-ray bursts (GRBs) were classified into short and long bursts depending on whether their T_{90} duration is longer or shorter than 2 s (Klebesadel 1992; Dezalay et al. 1992; Kouveliotou et al. 1993; Tavani 1998). In the meantime, short bursts have been shown to originate from a variety of astrophysical origins and not from a homogeneous class. In the Fireshell model (Ruffini et al. 2001a, 2001b, 2001c, 2010), the canonical GRB has two components: an emission occurring at the transparency of the optically thick expanding e^+e^--baryon plasma (Ruffini et al. 2000), the Proper-GRB (P-GRB), followed by the extended afterglow due to the interactions between the accelerated baryons and the CircumBurst Medium (CBM). Such an extended afterglow comprises the prompt emission as well as the late phase of the afterglow (Bianco & Ruffini 2005a, 2005b). The relative energy of these two components, for a given total energy of the plasma $E^{\rm tot}_{e^+e^-}$, is uniquely a function of the baryon load $B = M_B c^2/E^{\rm tot}_{e^+e^-}$, where M_B is the total baryon mass (see Figure 1, left panel).

The genuine short GRBs (Ruffini et al. 2001b) are the bursts occurring for $B \lesssim 10^{-5}$. The first example of such systems has indeed been recently identified, originating in a binary neutron star merger (Muccino et al. 2013).

The existence of disguised short GRBs, with baryon load $3 \times 10^{-4} \leqslant B \leqslant 10^{-2}$ (Bernardini et al. 2007, 2008), has also been proved. In this class the extended afterglow is indeed energetically predominant but results in a "deflated" emission, less intense than the P-GRB due to the low density of the CBM, $\langle n_{\rm CBM}\rangle \approx 10^{-3}$ particles cm^{-3}, which is much lower than the canonical value $\langle n_{\rm CBM}\rangle \approx 1$ particles cm^{-3}. The majority of the declared short bursts in the current literature appear to be disguised short GRBs (Bernardini et al. 2007, 2008; Caito et al. 2009, 2010; de Barros et al. 2011).

In this paper we show a yet different kind of a disguised short GRB, GRB 090510, again, with $3 \times 10^{-4} \leqslant B \leqslant 10^{-2}$ and Lorentz factor $\Gamma_{\rm tr} \approx 700$, occurring in a medium with $\langle n_{\rm CBM}\rangle \approx 10^3$ particles cm^{-3}. We define, indeed, these GRBs as "disguised short burst by excess," since their $\langle n_{\rm CBM}\rangle$ is much larger than the canonical one. Correspondingly, we indicate the disguised short GRBs with a CBM density typical of the galactic halo environments, $\langle n_{\rm CBM}\rangle \approx 10^{-3}$ particles cm^{-3}, as "disguised short GRBs by defect" (see Figure 1, right panel).

The possibility of GRBs exploding in high density CBM has been already considered in the literature (Dai & Lu 1999; Lazzati et al. 1999; Piro et al. 2001; Wang et al. 2003; Prochaska et al. 2008; Izzo et al. 2012). In Dai & Lu (1999), Piro et al. (2001), and Wang et al. (2003), the high density has been inferred from the steepening in the afterglows, respectively, of GRB 990123 in the R band about ∼2.5 days after the burst, of GRB 000926 in the R band after ∼2 days, and of GRB 990705 in the H band after ∼1 day, due to the transition to the nonrelativistic regime of the fireball. Lazzati et al. (1999) discuss the possibility that the detection of Fe lines in the afterglows of GRB 970508 and GRB 970828 could be due to recombination processes in extremely high densities during the X-ray afterglow. In Prochaska et al. (2008), the authors inferred dense environments, $n \gtrsim 10^3$ particles cm^{-3}, from a survey for N v absorption in GRB afterglow spectra. In particular, in Izzo et al. (2012) the Fireshell model has been applied in the analysis of GRB 970828, discussed also in Lazzati et al. (1999), inferring a dense environment with $\langle n_{\rm CBM}\rangle = 3.4 \times 10^3$ particles cm^{-3}, consistent with the large column density environment in Yoshida

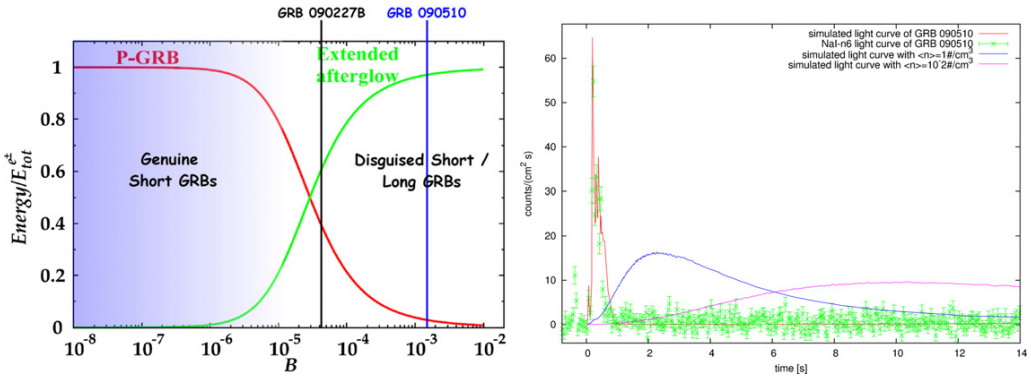

Figure 1. Left panel: the energy emitted in the extended afterglow (green curve) and in the P-GRB (red curve) in units of $E^{\rm tot}_{e^+e^-}$ are plotted as functions of B. The values of B of GRB 090510 (in blue) and of the genuinely short GRB 090227B (in black) are compared. Right panel: the 50 ms time-binned NaI-n6 light curve (green data) and the extended afterglow simulations corresponding to CBM average densities of a "disguised short GRB by excess" with $\langle n_{\rm CBM}\rangle \approx 10^3$ particles cm^{-3} (red curve), of a canonical long GRB with $\langle n_{\rm CBM}\rangle = 1$ particle cm^{-3} (blue curve), and of a "disguised short GRB by defect" with $\langle n_{\rm CBM}\rangle = 10^{-2}$ particles cm^{-3} (purple curve). For larger densities the extended afterglow compresses in time and "inflates" in intensity.

(A color version of this figure is available in the online journal.)

Table 1
ΔT_1 Time Interval: Parameters of PL, BB+PL, Band, Compt, Band+BB, and Compt+BB Models in the Energy Range 8–7000 keV

Interval	Model	kT (keV)	α	β	E_p (keV)	γ	$F_{\rm tot}\times 10^{-6}$ (erg (cm^2 s)$^{-1}$)	C-STAT/DOF	Significance
	PL	...	...	...	...	-1.22 ± 0.06	9.2 ± 1.3	195.41/195	
	BB+PL	34.2 ± 7.5	...	...	...	-1.10 ± 0.14	7.6 ± 1.3	188.60/193	0.03
	Band	...	unc	-1.44 ± 0.11	94 ± 74	...	7.4 ± 1.5	187.11/193	
ΔT_1	Compt	...	-0.81 ± 0.22	...	990 ± 554	...	4.4 ± 1.6	189.97/194	
	Band+BB	24.3 ± 5.6	unc	-1.76 ± 0.62	unc	...	7.1 ± 2.0	186.90/191	0.57
	Compt+BB	27.2 ± 6.7	-0.72 ± 0.39	...	2967 ± 1570	...	8.4 ± 2.3	187.23/192	0.90
ΔT_2 (a)	Band+PL	...	-0.70 ± 0.10	-3.13 ± 0.97	3941 ± 346	-1.55 ± 0.54	43.6 ± 1.9	207.78/236	
ΔT_2 (b)	Band+PL	...	-0.71 ± 0.07	-2.97 ± 0.26	4145 ± 398	-1.62 ± 0.05	83.3 ± 6.8	199.20/256	

Notes. ΔT_2 time interval: parameters of the best fits (Band+PL) in the energy ranges (a) 8–40,000 keV (GBM) and (b) 8 keV–30 GeV (GBM+LAT). In the last column of ΔT_1, we list the significance levels from the comparison between nested models (BB+PL over PL, Band+BB over Band, and Compt+BB over Compt).

et al. (2001). In the case of GRB 090510, the joint effect of the very dense CBM and the high Lorentz factor at the transparency, $\Gamma_{\rm tr}\sim 700$, leads to an extended afterglow with $T_{90}<2$ s (see Figure 1, right panel). These high values of the CBM density $n_{\rm CBM}$ and of the Lorentz factor $\Gamma_{\rm tr}$ may represent an important step toward the explanation of the GeV emission.

The work is organized as follows: in Section 2 we present the data analysis of GRB 090510; in Section 3 we give our theoretical interpretation on the source; and in Section 4 we summarize our conclusions.

2. GRB 090510 DATA ANALYSIS

At 00:22:59.97 UT on 2009 May 10, the *Fermi*-GBM detector (Guiriec et al. 2009) triggered and located the short and bright burst GRB 090510, which was also detected by *Swift* (Hoversten et al. 2009), *Fermi*-LAT (Ohno & Pelassa 2009), *AGILE* (Longo et al. 2009), Konus-*Wind* (Golenetskii et al. 2009), and *Suzaku*-WAM (Ohmori et al. 2009). Optical observations by the Very Large Telescope/FORS2 located the host galaxy of GRB 090510 at the redshift of $z=0.903\pm0.003$ (Rau et al. 2009). The offset with respect to the Nordic Optical Telescope refined afterglow position (Olofsson et al. 2009) corresponds to 5.5 kpc.

We have analyzed the *Fermi*-GBM data from NaI-n6 (8–900 keV) and BGO-b1 (260 keV–40 MeV) detectors and the LAT data in the energy range 100 MeV–30 GeV.

The light curve of GRB 090510 is composed of two different episodes, 0.5 s apart. The first episode, from $T_0-0.064$ s to $T_0+0.016$ s (in the following denoted as ΔT_1 time interval; T_0 indicates the trigger time), was not considered by Ackermann et al. (2010), Giuliani et al. (2010), and Guiriec et al. (2010) because of the small content of detected photons. Even though the statistical content of this first episode is very poor, in this paper we show its great relevance for theoretical analysis, since it can be identified with the P-GRB. The second episode can be interpreted as the extended afterglow. In the statistical analysis of the first episode, we have considered power-law (PL), black body (BB) plus PL, Band (Band et al. 1993), Comptonized (Compt), Band+BB, and Compt+BB models. Following the statistical analysis for nested models by Guiriec et al. (2010), models more complicated than the simplest Band and Compt are singled out (see the last column of Table 1). The direct statistical comparison between the BB+PL and PL models gives a significance level of 3% (see Table 1). This means that the BB+PL model improves the fit of the data of the first episode with respect to the PL model, which is excluded at the 97% confidence level. The simple Band model has an unconstrained α index and a large error on the energy peak E_p, as well as in the case of the Compt model, for which the total flux is underestimated with respect to the Band and BB+PL models. The quality of data does not allow us to favor the BB+PL model versus the Compt one from a purely statistical analysis. In order

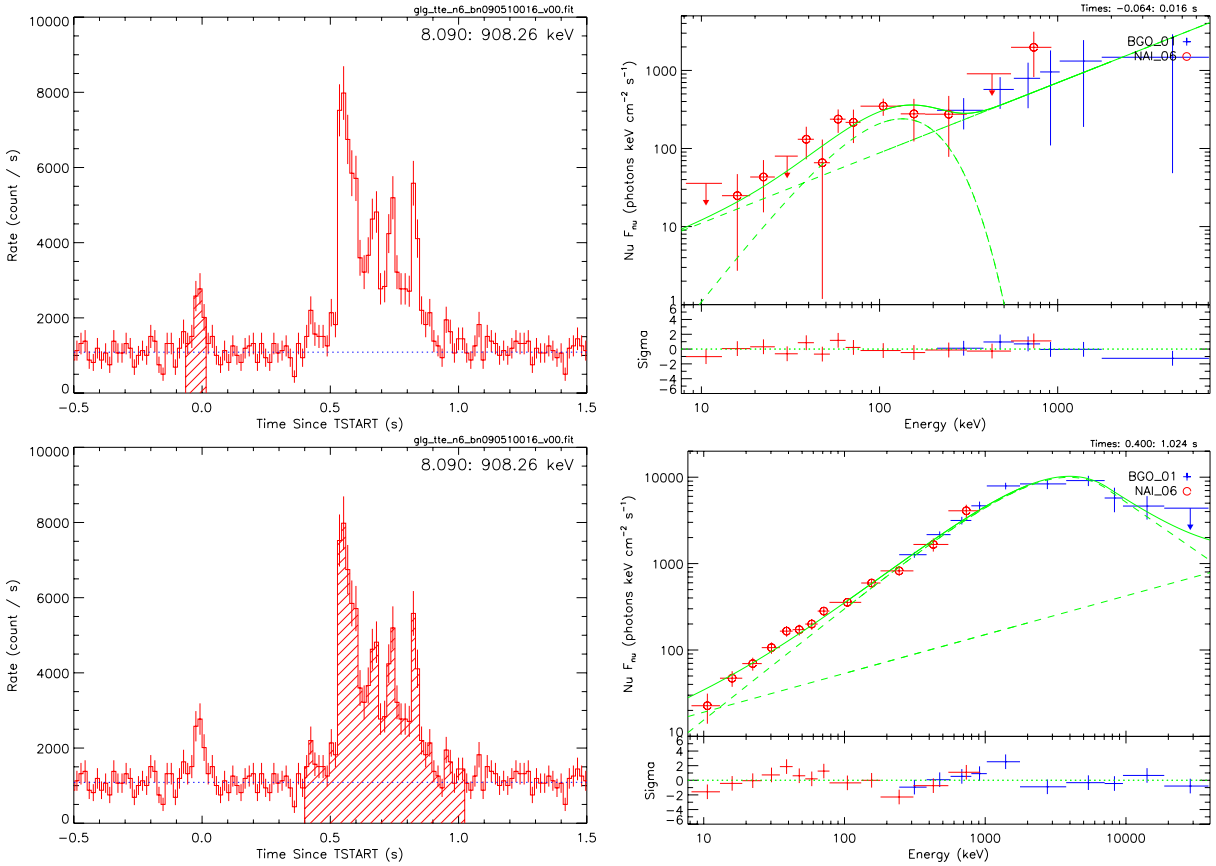

Figure 2. Upper panels: on the left, the 16 ms time-binned NaI-n6 light curve and, on the right, the NaI-n6+BGO-b1 νF_ν spectrum (best fit BB+PL) in the ΔT_1 time interval. Lower panels: on the left, the 16 ms time-binned NaI-n6 light curve and, on the right, the NaI-n6+BGO-b1 νF_ν spectrum (best fit Band+PL) in the ΔT_2 time interval.

(A color version of this figure is available in the online journal.)

to clarify such a fundamental issue, it is appropriate that future space missions with larger collecting area and X/γ-rays timing be flown in the near future (see, e.g., LOFT mission; Feroci et al. 2012). From our theoretical interpretation, the BB+PL, being equally probable as the Compt model, is adopted for its physical meaning and because it is not ruled out by the data. The BB observed temperature is $kT_{\rm obs} = (34.2 \pm 7.5)$ keV (see Figure 2, top right panel, and table below) and the total energy of the first episode is $E_1 = (2.28 \pm 0.39) \times 10^{51}$ erg.

We then analyzed the second episode in the time interval from $T_0 + 0.400$ s to $T_0 + 1.024$ s (in the following ΔT_2). The best fit in the energy range 8 keV–40 MeV is Band+PL (Ackermann et al. 2010) or alternatively Compt+PL (Giuliani et al. 2010; Guiriec et al. 2010). The results are shown in Figure 2 and in Table 1. Including the LAT data, the spectrum is again best fitted by Band+PL (see the last row in Table 1), with the PL observed up to 30 GeV (Ackermann et al. 2010). The total energy is $E_2 = (1.08 \pm 0.06) \times 10^{53}$ erg.

3. GRB 090510: THEORETICAL INTERPRETATION

In the Fireshell model (Ruffini et al. 2001a, 2001b, 2001c) GRBs originate from an optically thick e^+e^- plasma created by vacuum polarization processes in the gravitational collapse to a black hole (Damour & Ruffini 1975; Ruffini et al. 2010). The dynamics of such an expanding plasma in the optically thick phase is described by its total energy $E^{\rm tot}_{e^+e^-}$ and by the amount of the engulfed baryons B. Spherical symmetry of the system is assumed. The canonical GRB light curve is then characterized by a first emission due to the transparency of the e^+e^--photon-baryon plasma, the P-GRB, followed by a multi-wavelength emission, the extended afterglow, due to the collisions, in a fully radiative regime, between the accelerated baryons and the CBM. The radius at which the transparency occurs, $r_{\rm tr}$, the theoretical temperature blueshifted toward the observer $kT_{\rm blue}$, and the Lorentz factor $\Gamma_{\rm tr}$, and the amount of the energy emitted in the P-GRB are functions of $E^{\rm tot}_{e^+e^-}$ and B (Ruffini et al. 2001b, 2009). The structures observed in the extended afterglow of a GRB are described by two quantities associated with the environment: the CBM density profile $n_{\rm CBM}$, which determines the temporal behavior of the light curve, and the filling factor $\mathcal{R} = A_{\rm eff}/A_{\rm vis}$, where $A_{\rm eff}$ is the effective emitting area of the Fireshell and $A_{\rm vis}$ is its total visible area (Ruffini et al. 2002, 2005). This second parameter takes into account the inhomogeneities in the CBM and its filamentary structure (Ruffini et al. 2004). The density of each filament is simply defined as $n_{\rm fil} = n_{\rm CBM}/\mathcal{R}$.

We identified the first episode, where the thermal component is not statistically excluded, with the P-GRB. Then we started the simulation using our numerical code (for details, see, e.g., Ruffini et al. 2007). The input parameters are $E^{\rm tot}_{e^+e^-}$, constrained to the isotropic energy of the burst, $E_{\rm iso} = (1.10 \pm 0.06) \times 10^{53}$ erg, and the baryon load $B = (1.45 \pm 0.28) \times 10^{-3}$,

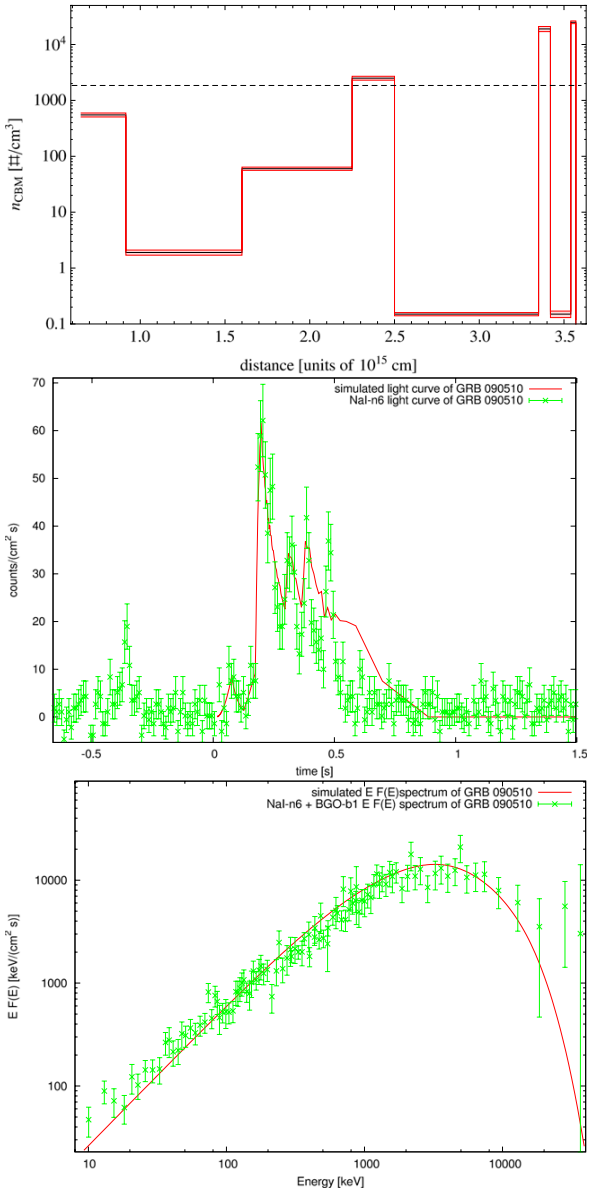

Figure 3. In the top panel, the radial CBM density distribution of GRB 090510 (red solid line) with its uncertainty (light red shaded region) and mean value (black dashed line) are shown. The simulated NaI-n6 light curve (8–1000 keV) of the extended afterglow (middle panel) and the corresponding spectrum of the early ∼0.4 s of the emission in the energy range 8 keV–40 MeV (bottom panel) are consequently obtained.

(A color version of this figure is available in the online journal.)

determined by matching the theoretically simulated energy $E_{\rm tr}$ and temperature $kT_{\rm th} = kT_{\rm blue}/(1+z)$ of the P-GRB with the ones observed in the faint pulse, E_1 and $kT_{\rm obs}$. The results of our simulation are the following:

$$\Gamma_{\rm tr} = (6.7 \pm 1.6) \times 10^2, \quad r_{\rm tr} = (6.51 \pm 0.92) \times 10^{13}\ {\rm cm},$$
$$E_{\rm tr} = (2.94 \pm 0.50)\% E^{\rm tot}_{e^+e^-}, \quad kT_{\rm th} = (34.2 \pm 7.5)\ {\rm keV}. \tag{1}$$

The theoretically predicted P-GRB energy slightly differs from the observed $E_1 = (2.28 \pm 0.39) \times 10^{51}$ erg $= (2.08 \pm 0.35)\% E_{\rm iso}$, since emission below the threshold is expected between the small precursor and the main emission (see light curves in Figure 2), thus the value of E_1 is certainly underestimated.

In the following analysis, we focus our attention on the main emission. Since in ΔT_2 no evidence of a thermal component has been found (see Figure 2, bottom right panel, and table below), we have interpreted this emission as the extended afterglow. Using the above values of $E^{\rm tot}_{e^+e^-}$ and B, we have simulated the light curve of the extended afterglow by defining the radial number density distribution of the CBM (assuming spherically symmetrically distributed clouds) and the value of the filling factor $\mathcal{R}$, following a trial and error procedure to reproduce the pulses observed in the light curve and the corresponding spectrum. The errors on the densities and the filling factors are obtained by varying them within the observational errors; typically the errors are about 10% of the value. The average value is indeed very high, $\langle n_{\rm CBM}\rangle = (1.85 \pm 0.14) \times 10^3$ particles cm^{-3}, assuming spherically distributed clouds (see Figure 3, top plot). Basically this high average density is due to the second and the third brightest spikes of the light curve (see Figure 3, middle panel), where the density of the clouds is $\sim 2 \times 10^4$ particles cm^{-3} (see Table 2, second column). The filling factor assumes values $1.5 \times 10^{-10} \leqslant \mathcal{R} \leqslant 3.8 \times 10^{-8}$ (see Table 2, third column). Correspondingly, the values of the densities of the filaments $n_{\rm fil}$ are estimated (see Table 2, fourth column). In Figure 3, we show also the simulated extended afterglow light curve from the NaI-n6 detector (middle panel) and the corresponding spectrum of the early ∼0.4 s of the emission (bottom panel) in the energy range 8 keV–40 MeV, using the spectral model described in Ruffini et al. (2004) and Patricelli et al. (2012). The last part of the simulation requires a more detailed three-dimensional code to take into account the distribution of the CBM.

4. CONCLUSIONS

We list our conclusions as follows.

1. The simulated spectrum of the extended afterglow in the time interval ΔT_2, considered in the analysis by Ackermann et al. (2010), is in excellent agreement with the one in Figure 2 in the sub-MeV and MeV region. The baryon load $B = (1.45 \pm 0.28) \times 10^{-3}$ used in this simulation has been determined from analysis of the first episode, which has been identified with the P-GRB. The current quality of the data does not allow us to properly distinguish between BB+PL and Compt spectral models. From our theoretical interpretation, the BB+PL model was adopted, since it is not ruled out by the data. Such a fundamental issue will be further clarified by future space missions with larger collecting area and X-/γ-ray timing, as, e.g., the LOFT mission (Feroci et al. 2012).
2. We have stressed a key difference between the Fireshell and the Fireball approaches. In the Fireshell model, the extended afterglow encompasses the prompt emission and the afterglow of the traditional Fireball model. The density of the CBM is inferred from the prompt emission by assuming fully radiative condition emission in an optically thin regime (Ruffini et al. 2002, 2004, 2005) and a precise spectrum in the comoving frame is assumed (Patricelli et al. 2012) and convoluted over the equitemporal Surfaces (Bianco & Ruffini 2005a, 2005b). In the Fireball model, the density is instead estimated from the afterglow emission by analyzing emission or absorption

Table 2
We Report for Each Cloud, Respectively, the Distance from the Black Hole, the Average Number Density (Assuming Spherically Distributed Clouds), the Filling Factor, and the Number Density of the Filaments

Distance (cm)	$n_{\rm CBM}$ (#/cm^3)	$\mathcal{R}$	$n_{\rm fil}$ (#/cm^3)
6.5×10^{14}	550 ± 45	$(3.2 \pm 0.3) \times 10^{-9}$	$(1.72 \pm 0.21) \times 10^{11}$
9.2×10^{14}	1.90 ± 0.60		$(5.94 \pm 0.84) \times 10^{8}$
1.6×10^{15}	60.0 ± 4.1		$(1.88 \pm 0.22) \times 10^{10}$
2.3×10^{15}	$(2.50 \pm 0.20) \times 10^{3}$		$(7.81 \pm 0.96) \times 10^{11}$
2.5×10^{15}	0.15 ± 0.01		$(4.69 \pm 0.53) \times 10^{7}$
3.3×10^{15}	$(1.90 \pm 0.20) \times 10^{4}$	$(1.5 \pm 0.2) \times 10^{-10}$	$(1.27 \pm 0.22) \times 10^{14}$
3.4×10^{15}	0.15 ± 0.02		$(1.00 \pm 0.19) \times 10^{9}$
3.5×10^{15}	$(2.50 \pm 0.14) \times 10^{4}$	$(3.8 \pm 0.4) \times 10^{-8}$	$(6.58 \pm 0.78) \times 10^{11}$
3.6×10^{15}	0.10 ± 0.02		$(2.63 \pm 0.59) \times 10^{6}$

lines in the X-ray spectra (see, e.g., Lazzati et al. 1999; Prochaska et al. 2008), or by observing steepening or breaks of the optical afterglow light curves (see, e.g., Dai & Lu 1999; Piro et al. 2001; Wang et al. 2003). From the fully radiative condition, we have found that GRB 090510 occurs in an overdense medium with an average value of $\langle n_{\rm CBM} \rangle \approx 10^3$ particles cm^{-3} (for spherically symmetrically distributed clouds). This high CBM density and the small value of the filling factor, $1.5 \times 10^{-10} \leqslant \mathcal{R} \leqslant 3.8 \times 10^{-8}$, leads to local overdense CBM clouds, in the form of filaments, bubbles, and clumps, with a range of densities $n_{\rm fil} = n_{\rm CBM}/\mathcal{R} \approx (10^6$–$10^{14})$ particles cm^{-3}.

3. The joint effect of the high value of the Lorentz factor, $\Gamma_{\rm tr} = (6.7 \pm 1.6) \times 10^2$, and the high density compresses the emission of the extended afterglow in time. Therefore its light curve is shortened in time and "inflated" in intensity with respect to the canonical one for disguised short bursts (see Figure 1, right panel), making it apparently closer to the genuine short class of GRBs (Muccino et al. 2013). It is interesting to note that in this GRB, with an abnormally high value of the CBM density, the extended afterglow does not fulfill the Amati relation (Amati 2006).
4. From the values of $n_{\rm fil}$, we obtain a range of grammages of $m_{\rm H} n_{\rm fil} \Delta r_c \approx (10^{-2}$–$10^4)$ g cm^{-2}, where $m_{\rm H}$ is the mass of the hydrogen atom and Δr_c is the size of the cloud inferred from our simulation (see Figure 3 and the first column in Table 2). This high value of the grammage may be relevant in the explanation of the observed GeV emission as originating in the collisions between ultra-high energy protons, with the bulk Lorentz factor of $\Gamma_{\rm tr} = (6.7 \pm 1.6) \times 10^2$, and the CBM.

We thank the referee for suggestions which have allowed us to significantly improve the presentation of the new results. A. V. Penacchioni and G. B. Pisani are supported by the Erasmus Mundus Joint Doctorate Program by grant Nos. 2010-1816 and 2011-1640, respectively, from the EACEA of the European Commission.

REFERENCES

Ackermann, M., Asano, K., Atwood, W. B., et al. 2010, ApJ, 716, 1178
Amati, L. 2006, MNRAS, 372, 233
Band, D., Matteson, J., Ford, L., et al. 1993, ApJ, 413, 281
Bernardini, M. G., Bianco, C. L., Caito, L., et al. 2007, A&A, 474, L13
Bernardini, M. G., Bianco, C. L., Caito, L., et al. 2008, in The Eleventh Marcel Grossmann Meeting On Recent Developments in Theoretical and Experimental General Relativity, Gravitation and Relativistic Field Theories, ed. H. Kleinert, R. T. Jantzen, & R. Ruffini (Singapore: World Scientific), 1992
Bianco, C. L., & Ruffini, R. 2005a, ApJL, 633, L13
Bianco, C. L., & Ruffini, R. 2005b, ApJL, 620, L23
Caito, L., Amati, L., Bernardini, M. G., et al. 2010, A&A, 521, A80
Caito, L., Bernardini, M. G., Bianco, C. L., et al. 2009, A&A, 498, 501
Dai, Z. G., & Lu, T. 1999, ApJL, 519, L155
Damour, T., & Ruffini, R. 1975, PhRvL, 35, 463
de Barros, G., Amati, L., Bernardini, M. G., et al. 2011, A&A, 529, A130
Dezalay, J.-P., Barat, C., Talon, R., et al. 1992, in AIP Conf. Proc. 265, Gamma-ray Bursts, ed. W. S. Paciesas & G. J. Fishman (Melville, NY: AIP), 304
Feroci, M., den Herder, J. W., Bozzo, E., et al. 2012, Proc. SPIE, 8443, 84432D
Giuliani, A., Fuschino, F., Vianello, G., et al. 2010, ApJL, 708, L84
Golenetskii, S., Aptekar, R., Mazets, E., et al. 2009, GCN, 9344, 1
Guiriec, S., Briggs, M. S., Connaugthon, V., et al. 2010, ApJ, 725, 225
Guiriec, S., Connaughton, V., & Briggs, M. 2009, GCN, 9336, 1
Hoversten, E. A., Barthelmy, S. D., Burrows, D. N., et al. 2009, GCN, 9331, 1
Izzo, L., Ruffini, R., Bianco, C. L., et al. 2012, arXiv:1205.6651
Klebesadel, R. W. 1992, in The Durations of Gamma-ray Bursts, ed. C. Ho, R. I. Epstein, & E. E. Fenimore (Cambridge: Cambridge Univ. Press), 161
Kouveliotou, C., Meegan, C. A., Fishman, G. J., et al. 1993, ApJL, 413, L101
Lazzati, D., Campana, S., & Ghisellini, G. 1999, MNRAS, 304, L31
Longo, F., Moretti, E., Barbiellini, G., et al. 2009, GCN, 9343, 1
Meegan, C. A. 1997, STIN, 1, 70758
Muccino, M., Ruffini, R., Bianco, C. L., Izzo, L., & Penacchioni, A. V. 2013, ApJ, 763, 125
Ohmori, N., Noda, K., Sonoda, E., et al. 2009, GCN, 9355, 1
Ohno, M., & Pelassa, V. 2009, GCN, 9334, 1
Olofsson, G., Ergon, M., Malesani, D., et al. 2009, GCN, 9338, 1
Patricelli, B., Bernardini, M. G., Bianco, C. L., et al. 2012, ApJ, 756, 16
Piro, L., Garmire, G., Garcia, M. R., et al. 2001, ApJ, 558, 442
Prochaska, J. X., Dessauges-Zavadsky, M., Ramirez-Ruiz, E., & Chen, H.-W. 2008, ApJ, 685, 344
Rau, A., McBreen, S., & Kruehler, T. 2009, GCN, 9353, 1
Ruffini, R., Aksenov, A. G., Bernardini, M. G., et al. 2009, in AIP Conf. Proc. 1132, XIII Brazilian School on Cosmology and Gravitation, ed. M. Novello & S. Perez (Melville, NY: AIP), 199
Ruffini, R., Bernardini, M. G., Bianco, C. L., et al. 2005, in AIP Conf. Proc. 782, XIth Brazilian School of Cosmology and Gravitation, ed. M. Novello & S. E. Perez Bergliaffa (Melville, NY: AIP), 42
Ruffini, R., Bernardini, M. G., Bianco, C. L., et al. 2007, in AIP Conf. Proc. 910, XIIth Brazilian School of Cosmology and Gravitation, ed. M. Novello & S. E. Perez Bergliaffa (Melville, NY: AIP), 55
Ruffini, R., Bianco, C. L., Chardonnet, P., Fraschetti, F., & Xue, S. 2002, ApJL, 581, L19
Ruffini, R., Bianco, C. L., Fraschetti, F., Xue, S., & Chardonnet, P. 2001a, ApJL, 555, L117
Ruffini, R., Bianco, C. L., Fraschetti, F., Xue, S.-S., & Chardonnet, P. 2001b, ApJL, 555, L113
Ruffini, R., Bianco, C. L., Fraschetti, F., Xue, S.-S., & Chardonnet, P. 2001c, ApJL, 555, L107
Ruffini, R., Bianco, C. L., Xue, S.-S., et al. 2004, IJMPD, 13, 843
Ruffini, R., Salmonson, J. D., Wilson, J. R., & Xue, S. 2000, A&A, 359, 855
Ruffini, R., Vereshchagin, G., & Xue, S.-S. 2010, PhR, 487, 1
Tavani, M. 1998, ApJL, 497, L21
Wang, X. Y., Dai, Z. G., & Lu, T. 2003, A&A, 401, 593
Yoshida, A., Namiki, M., Yonetoku, D., et al. 2001, ApJL, 557, L27

"Charm is a way of getting the answer
yes without asking a clear question."
Albert Camus

Chapter 4

GRB - SN association

The source of GRBs is associated with a catastrophic energy release (Mészáros 2006). For long bursts, this is associated with the late stages of the evolution of a massive star, namely, the collapse of its core. For short bursts, it has been long assumed that they are associated with compact binary mergers (NS-NS or NS-BH).

The possible connection between GRBs and SNe was first studied observationally by Klebesadel (Klebesadel et al. 1973), following the suggestion that GRBs would be produced in SN shock breakouts (Colgate 1968). A few years later, Paczynski (1986) noted that cosmological distances of GRBs would imply that the energy release in gamma rays would be comparable to the energy release in a typical SN explosion. This connection was then well described in what is now known as the "Collapsar model" (Woosley 1993, 1996; MacFadyen & Woosley 1999). This model involves the core-collapse explosion of a stripped-envelope massive star. Matter flows towards a newly formed BH or a rapidly spinning, highly magnetized NS. Powerful jets plow through the collapsing star along the spin axis, eventually obtain relativistic speeds and produce GRBs. Enough ^{56}Ni is produced near the central compact source to power a SN explosion of the star (see Hjorth & Bloom (2012)).

4.1 Spectroscopic evidence for GRBs and SNe

After the first few afterglow localizations of long GRBs, a qualitative connection of the events with star formation regions and star forming galaxies began to emerge. The close proximity of GRBs to star formation implicated models where the progenitor does not move far from its birth site and produces a GRB on timescales smaller than the typical duration of star-formation episodes. As statistical statements accumulated about the physical connection of cosmological GRBs with on-going star formation, individual events began to exhibit incredible photometric evidence for a SN explosion contemporaneous with the GRB (Lu & Shi 1990; Bloom et al. 1999; Galama et al. 2000; Bloom et al. 2002; Garnavich et al. 2003; Zeh et al. 2004). The definitive evidence of the GRB-SN connection was finally established by a few events which, through spectroscopic identification of SN features well after the GRB event, clinched the physical association.

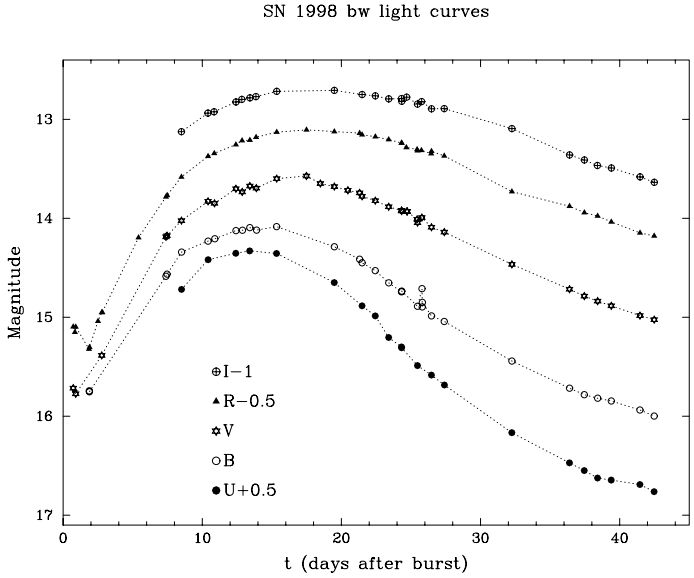

Figure 4.1: UBVRI light curves of SN 1998bw. Time is in days since April 25.90915 UT. A photometric (U, B, V, R and I) calibration was determined for a number of reference stars using NTT (May 4.4 UT) and 1.5D (May 8.3 UT) observations of the Landolt35 elds Mark A and SA110 (stars 496-507). We corrected for atmospheric extinction and, for U and B, also for a first-order color term. By comparison of these two calibration nights we estimate an error of the absolute calibration of 0.10 mag in U and 0.05 mag for B, V, R and I. We consider a conservative minimum error of 0.03 mag realistic for the differential U, B, V, R and I light curves to account for the effect of seeing on the contribution of the underlying galaxy (¡ 0.01 mag for each band) and the different instruments used. Taken from Galama et al. (1998).

4.1.1 GRB 980425 and SN 1998bw

GRB 980425 was discovered early in the afterglow era, at a redshift of z = 0.0085. Two X-ray sources were found in the error circle, therefore the identification of the true X-ray counterpart was controversial (Kouveliotou et al. 2004).

SN1998bw was a bright (M_B=-18.7 mag at peak), broad-lined Type Ic SN (Galama et al. 1998), suggesting a significant amount of mass with very fast photospheric expansion. Fig.4.1 shows the light curve.

At the time, SN 1998bw was also the brightest radio SN known, indicating, as a means to explain the very high apparent-brightness temperature, that the SN was accompanied by a shock wave moving at mildly relativistic speeds (Kulkarni et al. 1998). Iwamoto et al. (1998) suggested that these observations can be reproduced by an extremely energetic explosion of a massive star composed mainly of carbon and oxygen (having lost its H and He envelopes). He used the

term 'hypernova' (Paczyński 1998) to describe it[1].

No traditional optical afterglow was detected for GRB 980425, but the comparatively low-energy output and its low redshift were considered as a pointing to a different class of GRB, not necessarily of the same progenitor origin as the truly cosmological GRBs that had been detected so far.

4.1.2 GRB 030329 and SN 2003dh

GRB 030329 eliminated doubts as to the deep connection between GRBs and SNe. It was a bright burst detected by the HETE-2 satellite (Lipkin et al. 2004) and had an inferred redshift of $z = 0.1685$ (Greiner et al. 2003). It was followed by a bright optical afterglow, which established this event as part of the cosmological GRB class. Several days after the burst, by subtracting the afterglow contribution, the SN spectrum could be isolated. It was shown to follow that of SN 1998bw, thus showing that the GRB afterglow and the SN were spatially coincident (Hjorth et al. 2003) (see Fig.4.2). The SN light curve was almost completely masked by the bright afterglow.

The GRB 030329/SN 2003dh connection also eliminated any doubts about the association between GRB 980425 and SN 1998bw.

4.1.3 GRB 031203 and SN 2003lw

GRB 031203 was localized by INTEGRAL (Sazonov et al. 2004), and its afterglow later by Chandra (Gal-Yam et al. 2004), XMM-Newton (Vaughan et al. 2004) and the VLA (Gal-Yam et al. 2004) to a galaxy at $z = 0.1055$. No optical afterglow was detected, but through photometric monitoring of the galaxy a SN-bump was detected (Cobb et al. 2004).

Spectra of the SN obtained by Malesani et al. (2004) revealed broad-line features similar to those seen in SN 1998bw and SN 2003dh. The large column density of the galactic dust allowed to see two radially expanding halos of X-ray emission centered on the GRB. Because of the time delay due to the longer distance travelled by the light in the rings, this allowed a reconstruction of the prompt X-ray flux of GRB 031203. The fluence in X-rays dominates that of the hard energy emission, so this source should have been classified as an XRF.

[1] In the SN that were related to GRB events, the optical spectra indicated high intrinsic velocities and consequently very energetic explosions. It was pointed out by Paczynski (2001) that the optical afterglow of GRB 970508 was 100 times as bright as might be expected from normal optical SN and that it might therefore be appropriate to call these events hypernovae. There is speculation that these energetic explosions might be caused by massive star core collapse to a black hole rather than to the usual neutron star. So long GRBs might all originate in super or hypernovae. Gravitational collapse of a rotating star produces a BH surrounded by an accretion disc, the final accretion of which blows a narrow jet of relativistic material out along the spin axis. Because the beam of radiation is narrow, energy requirements of the GRB are not as severe, and the supernova explosion can supply the observed burst intensity. Since most GRBs are not aimed at us, it is estimated that the real GRB rate could be 500 times grater than that observed. This is quite reasonable given the locally estimated SN rate of 1 per 100 years per Milky Way-sized galaxy, and that there are ~ 1000 such galaxies in our Universe.

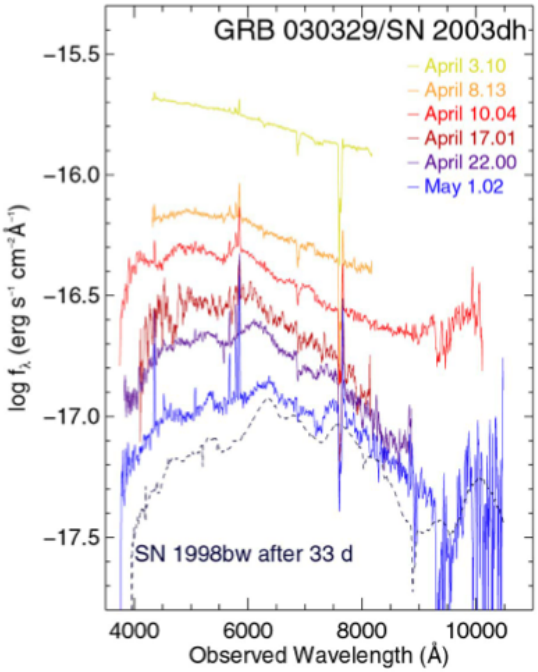

Figure 4.2: Spectral evolution of the combined optical flux density f_λ of the afterglow of GRB 030329, the associated SN 2003dh, and its host galaxy. The upper spectrum is rather well fitted by a power law, as usually seen in afterglow spectra. The middle spectra show clear deviations from a power law, similar to SN 1998bw at the same phase. The lower spectra, dominated by SN 2003dh, reveal the SN signatures. For comparison, the spectrum of SN 1998bw after 33 days is shown (dashed line) shifted to the GRB 030329 redshift. All SN 2003dh spectra are presented in observed wavelengths, and no reddening correction has been applied. Taken from Hjorth et al. (2003).

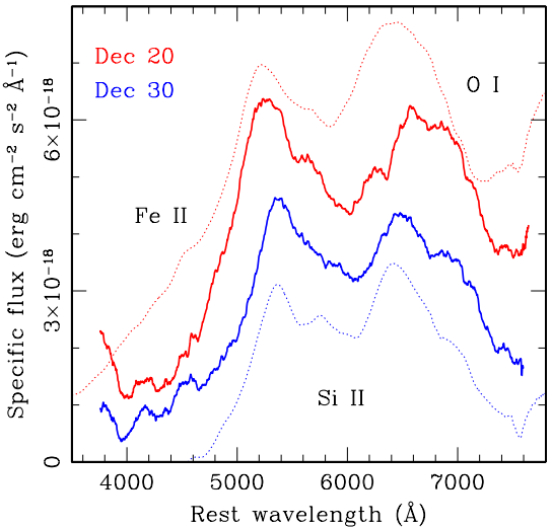

Figure 4.3: Spectra of SN 2003lw, taken on 2003 Dec. 20 and Dec. 30 (solid lines), smoothed with a boxcar filter 250 A wide. Dotted lines show the spectra of SN 1998bw, taken on 1998 May 9 and May 19 (13.5 and 23.5 days after the GRB, or 2 days before and 7 days after the V-band maximum), extinguished with EBV = 1 : 1 and a Galactic extinction law. Taken from Covino et al. (2004).

4.1.4 GRB 060218 and SN 2006aj

GRB 060218 was localized by *Swift* in a galaxy at $z = 0.0335$ (Mirabal et al. 2006). SN 2006aj was fainter than the other GRB-SNe, providing additional evidence for a substantial dispersion in the peak magnitudes and rise times of GRB-SNe (Ferrero et al. 2006). GRB 0600218 was classified as an XRF, though the duration of the event (> 1000 s) was very long compared to other XRFs.

4.1.5 GRB 100316D and SN 2010bh

GRB 100316D was also discovered by *Swift*, at a redshift of $z = 0.0591$. Its high-energy prompt properties were remarkably similar to those of GRB 060218. It was also an XRF of unusually long duration (1300 s) and it had a thermal component in addition to a synchrotron emission component with a low peak energy, a slow X-ray decay, and similar spectral hardness evolution. Fig.4.5 shows the evolution of the spectrum.

The SN features were typical of broad-lined SNe Ic and generally consistent with other spectroscopic GRB-SNe.

4.2 Supporting evidence of the GRB-SN connection

The highest redshift among the secure GRB-SNe is 0.1685, while the median redshift of *Swift* GRBs is above 2. It is important to consider the evidence for

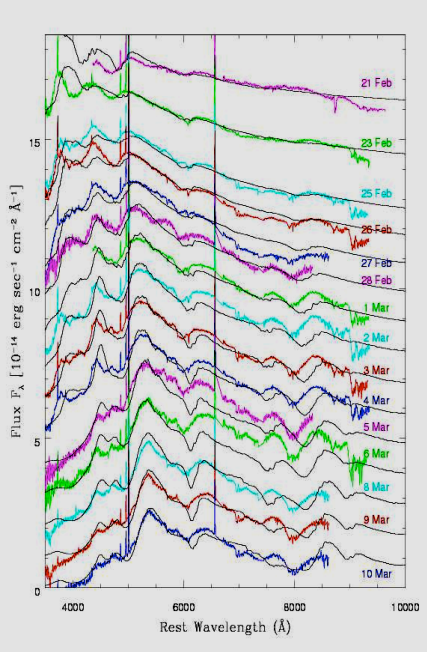

Figure 4.4: Spectra of SN 2006aj acquired with the VLT and Lick telescopes. Taken from (Pian et al. 2006).

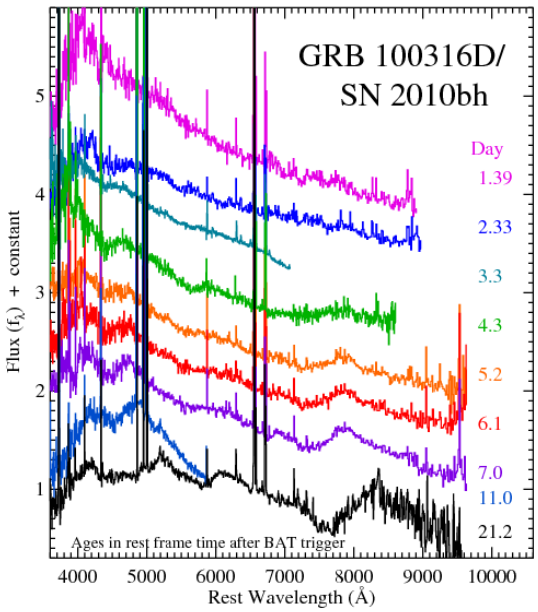

Figure 4.5: Optical spectra from Magellan and Gemini-South demonstrating the emergence of the spectral features of a broad-lined SN Ic. The spectra have been rebinned for clarity. Taken from Chornock et al. (2010).

GRB-SNe at higher redshifts and for GRBs with $E_{\gamma,iso}$ in the range $10^{50} - 10^{54}$ erg (Frail et al. 2001). At higher redshift, SN identification becomes difficult because the SN appears fainter, making it hard to obtain a sufficient signal-to-noise ratio in the broad SN features. The picture supports the conclusion that SNe are ubiquitous in GRB light curves and that there is a real diversity among such events. GRB-SNe are generally consistent with being broad-lined Type Ic, with a dispersion in both peak brightness, rise time, light curve width and spectral broadness.

At radio wavebands, GRB afterglows can be 10^4 times brighter at peak than typical Ib and Ic SNe (Soderberg 2006): the reason is likely the difference between the coupling of energy to highly relativistic ($\Gamma \geq 50$) ejecta (in the GRB/XRF case) versus subrelativistic ($\beta\Gamma \leq 1$) ejecta (in the normal Ib/Ic case). The early radio brightness of SN 1998bw can be attributed to the large coupling of energy to trans-relativistic ejecta ($\beta\Gamma \approx$ a few) (Kouveliotou et al. 2012).

4.3 First examples of GRB-SN connection within the Fireshell model

Many sources have been studied after the Fireshell model had been presented, but one of the most important ones was GRB 090618. It is considered the prototype of the sample, as data are available in almost the whole range of the electromagnetic spectrum and are of very good quality. There is another

source, GRB 101023, which has been also studied within the fireshell scenario. Both sources have played a crucial role in the understanding of the physical phenomena that take place in the collapse to a BH and the emission of the GRB. Furthermore, they have set the basis to develop a further scenario that includes the Fireshell: the Induced Gravitational Collapse (IGC) Model. This model is presented in chapter 5. In this chapter we present GRB 090618 and GRB 101023, analyzing them in the Fireshell scenario and showing their special features (both in their shape and their spectra), which are common between them but different from the features of other sources. This led us to introduce a new family of GRB sources, which will be explained in the present and following chapters.

4.3.1 GRB 090618: Observations

On 18 June 2009, the Burst Alert Telescope (BAT) onboard the *Swift* satellite (Gehrels et al. 2009) triggered on GRB 090618 (Schady et al. 2009). After 125 s the X-Ray Telescope (XRT) (Burrows et al. 2005) and the Ultra-Violet Optical Telescope (UVOT) (Roming et al. 2005), other detectors of *Swift*, started the follow-up and detected the afterglow (Beardmore & Schady 2009; Schady 2009). There have been also observations by the Gamma-Burst Monitor (GBM) onboard the *Fermi* satellite (Meegan et al. 2009) (see Fig.4.6), and by other satellites like AGILE (Longo et al. 2009b), *Konus* (in particular its detector WIND) (Golenetskii et al. 2009a), *CORONAS*-PHOTON (Kotov et al. 2008) and *Suzaku*, with its Wide-band All-sky Monitor (WAM) detector (Kono et al. 2009). Besides, the afterglow has been detected and followed by on-ground telescopes, like VLA (Chandra & Frail 2009), KAIT (Perley 2009), HCT (Anupama et al. 2009), etc.

The BAT on-board calculated location is RA= 294.021, Dec= 78.353 with an uncertainty of 3 arcmin (Schady et al. 2009). The light curve shows a multi peak structure with a duration of ~ 130 s. It can be divided in two parts, of 50 and 100 s of duration. The first part is smooth, while the second one is spiky, composed by three peaks at 62, 80 and 112 s after the trigger, respectively. The time-integrated spectrum from T$-$4.4 to T+213.6 is best fit by a PL model with an exponential cutoff (Sakamoto et al. 2009), with a photon index $\gamma = 1.42 \pm 0.08$ and a peak energy $E_{peak} = 134 \pm 19$ keV.

The redshift of GRB 090618 is $z = 0.54$ (Cenko et al. 2009), determined thanks to the identification of the MgII, MgI and FeII absorption lines by the KAST spectrograph at the Lick observatory. The emitted isotropic energy in the $(8 - 10000$ keV) energy range was computed using the Schaefer formula

$$E_{\gamma,iso} = 4\pi d_L^2 S_{bolo}(1+z)^{-1}, \tag{4.1}$$

where d_L is the luminosity distance of the burst and S_{bolo} is the bolometric fluence of the gamma-rays in the burst. We used the fluence in the $(8 - 10000$ keV) band as observed by *Fermi*-GBM, $S = 2.7 \times 10^{-4}$ erg/cm^2 (McBreen 2009) and the ΛCDM cosmological standard model: $H_0 = 70$ km s^{-1} Mpc^{-1}, $\Omega_m = 0.27$ and $\Omega_\Lambda = 0.73$. The value of the isotropic energy is $E_{iso} = 2.9 \times 10^{53}$ erg.

Thanks to the complete data coverage of the optical afterglow of GRB 090618, the possible presence of a Supernova underlying the emission of the

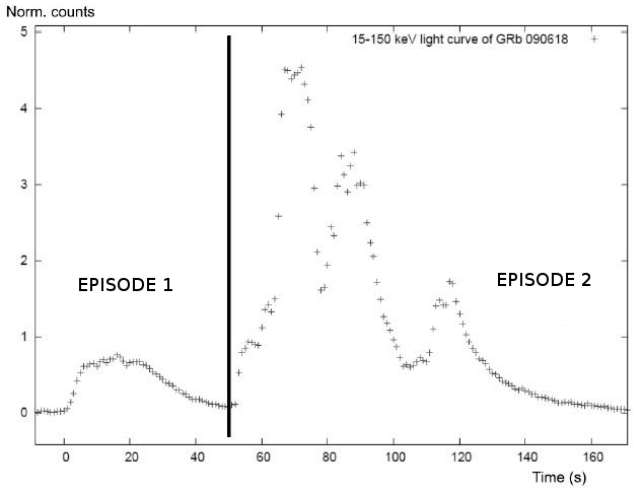

Figure 4.6: Count light curve of GRB 090618 obtained from Fermi GBM, with a bin time of 1 s. The two-episode nature of the emission can be appreciated. We called episode 1 the interval from 0 to 50 s after the trigger, and episode 2 the following 100 s.

optical afterglow was reported (Cano et al. 2011). The evidence of this emission came from the presence of several bumps in the light curve and the change in the $R_c - i$ color index over time. In the early phases the blue color is dominant (typical of the GRB afterglow) but then the color index increases, suggesting a core-collapse SN.

4.3.2 Data analysis

We considered the BAT and XRT data from the *Swift* satellite, the GBM data from the *Fermi* satellite and the RT2 data from the *Coronas-PHOTON* satellite. We reduced the *Swift* data using the Heasoft v6.10 packages[2]. The *Fermi* data was reduced with the *Fermi*-Science tools.

It can be noticed at first sight that the emission of GRB 090618 is divided in two parts. We called episode 1 the interval from 0 to 50 s after the trigger, and episode 2 the following 100 s. The first episode is smooth, while the second one presents a spiky structure.

We proceeded to the spectral analysis of GRB 090618 by dividing the *Fermi* GBM light curve into six time intervals. We made a spectral fit for each interval with a Band model (Band et al. 1993) and a Blackbody with an extra power-law (BB+PL) model (see Table 4.1). The first 50 s of emission are well fit by a Band model as well as a BB+PL model, see Fig.4.7. The same happens for the 9 s of the second time interval (from 50 to 59 s after the trigger time). For the subsequent three intervals corresponding to the main peaks in the light curve, the black-body plus a power-law model does not provide a satisfactory fit. Only the Band model fits the spectrum with good accuracy, with the exception of the first main spike (compare the values of χ^2 in the table). The last peak can be

[2]http://heasarc.gsfc.nasa.gov/lheasoft/

Table 4.1: Time-resolved spectral analysis of GRB 090618. We have considered six time intervals, each one corresponding to a particular emission feature in the light curve. We fit the GBM (8 keV - 10 MeV) observed emission with a Band model (Band et al. 1993) and a PL function with an exponential cut-off. In the columns 2, 3 and 4 are listed the Band low energy index α, the high-energy index β and the break energy E_0^{Band}, with the reduced chi-square value in the 5^{th} column. In the last three columns are listed the power-law index γ, the cut-off energy E_0^{cut} and the reduced chi-square value respectively, as obtained from the spectral fit with the cut-off PL spectral function.

Time Int.	α	β	E_0^{Band} [keV]	$\tilde{\chi}^2$	γ	E_0^{cut} [keV]	$\tilde{\chi}^2_{cut}$
0-50	$-0.77^{+0.38}_{-0.28}$	$-2.33^{+0.33}_{-0.28}$	$128.12^{+109.4}_{-56.2}$	1.11	$0.91^{+0.18}_{-0.21}$	$180.9^{+93.1}_{-54.2}$	1.13
50-57	$-0.93^{+0.48}_{-0.37}$	-2.3 ± 0.1	$104.98^{+142.3}_{-51.7}$	1.22	$1.11^{+0.25}_{-0.30}$	$168.3^{+158.6}_{-70.2}$	1.22
57-68	$-0.93^{+0.09}_{-0.08}$	$-2.43^{+0.21}_{-0.67}$	$264.0^{+75.8}_{-54.4}$	1.85	$1.01^{+0.06}_{-0.06}$	$340.5^{+56.0}_{-45.4}$	1.93
68-76	$-1.05^{+0.08}_{-0.07}$	$-2.49^{+0.21}_{-0.49}$	$243.9^{+57.1}_{-53.0}$	1.88	$1.12^{+0.04}_{-0.04}$	$311.0^{+38.6}_{-32.9}$	1.90
76-103	$-1.06^{+0.08}_{-0.08}$	$-2.65^{+0.19}_{-0.34}$	$125.7^{+23.27}_{-19.26}$	1.23	$1.15^{+0.06}_{-0.06}$	$157.7^{+22.2}_{-18.6}$	1.39
103-150	$-1.50^{+0.20}_{-0.18}$	-2.3 ± 0.1	$101.1^{+58.3}_{-30.5}$	1.07	$1.50^{+0.18}_{-0.20}$	$102.8^{+56.8}_{-30.4}$	1.06

fitted by a simple PL model with a photon index $\gamma = 2.20 \pm 0.03$, better than by a Band model.

Analysis in the Fireshell scenario: Episode 1 as the P-GRB

We first tried to analyze GRB 090618 within the Fireshell scenario by considering that we are in presence of a single GRB. We need to find the P-GRB emission. We know that Episode 1 is well fit by a BB+PL model, so we assumed that Episode 1 could be the P-GRB. The energy emitted considering only the BB component is $E_{BB} = 8.35^{+0.27}_{-0.36} \times 10^{51}$ erg. Recalling that the isotropic energy of the whole GRB is $E_{iso} = (2.90 \pm 0.02) \times 10^{53}$ erg, this means that the BB component is $\sim 2.9\%$ of the total energy emitted in the burst. This would imply a baryon load $B = 10^{-3}$, a Lorentz gamma factor $\Gamma \sim 800$ and a temperature of 52 keV (see Fig 2.2 in Chapter 2). However, this last value disagrees with the observed temperature, $kT_{obs} = 32.07$ keV. We therefore conclude that Episode 1 cannot be the P-GRB.

Analysis in the Fireshell scenario: Episode 2 as a canonical GRB

We now consider Episode 2 as a canonical GRB. We consider the possibility that the first 9 s of emission are the P-GRB, since there is a BB signature in the spectrum (see Table 4.1), but considerations on the time variability of the thermal component lead us to consider just the first 4 s as the P-GRB. The spectrum of this four-second interval in the $(8 - 440)$ keV energy range is well fit by a BB+PL model, with $kT = 29.22 \pm 2.21$ keV, $norm_{BB} = 3.5 \pm 0.4$, $\gamma = 1.85 \pm 0.06$, $norm_{PL} = 46 \pm 10$ and $Red\chi^2 = 1.15$ (see Fig.4.8). The fit with a Band model is also acceptable, with a low-energy PL index $\alpha = -1.22 \pm 0.08$, a high-energy PL index $\beta = -2.32 \pm 0.21$, a break energy $E_0 = 193 \pm 50$ and a Red$\chi^2 = 1.25$. However, in view of the theoretical understanding of the thermal component in the P-GRB within the Fireshell model, we focus on the BB+PL

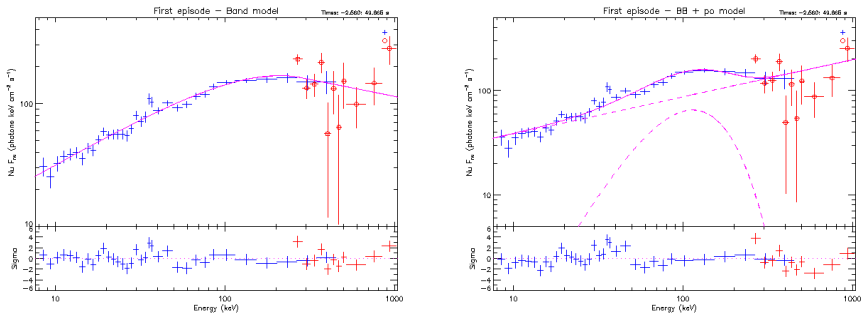

Figure 4.7: Time integrated spectral analysis of the first 50 s of emission of GRB 090618 with a Band model (left) and a BB+PL model (right). We used the fourth NaI detector in the $(8 - 440$ keV) energy range and the b0 BGO detector in the (260 keV - 40 MeV) energy range.

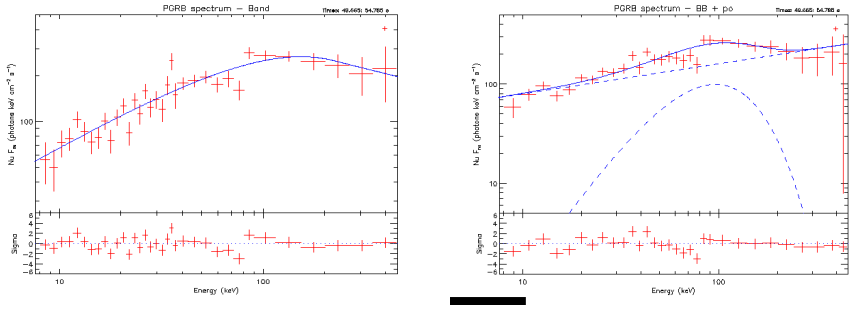

Figure 4.8: Time-integrated spectrum of the P-GRB emission of GRB 090618 (from 50 to 54 s after the trigger) in the $(8 - 440)$ keV energy range, with a Band model (left, $\chi^2 = 1.25$) and a BB+PL model (right, $\chi^2 = 1.15$).

spectral model.

Simulation of the extended afterglow within the Fireshell model

The isotropic energy of Episode 2 is $E_{iso} = (2.49 \pm 0.02) \times 10^{53}$ erg. The simulation of the light curve and spectrum within the Fireshell scenario is made assuming $E_{tot}^{e^\pm} = E_{iso}$, i.e. that the isotropic energy is equal to the energy of the $e^\pm$ plasma in the dyadosphere. For this energy and from Fig.2.2 in Chapter 2 we obtain a baryon load $B = (1.9 \pm 0.1) \times 10^{-3}$, and a P-GRB energy of $4.33^{+0.25}_{-0.28} \times 10^{51}$ erg. We can also derive the radius at the transparency point, $r_{tr} = 1.46 \times 10^{14}$ cm, and the bulk Lorentz factor, $\Gamma_{th} = 4.95 \times 10^2$. These theoretical estimates are based on a non-rotating BH of $10 M_\odot$, a total energy $E_{tot}^{e^\pm} = 2.49 \times 10^{53}$ erg and a mean temperature of the initial $e^\pm$ plasma of 2.4 MeV.

To simulate the extended afterglow emission, we need to determine the radial distribution of the CBM, which we assume to be spherically symmetric. Using the numerical code developed at the University of rome “Sapienza”, we obtained

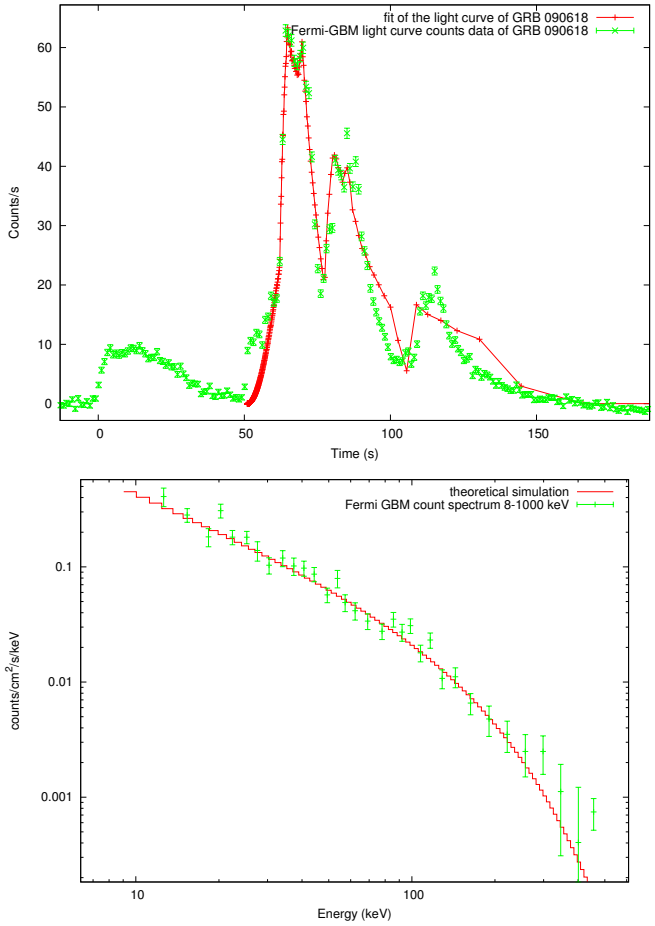

Figure 4.9: Numerical simulation of the Fermi light curve (left) and time-integrated spectrum (right) of GRB 090618.

the radial distribution of the CBM shown in Fig.4.10. The mean value of the density is $\langle n \rangle = 0.6$ part/cm^3.

Fig.4.9 shows the simulated light curve and spectrum of GRB 090618 and Table 4.2 shows the parameters of the simulation.

We are not able to accurately reproduce the last spikes of the light curve, since the equations of motion of the accelerated baryons become very complicated after the first interactions of the fireshell with the CBM (Ruffini et al. 2007). This happens for different reasons. First, a possible fragmentation of the fireshell can occur. Second, at larger distances from the progenitor the fireshell visible area becomes larger than the transverse dimension of a typical blob of matter, consequently a modification of the code for a three-dimensional description of the interstellar medium will be needed.

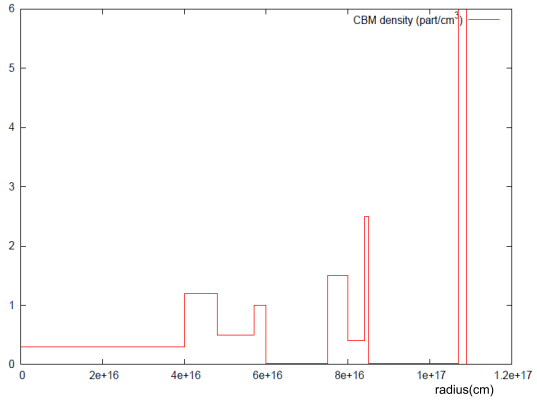

Figure 4.10: CBM particle density distribution for GRB 090618.

Table 4.2: Final results of the simulation of GRB 090618 in the Fireshell scenario.

Parameter	Value
$E_{tot}^{e^+e^-}$	$2.49 \pm 0.02 \times 10^{53}$ ergs
B	$1.98 \pm 0.15 \times 10^{-3}$
Γ_0	495 ± 40
kT_{th}	29.22 ± 2.21 keV
$E_{P-GRB,th}$	$4.33 \pm 0.28 \times 10^{51}$ ergs
$< n >$	$0.6\, part/cm^3$
$< \delta n/n >$	$2\, part/cm^3$

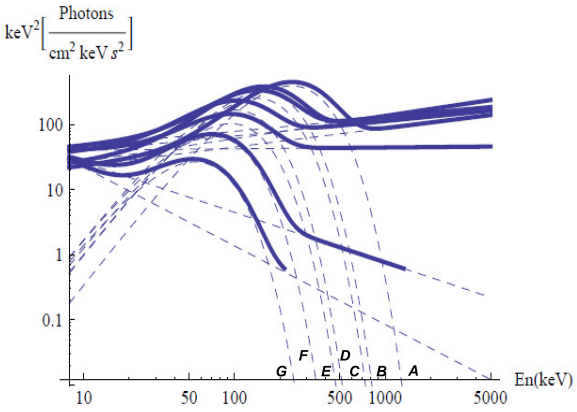

Figure 4.11: $\nu F(\nu)$ time-resolved spectra of the first emission of GRB 090618. It is clear the evolution (cooling) of the Blackbody component with time. The dashed lines show the blackbody and power-law components, while the solid line shows the results of the fits.

4.3.3 Analysis of the first episode

As we mentioned before, we believe that the first emission does not correspond to a canonical GRB nor to the P-GRB. We thus performed a time-resolved analysis to Episode 1 using a Band model (Band et al. 1993) and a Blackbody plus a power-law model. We used the data from the n4 NaI and the b0 BGO detectors together, covering an energy range from 8 keV to 10 MeV (we did not consider the high-energy band of the BGO detector in order to avoid some bias from low-photon statistics).

Both models fit the observed data very well. We notice a very clear and strong evolution of the thermal and power-law components in the time-resolved spectra, as suggested in Ryde (2004) (see Figs. 4.11 and 4.12). The most notorious one is the blackbody temperature evolution, which follows a broken power-law. The indices of the power-laws at early and late times are, respectively, $\alpha = -0.33 \pm 0.07$ and $\beta = -0.6 \pm 0.1$. There is a break at ~ 11 s after the trigger. The results suggest that such a swift cooling of the blackbody temperature has an influence in the evolution of the non-thermal emission, which spectral index softens with time.

We also estimate the radius of the emitting region, from non-relativistic considerations. We know that the temperature of the emitter in the co-moving frame is $T_{em} = T_{obs}(1+z)$. On the other hand, the luminosity of the emitter due to the blackbody emission is

$$L = 4\pi r_{em}^2 \sigma T_{em}^4 = 4\pi r_{em}^2 \sigma T_{obs}^4 (1+z)^4, \tag{4.2}$$

where r_{em} is the radius of the emitter and σ is the Stefan constant. The observed flux is given by

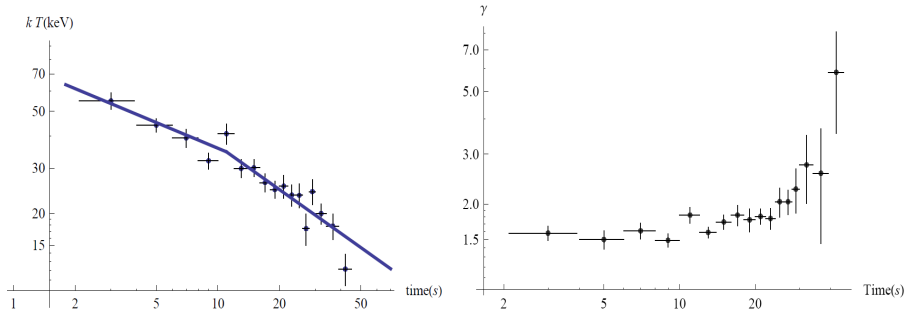

Figure 4.12: Evolution of the blackbody temperature (left) and the photon index of the power-law component (right) of the first episode. The solid line represents the fit with a broken power-law. There is a break at $t = 11$ s after the trigger. The indices of the broken power-law are $\alpha = -0.33 \pm 0.07$ and $\beta = -0.6 \pm 0.1$.

$$\phi_{obs} = \frac{L}{4\pi d_L^2} = \frac{r_{em}^2 \sigma T_{obs}^4 (1+z)^4}{d_L^2}. \tag{4.3}$$

In this expression,

$$d_L(z) = \frac{c}{H_0} \int_0^z \frac{dz'}{\sqrt{\Omega_m (1+z)^3 + \Omega_k (1+z)^2 + \Omega_\Lambda}} \tag{4.4}$$

is the luminosity distance.

Therefore, the radius of the emitter is given by

$$r_{em} = \left(\frac{\phi_{obs}}{\sigma T_{obs}^4} \right)^{1/2} \frac{d_L}{(1+z)^2}. \tag{4.5}$$

Fig.4.13 shows the evolution of the surface radius with time, assuming a flat universe ($\Omega_k = 0$) and a standard cosmological model ($H_0 = 70$ km s^{-1} Mpc^{-1}, $\Omega_m = 0.27$ and $\Omega_\Lambda = 0.73$) . It increases monotonically with time, but at non-relativistic velocities ($v \sim 4000$ km s^{-1}), between 12000 and 70000 km.

4.3.4 Conclusions

Having obtained these results, we interpret episode 1 within the fireshell model as a "Proto-black hole", namely the collapsing bare core leading to the black hole formation. The isotropic energy of this episode is $E_{iso}^{(1)} = 4.1 \times 10^{52}$ erg.

Episode 2 is identified with a canonical GRB, originated from the process of black hole formation. The first 4 s of emission are in accordance with the theoretically predicted P-GRB. The spectrum is well-fit by a BB+PL component, where the non thermal component is due to the extended afterglow emission. The isotropic energy of this episode is $E_{iso}^{(2)} = 2.49 \times 10^{53}$ erg. From the simulation of the *Fermi*-GBM light curve and spectrum we obtained a baryon load $B = (1.98 \pm 0.15) \times 10^{-3}$ and a Lorentz factor at the transparency $\Gamma \sim 495$. We also found that the CBM is formed by blobs of matter at a distance of $\sim 10^{16}$ cm, with an average density of 1 particle cm^{-3}.

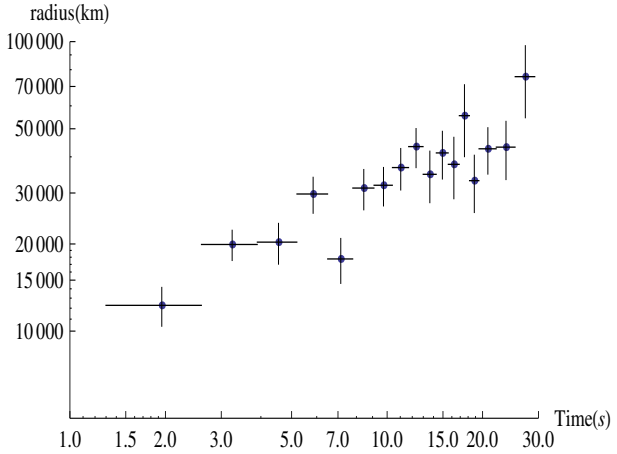

Figure 4.13: Evolution of the radius of the emitter of the first episode, as given by Eq. (4.5). It varies smoothly between 12000 and 70000 km.

4.3.5 GRB 101023: Observations

On 23 October 2010 the *Fermi*-GBM (Briggs 2010) detector was triggered by a source quite similar to GRB 090618 (22:50:04.73 UT). The burst was also detected by BAT (Saxton et al. 2010) onboard the *Swift* satellite (Gehrels et al. 2004), with a trigger time of 436981 (in MET seconds) and the following location coordinates: RA(J2000) = 21h11m49s, Dec(J2000) = -65°23' 37" with an uncertainty of 3 arcmin. The *Swift*-XRT detector (Page & Saxton 2010; Burrows et al. 2005) has also observed this source from 88 s to 6.0 ks after the BAT trigger (see Fig.4.14). GRB 101023 was also detected by the Wind instrument onboard the *Konus* satellite, in the energy range (10 - 770) keV (Golenetskii et al. 2010). The inferred location is in complete agreement with that determined by *Swift* and *Fermi*. There have been also detections in the optical band by the Gemini telescope (Levan et al. 2010).

The GBM light curve (see Fig.4.15) shows two major pulses.The first one starts at the trigger time and lasts 45 s. It consists of a small peak that lasts about 10 s, followed by a higher emission that decays slowly with time. The duration, as well as the topology of this curve, lead us to think that this may not be a canonical GRB, but its origin may lie on another kind of source, which remains unidentified. The second pulse starts at 45 s after the trigger time and lasts 44 s. It presents a peaky structure, composed of a short and weak peak at the beginning, followed by several bumps, big not only in magnitude but also in duration. This second emission, in contrast, does have all the characteristics that describe a canonical GRB (Ruffini et al. 2010a).

There is a striking morphological analogy between GRB 101023 and GRB 090618. Both light curves present a first emission that lasts ~ 50 s, followed by a spiky structure in the remaining part. Following the analysis for GRB 090618, we identify the first 45 s of GRB 101023 with episode 1 and the remaining 44 s with episode 2. There is, however, a substantial difference between these two sources. The cosmological redshift is unknown for GRB 101023. However, it is possible to theoretically derive an expected cosmological redshift through some

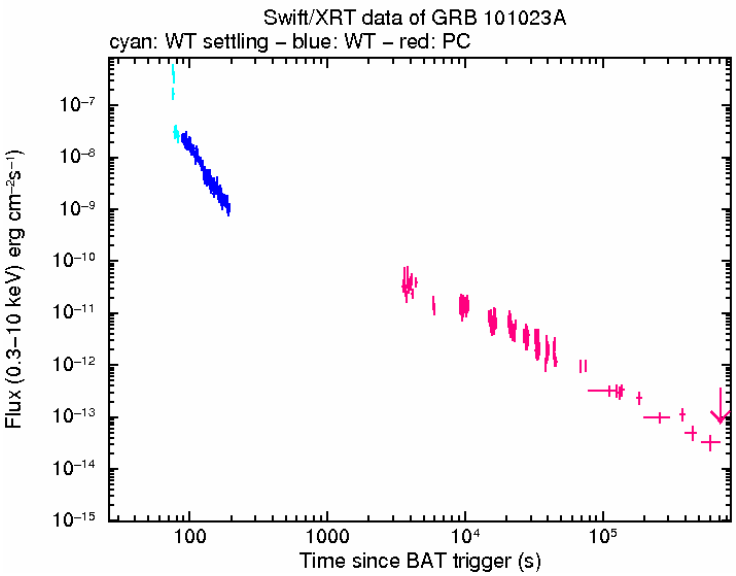

Figure 4.14: Flux light curve of GRB 101023 obtained from the *Swift*-XRT detector.

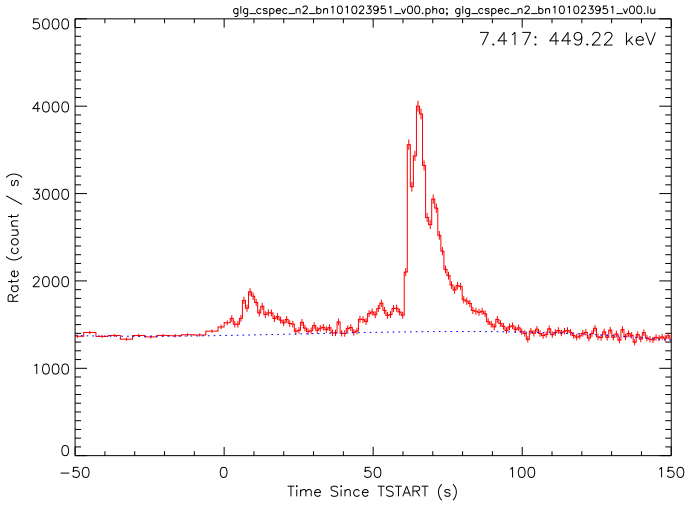

Figure 4.15: Count light curve of GRB 101023 obtained from the *Fermi*-GBM detector, with a bin time of 1 s. The time is given with respect to the GBM trigger time of 22:50:04.73 UT, 2010 October 23. The plot was obtained with the RMFIT program.

phenomenological methods, explained below.

4.3.6 Redshift determination

Due to the lack of data in the optical band, the redshift of GRB 101023 is unknown, so we employed four phenomenological methods to constrain it.

nH column density

We followed the method by Grupe et al. (2007), in which the authors comment on a possible relation between the absorption column density in excess of the galactic absorption column density $\Delta N_H = N_{H,fit} - N_{H,gal}$ and the redshift z. We considered the galactic absorption component in Kalberla et al. (2005) and the galactic coordinates of the source: $l = 328.88$, $b = -38.88$, which we entered in the Lab Survey website to obtain a value of $n_H = 2.59 \times 10^{20}$ cm^{-2} for the galactic H column density[3]. With the spectrum and response files taken from the XRT website[4] we made a spectral analysis with the program XSPEC. We first fit the model *wabs*, which is the photoelectric absorption using Wisconsin cross-sections: $M(E) = exp[-n_H\sigma(E)]$ (Morrison & McCammon 1983). In this expression, $\sigma(E)$ is the photoelectric cross-section (not including Thomson scattering) and n_H is the equivalent hydrogen column density in units of 10^{22} atoms cm^{-2}. Then we fit a power-law model with a photoelectric absorption component (related to the intrinsic absorption). We obtained a value of $n_H^{intr} = 0.18 \pm 0.02 \times 10^{22}$ cm^{-2}. We put this result in Eq.(1) of Grupe et al. (2007)

$$log(1+z) < 1.2 - 0.5[log(1+\Delta N_H)], \tag{4.6}$$

and obtained an upper limit for the redshift of 3.8.

Amati relation

The Amati relation involves the isotropic energy E_{iso} of a GRB and the rest-frame peak energy $E_{p,i}$ of the $\nu F\nu$ electromagnetic spectrum (Amati 2006a; Amati et al. 2009). The isotropic energy is given by

$$E_{iso} = \frac{4\pi d_L^2}{(1+z)} S_{bol}, \tag{4.7}$$

where d_L is the luminosity distance (see Eq. (4.4)) and S_{bol} is the bolometric fluence, related to the observed fluence in a given energy band (E_{min}, E_{max}) by

$$S_{bol} = S_{obs} \frac{\int_{1/(1+z)}^{10^4/(1+z)} E\phi(E)dE}{\int_{E_{min}}^{E_{max}} E\phi(E)dE}. \tag{4.8}$$

Here, ϕ is the spectral model considered for the fit of the spectrum (generally a Band model). The peak energy $E_{p,i}$ in the rest frame is related to that in the observer frame E_p by

$$E_{p,i} = E_p(1+z). \tag{4.9}$$

[3] http://www.astro.uni-bonn.de/~webaiub/english/tools_labsurvey.php
[4] http://www.swift.ac.uk/xrt_curves/

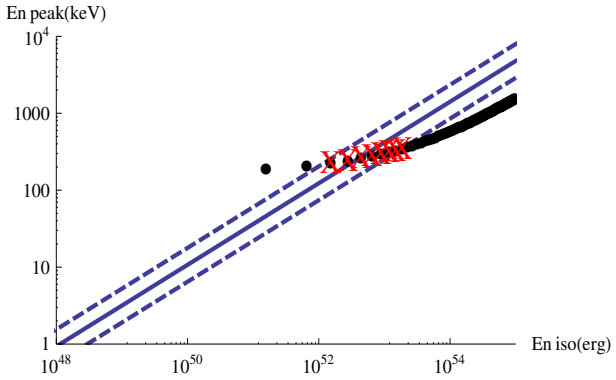

Figure 4.16: Plot of the relation between $E_{p,i}$ and E_{iso} for episode 2 of GRB 101023, for different values of the redshift. The plot lies within 1σ for the range $0.3 < z < 1.0$.

We supposed for our purposes that episode 2 is a long GRB. We calculated E_{iso} and $E_{p,i}$ for different values of z and plot the Amati relation (see Fig.4.16). The relation is satisfied for values of z between 0.3 and 1.0, with a significance of 1σ.

Atteia pseudo-redshift

There is another method, according to Atteia (2003) and Pélangeon et al. (2006), which consists in determining a pseudo-redshift from the GRB spectral properties. Using the Band parameters (the low-energy power-law index α and the break energy E_0), we can compute the value of the peak energy $E_p = E_0(2+\alpha)$. We define the isotropic-equivalent number of photons in a GRB, N_γ, as the number of photons below the break, integrated from $E_p/100$ to $E_p/2$. We define also the redshift indicator for each GRB

$$X = \frac{N_\gamma}{E_p\sqrt{T_{90}}}, \tag{4.10}$$

where T_{90} is the duration of the GRB. We computed the theoretical evolution of X with the redshift, i.e. $X = f(z)$, for a sample of 17 GRBs reported in Atteia (2003). Then, we inverted the function to derive a pseudo-redshift from the value of X, $\hat{z} = f^{-1}(X)$, for episode 2 of GRB 101023. This whole process is summarized in the Cosmos website[5]. We just introduced the spectral parameters of the Band model and obtained a redshift $z = 0.90 \pm 0.08$. However, the error is a statistical one, while the systematical error is much bigger, on the order of 1.5 (Atteia 2003; Pélangeon et al. 2006, 2008). This result is in agreement with the ones found with the above mentioned methods.

Rescaling of the late X-ray afterglow light curves

We developed another method which consists in comparing the late decay of the rest-frame X-ray light curves of different GRBs with that of GRB 090618, which

[5]http://cosmos.ast.obs-mip.fr/projet/v2/fast_computation.html

we considered as the benchmark due to the such good quality and quantity of the data in a wide energy range.

The method consists in four steps:

1) we need to obtain the *Swift*-XRT observed flux light curve of both the GRB of interest and the benchmark in the (0.3-10) keV energy band[6].

2) we need to transform the flux from the observer frame to the rest frame. To do it we must define a conversion factor C_f

$$C_f = \frac{\int_{E_1/(1+z)}^{E_2/(1+z)} \phi(E)dE}{\int_{E_{min}}^{E_{max}} \phi(E)dE}, \tag{4.11}$$

where (E_1, E_2) is the energy range in the rest frame, (E_{min}, E_{max}) is the energy range in the observer frame (in this case $0.3 - 10$ keV, the XRT energy range) and ϕ is the flux. If we assume that the light curve decays as a power-law, then $\phi \sim E^{-\gamma}$. Besides, if we consider $E_{min} = E_1 = 0.3$ keV and $E_{max} = E_2 = 10$ keV, the whole expression simplifies and we obtain

$$C_f = (1+z)^{(\gamma-1)}. \tag{4.12}$$

Finally, the flux in the rest frame F_{rf} is given by

$$F_{rf} = C_f F_{obs}. \tag{4.13}$$

3) we must transform the time from the observer frame to the rest frame, simply by correcting for the redshift:

$$t_{rf} = \frac{t_{obs}}{(1+z)}. \tag{4.14}$$

4) we define the luminosity in the rest frame as:

$$L = 4\pi d_L^2 F_{rf}, \tag{4.15}$$

where d_L is the luminosity distance given in Eq.(4.4), assuming a standard cosmology.

Once we have applied this method to both GRBs we can plot the late X-ray luminosity light curves together (see Fig. 4.17).

In the light of these results, we chose the value $z = 0.9$ for GRB 101023, which we used in the following analysis.

4.3.7 Data analysis

We obtained the *Fermi*-GBM light curve and spectrum in the band (8-440) keV with the RMFIT program. We used the light curves from the second and fifth NaI detectors and the b0 BGO detector, which we downloaded from the *gsfc* website[7]. Then we defined the time intervals we wanted to analyze; episode 1 from the trigger time $t_0 = 0$ s to 45 s after it and episode 2 from 45 s to 89 s after the trigger time.

[6] http://www.swift.ac.uk/

[7] ftp://legacy.gsfc.nasa.gov/fermi/data/gbm/bursts

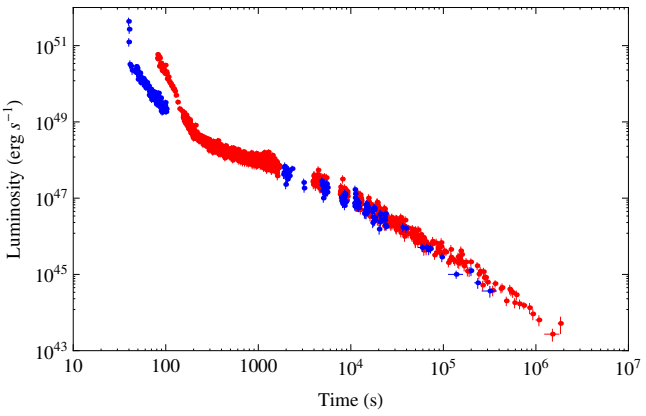

Figure 4.17: X-ray luminosity light curves of GRB 101023 (blue) and GRB 090618 (red) in the rest-frame energy band (0.3-10) keV. We chose $z = 0.9$ for GRB 101023, since for this value the two light curves overlap.

Table 4.3: Spectral analysis of episodes 1 and 2 of GRB 101023. We have proposed for each episode a Band spectral model (up) and a BB+PL model (down).

Time[s]	α	β	E_0^{Band}[keV]	Redχ^2	Norm
0-44	-1.3±0.8	-1.9±0.2	87±147	0.98	0.006±0.01
45-89	-0.9±0.1	-2.0±0.1	151±24	1.09	0.043±0.008
Time[s]	kT[keV]	γ	Redχ^2	Norm^{po}	Norm^{BB}
0-44	14±6	-1.7±0.1	0.98	0.0003±0.0004	$(4.1\pm7.4)\times10^{-5}$
45-89	26±1	-1.58±0.03	1.12	0.0124±0.0006	$(4.2\pm1.1)\times10^{-5}$

Analysis in the Fireshell scenario: Episode 1

We first interpreted the whole emission as a single GRB, with episode 1 as the P-GRB within the fireshell scenario. We performed a time-integrated analysis of each episode by fitting two spectral models to the data, a BB+PL and a Band model (Band et al. 1993). The results are shown in Table 4.3.7, and a fit of each spectra with both models is shown in Fig.4.18 for each episode.

With the knowledge of the spectral parameters we calculated the isotropic energy of the burst, $E_{iso} = 4.03 \times 10^{53}$ erg, and the P-GRB energy, $E_{P-GRB} = 1.6 \times 10^{52}$ erg. This gives a ratio $E_{P-GRB}/E_{iso} = 0.04$. We then performed a numerical simulation to determine the baryon load and the temperature for a given value of the total and P-GRB energy. We found a theoretically predicted temperature of $kT_{th} = 110.6$ keV, which is by far much higher than the observed one. Consequently, we conclude that episode 1 cannot be the P-GRB and the whole emission cannot be treated as a single GRB.

The second step was to consider episode 1 and episode 2 as two different GRBs. For episode 1 we did not find an agreement between the theoretically predicted and the observed temperatures. Therefore, we concluded that it cannot be a GRB but is related to the phases previous to the gravitational collapse to a BH to emit the GRB. A more detailed analysis will be performed in the

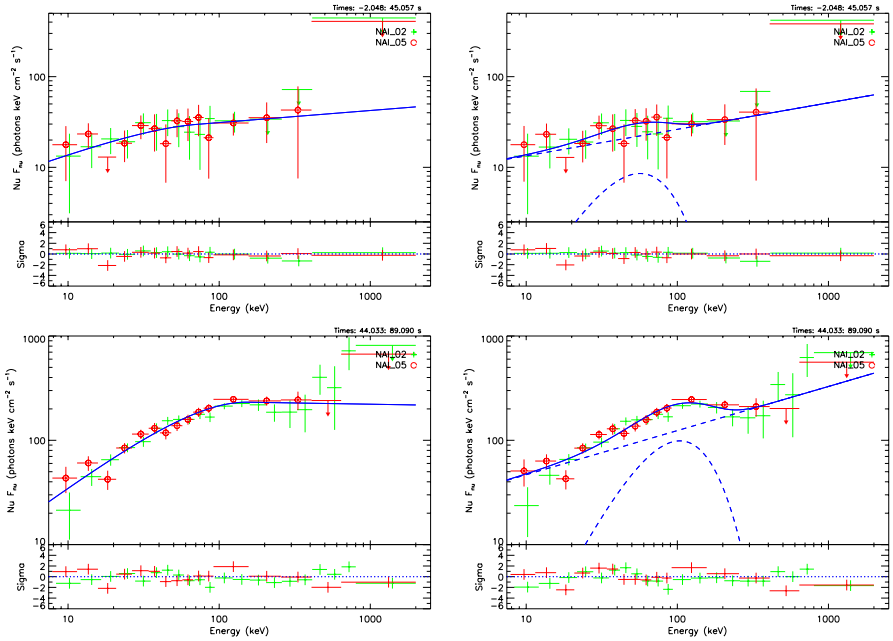

Figure 4.18: *Upper panel*: fit of the spectrum of episode 1 with a Band model (left) and a Black body plus a power-law model (right). Both models fit well the spectrum, with a reduced Chi squared of 0.98 in both cases. *Lower panel*: fit of the spectrum of episode 2 with a Band model (left) and a Black body plus a power-law model (right). Both models fit well the entire energy range, with a Redχ^2 of 0.79 and 0.84, respectively. The data points have been grouped according a signal to noise ratio of SNR=10, and rebinned at higher energies in order to have better statistics and reduce the error bars.

Sec.4.3.8.

Analysis in the Fireshell scenario: Episode 2 as a canonical GRB

With regard to episode 2, we performed a time-resolved spectral analysis every 1 second to individuate the interval in which the thermal component dominates, as this should belong to the P-GRB emission. We found a P-GRB that lasts 5 s from the beginning of the episode. The energy of the whole episode 2 is $E^{(2)}_{iso} = 1.8 \times 10^{53}$ erg, while the energy of the P-GRB is $E_{P-GRB} = 2.51 \times 10^{51}$ erg. To simulate the afterglow emission (light curve and spectrum) we made use of a numerical code developed at *Sapienza University*, called *GRBsim*. The main purpose of this code is to solve the fireshell equations of motion by taking into account the effect of the EQTS (Bianco & Ruffini 2005a). We found at the transparency point a laboratory radius $r = 1.34 \times 10^{14}$ cm, a theoretically predicted temperature $kT_{th} = 13.26$ keV (after cosmological correction), and a Lorentz Gamma factor $\Gamma \sim 260$. The P-GRB observed temperature is 28.4 keV and the baryon load is $B = 3.8 \times 10^{-3}$. The simulated spectrum and light curve are shown in Fig. 4.19.

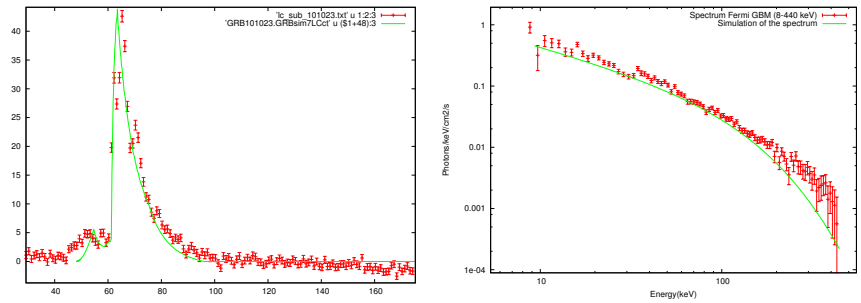

Figure 4.19: Simulation of the *Fermi* GBM light curve (left) and spectrum (right) of GRB 101023 with the numerical code GRBsim. The spectral data is in the range (8-440) keV.

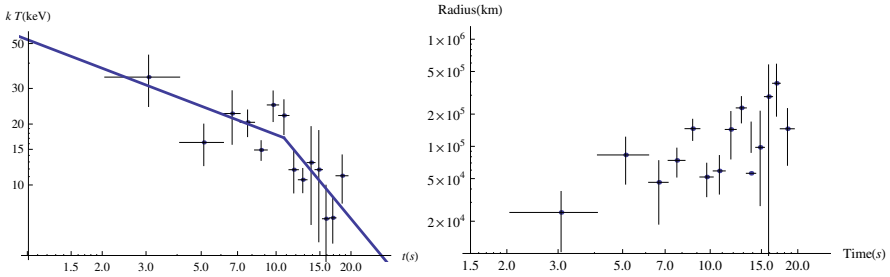

Figure 4.20: *Left*: Evolution of the observed temperature kT of the blackbody component of episode 1. The blue line corresponds to a broken power-law fit. The indices of the first and second power-law are $\alpha = -0.47 \pm 0.34$ and $\beta = -1.48 \pm 1.13$. The break occurs at 11 s after the trigger time. *Right*: Evolution of the radius of the outermost shell with time. The time is in the rest-frame.

4.3.8 Analysis of the first episode: radius of the emitting region

In order to identify the origin of episode 1 we plotted the evolution of the blackbody component with time, for the first 20 s of emission. Fig. 4.20 shows the results. There is a marked evolution of the temperature which can be reproduced by a broken power-law (Ryde 2004) with indices $\alpha = -0.47 \pm 0.34$ and $\beta = -1.48 \pm 1.13$. We calculated the evolution of the radius of the most external shell as a function of the rest-frame time, according to Eq.(4.5), see Fig. 4.20. It is evident that the plasma is moving at non relativistic velocities, which supports the fact that episode 1 cannot be a GRB.

4.3.9 Conclusions

GRB 101023 has a striking similarity with GRB 090618 (Izzo et al. 2012c), which can be seen from the morphology of the light curve and the energetics. We have divided the emission into two episodes also for GRB 101023. Episode 1 lasts 45 s and has an isotropic energy $E_{iso}^{(1)} = 4.03 \times 10^{53}$ erg. Episode 2 lasts

44 s and has an isotropic energy $E_{iso}^{(1)} = 1.8 \times 10^{53}$ erg. There is one important aspect of GRB 101023 that makes it different from GRB 090618, which is the absence of a direct measurement of the redshift. Therefore, we inferred it by applying some phenomenological methods: the Amati relation (Amati 2006a), the Atteia relation (Atteia 2003), the Grupe relation (Grupe et al. 2007) and the overlapping of the late X-ray light curves of GRB 101023 and GRB 090618. We derived a value for the redshift of $z = 0.9$. We performed a spectral analysis of both episodes. Episode 1 is well fit by a black body plus a power-law model. The temperature of the blackbody component decreases monotonically with time during the first 20 s following a broken power-law. This behavior is also found in GRB 090618. We analyzed episode 2 within the fireshell model. We simulated its light curve and spectrum with a numerical code and found all the relevant parameters. While episode 2 has all the characteristics of a canonical GRB, we conclude that episode 1 is related to the phases of the progenitor before the gravitational collapse to a BH and the emission of the GRB. We called this phase the "Proto-Black hole", as in the case of GRB 090618. We are led to think that GRB 101023 and GRB 090618 are both members of a specific new family of GRBs. It is also appropriate to remark that this new kind of sources do not present any GeV emission. Finally, the existence of precise scaling laws between these two sources opens a new window on the use of GRBs as distance indicators.

A&A 543, A10 (2012)
DOI: 10.1051/0004-6361/201117436

Astronomy & Astrophysics

A double component in GRB 090618: a proto-black hole and a genuinely long gamma-ray burst

L. Izzo[1,2], R. Ruffini[1,2,5], A. V. Penacchioni[1,5], C. L. Bianco[1,2], L. Caito[1,2], S. K. Chakrabarti[3,4], J. A. Rueda[1,2], A. Nandi[4], and B. Patricelli[1,2]

[1] Dip. di Fisica and ICRA, Sapienza Università di Roma, Piazzale Aldo Moro 5, 00185 Rome, Italy
e-mail: [Ruffini;luca.izzo;ana.penacchioni;bianco;letizia.caito;jorge.rueda]@icra.it
[2] ICRANet, Piazza della Repubblica 10, 65122 Pescara, Italy
e-mail: barbara.patricelli@icranet.org
[3] S. N. Bose National Center for Basic Sciences, Salt Lake, 700098 Kolkata, India
e-mail: chakraba@bose.res.in
[4] Indian Center for Space Physics, Garia, 700084 Kolkata, India
[5] Universite de Nice Sophia Antipolis, CEDEX 2, Grand Chateau Parc Valrose, Nice, France

Received 7 June 2011 / Accepted 3 April 2012

ABSTRACT

Context. The joint X-ray and gamma-ray observations of GRB 090618 by very many satellites offer an unprecedented possibility of testing crucial aspects of theoretical models. In particular, they allow us to test (a) in the process of gravitational collapse, the formation of an optically thick e^+e^--baryon plasma self-accelerating to Lorentz factors in the range $200 < \Gamma < 3000$; (b) its transparency condition with the emission of a component of 10^{53-54} baryons in the TeV region and (c) the collision of these baryons with the circumburst medium (CBM) clouds, characterized by dimensions of 10^{15-16} cm. In addition, these observations offer the possibility of testing a new understanding of the thermal and power-law components in the early phase of this GRB.
Aims. We test the fireshell model of GRBs in one of the closest ($z = 0.54$) and most energetic ($E_{\rm iso} = 2.90 \times 10^{53}$ erg) GRBs, namely GRB 090618. It was observed at ideal conditions by several satellites, namely *Fermi*, *Swift*, Konus-WIND, AGILE, RT-2, and *Suzaku*, as well as from on-ground optical observatories.
Methods. We analyzed the emission from GRB 090618 using several spectral models, with special attention to the thermal and power-law components. We determined the fundamental parameters of a canonical GRB within the context of the fireshell model, including the identification of the total energy of the e^+e^- plasma, $E_{\rm tot}^{e^+e^-}$, the proper GRB (P-GRB), the baryon load, the density and structure of the CBM.
Results. We find evidence of the existence of two different episodes in GRB 090618. The first episode lasts 50 s and is characterized by a spectrum consisting of a thermal component, which evolves between $kT = 54$ keV and $kT = 12$ keV, and a power law with an average index $\gamma = 1.75 \pm 0.04$. The second episode, which lasts for ∼100 s, behaves as a canonical long GRB with a Lorentz gamma factor at transparency of $\Gamma = 495$, a temperature at transparency of 29.22 keV and with a characteristic size of the surrounding clouds of $R_{\rm cl} \sim 10^{15-16}$ cm and masses of $\sim 10^{22-24}$ g.
Conclusions. We support the recently proposed two-component nature of GRB 090618, namely, *episode 1* and *episode 2*, with a specific theoretical analysis. We furthermore illustrate that episode 1 cannot be considered to be either a GRB or a part of a GRB event, but it appears to be related to the progenitor of the collapsing bare core, leading to the formation of the black hole, which we call a "proto-black hole". Thus, for the first time, we are witnessing the process of formation of a black hole from the phases just preceding the gravitational collapse all the way up to the GRB emission.

Key words. gamma-ray burst: general – gamma-ray burst: individual: GRB 090618 – black hole physics

1. Introduction

After the discovery of the gamma-ray bursts (GRBs) by the Vela satellites (Klebesadel et al. 1973; Strong & Klebesadel 1974; Strong et al. 1974; Strong 1975), the first systematic analysis on a large sample of GRBs was possible thanks to the observations of the BATSE instrument on board the *Compton* Gamma-Ray Observer (CGRO) satellite (Meegan et al. 1992). The 4BATSE catalog (Meegan 1997; Paciesas et al. 1999; Kaneko et al. 2006) consists of 2704 confirmed GRBs, and it is widely used by the science community as a reference for spectral and timing analyses on GRBs. One of the outcomes of this early analysis of GRBs led to the classification of GRBs as a function of their observed time duration. T_{90} was defined as the time interval over which the 90% of the total BATSE background-subtracted counts are observed. The distribution of the T_{90} duration was bi-modal: the GRBs with T_{90} less than 2 s were classified as "short" while those with T_{90} longer than 2 s were classified as "long" (Klebesadel 1992; Dezalay et al. 1992; Kouveliotou et al. 1993; Tavani 1998).

After the success of BATSE, a very many of space missions dedicated to GRB observations were launched. Particularly significant was the discovery of an additional prolonged soft X-ray emission by *Beppo*-SAX (Costa et al. 1997), following the usual hard X-ray emission observed by BATSE. The *Beppo*-SAX observed emission was named "afterglow", while the BATSE one was called "prompt" radiation. The afterglow allowed pinpointing the GRB position in the sky more accurately and permitted identifying its optical counterpart by space- and ground-based telescopes. The measurement of the cosmological redshift for GRBs became possible and their cosmological nature was firmly established (van Paradijs et al. 1997).

The *Beppo*-SAX and related results enabled ruling out literally hundreds of theoretical models of GRBs (see for a review Ruffini 2001). Among the handful of surviving models was the one by Damour & Ruffini (1975), which is based on the mass-energy formula of black holes. This model can naturally explain the energetics up to 10^{54-55} erg, as requested by the cosmological nature of GRBs, through the creation of an e^+e^--plasma by vacuum polarization processes in the Kerr-Newman geometry (for a recent review see Ruffini et al. 2010b). This model was proposed a few months after the presentation of the discovery of GRBs by Strong (Strong 1975) at the AAAS meeting in San Francisco.

It soon became clear that, as suggested by Goodman and Paczynski (Goodman 1986; Paczynski 1986), a Lorentz gamma factor larger than 100 could overcome the problem of opacity of the e^+e^--plasma and justify the γ-ray emission of GRBs at cosmological distances (see e.g. Piran 2005). That the dynamics of an e^+e^--plasma with a baryon load with mass M_B would naturally lead to Lorentz gamma factor in the range $(10^2$–$10^3)$ was demonstrated by Shemi & Piran (1990), Piran et al. (1993) and Meszaros et al. (1993). The general solution for a baryon load $B = M_Bc^2/E_{\rm tot}^{e^+e^-}$ between 0 and 10^{-2} was obtained in Ruffini et al. (2000). The interaction between the accelerated baryons with the CBM, indicated by Meszaros & Rees (1993), was advocated to explain the nature of the afterglow (see e.g. Piran 1999, and references therein).

The unprecedented existence of such large Lorentz gamma factors led to the relativistic space-time transformations paradigm for GRBs (Ruffini et al. 2001b). This paradigm made it a necessity to have a global, instead of a piecewise, description of the GRB phenomenon (Ruffini et al. 2001b). This global description led to the conclusion that the emission by the accelerated baryons interacting with the CBM indeed occurs already in the prompt emission phase in a fully radiative regime. A new interpretation of the burst structure paradigm was then introduced (Ruffini et al. 2001a): the existence of a characteristic emission at the transparency of an e^+e^--plasma, the proper-GRB, followed by an extended-afterglow emission. The relative intensity of these two components is a function of the baryon load. It was proposed that $B < 10^{-5}$ corresponds to the short GRBs, while $B > 3 \times 10^{-4}$ corresponds to the long GRBs.

This different parametrization of the prompt – afterglow versus that of the P-GRB – extended-afterglow could have originated years of academic discussions. However, a clear-cut observational evidence came from the *Swift* satellite, in favor of the second parametrization. The Norris-Bonnell sources, characterized by an initial short spike-like emission in the hard X-rays followed by a softer extended emission, had been indicated in the literature as short bursts. There is clear evidence that they belong to a new class of "disguised" short GRB (Bernardini et al. 2007; Caito et al. 2009, 2010; de Barros et al. 2011), where the initial spike is identified as the P-GRB while the prolonged soft emission occurring from the extended-afterglow emission in a CBM typically of the galatic halo. These sources have a baryon load $10^{-4} < B < 7 \times 10^{-4}$: they are just long GRBs exploding in a particularly low-density CBM of the order of 10^{-3} particles/cm^3. This class of sources has given the first evidence of GRBs originating from binary mergers, which is also strongly supported from direct optical observations (Bloom et al. 2006; Fong et al. 2010).

It is interesting that independent of the development of new missions, the BATSE data continue to attract full scientific interests, even after the end of the mission in the 2000. Important inferences, based on the BATSE data, on the spectra of the early emission of the GRB have been made by Ryde (2004) and Ryde et al. (2006). These authors have convincingly demonstrated that the spectral feature composed of a blackbody and a power-law plays an important role in selected episodes in the early part of the GRB emission (see also Zhang et al. 2011 for further comments on the origin of this blackbody and power-law behavior). They have also shown, in some cases, a power-law variation of the thermal component as a function of time, following a broken power-law behavior, see Fig. 17.

The arrival of the *Fermi* and other satellites allowed further progresses in the understanding of the GRB phenomenon in a much wider energy range. Thanks to the Gamma-Ray Burst Monitor (GBM) (Meegan et al. 2009) and the Large Area Telescope (LAT) (Atwood et al. 2009), additional data are obtained in the 8 keV–40 MeV and 100 MeV–300 GeV energy range. This allowed, among others, this first evidence of a GRB originating from the collapse of a core in the late evolution of a massive star, which we called the proto black hole (Ruffini 2011; Penacchioni et al. 2012).

In the specific case of GRB 090618, it has been possible to obtain a complete temporal coverage of the emission in gamma and X-rays, thanks to the joint observations by the *Swift*, *Fermi*, AGILE, RT-2/Coronas-PHOTON, Konus-WIND, and *Suzaku*-WAM telescopes. A full coverage in the optical bands, up to 100 days from the burst trigger, has been obtained. This has allowed determining the redshift, $z = 0.54$, of the source from spectroscopical identification of absorption lines (Cenko et al. 2009) and a recent claim of a possible supernova emission ~10 days after the GRB trigger. This GRB lasts for ~150 s in hard X-rays, and it is characterized by four prominent pulses. In the soft X-rays there are observations up to 30 days from the burst trigger.

We have pointed out in Ruffini et al. (2010a) that two different episodes are present in GRB 090618. We have also showed that while the second episode may fit a canonical GRB, the first episode is not expected to be either a part of a GRB or an independent GRB (Ruffini et al. 2011).

In the present paper we discuss the nature of these two episodes. In particular:

- in Sect. 2, we describe the observations, data reduction and analysis. We obtain the *Fermi* GBM (8 keV–1 MeV and 260 keV–40 MeV) flux light curves, shown in Fig. 2, following the standard data reduction procedure, and make a detailed spectral analysis of the main emission features, using a Band model and a power-law with exponential high-energy cut-off spectral models;
- in Sect. 3, after discussing about the most often quoted GRB model, the fireball, we recall the main features of the fireshell scenario, focusing on the reaching of transparency at the end of the initial optically thick phase, with the emission of the proper-GRB (P-GRB). In Fig. 3 we give the theoretical evolution of the Lorentz Γ factor as a function of the radius for selected values of the baryon load, corresponding to fixed values of the total energy $E_{\rm tot}^{e^+e^-}$. The identification of the P-GRB is crucial in determining the main fireshell parameters, which describe the canonical GRB emission. The P-GRB emission is indeed characterized by the temperature, the radius, and the Lorentz Γ factor at the transparency, which are related with the $E_{\rm tot}^{e^+e^-}$ energy and the baryon load, see Fig. 4. We then recall the theoretical treatment, the simulation of the light curve and spectrum of the extended-afterglow and, in particular, the determination of the equations of motion, the role of the EQuiTemporal Surfaces (EQTS) (Bianco & Ruffini 2004, 2005a), as well as

the ansatz of the spectral energy distribution in the fireshell comoving frame, (see Patricelli et al. 2011, and references therein).
The temporal variability of a GRB light curve has been interpreted in some current models as caused by internal shock (Rees & Meszaros 1994). In the fireshell model this temporal variability is instead produced by the interaction of the ultra-relativistic baryons colliding with the inhomogeneities of the circumburst medium (CBM). This allows one to perform a tomography of the CBM medium around the location of the black hole formation, see Fig. 10, gaining important information on its structure. These collisions are described by three parameters: the $n_{\rm CBM}$ average density, the filling factor $\mathcal{R}$, the clumpiness on scales of 10^{15-16} cm, and average density contrast $10^{-1} \lesssim \langle \delta n/n \rangle \lesssim 10$. We then refer also to the explanation of the observed hard-to-soft behavior due to the drop of the Lorentz Γ factor and the curvature effect of the EQTS. We then recall the determination of the instantaneous spectra and the simulations of the observed multi-band light curves in the chosen time interval, taking into account all the thousands of convolutions of comoving spectra over each EQTS leading to the observed spectrum. We also emphasize that these simulations have to be performed together and that they need to be optimized;
– in Sect. 4, we perform a spectral analysis of GRB 090618. We divided the total GRB emission into six time intervals, see Table 1, each one identifying a significant feature in the emission process, see also Rao et al. (2011). We considered two different spectral models in the data fitting procedure: a Band model (Band et al. 1993) and one by a blackbody plus a power-law component, following e.g. Ryde (2004). We find that the first 50 s of emission are well-fitted by both models, equally the following 9 s, from 50 to 59 s. The remaining part, from 59 to 151 s, is fitted satisfactorily only with the Band model, see Table 1;
– in Sect. 5, we proceed to the analysis of GRB 090618 in the fireshell scenario; In Sect. 5.1, we attempt our first interpretation of GRB 090618 assuming it to be a single GRB. We recall that the blackbody is an expected feature in the theory of P-GRB. From the spectral analysis of the first 50 s, we find a spectral distribution consistent with a blackbody plus a power-law component. We first attempted a fit of the source identifying these first 50 s as the P-GRB, see Fig. 6. We confirm the conclusion reached in Ruffini et al. (2010a) that this interpretation is not sustainable for three different reasons, based on 1) the energetics of the source; 2) the time duration; and 3) the theoretical expected temperature for the P-GRB. We then proceed, in Sect. 5.2, to an interpretation of GRB 090618 as a multi-component system, following the procedure outlined in Ruffini et al. (2011), in which we outlined the possibility that the second episode between 50 and 151 s is an independent GRB.
We identify the P-GRB of this second episode as the first 4 s of emission. We find that the spectrum in this initial emission can be fitted by a blackbody plus a power-law component, see Fig. 8. Since this extra power-law component can be generated by to the early onset of the extended afterglow, we took this into account to perform a fireshell simulation, which is shown in Fig. 8, with an energy $E_{\rm tot}^{\rm e^+e^-} = 2.49 \times 10^{53}$ erg and a baryon load $B = 1.98 \pm 0.15 \times 10^{-3}$. In Figs. 10–12 we report the results of our simulations, summarized in Table 3. We notice, in particular, the presence of a strong time lag in this GRB. A detailed analysis, see Rao et al. (2011), of the time lags in the mean energy ranges of 35 keV, 68 keV and 125 keV, reports quite a long lag, ~7 s, in the first 50 s of the emission, which is unusual for GRBs, while in the following emission, from 51 to 151 s, the observed lags are quite normal, ~1 s;
– in Sect. 6, we perform a spectral analysis of the first 50 s, where we find a strong spectral variation with time, as reported in Table 5 and in Figs. 16, 17, with a chacteristic power-law time variation similar to those identified by Ryde & Pe'er (2009) in a sample of 49 BATSE GRBs;
– in Sect. 7, we estimate the variability of the radius emitter, Fig. 18, and proceed to an estimate of the early expansion velocity. We interpret these data as originating in the expansion process occurring previous to the collapse of the core of a massive star to a black hole, see e.g. Arnett & Meakin (2011): these early 50 s of the emission are then defined as the proto-black hole phenomenon;
– In Sect. 8 we conclude.

2. Observations

On 18 June 2009, the Burst Alert Telescope (BAT) on board the *Swift* satellite (Gehrels et al. 2009) observed GRB 090618 (Schady et al. 2009). After 120 s the X-Ray Telescope (XRT) (Burrows et al. 2005) and the UltraViolet Optical Telescope (UVOT) (Roming et al. 2005) on board the same satellite started the observations of the afterglow of GRB 090618. UVOT found a very bright optical counterpart, with a white filter magnitude of 14.27 ± 0.01 (Schady 2009) not corrected for the extinction, at the coordinates RA(J2000) = 19:35:58.69 = 293.99456, Dec(J2000) = +78:21:24.3 = 78.35676. The BAT light curve shows a multi-peak structure, whose total estimated duration is ~320 s, whose T_{90} duration in the (15–350) keV range was 113 s (Baumgartner et al. 2009). The first 50 s of the light curve present a smooth decay trend, followed by a spiky emission, with three prominent peaks at 62, 80, and 112 s after the trigger time, respectively, and each have the typical appearance of the FRED pulse (see e.g. Fishman et al. 1994), see Fig. 2. The time-integrated spectrum, (t_0 − 4.4, t_0 + 213.6) s in the (15−150) keV range, was found to agree with a power-law spectral model with an exponential cut-off, whose photon index was $\gamma = 1.42 \pm 0.08$ and a cut-off energy $E_{\rm peak} = 134 \pm 19$ keV (Sakamoto et al. 2009). The XRT observations started 125 s after the BAT trigger time and lasted ~25.6 ks (Beardmore & Schady 2009) and reported an initially bright uncataloged source, identified as the afterglow of GRB 090618. Its early decay was very steep, ending at 310 s after the trigger time, when it starts a shallower phase, the plateau. Then the light curve breaks into a more steep last phase.

GRB 090618 was observed also by the Gamma-ray Burst Monitor (GBM) on board the *Fermi* satellite (Meegan et al. 2009). From a first analysis, the time-integrated spectrum, (t_0, t_0 + 140) s in the (8–1000) keV range, was fitted by a Band (Band et al. 1993) spectral model, with a peak energy $E_{\rm peak}$ = 155.5 keV, $\alpha = -1.26$ and $\beta = -2.50$ (McBreen 2009), but with strong spectral variations within the considered time interval.

It is appropriate to compare and contrast the considerations of the time-integrated spectral analysis, often adopted in the current literature of GRBs, with the information from the time-resolved spectral analysis, as presented e.g. in this article (see also Zhang et al. 2011). For a traditional astrophysical source, steady during the observation time, the time-integrated and time-resolved spectral analysis usually coincide. In the case of GRBs, although the duration is only a few seconds, each instantaneous observation corresponds to a very different physical process and

the two approaches have an extremely different physical and astrophysical content.

The redshift of the source is $z = 0.54$ and it was determined thanks to the identification of the MgII, Mg I, and FeII absorption lines, using the KAST spectrograph mounted at the 3-m Shane telescope at the Lick observatory (Cenko et al. 2009). Given the redshift and the distance of the source, we computed the emitted isotropic energy in the 8−10 000 keV energy range, with the Schaefer formula (Schaefer 2007): using the fluence in the (8–1000 keV) as observed by *Fermi*-GBM, $S_{\rm obs} = 2.7 \times 10^{-4}$ (McBreen 2009), and the ΛCDM cosmological standard model $H_0 = 70$ km s^{-1} Mpc^{-1}, $\Omega_{\rm m} = 0.27$, $\Omega_\Lambda = 0.73$, we obtain for the emitted isotropic energy the value of $E_{\rm iso} = 2.90 \times 10^{53}$ erg.

This GRB was observed also by Konus-WIND (Golenetskii et al. 2009), *Suzaku*-WAM (Kono et al. 2009), and by the AGILE satellite (Longo et al. 2009), which detected emission in the (18–60) keV and in the MCAL instrument, operating at energies greater than 350 keV, but it did not observe high-energy photons above 30 MeV. GRB 090618 was the first GRB observed by the Indian payloads RT-2 on board the Russian Satellite CORONAS-PHOTON (Kotov et al. 2008; Nandi et al. 2009; Rao et al. 2011). Two detectors, namely, RT-2/S and RT-2/G, consist of NaI(Tl)/CsI(Na) scintillators in phoswich assembly viewed by a photomultiplier tube (PMT). RT-2/S has a viewing angle of 4° × 4° and covers an energy range of 15 keV to 1 MeV, whereas RT-2/G has an Al filter that sets the lower energy to ∼20 keV. The mission was launched from Plesetsk Cosmodrom, Russia on 30 January 2009. During the event the RT-2 payload was in the SHADOW mode (away from the Sun) during 08:16:10.207 UT and ended at 08:37:35.465 UT and the GRB 090618 was detected at 77° off-axis angle. During this period, the spectrum was accumulated every 100 s, while the eight channel count rates for each detector were accumulated every second. The entire episode was observed for a duration of more than 200 s. A closer examination of the data in the accumulated channels 1:15–102 keV, 2:95–250 keV and 3:250–1000 keV indicates that the most significant counts is in channel 2 with a clear evidence of the following: (a) the emission in the first 50 s is prominent and broader in the lower channels, see Fig. 1 (b) after the first 50 s, there is evidence of a precursor of about 6 s duration before the main pulse (c) a break up into two peaks of the main pulse at intermediate energies (35–200 keV), while at higher energies (250–1000 keV) only the first peak of the main pulse survives, see Rao et al. (2011) and also Fig. 2 here.

Thanks to the complete data coverage of the optical afterglow of GRB 090618, the possible presence of a supernova underlying the emission of the GRB 090618 optical afterglow (Cano et al. 2011) was reported. The evidence of a supernova emission came from the presence of several bumps in the light curve and by the change in $R_{\rm c} - i$ color index over time: in the early phases, the blue color is dominant, typical of the GRB afterglow, but then the color index increases, suggesting a core-collapse SN. At late times, the contribution from the host galaxy was dominant.

2.1. Data analysis

We considered the BAT and XRT data of the *Swift* satellite together with the *Fermi*-GBM and RT2 data of the Coronas-PHOTON satellite. The data reduction was made with the Heasoft v6.10 packages[1] for BAT and XRT, and the *Fermi*-Science tools for GBM.

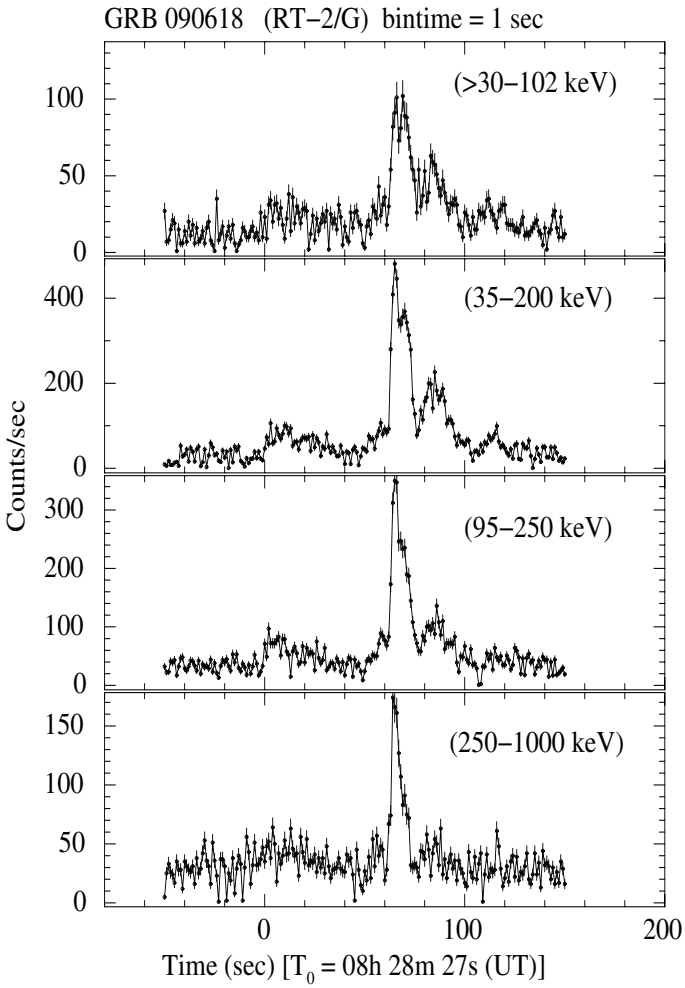

Fig. 1. RT2 light curves of GRB 090618.

We obtained the BAT light curve and spectra using the standard `headas` procedure. After the data download from the `gsfc` website[2], we made a detector quality map and corrected the event data for the known errors of the detector and the hot pixels. We subtracted the background from the data, corrected for the improved position, using the tool `batmaskwtevt` and obtained the 1-s binned light curves and spectra in the main BAT energy band 15–150 keV and its subranges, using the tool `batbinevt`. After the systematic corrections to the spectrum, we created the response matrices and obtained the final spectra.

For the XRT data, we obtained a total dataset using the standard pipeline, while for a time-resolved analysis we considered the on-line recipe, which is well described in literature, see Evans et al. (2007, 2009). The GBM data[3], in particular the fourth NaI detector in the (8–440 keV) and the b0 BGO detector (260 keV–40 MeV), were analyzed using the `gtbindef` tool to obtain a GTI file for the energy distribution and the `gtbin` for the light curves and final spectra. To obtain an energy flux lightcurve, we made a time-resolved spectral analysis dividing the count lightcurve into six time intervals, each of them corresponding to a particular pulse, as described in the work of Rao et al. (2011). All time-resolved spectra were fitted using the XSPEC data analysis software (Arnaud 1996) version 12.6.0q, included in the Heasoft data package, and considering for each

[1] `http://heasarc.gsfc.nasa.gov/lheasoft/`

[2] `ftp://legacy.gsfc.nasa.gov/swift/data/obs/`

[3] `ftp://legacy.gsfc.nasa.gov/fermi/data/gbm/`

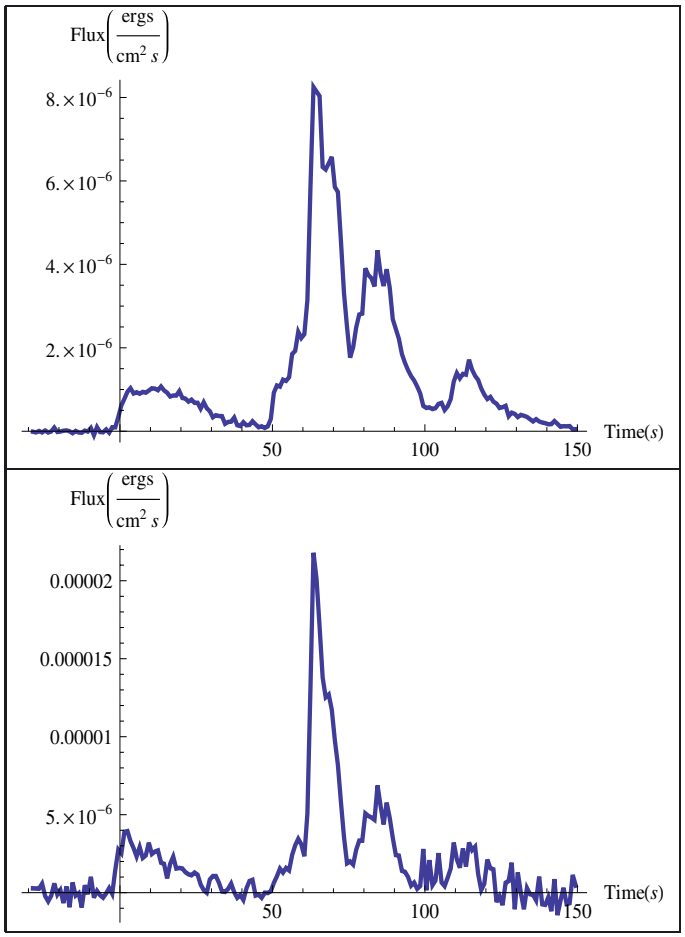

Fig. 2. *Fermi*-GBM flux light curve of GRB 090618 referring to the NaI (8–440 keV, *upper panel*) and BGO (260 keV–40 MeV, *lower panel*) detectors.

spectrum a classical Band spectral model (Band et al. 1993) and a power-law model with an exponential energy cut-off, folded through the detector response matrix. After subtracting the background, we fitted the spectrum by minimizing the χ^2 between the spectral models described above and the observed data, obtaining the best-fit spectral parameters and the respective model normalization. In Table 1 we give the results of our spectral analysis. The time reported in the first column corresponds to the time after the GBM trigger time $t_{\rm trig} = 267\,006\,508$ s, where the β parameter was not constrained, we used its averaged value, as delineated in Guetta et al. (2011) $\beta = -2.3 \pm 0.10$. We considered the chi-square statistic for testing our data fitting procedure. The reduced chi-square $\tilde{\chi}^2 = \chi^2/N$, where N is the number of degrees of freedom (d.o.f.), which is $N = 82$ for the NaI dataset and $N = 121$ for that of BGO.

For the last pulse of the second episode, the Band model is not very precise ($\tilde{\chi}^2 = 2.24$), but a slightly better approximation is given by the power-law with an exponential cut-off, whose fit results are shown for the same intervals in the last two columns. From these values, we built the flux light curves for both detectors, which are shown in Fig. 2.

We turn now to the XRT, which started to observe GRB 090618 ~ 120 s after the BAT trigger. Its early data show a continued activity of the prompt emission, fading away ~200 s after the BAT trigger time. Then the light curve is well approximated with a power-law decay. In view of the lack of soft X-ray data before the onset of the XRT, we cannot exclude a previous pulse in the X-ray light curve emission of GRB 090618. The following shallow and late decay phases, well-known in literature (Sari et al. 1999; Nousek et al. 2006), will not be analyzed in this paper since we focus on the first 200 s of the GRB emission.

3. A brief review of the fireshell and alternative models

3.1. The GRB prompt emission in the fireball scenario

A variety of models have been developed to theoretically explain the observational properties of GRBs. One of the most quoted is the fireball model (see for a review Piran 2005). The model was first proposed by Cavallo & Rees (1978), Goodman (1986) and Paczynski (1986), who have shown that the sudden release of a large quantity of energy in a compact region can lead to an optically thick photon-lepton plasma and to the production of e^+e^- pairs. The total annihilation of the e^+e^- plasma was assumed, leading to a vast release of energy pushing on the CBM: the "fireball".

An alternative approach, originating in the gravitational collapse to a black hole, is the fireshell model (see for a review Ruffini et al. 2010b; Ruffini 2011). There the GRBs originate from an optically thick electron–positron plasma in thermal equilibrium, with a total energy of $E_{\rm tot}^{\rm e^\pm}$. This plasma is initially confined between the radius of a black hole $r_{\rm h}$ and the dyadosphere radius

$$r_{\rm ds} = r_{\rm h}\left[2\alpha\frac{E_{\rm tot}^{\rm e^+e^-}}{m_{\rm e}c^2}\left(\frac{\hbar/m_{\rm e}c}{r_{\rm h}}\right)^3\right]^{1/4}, \quad (1)$$

where α is the usual fine structure constant, $\hbar$ and c the Planck constant and the speed of light, and $m_{\rm e}$ the mass of the electron. The lower limit of $E_{\rm tot}^{\rm e^\pm}$ coincides with $E_{\rm iso}$. The condition of thermal equilibrium assumed in this model as shown by Aksenov et al. (2007), differentiates this approach from the alternative ones (e.g. the one by Cavallo & Rees 1978), see Sect. 3.2.

In the fireball model, the prompt emission, including the sharp luminosity variations (Ramirez-Ruiz & Fenimore 2000) are caused by the prolonged and variable activity of the "inner engine" (Rees & Meszaros 1994; Piran 2005). The conversion of the fireball energy to radiation originates in shocks, either internal (when faster moving matter takes over a slower moving shell, Rees & Meszaros see 1994) or external (when the moving matter is slowed down by the external medium surrounding the burst, see Rees & Meszaros 1992). Much attention has been given to the synchrotron emission from relativistic electrons, possibly accompanied by SSC emission to explain the observed GRB spectrum. These processes were found to be consistent with the observational data of many GRBs (Tavani 1996; Frontera et al. 2000). However, several limitations have been reported in relation with the low-energy spectral slopes of time-integrated spectra (Crider et al. 1997; Preece et al. 2002; Ghirlanda et al. 2002, 2003; Daigne et al. 2009) and time-resolved spectra (Ghirlanda et al. 2003). Additional limitations on SSC have also been pointed out by Kumar & McMahon (2008a) and Piran et al. (2009).

The latest phases of the afterglow are described in the fireball model by assuming an equation of motion given by the Blandford-McKee self-similar power-law solution (Blandford & McKee 1976). The maximum Lorentz factor of the fireball is estimated from the temporal occurrence of the peak of the

Table 1. Time-resolved spectral analysis of GRB 090618.

Time interval	α	β	$E_0^{\rm BAND}$ (keV)	$\tilde{\chi}^2_{\rm BAND}$	γ	$E_0^{\rm cut}$ (keV)	$\tilde{\chi}^2_{\rm cut}$
0–50	$-0.77^{+0.38}_{-0.28}$	$-2.33^{+0.33}_{-0.28}$	$128.12^{+109.4}_{-56.2}$	1.11	$0.91^{+0.18}_{-0.21}$	$180.9^{+93.1}_{-54.2}$	1.13
50–57	$-0.93^{+0.48}_{-0.37}$	-2.30 ± 0.10	$104.98^{+142.3}_{-51.7}$	1.22	$1.11^{+0.25}_{-0.30}$	$168.3^{+158.6}_{-70.2}$	1.22
57–68	$-0.93^{+0.09}_{-0.08}$	$-2.43^{+0.21}_{-0.67}$	$264.0^{+75.8}_{-54.4}$	1.85	$1.01^{+0.06}_{-0.06}$	$340.5^{+56.0}_{-45.4}$	1.93
68–76	$-1.05^{+0.08}_{-0.07}$	$-2.49^{+0.21}_{-0.49}$	$243.9^{+57.1}_{-53.0}$	1.88	$1.12^{+0.04}_{-0.04}$	$311.0^{+38.6}_{-32.9}$	1.90
76–103	$-1.06^{+0.08}_{-0.08}$	$-2.65^{+0.19}_{-0.34}$	$125.7^{+23.27}_{-19.26}$	1.23	$1.15^{+0.06}_{-0.06}$	$157.7^{+22.2}_{-18.6}$	1.39
103–150	$-1.50^{+0.20}_{-0.18}$	-2.30 ± 0.10	$101.1^{+58.3}_{-30.5}$	1.07	$1.50^{+0.18}_{-0.20}$	$102.8^{+56.8}_{-30.4}$	1.06

Notes. We considered six time intervals, each one corresponding to a particular emission feature in the light curve. We fitted the GBM (8 keV–10 MeV) observed emission with a Band model (Band et al. 1993) and a power-law function with an exponential cut-off. In Cols. 2–4 we list the Band model low-energy index α, the high-energy β and the break energy $E_0^{\rm BAND}$, with the reduced chi-square value in the 6th column. In the last three columns are listed the power-law index γ, the cut-off energy $E_0^{\rm cut}$ and the reduced chi-square value respectively, as obtained from the spectral fit with the cut-off power-law spectral function.

optical emission, which is identified with the peak of the forward external shock emission (Molinari et al. 2007; Rykoff et al. 2009) in the thin shell approximation (Sari & Piran 1999). Several partly alternative and/or complementary scenarios have been developed to the fireball model, e.g. based on quasi-thermal Comptonization (Ghisellini & Celotti 1999), Compton drag emission (Zdziarski et al. 1991; Shemi 1994), synchrotron emission from a decaying magnetic field (Pe'er & Zhang 2006), jitter radiation (Medvedev 2000), Compton scattering of synchrotron self-absorbed photons (Panaitescu & Mészáros 2000; Stern & Poutanen 2004), photospheric emission (Eichler & Levinson 2000; Mészáros & Rees 2000; Mészáros 2002; Daigne & Mochkovitch 2002; Giannios 2006; Ryde & Pe'er 2009; Lazzati & Begelman 2010). In particular, Ryde & Pe'er (2009) pointed out that the photospheric emission overcomes some of the difficulties of pure non-thermal emission models.

3.2. The fireshell scenario

In the fireshell model, the rate equation for the e^+e^- pairs and its dynamics have been given by Ruffini et al. (2000) (the pair-electromagnetic pulse or PEM pulse for short). This plasma engulfs the baryonic material left over in the process of gravitational collapse having mass M_B, still keeping thermal equilibrium between electrons, positrons, and baryons. The baryon load is measured by the dimensionless parameter $B = M_B c^2/E_{\rm tot}^{e^+e^-}$. It was shown (Ruffini 1999) that no relativistic expansion of the plasma can be found for $B > 10^{-2}$. The fireshell is still optically thick and self-accelerates to ultrarelativistic velocities (the pair-electromagnetic-baryonic pulse or PEMB pulse for short, Ruffini 1999). Then the fireshell becomes transparent and the proper – GRB (P-GRB) is emitted (Ruffini et al. 2001a). The final Lorentz gamma factor at transparency can vary in a vast range between 10^2 and 10^3 as a function of $E_{\rm tot}^{e^+e^-}$ and B, see Fig. 3. For the final determination it is necessary to explicitly integrate the rate equation of the e^+e^- annihilation process and evaluate, for a given black hole mass and a given e^+e^- plasma radius, the reaching of the transparency condition, Ruffini et al. (2000), see Fig. 4.

The fireshell scenario does not require any prolonged activity of the inner engine. After transparency, the remaining accelerated baryonic matter still expands ballistically and starts to slow down by the collisions with the CBM, having average density $n_{\rm cbm}$. In the standard fireball scenario (Meszaros 2006), the spiky light curve is assumed to be caused by internal shocks. In the fireshell model the entire extended-afterglow emission is assumed to originate from an expanding thin shell, which enforces energy and momentum conservation in the collision with the CBM. The condition of a fully radiative regime is assumed (Ruffini et al. 2001a). This, in turn, allows one to estimate the characteristic inhomogeneities of the CBM, as well as its average value.

It is appropriate to recall another difference between our treatment and those in the current literature. The complete analytic solution of the equations of motion of the baryonic shell has been developed (Bianco & Ruffini 2004, 2005b), while in the current literature usually the Blandford-McKee (Blandford & McKee 1976) self-similar solution has been uncritically adopted (e.g. Meszaros et al. 1993; Sari 1997, 1998; Waxman 1997; Rees & Meszaros 1998; Granot et al. 1999; Panaitescu & Meszaros 1998; Gruzinov & Waxman 1999; van Paradijs et al. 2000; Mészáros 2002). The analogies and differences between the two approaches have been explicitly pointed out in Bianco & Ruffini (2005a).

From this general approach, a canonical GRB bolometric light curve composed of two different parts is defined: the P-GRB and the extended afterglow. The relative energetics of these two components, the observed temporal separation between the corresponding peaks, is a function of the above three parameters $E_{\rm tot}^{e^+e^-}$, B, and the average value of the $n_{\rm cbm}$; the first two parameters are inherent to the accelerator characterizing the GRB, i.e., the optically thick phase, while the third one is inherent to the GRB surrounding environment, which gives rise to the extended-afterglow. Regarding the observational properties of this model of a relativistic expanding shell, a crucial concept has been the introduction of the EQTS. In this topic, also, our model differs from those in the literature for deriving the analytic expression of the EQTS from the analytic solutions of the equations of motion (Bianco & Ruffini 2005a).

We assumed $E_{\rm tot}^{e^+e^-} = E_{\rm iso}$. This assumption is based on the very accurate information we have on the luminosity and the spectral properties of the source. In other GRBs, we have assumed $E_{\rm tot}^{e^+e^-} > E_{\rm iso}$ to take into account the observational limitations, owing to detector thresholds, distance effects, and lack of data.

3.3. The emission of the P-GRB

The lower limit of $E_{\rm tot}^{e^+e^-}$ is given by the observed isotropic energy emitted in the GRB, $E_{\rm iso}$. The identification of the energy

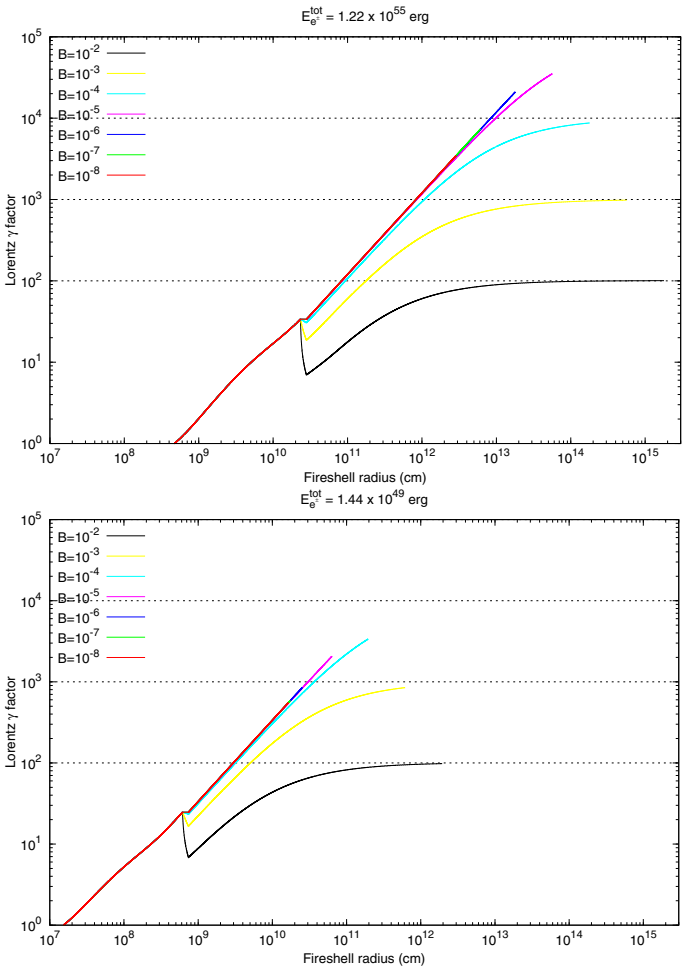

Fig. 3. Evolution of the Lorentz Γ factor until the transparency emission for a GRB of a fixed $E_{\rm tot}^{\rm e^+e^-} = 1.22 \times 10^{55}$ (*upper panel*), and $E_{\rm tot}^{\rm e^+e^-} = 1.44 \times 10^{49}$, for different values of the baryon load B. This computation refers to a mass of the black hole of 10 $M_\odot$ and a $\tau = \int_R {\rm d}r(n_{\rm e^\pm} + n_{\rm e^-}^b)\sigma_{\rm T} = 0.67$, where $\sigma_{\rm T}$ is the Thomson cross-section and the integration is over the thickness of the fireshell (Ruffini 1999).

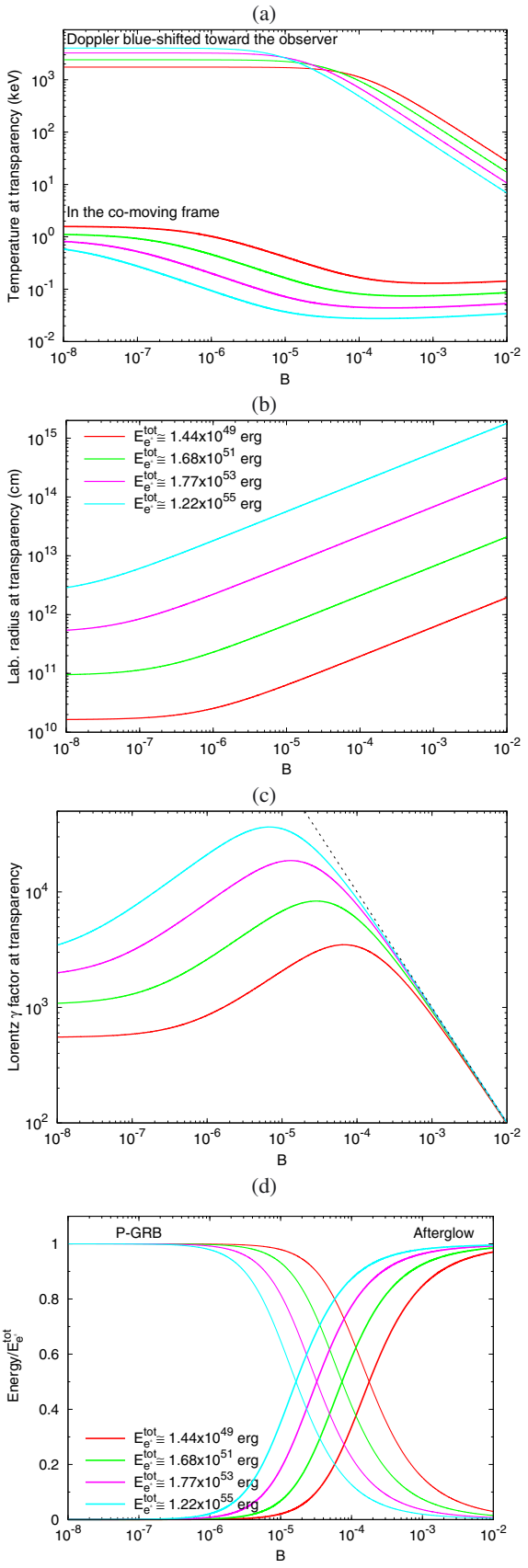

Fig. 4. Fireshell temperature in the comoving and observer frame and the laboratory radius at the transparency emission (panels **a)** and **b)**), the Lorentz Γ factor at the transparency (panel **c)**) and the energy radiated in the P-GRB and in the afterglow in units of $E_{\rm tot}^{\rm e^+e^-}$ (panel **d)**) as a function of the baryon load B for four different values of $E_{\rm tot}^{\rm e^+e^-}$.

of the afterglow and of the P-GRB determines the baryon load B and, from these, it is possible to determine the value of the Lorentz Γ factor at transparency, the observed temperature as well as the temperature in the comoving frame and the laboratory radius at transparency, see Fig. 4. We can indeed determine from the spectral analysis of the P-GRB candidate the temperature $kT_{\rm obs}$ and the energy emitted in the transparency $E_{\rm PGRB}$. The relation between these parameters cannot be expressed by an analytical formulation: they can be only obtained by a numerical integration of the entire fireshell equations of motion. In practice we need to perform a trial-and-error procedure to find the set of values that fits the observations.

As we will see in the case of GRB 090618, the direct measure of the temperature of the thermal component at the transparency offers a very important new information on the determination of the GRB parameters. In the emission of the P-GRB two different phases are present: one corresponding to the emission of the photons when the transparency is reached, and the second is the early interaction of the ultra-relativistic protons and electrons with the CBM. A spectral energy distribution with a thermal component and a non-thermal one should be expected to occur.

3.4. The extended afterglow

The majority of works in the current literature has addressed the analysis of the afterglow emission as due to various combinations of synchrotron and inverse Compton processes, see e.g. Piran (2005). It appears, however, that this description is not fully satisfactory (see e.g. Ghirlanda et al. 2003; Kumar & McMahon 2008b; Piran et al. 2009).

We adopted in the fireshell model a pragmatic approach by making full use of the knowledge of the equations of motion, of the EQTS formulations (Bianco & Ruffini 2005b) and of the correct relativistic transformations between the comoving frame of the fireshell and the observer frame. These equations, which relate the four time variables, are necessary for interpreting the GRB data. They are: a) the comoving time, b) the laboratory time, c) the arrival time, and d) the arrival time at the detector corrected for cosmological effects. This is the content of the relative space-time transformations paradigm, essential for the interpretation of GRBs data (Ruffini et al. 2001b). This paradigm required a global, instead of a piecewise, description of the GRB phenomenon (Ruffini et al. 2001b). This global description led to a new interpretation of the burst structure paradigm (Ruffini et al. 2001a). As recalled in the introduction, a new conclusion, arising from the burst structure paradigm, has been that the emission by the accelerated baryons interacting with the CBM is indeed occurring already in the prompt emission phase, just after the P-GRB emission. This is the extended-afterglow emission, which presents in its "light curve" a rising part, a peak, and a decaying tail. Following this paradigm, the prompt emission phase consists therefore of the P-GRB emission and the peak of the extended afterglow.

To evaluate the extended-afterglow spectral properties, we adopted an ansatz on the spectral properties of the emission in the collisions between the baryons and the CBM in the comoving frame. We then evaluated all observational properties in the observer frame by integrating on the EQTS. The initial ansatz of thermal spectrum (Ruffini et al. 2001a), has recently been modified to

$$\frac{\mathrm{d}N_\gamma}{\mathrm{d}V\mathrm{d}\epsilon} = \left(\frac{8\pi}{h^3c^3}\right)\left(\frac{\epsilon}{k_BT}\right)^{\alpha}\frac{\epsilon^2}{\exp\left(\frac{\epsilon}{k_BT}\right)-1}, \tag{2}$$

where α is a phenomenological parameter defined in the comoving frame of the fireshell (Patricelli et al. 2011), determined by the optimization of the simulation of the observed data. It is well known that in the ultrarelativistic collision of protons and electrons with the CBM, collective processes of ultrarelativistic plasma physics are expected, which are not yet fully explored and understood (e.g. Weibel instability, Medvedev & Loeb see 1999). Promising results along this line have already been obtained by Spitkovsky (2008) and Medvedev & Spitkovsky (2009), and may lead to the understanding of the physycal origin of the α parameter in Eq. (2).

To take into due account the filamentary, clumpy and porous structure of the CBM, we introduced the additional parameter $\mathcal{R}$, which describes the fireshell surface filling factor. It is defined as the ratio between the effective emitting area of the fireshell $A_{\rm eff}$ and its total visible area $A_{\rm vis}$ (Ruffini et al. 2002, 2005).

One of the main features of the GRB afterglow has been the observation of hard-to-soft spectral variation, which is generally absent in the first spike-like emission, which we have identified as the P-GRB, Bernardini et al. (2007); Caito et al. (2009, 2010); de Barros et al. (2011). An explanation of the hard-to-soft spectral variation has been advanced on the grounds of two different contributions: the curvature effect and the intrinsic spectral evolution. In particular, in the work of Peng et al. (2011) the authors used the model developed in Qin (2002) for the spectral lag analysis, taking into account an intrinsic Band model for the GRBs and a Gaussian profile for the GRB pulses to take into account the angular effects, and they found that both causes provide a very good explanation for the observed time lags. Within the fireshell model we can indeed explain a hard-to-soft spectral variation very naturally, in the extended-afterglow emission. Since the Lorentz Γ factor decreases with time, the observed effective temperature of the fireshell will drop as the emission goes on, consequently the peak of the emission will occur at lower energies. This effect is amplified by the curvature effect, which originates in the EQTS concept. Both these observed features are considered as responsible for the time lag observed in GRBs.

3.5. The simulation of a GRB light curve and spectra of the extended afterglow

The simulation of a GRB light curve and the respective spectrum also requires the determination of the filling factor $\mathcal{R}$ and of the CBM density $n_{\rm CBM}$. These extra parameters are extrinsic and they are just functions of the radial coordinate from the source. The parameter $\mathcal{R}$, in particular, determines the effective temperature in the comoving frame and the corresponding peak energy of the spectrum, while $n_{\rm cbm}$ determines the temporal behavior of the light curve. It is found that the CBM is typically formed of "clumps" of width $\sim 10^{15-16}$ cm and average density contrast $10^{-1} \lesssim \langle \delta n/n \rangle \lesssim 10$ centered on the value of four particles/cm^3, see Fig. 10, and clumps of masses $M_{\rm clump} \approx 10^{22-24}$ g. Particularly important is the determination of the average value of $n_{\rm cbm}$. Values on the order of 0.1−10 particles/cm^3 have been found for GRBs exploding inside star-forming region galaxies, while values on the order of 10^{-3} particles/cm^3 have been found for GRBs exploding in galactic halos (Bernardini et al. 2007; Caito et al. 2009; de Barros et al. 2011). This clumpy medium, already predicted in pioneering works of *Fermi* in the theoretical study of interstellar matter in our galaxy (Fermi 1949, 1954), is by now well-established both from the GRB observations and by additional astrophysical observations, see e.g. the circum-burst medium observed in novae (Shara et al. 1997), or by theoretical considerations on supergiant, massive stars, clumpy wind (Ducci et al. 2009). Interesting are the considerations by Arnett and Meakin (Arnett & Meakin 2011), who have shown how realistic 2D simulations of the late evolution of a core collapse show processes of violent emission of clouds: there the 2D simulations differ from those in 1D, which show a much more regular and wind behavior around the collapsing core. Consequently, attention should be given also to instabilities prior to the latest phases of the evolution of the core, possibly giving rise to the cloud pattern observed in the CBM of GRB phenomenon (Arnett, priv. comm.).

The determination of the $\mathcal{R}$ and $n_{\rm CBM}$ parameters depends essentially on the reproduction of the shape of the extended-afterglow and of the respective spectral emission, in a fixed energy range. Clearly, the simulation of a source within the fireshell model is much more complex than simply fitting the $N(E)$ spectrum with phenomenological analytic formulas for a finite temporal range of the data. It is a consistent picture, which has to find the best value for the parameters of the source, the P-GRB (Ruffini et al. 2001a), its spectrum, its temporal structure, as well as its energetics. For each spike in the light curve the parameters of the corresponding CBM clumps are computed, taking into account all the thousands of convolutions of

comoving spectra over each EQTS that lead to the observed spectrum (Bianco & Ruffini 2005b,a). It is clear that, since the EQTS encompass emission processes occurring at different comoving times weighted by their Lorentz and Doppler factors, the "fitting" of a single spike is not only a function of the properties of the specific CBM clump but of the entire previous history of the source. Any mistake at any step of the simulation process affects the entire evolution that follows and, conversely, at any step a fit must be made consistently with the entire previous history: because of the non-linearity of the system and the EQTS, any change in the simulation produces observable effects up to a much later time. This leads to an extremely complex procedure by trial and error in the data simulation, in which the variation of the parameters defining the source are increasingly narrowed down, reaching the uniqueness very quickly. Of course, we cannot expect the latest parts of the simulation to be very accurate, since some of the basic hypothesis on the equations of motion, and possible fragmentation of the shell, can affect the procedure.

In particular, the theoretical photon number spectrum to be compared with the observational data is obtained by an averaging procedure of instantaneous spectra. In turn, each instantaneous spectrum is linked to the simulation of the observed multiband light curves in the chosen time interval. Therefore, the simulation of the spectrum and of the observed multiband light curves have to be performed together and have optimized simultaneously.

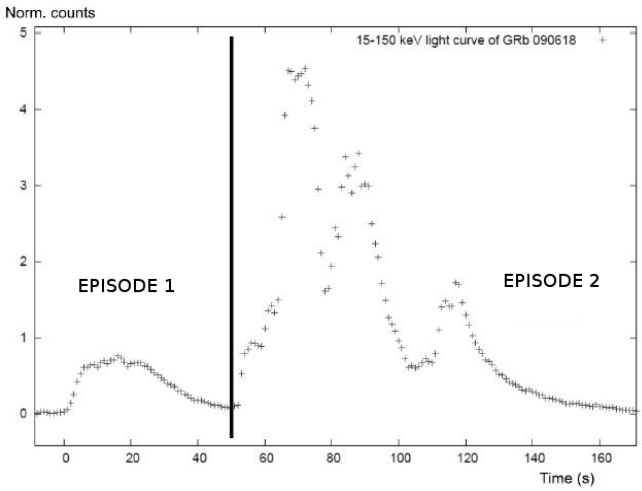

Fig. 5. Two episode nature of GRB 090618.

4. Spectral analysis of GRB 090618

We proceed now to the detailed spectral analysis of GRB 090618. We divide the emission in six time intervals, shown in Table 1, each one identifying a significant feature in the emission process. We then fit for each time interval the spectra by a Band model and a blackbody with an extra power-law component, following Ryde (2004). In particular, we are interested in estimating the temperature kT and the observed energy flux $\phi_{\rm obs}$ of the blackbody component. The specific intensity of emission of a thermal spectrum at energy E in energy range dE into solid angle $\Delta\Omega$ is

$$I(E)\mathrm{d}E = \frac{2}{h^3c^2}\frac{E^3}{\exp(E/kT)-1}\Delta\Omega\mathrm{d}E. \tag{3}$$

The source of radius R is seen within a solid angle $\Delta\Omega = \pi R^2/D^2$, and its full luminosity is $L = 4\pi R^2\sigma T^4$. What we are fitting, however, is the background-subtracted photon spectra $A(E)$, which is obtained by dividing the specific intensity $I(E)$ by the energy E:

$$A(E)\mathrm{d}E \equiv \frac{I(E)}{E}\mathrm{d}E = \frac{k^4L}{2\sigma(kT)^4D^2h^3c^2}\frac{E^2\mathrm{d}E}{\exp(E/kT)-1} = \frac{15\phi_{\rm obs}}{\pi^4(kT)^4}\frac{E^2\mathrm{d}E}{\exp(E/kT)-1}, \tag{4}$$

where h, k and σ are the Planck, the Boltzmann, and the Stefan-Boltzmann constants respectively, c is the speed of light and $\phi_{\rm obs} = L/(4\pi D^2)$ is the observed energy flux of the blackbody emitter. The great advantage of Eq. (4) is that it is written in terms of the observables $\phi_{\rm obs}$ and T, so from a spectral fitting procedure we can obtain the values of these quantities for each time interval considered. To determine these parameters, we must perform an integration of the actual photon spectrum $A(E)$ over the instrumental response $R(i, E)$ of the detector that observes the source, where i denotes the different instrument energy channels. The result is a predicted count spectrum

$$C_p(i) = \int_{E_{\rm min}(i)}^{E_{\rm max}(i)} A(E)R(i,E)\mathrm{d}E, \tag{5}$$

where $E_{\rm min}(i)$ and $E_{\rm max}(i)$ are the boundaries of the ith energy channel of the instrument. Equation (5) must be compared with the observed data by a fit statistic.

The main parameters obtained from the fitting procedure are shown in Table 2. We divide the entire GRB in two main episodes, as advanced in Ruffini et al. (2011): one lasting the first 50 s and the other from 50 to 151 s after the GRB trigger time, see Fig. 5. Clearly, the first 50 s of emission, corresponding to the first episode, are well-fitted by a Band model as well as a blackbody with an extra power-law model, Fig. 6. The same happens for the first 9 s of the second episode (from 50 to 59 s after the trigger time), Fig. 7. For the subsequent three intervals corresponding to the main peaks in the light curve, the blackbody plus a power-law model does not provide a satisfactory fit. Only the Band model fits the spectrum with good accuracy, with the exception of the first main spike (compare the values of χ^2 in the table). We find also that the last peak can be fitted by a simple power-law model with a photon index $\gamma = 2.20 \pm 0.03$, better than by a Band model.

The result of this analysis points to a different emission mechanism in the first 50 s of GRB 090618 and in the following 9 s. A sequence of very strong pulses follows, whose spectral energy distribution is not attributable either to a blackbody or a blackbody and an extra power-law component. The evidence for the transition is well represented by the test of the data fitting, whose indicator is given by the changing of the $\tilde{\chi}^2$ ($N_{\rm d.o.f.} = 169$) for the blackbody plus a power-law model for the different time intervals, see Table 2. Although the Band spectral model is an empirical model without a clear physical origin, we checked its validity in all time-detailed spectra with the sole exception of the first main pulse of the second episode. The χ^2 corresponding to the Band model for this main pulse, although better than that corresponding to the blackbody and power-law case, is unsatisfactory. We now directly apply the fireshell model to make the above conclusions more stringent and reach a better understanding of the source.

Table 2. Time-resolved spectral analysis (8 keV–10 MeV) of the second episode in GRB 090618.

	Time interval (s)	α	β	E_0(keV)	$\tilde{\chi}^2_{\rm BAND}$	kT(keV)	γ	$\tilde{\chi}^2_{\rm BB+po}$
A	0–50	−0.74 ± 0.10	−2.32 ± 0.16	118.99 ± 21.71	1.12	32.07 ± 1.85	1.75 ± 0.04	1.21
B	50–59	−1.07 ± 0.06	−3.18 ± 0.97	195.01 ± 30.94	1.23	31.22 ± 1.49	1.78 ± 0.03	1.52
C	59–69	−0.99 ± 0.02	−2.60 ± 0.09	321.74 ± 14.60	2.09	47.29 ± 0.68	1.67 ± 0.08	7.05
D	69–78	−1.04 ± 0.03	−2.42 ± 0.06	161.53 ± 11.64	1.55	29.29 ± 0.57	1.78 ± 0.01	3.05
E	78–105	−1.06 ± 0.03	−2.62 ± 0.09	124.51 ± 7.93	1.20	24.42 ± 0.43	1.86 ± 0.01	2.28
F	105–151	−2.63 ± −1	−2.06 ± 0.02	unconstrained	1.74	16.24 ± 0.84	2.23 ± 0.05	1.15

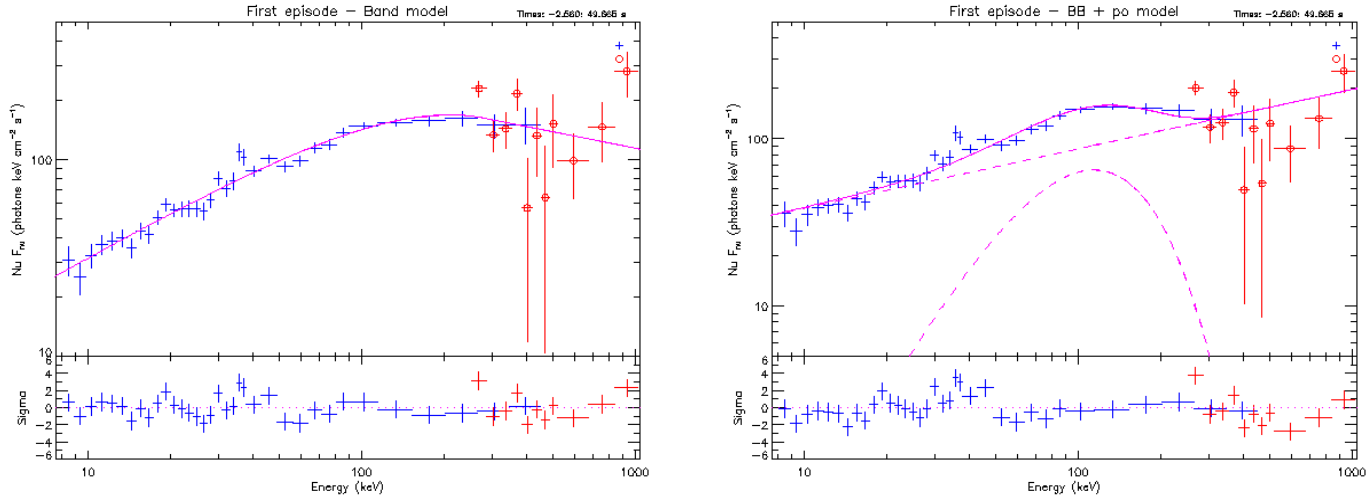

Fig. 6. Time-integrated spectra for the first episode (from 0 to 50 s) of GRB 090618 fitted with the Band, $\tilde{\chi}^2 = 1.12$ (*left*) and blackbody + power-law (*right*) models, $\tilde{\chi}^2 = 1.28$. In the following we will consider the case of a blackbody + power-law model and infer some physical consequences. The corresponding considerations for the Band model are currently being considered and will be published elsewhere.

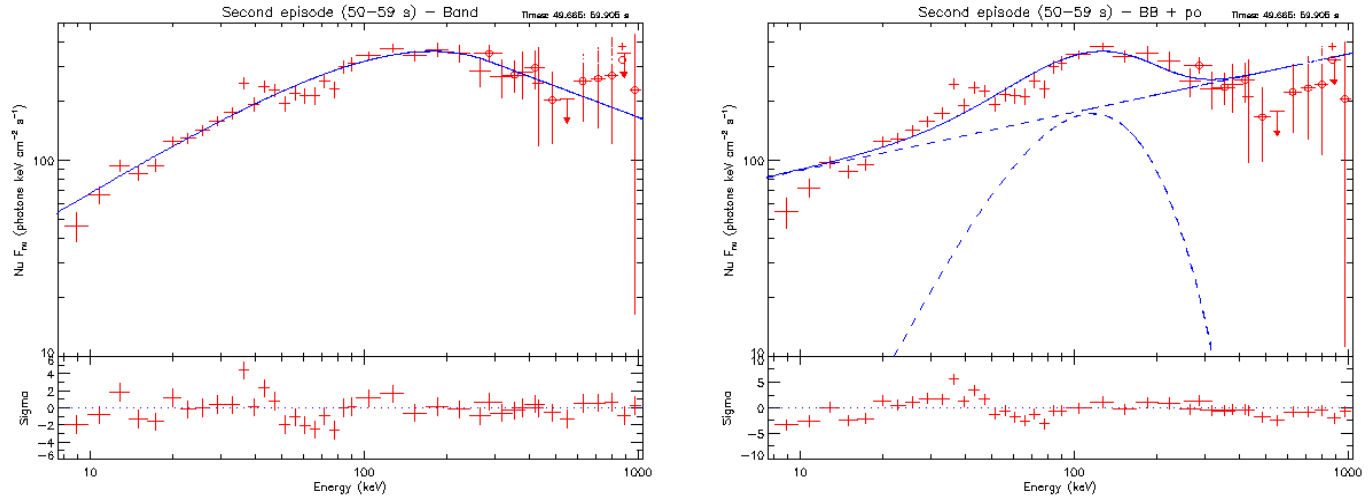

Fig. 7. Time-integrated spectra for the first 9 s of the second episode (from 50 to 59 s after the trigger time) of GRB 090618 fitted with the Band, $\tilde{\chi}^2 = 1.23$ (*left*) and blackbody + power-law (*right*) models, $\tilde{\chi}^2 = 1.52$.

5. Analysis of GRB 090618 in the fireshell scenario: from a single GRB to a multi-component GRB

5.1. Attempt for a single GRB scenario: the role of the first episode

We first approach the analysis of GRB 090618 by assuming that we observe a single GRB and attempt to identify its components in a canonical GRB scenario, based on the fireshell model. We first attempt the identification of the P-GRB emission. We have already seen that the integrated first 50 s can be well-fitted with a blackbody at a temperature $kT = 32.07 \pm 1.85$ keV and an extra power-law component with the photon index $\gamma = -1.75 \pm 0.04$, see panel A in Fig. 7 and Table 2. Because a blackbody component is the distinctive feature of the P-GRB, we first attempted an interpretation of GRB 090618 as a single GRB with the first 50 s as the P-GRB, Ruffini et al. (2010a). We first proceeded to evaluate if the energetics of the emission in the first 50 s can be interpreted as caused by a P-GRB. The energy emitted by the sole blackbody is $E_{\rm BB} = 8.35^{+0.27}_{-0.36} \times 10^{51}$ erg. Recalling that the isotropic energy of the entire GRB 090618 is $E_{\rm iso} = (2.90 \pm 0.02) \times 10^{53}$ erg, this means that the blackbody

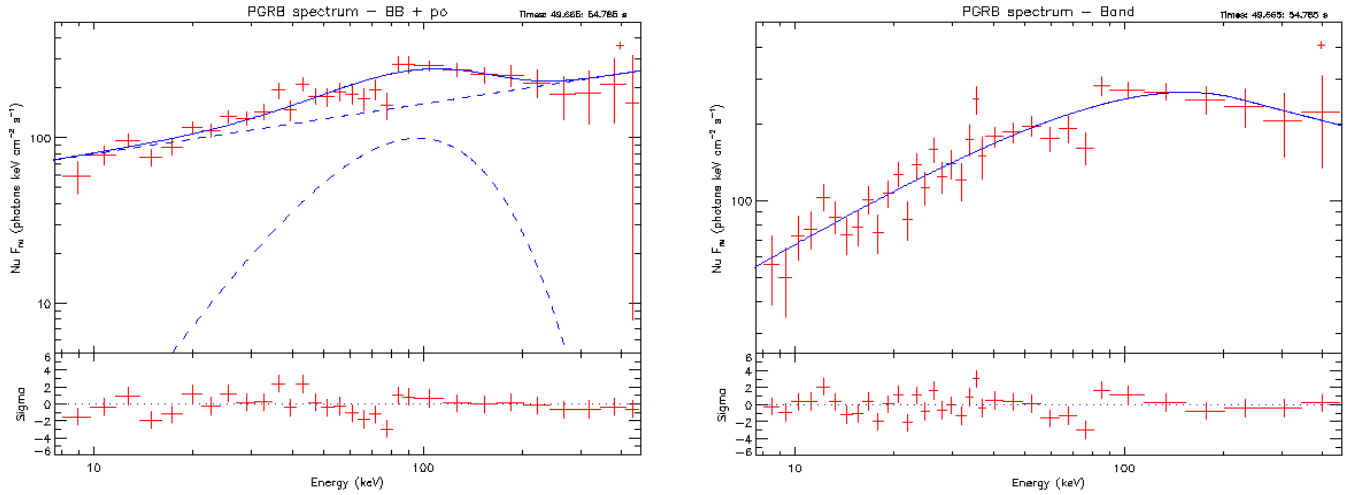

Fig. 8. *Left panel*, the time-integrated spectrum (8–440 keV) for the P-GRB emission episode (from 50 to 54 s after the trigger time) of GRB 090618 fitted with the blackbody + power-law models, $\tilde{\chi}^2 = 1.15$, while the *right panel* shows the fit with a Band model, $\tilde{\chi}^2 = 1.25$.

component would be ∼2.9% of the total energy emitted in the burst. This would imply, see lower panel in Fig. 4, a baryon load $B \sim 10^{-3}$ with a corresponding Lorentz Γ factor of ∼800 and a temperature of ∼52 keV. This value disagrees with the observed temperature $kT_{\rm obs} = 32.07$ keV.

One may attempt to reconcile the value of the theoretically predicted GRB temperature with the observed one by increasing $E_{\rm tot}^{\rm e^+e^-}$. This would lead to an $E_{\rm tot}^{\rm e^+e^-} = 4 \times 10^{54}$ erg and a corresponding baryon load of $B \approx 10^{-4}$. This would imply three major discrepancies: a) there would be an unjustified complementary unobserved energy; b) in view of the value of the baryon load, and the corresponding Lorentz Γ factor, the duration of the extended-afterglow emission would be more than an order of magnitude lower than the observed 100 s (Bianco et al. 2008); c) the duration of the first 50 s is much longer than the one typically expected for all P-GRBs identified in other GRBs (Ruffini et al. 2007), which is at maximum on the order of ∼10 s. We have therefore considered this approach to be hopeless and proceeded to a different one looking for multiple components.

5.2. The multi-component scenario: the second episode as an independent GRB

5.2.1. The identification of the P-GRB of the second episode

We now proceed to the analysis of the data between 50 and 150 s after the trigger time as a canonical GRB in the fireshell scenario, namely the second episode, see Fig. 5 (Ruffini et al. 2011). We proceed to identify the P-GRB within the emission between 50 and 59 s, since we find a blackbody signature in this early second-episode emission. Considerations based on the time variability of the thermal component bring us to consider the first 4 s of this time interval as caused by the P-GRB emission. The corresponding spectrum (8–440 keV) is well fitted ($\tilde{\chi}^2 = 1.15$) with a blackbody of a temperature $kT = 29.22 \pm 2.21$ keV (norm = 3.51 ± 0.49), and an extra power-law component with photon index $\gamma = 1.85 \pm 0.06$, (norm = 46.25 ± 10.21), see Fig. 8. The fit with the Band model is also acceptable ($\tilde{\chi}^2 = 1.25$). The fit gives a low-energy power-law index $\alpha = -1.22 \pm 0.08$, a high-energy index $\beta = -2.32 \pm 0.21$ and a break energy $E_0 = 193.2 \pm 50.8$, see Fig. 8. In view of the theoretical understanding of the thermal component in the P-GRB, see Sect. 3.2, we focus below on the blackbody + power-law spectral model.

The isotropic energy of the second episode is $E_{\rm iso} = (2.49 \pm 0.02) \times 10^{53}$ ergs. The simulation within the fireshell scenario is made assuming $E_{\rm tot}^{\rm e^+e^-} \equiv E_{\rm iso}$. From the upper panel in Fig. 4 and the observed temperature, we can then derive the corresponding value of the baryon load. The observed temperature of the blackbody component is $kT = 29.22 \pm 2.21$, so that we can determine a value of the baryon load of $B = 1.98 \pm 0.15 \times 10^{-3}$, and deduce the energy of the P-GRB as a fraction of the total $E_{\rm tot}^{\rm e^+e^-}$. We therefore obtain a value of the P-GRB energy of $4.33^{+0.25}_{-0.28} \times 10^{51}$ erg.

Now, from the second panel in Fig. 4 we can derive the radius of the transparency condition, to occur at $r_{\rm tr} = 1.46 \times 10^{14}$ cm. From the third panel we derive the bulk Lorentz factor of $\Gamma_{\rm th} = 495$. We compare this value with the energy measured in the sole blackbody component of $E_{\rm BB} = 9.24^{+0.50}_{-0.58} \times 10^{50}$ erg, and with the energy in the blackbody plus the power-law component of $E_{\rm BB+po} = 5.43^{+0.07}_{-0.11} \times 10^{51}$ erg, and verify that the theoretical value is in between these observed energies. We have found this result quite satisfactory: it represents the first attempt to relate the GRB properties to the details of the black hole responsible for the overall GRB energetics. The above theoretical estimates were based on a non rotating black hole of 10 $M_\odot$, a total energy of $E_{\rm tot}^{\rm e^+e^-} = 2.49 \times 10^{53}$ erg and a mean temperature of the initial plasma of e^+e^- of 2.4 MeV, derived from the expression of the dyadosphere radius, Eq. (1). Any refinement of the direct comparison between theory and observations will have to address a variety of fundamental problems such as 1) the possible effect of rotation of the black hole, leading to a more complex dyadotorus structure; 2) a more detailed analysis of the transparency condition of the e^+e^- plasma, simply derived from the condition $\tau = \int_R {\rm d}r(n_{e^\pm} + n_{e^-}^{\rm b})\sigma_{\rm T} = 0.67$ (Ruffini 1999); 3) an analysis of the general relativistic, electrodynamical, strong interactions descriptions of the gravitational collapse core leading to a black hole formation, (Cherubini et al. 2009; Ruffini et al. 2003; Ruffini 1999).

5.2.2. The analysis of the extended afterglow of the second episode

The extended afterglow starts at the above given radius of the transparency, with an initial value of the Lorentz Γ factor of $\Gamma_0 = 495$. To simulate the extended-afterglow emission, we need to determine the radial distribution of the CBM around the burst

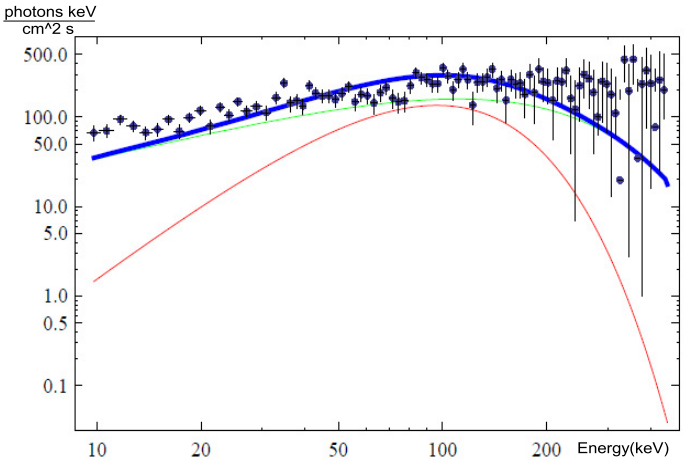

Fig. 9. Fireshell simulation, green line, and the sole blackbody emission, red line, of the time-integrated (t_0 + 50, t_0 + 54 s) spectrum of the P-GRB emission. The sum of the two components, the blue line, is the total simulated emission in the first 4 s of the second episode.

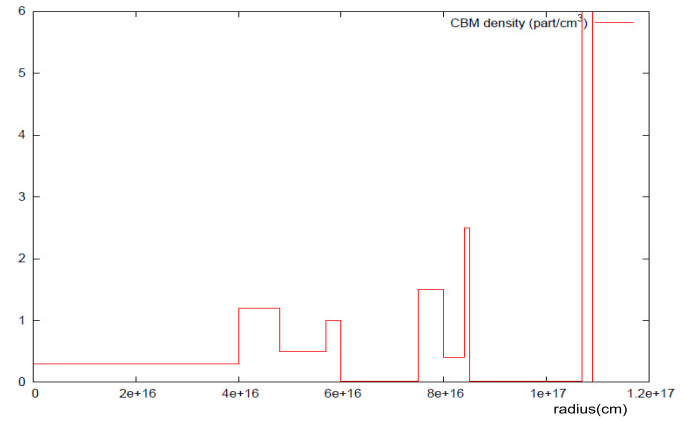

Fig. 10. Radial CBM density distribution for GRB 090618. The characteristic masses of each cloud are on the order of $\sim 10^{22-24}$ g and 10^{16} cm in radii.

site, which we assume for simplicity to be spherically symmetric, we infer a characteristic size of $\Delta R = 10^{15-16}$ cm. We already recalled how the simulation of the spectra and of the observed multi-band light curves have to be performed together and need to be jointly optimized, leading to the determination of the fundamental parameters characterizing the CBM medium (Ruffini et al. 2007). This radial distribution is shown in Fig. 10, and is characterized by a mean value of $\langle n \rangle = 0.6$ part/cm^3 and an average density contrast with a $\langle \delta n/n \rangle \approx 2$, see Fig. 10 and Table 4. The data up to 8.5×10^{16} cm are simulated with a value for the filling factor $\mathcal{R} = 3 \times 10^{-9}$, while the data from this value on with $\mathcal{R} = 9 \times 10^{-9}$. From the radial distribution of the CBM density, and considering the $1/\Gamma$ effect on the fireshell visible area, we found that the CBM clumps causing the spikes in the extended-afterglow emission have masses on the order of 10^{22-24} g. The value of the α parameter was found to be -1.8 along the total duration of the GRB.

In Fig. 11 we show the simulated light curve (8–1000 keV) of the GRB and the corresponding spectrum, using the spectral model described in Bianco & Ruffini (2004) and Patricelli et al. (2011).

We focus our attention on the structure of the first spikes. The comparison between the spectra of the first main spike (t_0 + 59, t_0 + 66 s) of the extended afterglow of GRB 090618, obtained with three different assumptions is shown in Fig. 12: in the upper panel we show the fireshell simulation of the integrated spectrum (t_0 + 59, t_0 + 66 s) of the first main spike, in the middle panel we show the best fit with a blackbody and a power-law component model and in the lower panel the best fit using a simple power-law spectral model.

We can see that the fit with the last two models is not satisfactory: the corresponding $\tilde{\chi}^2$ is 7 for the blackbody + power-law and ∼15 for the simple power-law. We cannot give the $\tilde{\chi}^2$ of the fireshell simulation, since it is not represented by an explicit analytic fitting function, but it originates in a sequence of complex high non-linear procedure, summarized in Sect. 3. It is clear from a direct scrutiny that it correctly reproduces the low-energy emission, thanks in particular to the role of the α parameter, which was described previously. At higher energies, the theoretically predicted spectrum is affected by the cut-off induced by the thermal spectrum. The temporal variability of the first two spikes is well simulated.

We are not able to accurately reproduce the last spikes of the light curve, since the equations of motion of the accelerated baryons become very complicated after the first interactions of the fireshell with the CBM (Ruffini et al. 2007). This happens for different reasons. First, a possible fragmentation of the fireshell can occur (Ruffini et al. 2007). Moreover, at larger distances from the progenitor the fireshell visible area becomes larger than the transverse dimension of a typical blob of matter, consequently a modification of the code for a three-dimensional description of the interstellar medium will be needed. This is unlike the early phases in the prompt emission, which is the main topic we address at the moment, where a spherically symmetric approximation applies. The fireshell visible area is smaller than the typical size of the CBM clouds in the early phases of the prompt radiation (Izzo et al. 2010).

The second episode, lasting from 50 to 151 s, agrees with a canonical GRB in the fireshell scenario. Particularly relevant is the problematic of the P-GRB. It interfaces with the fundamental physics problems, related to the physics of the gravitational collapse and the black hole formation. There is an interface between

Table 3. Final results of the simulation of GRB 090618 in the fireshell scenario.

Parameter	Value
$E_{\rm tot}^{\rm e^+e^-}$	$2.49 \pm 0.02 \times 10^{53}$ erg
B	$1.98 \pm 0.15 \times 10^{-3}$
Γ_0	495 ± 40
$kT_{\rm th}$	29.22 ± 2.21 keV
$E_{\rm P-GRB,th}$	$4.33 \pm 0.28 \times 10^{51}$ erg
$\langle n \rangle$	0.6 part/cm^3
$\langle \delta n \rangle$	2 part/cm^3

Table 4. Physical properties of the three clouds surrounding the burst site.

Cloud	Distance (cm)	r (cm)	ρ (#/cm^3)	M (g)
First	4.0×10^{16}	1×10^{16}	1	2.5×10^{24}
Second	7.4×10^{16}	5×10^{15}	1	3.1×10^{23}
Third	1.1×10^{17}	2×10^{15}	4	2.0×10^{22}

Notes. The table includes the distance from the burst site (2nd column), the radius r of the cloud (3rd column), the particle density ρ (4th column), and the mass M (the last column).

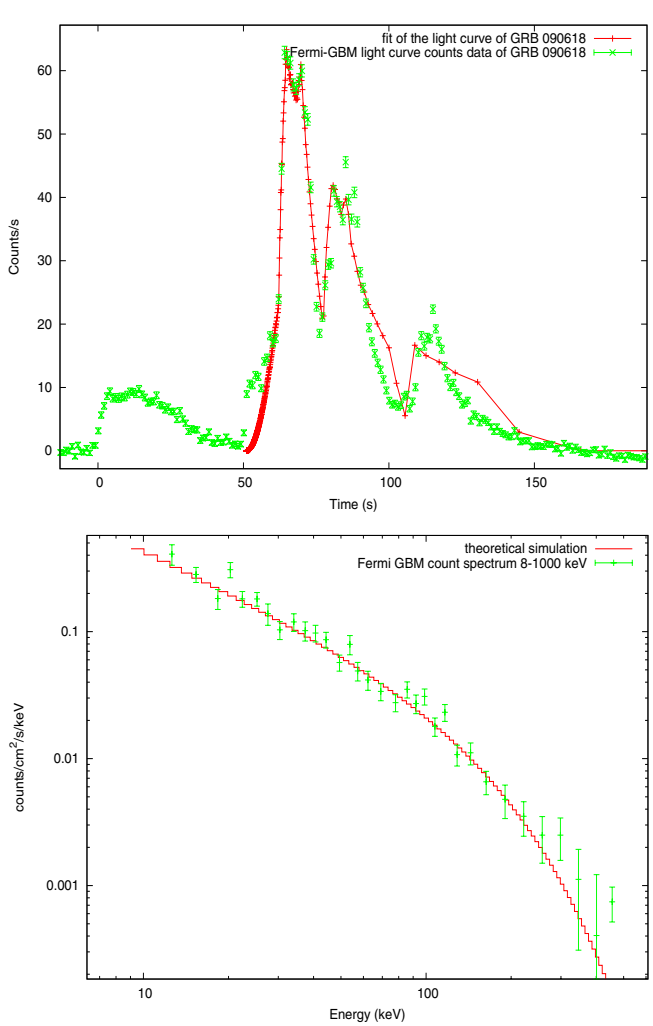

Fig. 11. Simulated light curve and time integrated (t_0 + 58, t_0 + 150 s) spectrum (8–440 keV) of the extended-afterglow of GRB 090618.

the reaching of transparency of the P-GRB and the early part of the extended afterglow. This connection has already been introduced in the literature (Pe'er et al. 2012). We studied this interface in the fireshell by analyzing the thermal emission at the transparency with the early interaction of the baryons with the CBM matter, see Fig. 9.

We now aim to reach a better understanding of the meaning of the first episode, between 0 and 50 s of the GRB emission. To this end we examine the two episodes with respect to 1) the Amati relation; 2) the hardness variation; and 3) the observed time lag.

6. The Amati relation, the HR, and the time lag of the two episodes

6.1. The first episode as an independent GRB?

We first checked if the two episodes separately fulfill the Amati relation, (Amati et al. 2002). By using the Band spectrum we verified that the first episode presents an intrinsic peak energy value of $E_{\rm p,1st}$ = 223.01 ± 24.15 keV, while the second episode presents an $E_{\rm p,2nd}$ = 224.57 ± 17.4 keV. The isotropic energies emitted in each single episode are $E_{\rm iso,1st} = 4.09 \pm 0.07 \times 10^{52}$ erg and $E_{\rm iso,2nd} = 2.49 \pm 0.02 \times 10^{53}$ erg, therefore both episodes satisfy the Amati relation, see Fig. 13. The fulfillment of the Amati

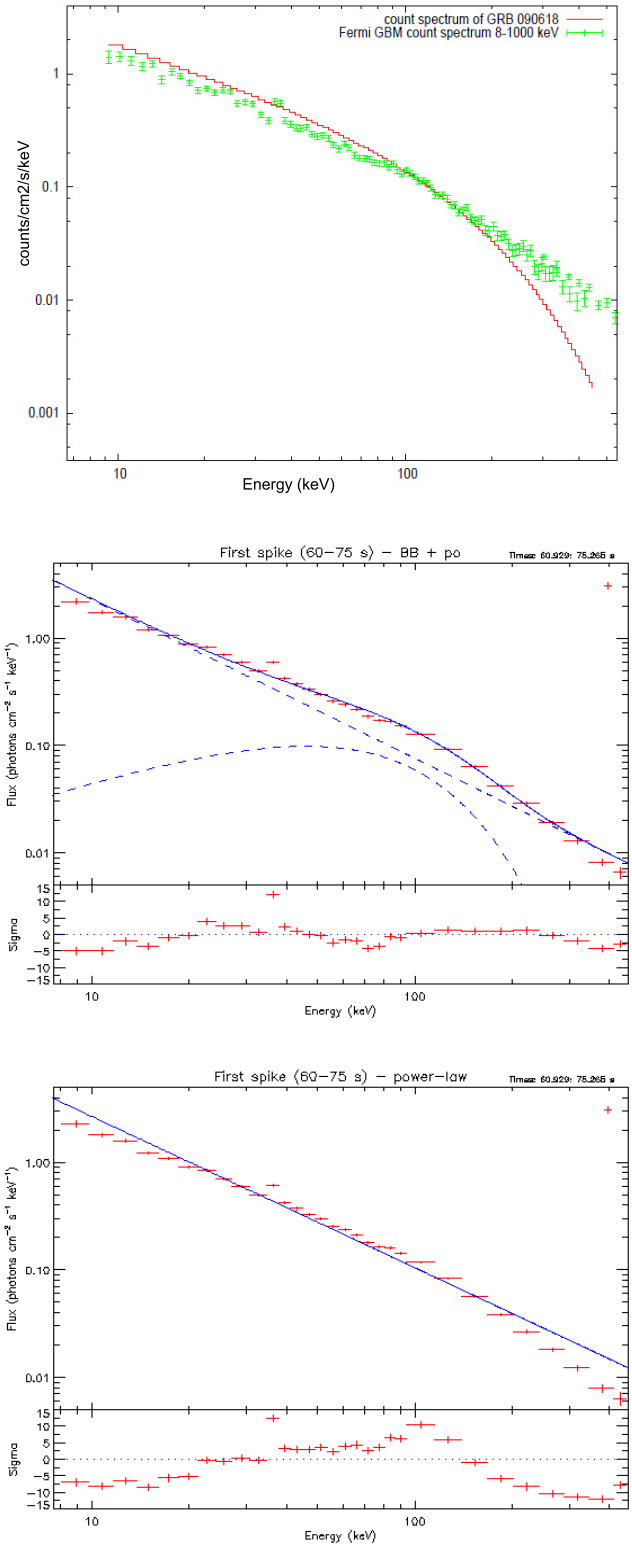

Fig. 12. Simulated time-integrated (t_0 + 58, t_0 + 66 s) count spectrum (8–440 keV) of the extended afterglow of GRB 090618 (*upper panel*), count spectrum (8 keV–10 MeV) of the main pulse emission (t_0 + 58, t_0+66), and best fit with a blackbody + power-law model (*middle panel*) and a simple power-law model (*lower panel*).

relation of episode 2 was expected, because the second episode is a canonical GRB. What we find surprising is the fulfillment of the Amati relation of the first episode.

We first examine episode 1 as a single GRB. We notice a sharp rise in the luminosity in the first 6 s of emission. We

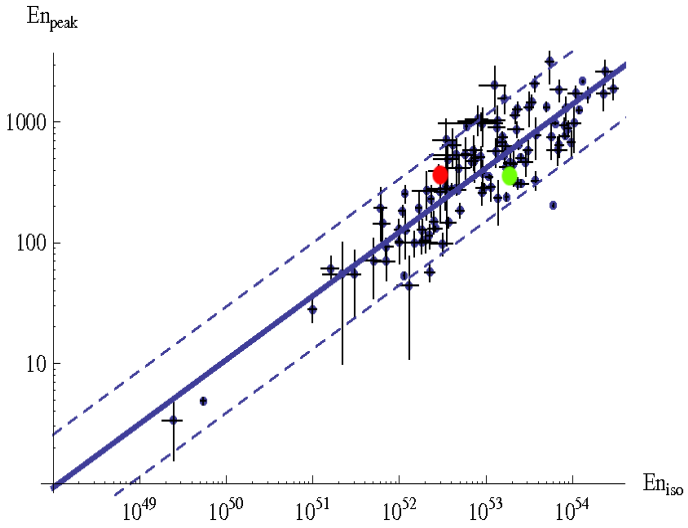

Fig. 13. Position of the first and second component of GRB 090618 in the $E_{\rm p,i}$ – $E_{\rm iso}$ plane with respect to the best fit of the Amati relation, as derived following the procedure described in Capozziello & Izzo (2010). The red circle corresponds to the first emission while the green circle corresponds to the second one.

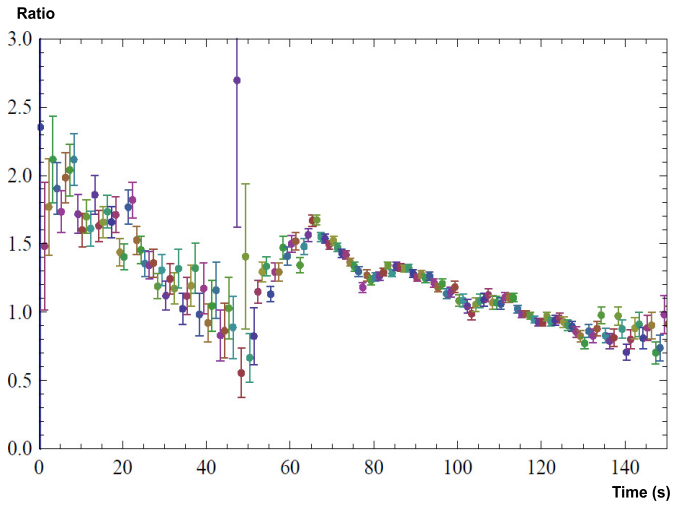

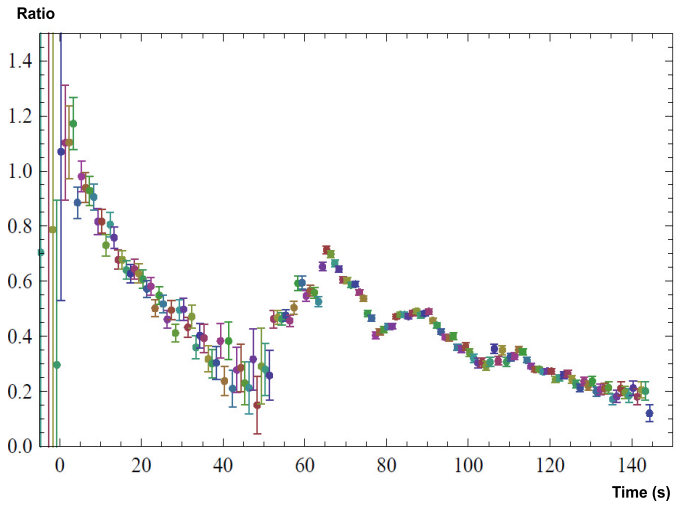

Fig. 14. Hardness-ratio **ratios** for the *Swift* BAT data in two different energy channels: HR1 = cts(25–50 keV)/cts(15–25 keV), HR2 = cts(50–150 keV)/cts(15–50 keV).

therefore attempted a first interpretation by assuming the first 6 s to the P-GRB component of this independent GRB, and the remaining 44 s to be the extended-afterglow of this GRB. A value of the fit gives $E_{\rm tot}^{\rm e^+e^-} = 3.87 \times 10^{52}$ erg and $B = 1.5 \times 10^{-4}$. This would imply a very high value for the Lorentz factor at the transparency of ~5000. In turn, this value would imply (Ruffini 1999) a spectrum of the P-GRB peaking around ~300 keV, which is in contrast with the observed temperature of 58 keV. Alternatively, we attempted a second simulation by assuming all observed data to be part of the extended afterglow of a GRB, with a P-GRB below the detector threshold. Assuming in this case $E_{\rm iso} = E_{\rm tot}^{\rm e^+e^-}$, $B = 10^{-2}$, and assuming for the P-GRB a duration shorter than 10 s, as confirmed from the observations of all existing P-GRBs (Ruffini et al. 2007), we should obtain an energy of the P-GRB greater than 10^{-8} erg/cm^2/s, which should have been easily detectable from *Fermi* and *Swift*. This second possibility is therefore not viable either. We can then generally conclude that we cannot interpret this episode either as a P-GRB of the second episode, as proved in Sect. 3.2 or, as proved here, as a separate GRB. We then conclude that the fulfillment of the Amati relation does not imply that the source is necessarily a GRB.

6.2. The HR variation and the time lag of the two episodes

We finally address another difference between the two episodes, related to the hardness-ratio behavior (HR) and their observed time-lag. The first evidence of an evolution of the GRBs power-law slope indexes with time was observed in the BATSE GRB photon spectra (Crider et al. 1997). In the context of the fireshell scenario, as recalled earlier, the spectral evolution naturally develops from the evolution of the comoving temperature, the decrease of the bulk Lorentz Γ factor, and from the curvature effect (Bianco & Ruffini 2004), with theoretically predicted values, in excellent agreement with observations in past GRBs.

To build the HR ratio, we considered the data from three different instruments: *Swift*-BAT, *Fermi*-GBM and the CORONAS-PHOTON-RT-2. The plots obtained with these instruments confirm the existence of a peculiar trend of the hardness behavior: in the first 50 s it shows a monotonic hard-to-soft behavior, as expected because of the blackbody evolution of the first episode. For the second episode, the following 50 to 151 s of the emission, there is a soft-to-hard trend in the first 4 s of emission, and a hard-to-soft behavior modulated by the spiky emission in the following 100 s. For the HR ratio we considered the ratio of the count rate detected from a higher energy channel to that of a lower energy channel: HR = ctg(HE)/ctg(LE). In particular, we considered the count rate subtracted for the background, although this choice provides poor HR data in the time region dominated by the background, where the count rate can be zero or negative. For the *Swift* data, we considered the HR for two different energy subranges: the HR1 shows the ratio of the (50–150 keV) over the (15–50 keV) emission while the HR2 ratio shows the ratio of the (25–50 keV) over the (15–25 keV) emission, see Fig. 14.

A similar trend was found for the *Fermi*-GBM NaI and RT-2 instruments, see Fig. 15. In particular, the HR data from the *Fermi* observations were assembled the counts observed by the b0 BGO detector in the range (260 keV–40 MeV) and those observed by the n4 NaI detector in the range (8–260 keV). In Fig. 15 we show the HR for the *Fermi* observations, where we rebinned the counts in time intervals of 3 s. From this analysis

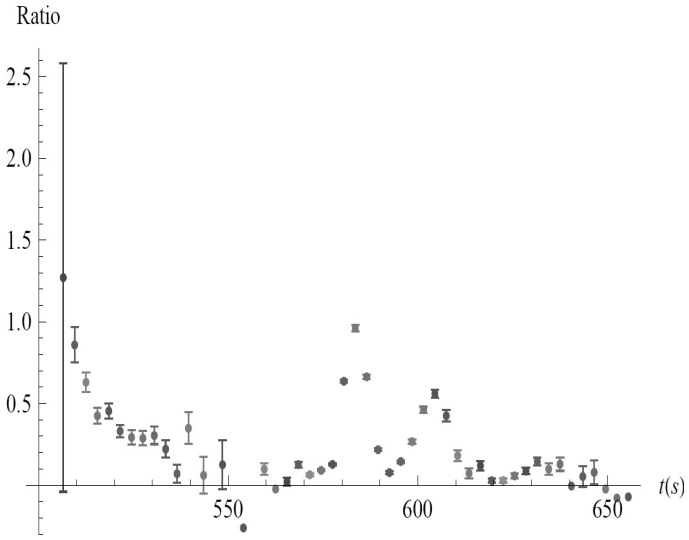

Fig. 15. Hardness-ratio for the *Fermi* data. We considered the cts observed in the (260 keV–40 MeV) energy range over the (8–260 keV) energy range. The time on the x-axis is reported in terms of the mission elapsed time (MET). Several negative data points arise because of noise, in other words the non-presence of GRB emission, in the background-subtracted BGO count light curve.

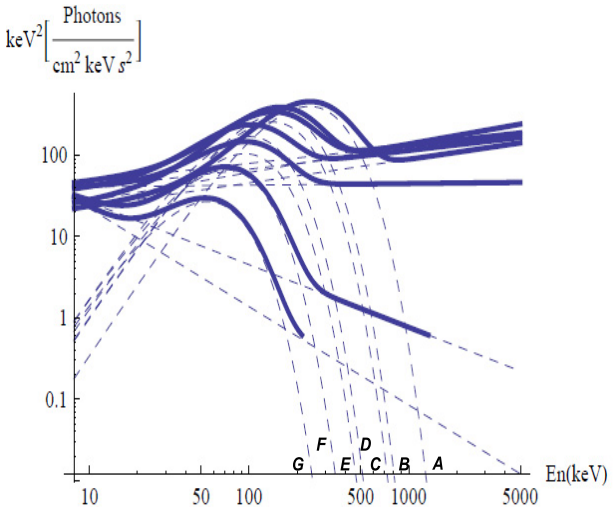

Fig. 16. Evolution of the BB+powerlaw spectral model in the $\nu F(\nu)$ spectrum of the first emission of GRB 090618. It shows the cooling of the blackbody and of the associated non-thermal component with time. We only plot the fitting functions for clarity.

we see that the HR peaks at the beginning of each pulse, also for the second-episode pulses, but each peak of the second-episode pulses is softer than the previous one, suggesting that these pulses are consequential in the second episode and generally agree with the advance of a fireshell in the CBM. Since RT-2 data clearly show both episodes up to 1 MeV, this complements the results obtained by *Swift* (up to 200 keV) and *Fermi* (up to 440 keV) in the high and the most interesting energy range. The hardness-ratio plot of (250–1000 keV)/(8–250 keV) indicates that the first phases of both episodes are the hardest.

Finally, the evident asymmetry of the first episode, supported by the observations of a long time lag in the high- and low-energy channels, see Fig. 2, suggests a different process at work. The first episode softens significantly, as reported in Rao et al. (2011), who observed a long time lag between the 15–25 keV energy range and 100–150 keV: the high-energy photons peak ~7 s before the photons detected in the 15–25 keV energy range. This long time lag is not observed in the second episode, where the lags are on the order of ~1 s.

Motivated by these results, we proceed to a most accurate time-resolved spectral analysis of the first episode to identify its physical and astrophysical origin.

7. A different emission process in the first episode

7.1. The time-resolved spectra and temperature variation

One of the most significant outcomes of the multi-year work of Felix Ryde and his collaborators, (see e.g. Ryde et al. 2010, and references therein), has been the identification and the detailed analysis of the thermal plus power-law features observed in time-limited intervals in selected BATSE GRBs. Similar features have also been observed in the data acquired by the *Fermi* satellite (Ryde et al. 2010; Guiriec et al. 2011). We propose to divide these observations into two broad families. The first family presents a thermal plus power-law(s) feature, with a temperature changing in time following a precise power-law behavior. The second family is also characterized by a thermal plus power-law component, but with the blackbody emission generally varying without a specific power-law behavior and on shorter time scales. It is our goal to study these features within the fireshell scenario to possibly identify the underlying physical processes. We have already showed in Sect. 4 that the emission of the thermal plus power-law component characterizes the P-GRB emission. We have also emphasized that the P-GRB emission is the most relativistic regime occurring in GRBs, uniquely linked to the process of the black hole formation, see Sect. 5. This process appears to belong to the second family considered above. Our aim here is to see if the first episode of GRB 090618 can lead to the identification of the first family of events: those whose temperature changes with time following a power-law behavior on time scales from 1 to 50 s. We have already pointed out in the previous section that the hardness-ratio evolution and the long time lag observed for the first episode (Rao et al. 2011) points to a distinct origin for the first 50 s of emission, corresponding to the first episode.

We made a detailed time-resolved analysis of the first episode, considering different time bin durations to obtain good statistics in the spectra and to take into account the sub-structures in the light curve. We then used two different spectral models to fit the observed data, a classical Band spectrum (Band et al. 1993), and a blackbody with a power-law component.

To obtain more accurate constraints on the spectral parameters, we made a joint fit considering the observations from both the n4 NaI and the b0 BGO detectors, covering a wider energy range in this way, from 8 keV to 40 MeV. To avoid some bias from low-photon statistics, we considered an energy upper limit of the value of 10 MeV. We report in the last three columns of Table 5 the spectral analysis performed in the energy range of the BATSE LAD instrument (20–1900 keV), as analyzed in Ryde & Pe'er (2009) as a comparison tool with the results described in that paper. Our analysis is summarized in Figs. 16, 17, and in Table 5, where we report the residual ratio diagram and the reduced-χ^2 values for the spectral models.

We conclude that both the Band and the proposed blackbody + power-law spectral models fit the observed data very well. Particularly interesting is the clear evolution in the time-resolved spectra, which corresponds to the blackbody and

Table 5. Time-resolved spectral analysis of the first episode in GRB 090618.

Time	α	β	E_0 (keV)	$\tilde{\chi}^2_{\rm BAND}$	kT (keV)	γ	$\tilde{\chi}^2_{\rm BB+po}$	$kT_{\rm LAD}$ (keV)	$\gamma_{\rm LAD}$	$\tilde{\chi}^2_{\rm BB+po,LAD}$
A:0–5	–0.45 ± 0.11	–2.89 ± 0.78	208.9 ± 36.13	0.93	59.86 ± 2.72	1.62 ± 0.07	1.07	52.52 ± 23.63	1.42 ± 0.06	0.93
B:5–10	–0.16 ± 0.17	–2.34 ± 0.18	89.84 ± 17.69	1.14	37.57 ± 1.76	1.56 ± 0.05	1.36	37.39 ± 2.46	1.55 ± 0.06	1.27
C:10–17	–0.74 ± 0.08	–3.36 ± 1.34	149.7 ± 21.1	0.98	34.90 ± 1.63	1.72 ± 0.05	1.20	36.89 ± 2.40	1.75 ± 0.06	1.10
D:17–23	–0.51 ± 0.17	–2.56 ± 0.26	75.57 ± 16.35	1.11	25.47 ± 1.38	1.75 ± 0.06	1.19	25.70 ± 1.76	1.75 ± 0.08	1.19
E:23–31	–0.93 ± 0.13	unconstr.	104.7 ± 21.29	1.08	23.75 ± 1.68	1.93 ± 0.10	1.13	24.45 ± 2.24	1.95 ± 0.12	1.31
F:31–39	–1.27 ± 0.28	–3.20 ± 1.00	113.28 ± 64.7	1.17	18.44 ± 1.46	2.77 ± 0.83	1.10	18.69 ± 1.89	4.69 ± 4.2	1.08
G:39–49	–3.62 ± 1.00	–2.19 ± 0.17	57.48 ± 50.0	1.15	14.03 ± 2.35	3.20 ± 1.38	1.10	14.71 ± 3.52	3.06 ± 3.50	1.09

Notes. We considered seven time intervals and used two spectral models, whose best-fit parameters are shown here. The last three columns, marked with a LAD subscript, report the same analysis but in the energy range 20−1900 keV, which is the same energy range of the BATSE-LAD detector as used in the work of Ryde & Pe'er (2009).

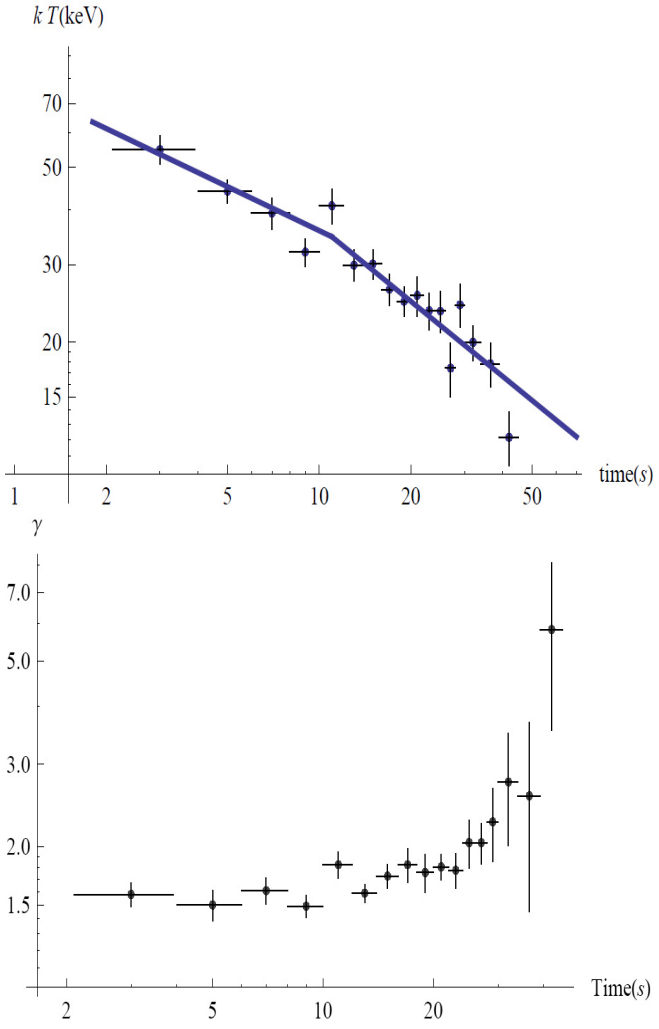

Fig. 17. Evolution of the kT observed temperature of the blackbody component and the corresponding evolution of the power-law photon index. The blue line in the upper panel corresponds to the fit of the time evolution of the temperature with a broken power-law function. It shows a break time $t_{\rm b}$ around 11 s after the trigger time, as obtained from the fitting procedure.

power-law component, see Fig. 16. The kT parameter of the blackbody, in particular, presents a strong decay, with a temporal behavior well-described by a double broken power-law function, see upper panel in Fig. 17. From a fitting procedure we obtain that the best fit (R^2-statistic = 0.992) for the two decay indexes for the temperature variation are $a_{kT} = -0.33 \pm 0.07$ and $b_{kT} = -0.57 \pm 0.11$. In Ryde & Pe'er (2009) an average value for these parameters on a set of 49 GRBs is given: $\langle a_{kT} \rangle = -0.07 \pm 0.19$ and $\langle b_{kT} \rangle = -0.68 \pm 0.24$. We note, however, that in the sample considered in Ryde & Pe'er (2009) only few bursts shows a break time around 10 s, as in our case, see Fig. 17. Two of these bursts present many similarities with our source GRB 090618: GRB 930214 and GRB 990102. These bursts are characterized by a simple FRED pulse, whose total duration is ∼40 s, quite close to the one corresponding to the first episode of GRB 090618. The break time $t_{\rm b}$ in these two bursts are at 12.9 and 8.1 s respectively, while the decay indexes are $a_{kT} = -0.25 \pm 0.02$ and $b_{kT} = -0.78 \pm 0.04$ for GRB 930214 and $a_{kT} = -0.36 \pm 0.03$ and $b_{kT} = -0.64 \pm 0.04$ for GRB 990102, see Table 1 in Ryde & Pe'er (2009), which agrees very well with the values observed for the first episode of GRB 090618. We conclude that the values we observe in GRB 090618 are very close to the values of these two bursts. We return to compare and contrast our results with the other sources considered in Ryde & Pe'er (2009), and GRB 970828 (Pe'er et al. 2007) in a forthcoming publication.

The results presented in Figs. 16, 17, and Table 5, point to a rapid cooling of the thermal emission with time of the first episode. The evolution of the corresponding power-law spectral component also appears to be strictly related to the change of the temperature kT. The power-law γ index falls, or softens, with temperature, see Fig. 16. An interesting feature appears to occur at the transition of the two power-laws describing the observed decrease of the temperature. The long time lag observed in the first episode that we reported in Sect. 6.1 has a clear explanation in the power-law behavior of the temperature and corresponding evolution of the photon index γ, Figs. 16 and 17.

7.2. The radius of the emitting region

We turn now to estimate an additional crucial parameter for the identifying of the nature of the blackbody component: the radius of the emitter $r_{\rm em}$. We have proved that the first episode is not an independent GRB and not part of a GRB. We can therefore provide the estimate of the emitter radius from non-relativistic considerations, just corrected for the cosmological redshift z. We have, in fact, that the temperature of the emitter $T_{\rm em} = T_{\rm obs}(1 + z)$, and that the luminosity of the emitter, due to the blackbody emission, is

$$L = 4\pi r_{\rm em}^2 \sigma T_{\rm em}^4 = 4\pi r_{\rm em}^2 \sigma T_{\rm obs}^4 (1+z)^4, \quad (6)$$

where $r_{\rm em}$ is the emitter radius and σ is the Stefan-Boltzmann constant. From the luminosity distance definition, we also have

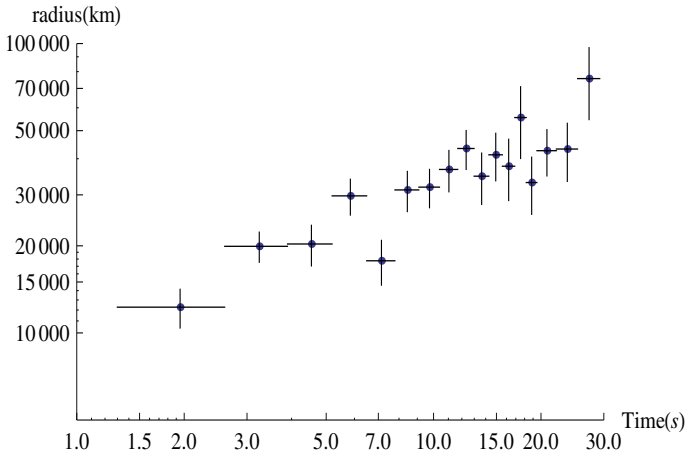

Fig. 18. Evolution of the first episode emitter radius, as given by Eq. (8).

that the observed flux $\phi_{\rm obs}$ is given by

$$\phi_{\rm obs} = \frac{L}{4\pi D^2} = \frac{r_{\rm em}^2 \sigma T_{\rm obs}^4 (1+z)^4}{D^2}. \quad (7)$$

We then obtain

$$r_{\rm em} = \left(\frac{\phi_{\rm obs}}{\sigma T_{\rm ob}^4}\right)^{1/2} \frac{D}{(1+z)^2}. \quad (8)$$

The above radius differs from the radius $r_{\rm ph}$ given in Eq. (1) of Ryde & Pe'er (2009), which was also clearly obtained by interpreting the early evolution of GRB 970828 as belonging to the photospheric emission of a GRB and assuming a relativistic expansion with a Lorentz gamma factor Γ

$$r_{\rm ph} = \hat{\mathcal{R}} D \left(\frac{\Gamma}{(1.06)(1+z)^2}\right), \quad (9)$$

where $\hat{\mathcal{R}} = \left(\phi_{\rm obs}/(\sigma T_{\rm ob}^4)\right)^{1/2}$ and the prefactor 1.06 arises from the dependence of $r_{\rm ph}$ on the angle of sight (Pe'er 2008). Typical values of $r_{\rm ph}$ are at least two orders of magnitude higher than our radius $r_{\rm em}$. We will return to the analysis of GRB 970828 in a forthcoming paper.

Assuming a standard cosmological model ($H_0 = 70\,{\rm km\,s^{-1}\ Mpc^{-1}}$, $\Omega_{\rm m} = 0.27$ and $\Omega_\Lambda = 0.73$) for estimating the luminosity distance D, and using the values for the observed flux $\phi_{\rm obs}$ and the temperature $kT_{\rm obs}$, we give in Fig. 18 the evolution of the surface radius that emits the blackbody $r_{\rm em}$ as a function of time.

Assuming an exponential evolution with time t^δ of the radius in the comoving frame, we obtain the value $\delta = 0.59 \pm 0.11$ from a fitting procedure, which is well compatible with $\delta = 0.5$. We also notice a steeper behavior for the variation of the radius with time corresponding to the first 10 s, which corresponds to the emission before the break of the double power-law behavior of the temperature. We estimate an average velocity of $\bar{v} = 4067 \pm 918\,{\rm km\,s^{-1}}$, $R^2 = 0.91$, in these first 10 s of emission. In episode 1 the observations lead to a core of an initial radius of ~12 000 km expanding in the early phase with a higher initial velocity of ~4000 km s^{-1}. The effective Lorentz Γ factor is very low, $\Gamma - 1 \sim 10^{-5}$.

8. Conclusions

GRB 090618 is one of the closest ($z = 0.54$) and most energetic ($E_{\rm iso} = 2.9 \times 10^{53}$ erg) GRBs up to date. It has been observed simultaneously by the largest number of X and γ ray telescopes: *Fermi*, *Swift*, AGILE, Konus-WIND, *Suzaku*-WAM, and the CORONAS-PHOTON-RT2. These circumstances have produced an unprecedented set of high-quality data as well as the coverage of the instantaneous spectral properties and of the time variability in luminosity of selected bandwidth of the source, see e.g. Figs. 1 and 2. In addition, there is also the possibility of identifying an underlying supernova event from the optical observations in the light curve of well-defined bumps, as well as from the corresponding change in color after about 10 days from the main event (Cano et al. 2011). Unfortunately, a spectroscopic confirmation of this supernova is lacking. We have restricted our attention in this paper to the sole X- and γ-ray emission of the GRB, without addressing the possible supernova component.

By applying our analysis within the fireshell scenario, see Sect. 4, we gained supporting evidence that GRB 090618 is indeed composed of two different episodes (Ruffini et al. 2010a): episode 1, lasting from 0 to 50 s, and episode 2 from 50 s to 151 s after the trigger time. We also illustrated the recent conclusions presented in Ruffini et al. (2011) that episode 1 cannot be a GRB or part of a GRB, see Sect. 5. With a time-resolved spectral analysis we fitted the instantaneous spectra with a blackbody plus an extra power-law component. The temperature of the blackbody appears to have a regular dependence with time, described by two power-law functions: a first power-law with decay index $a_{kT} = -0.33 \pm 0.07$ and the second one with $b_{kT} = -0.57 \pm 0.11$, see Sect. 7. All these features precisely follow some of the results obtained by Felix Ryde and his collaborators (Ryde & Pe'er 2009), who analyzed selected temporal episodes in some GRBs observed by BATSE.

We also examined with particular attention, see Sect. 6, the radius $r_{\rm em}$ of the blackbody emitter observed in the first episode, given by Eq. (8). We interpreted the nature of this episode 1 as originating from what we have defined as a proto-black hole (Ruffini et al. 2010a): the collapsing bare core leading to the black hole formation. Within this interpretation, the radius $r_{\rm em}$ depends only on the observed energy flux of the blackbody component $\phi_{\rm obs}$, the temperature kT and on the luminosity distance of the source D. We obtained a radius of the emitting region that smoothly varies between ~12 000 and 70 000 km, see Fig. 18. Other interpretations associating the origin of this early emission to the GRB main event (Pe'er et al. 2007) lead to a different definition for the radius of the blackbody emitter, which results to be larger than our radius by at least two orders of magnitude. We are planning a systematic search for other systems that present these particular features.

Episode 2 is identified as a canonical long GRB that originates from the black hole formation process and lasts in arrival time from 50 s to 151 s after the trigger time. The good quality of the data allowed us to search for the P-GRB signature in the early emission of the episode 2. From a detailed analysis we find that the first 4 s of episode 2 agree well with the theoretically predicted P-GRB emission, see Sect. 5.2. The observed spectrum integrated over these 4 s is well-fitted by a blackbody with an extra power-law component, where this latter component is mainly due to the early emission of the extended-afterglow, see Fig. 8. From the temperature observed in the P-GRB, $kT_{\rm PGRB} = 29.22 \pm 2.21$, and the $E_{\rm tot}^{\rm e^+e^-}$ energy of the second episode, which we assumed to be equal to the isotropic equivalent energy of this episode, $E_{\rm tot}^{\rm e^+e^-} = 2.49 \times 10^{53}$ erg, we

obtained the value of the baryon load of the GRB, see also Fig. 4, $B = (1.98 \pm 0.15) \times 10^{-3}$, and a consequent Lorentz Γ factor at the transparency of $\Gamma_\circ = 495 \pm 40$. We were able to simulate the temporal and spectral emission of the second episode as seen by the *Fermi*-GBM instrument (8 keV–10 MeV). As we showed in Fig. 12, our simulation succeeds in fitting the light curves as well as the spectral energy distribution emitted in the first main spike of the second episode. The residual emission of the last spikes is reasonably well-fitted, taking into account the difficulties in integrating the equations of motion, which after the first interactions of the fireshell with the CBM become hardly predictable. The energetic of the simulation is fulfilled and we find that the emission is caused by blobs of matter in the CBM with typical dimensions of $r_{\rm bl} = 10^{16}$ cm and average density contrast $\delta n/n \simeq 2$ particles/cm^3 in an overall average density of 1 particle/cm^3. We need to find additional cases of these phenomena to augment our statistics and improve our understanding of it.

Particularly relevant are the first two-dimensional hydrodynamical simulations of the progenitor evolution of a 23 $M_\odot$ star close to core-collapse, leading to a naked core, as shown in the recent work of Arnett and Meakin (Arnett & Meakin 2011). In that work, pronounced asymmetries and strong dynamical interactions between burning shells are seen: the dynamical behavior proceeds to high amplitudes, enlarging deviations from the spherical symmetry in the burning shells. It is highly desirable to find a possible connection between the proto-black-hole concept, introduced in this work, with the Arnett and Meakin results: to compare the radius, the temperature, and the dynamics of the core we found in the present work with the naked core obtained by Arnett and Meakin from the thermonuclear evolution of the progenitor star. Particularly relevant are the strong waves during this phase of collapse, which originate in the mixing of the different elements' shells. These waves should become able to compress, as they propagate inward, but they should also dissipate in non-convective regions, causing heating and slow mixing in these regions of the star. Since the wave heating is faster than radiative diffusion (which is very slow), an expansion phase of the boundary layers will occur, while the iron (Fe) core will contract (Arnett & Meakin 2011). There is also the interesting possibility that the CBM clouds observed in GRBs might be related to the vigorous dynamics in the violent activity of matter ejected in the evolution of the original massive star, well before the formation of the naked core (Arnett, priv. comm.).

It is appropriate to emphasize that these results have no relation with the study of precursors in GRBs performed in the current literature (see e.g. Burlon et al. 2008, and references therein). Episodes 1 and 2 are not temporally separated by a quiescent time. The spectral feature of episodes 1 and 2 are strikingly different and, moreover, episode 1 is very energetic, which is quite unusual for a typical precursor event. We finally conclude that for the first time we witness the process of formation of the black hole from the phases just preceding the gravitational collapse all the way up to the GRB emission.

There is now evidence that the proto black hole formation has been observed also in other GRB sources. After the submission of this article a second example has been found in GRB 101023, and a paper about this source was submitted on 4 November 2011 and was published on 1 February 2012 (Penacchioni et al. 2012). There, extremely novel considerations concerning the structure of the late phase of the emission in X-ray at times longer than 200 s have been presented which favor a standard signature in these sources (see also the considerations made in Page et al. 2011). The possible use of this new family of GRBs as distance indicators is being considered.

Acknowledgements. We thank David Arnett for most fruitful discussions, the participants of the Les Houches workshop "From Nuclei to White Dwarfs and Neutron Stars" held in April 2011 (ed. A. Mezzacappa & R. Ruffini, World Scientific 2011, in press), as well as the members of the AlbaNova University High Energy Astrophysics group. We are thankful to an anonymous referee for her/his important remarks both on the content and the presentation of our work, which have improved the presentation of our paper. L.I. is especially grateful to Marco Muccino for fruitful discussions about the work concerning this manuscript. We are also greateful to the *Swift* and *Fermi* teams for their assistance. One of us, A.V.P., acknowledges the support for the fellowship awarded for the Erasmus Mundus IRAP Ph.D. program. This work made use of data supplied by the UK *Swift* Science Data Centre at the University of Leicester.

References

Aksenov, A. G., Ruffini, R., & Vereshchagin, G. V. 2007, Phys. Rev. Lett., 99, 125003
Amati, L., Frontera, F., Tavani, M., et al. 2002, A&A, 390, 81
Arnaud, K. A. 1996, in Astronomical Data Analysis Software and Systems V, ed. G. H. Jacoby, & J. Barnes, ASP Conf. Ser., 101, 17
Arnett, W. D., & Meakin, C. 2011, ApJ, 733, 78
Atwood, W. B., Abdo, A. A., Ackermann, M., et al. 2009, ApJ, 697, 1071
Band, D., Matteson, J., Ford, L., et al. 1993, ApJ, 413, 281
Baumgartner, W. H., Barthelmy, S. D., Cummings, J. R., et al. 2009, GRB Coordinates Network, 9530, 1
Beardmore, A. P., & Schady, P. 2009, GRB Coordinates Network, 9528, 1
Bernardini, M. G., Bianco, C. L., Caito, L., et al. 2007, A&A, 474, L13
Bianco, C. L., & Ruffini, R. 2004, ApJ, 605, L1
Bianco, C. L., & Ruffini, R. 2005a, ApJ, 633, L13
Bianco, C. L., & Ruffini, R. 2005b, ApJ, 620, L23
Bianco, C. L., Bernardini, M. G., Caito, L., et al. 2008, in AIP Conf. Ser. 1065, ed. Y.-F. Huang, Z.-G. Dai, & B. Zhang, 223
Blandford, R. D., & McKee, C. F. 1976, Phys. Fluids, 19, 1130
Bloom, J. S., Prochaska, J. X., Pooley, D., et al. 2006, ApJ, 638, 354
Burlon, D., Ghirlanda, G., Ghisellini, G., et al. 2008, ApJ, 685, L19
Burrows, D., Hill, J., Nousek, J., et al. 2005, Space Sci. Rev., 120, 165
Caito, L., Bernardini, M. G., Bianco, C. L., et al. 2009, A&A, 498, 501
Caito, L., Amati, L., Bernardini, M. G., et al. 2010, A&A, 521, A80
Cano, Z., Bersier, D., Guidorzi, C., et al. 2011, MNRAS, 413, 669
Capozziello, S., & Izzo, L. 2010, A&A, 519, A73
Cavallo, G., & Rees, M. J. 1978, MNRAS, 183, 359
Cenko, S. B., Perley, D. A., Junkkarinen, V., et al. 2009, GRB Coordinates Network, 9518, 1
Cherubini, C., Geralico, A. J. A. Rueda, H., & Ruffini, R. 2009, Phys. Rev. D, 79, 124002
Costa, E., Frontera, F., Heise, J., et al. 1997, Nature, 387, 783
Crider, A., Liang, E. P., Smith, I. A., et al. 1997, ApJ, 479, L39
Daigne, F., & Mochkovitch, R. 2002, MNRAS, 336, 1271
Daigne, F., Bosnjak, Z., & Dubus, G. 2009 [arXiv:0912.3743]
Damour, T., & Ruffini, R. 1975, Phys. Rev. Lett., 35, 463
de Barros, G., Amati, L., Bernardini, M. G., et al. 2011, A&A, 529, A130
Dezalay, J.-P., Barat, C., Talon, R., et al. 1992, in AIP Conf. Ser. 265, ed. W. S. Paciesas, & G. J. Fishman, 304
Ducci, L., Sidoli, L., Mereghetti, S., Paizis, A., & Romano, P. 2009, MNRAS, 398, 2152
Eichler, D., & Levinson, A. 2000, ApJ, 529, 146
Evans, P. A., Beardmore, A. P., Page, K. L., et al. 2007, A&A, 469, 379
Evans, P. A., Beardmore, A. P., Page, K. L., et al. 2009, MNRAS, 397, 1177
Fermi, E. 1949, Phys. Rev., 75, 1169
Fermi, E. 1954, ApJ, 119, 1
Fishman, G. J., Meegan, C. A., Wilson, R. B., et al. 1994, ApJS, 92, 229
Fong, W., Berger, E., & Fox, D. B. 2010, ApJ, 708, 9
Frontera, F., Amati, L., Costa, E., et al. 2000, ApJS, 127, 59
Gehrels, N., Ramirez-Ruiz, E., & Fox, D. B. 2009, ARA&A, 47, 567
Ghirlanda, G., Celotti, A., & Ghisellini, G. 2002, A&A, 393, 409
Ghirlanda, G., Celotti, A., & Ghisellini, G. 2003, A&A, 406, 879
Ghisellini, G., & Celotti, A. 1999, A&AS, 138, 527
Giannios, D. 2006, A&A, 457, 763
Golenetskii, S., Aptekar, R., Mazets, E., et al. 2009, GRB Coordinates Network, 9553, 1
Goodman, J. 1986, ApJ, 308, L47
Granot, J., Piran, T., & Sari, R. 1999, ApJ, 513, 679
Gruzinov, A., & Waxman, E. 1999, ApJ, 511, 852

Guetta, D., Pian, E., & Waxman, E. 2011, A&A, 525, A53
Guiriec, S., Connaughton, V., Briggs, M. S., et al. 2011, ApJ, 727, L33
Izzo, L., Bernardini, M. G., Bianco, C. L., et al. 2010, JKPS, 57
Kaneko, Y., Preece, R. D., Briggs, M. S., et al. 2006, ApJS, 166, 298
Klebesadel, R. W. 1992, The durations of gamma-ray bursts, ed. C. Ho, R. I. Epstein, & E. E. Fenimore, 161
Klebesadel, R. W., Strong, I. B., & Olson, R. A. 1973, ApJ, 182, L85
Kono, K., Daikyuji, A., Sonoda, E., et al. 2009, GRB Coordinates Network, 9568, 1
Kotov, Y., Kochemasov, A., Kuzin, S., et al. 2008, in COSPAR, Plenary Meeting, 37th COSPAR Scientific Assembly, 37, 1596
Kouveliotou, C., Meegan, C. A., Fishman, G. J., et al. 1993, ApJ, 413, L101
Kumar, P., & McMahon, E. 2008a, MNRAS, 384, 33
Kumar, P., & McMahon, E. 2008b, MNRAS, 384, 33
Lazzati, D., & Begelman, M. C. 2010, ApJ, 725, 1137
Longo, F., Moretti, E., Barbiellini, G., et al. 2009, GRB Coordinates Network, 9524, 1
McBreen, S. 2009, GRB Coordinates Network, 9535, 1
Medvedev, M. V. 2000, ApJ, 540, 704
Medvedev, M. V., & Loeb, A. 1999, ApJ, 526, 697
Medvedev, M. V., & Spitkovsky, A. 2009, ApJ, 700, 956
Meegan, C. A. 1997, NASA STI/Recon Technical Report N, 1, 70758
Meegan, C. A., Fishman, G. J., Wilson, R. B., et al. 1992, Nature, 355, 143
Meegan, C., Lichti, G., Bhat, P. N., et al. 2009, ApJ, 702, 791
Mészáros, P. 2002, ARA&A, 40, 137
Meszaros, P. 2006, Rep. Prog. Phys., 69, 2259
Meszaros, P., & Rees, M. J. 1993, ApJ, 405, 278
Mészáros, P., & Rees, M. J. 2000, ApJ, 530, 292
Meszaros, P., Laguna, P., & Rees, M. J. 1993, ApJ, 415, 181
Molinari, E., Vergani, S. D., Malesani, D., et al. 2007, A&A, 469, L13
Nandi, A., Rao, A. R., Chakrabarti, S. K., et al. 2009 [arXiv:0912.4126]
Nousek, J. A., Kouveliotou, C., Grupe, D., et al. 2006, ApJ, 642, 389
Paciesas, W. S., Meegan, C. A., Pendleton, G. N., et al. 1999, ApJS, 122, 465
Paczynski, B. 1986, ApJ, 308, L43
Page, K. L., Starling, R. L. C., Fitzpatrick, G., et al. 2011, MNRAS, 416, 2078
Panaitescu, A., & Meszaros, P. 1998, ApJ, 493, L31
Panaitescu, A., & Mészáros, P. 2000, ApJ, 544, L17
Patricelli, B., Bernardini, M. G., Bianco, C. L., et al. 2011, Int. J. Mod. Phys. D, 20, 1983
Pe'er, A. 2008, ApJ, 682, 463
Pe'er, A., & Zhang, B. 2006, ApJ, 653, 454
Pe'er, A., Ryde, F., Wijers, R. A. M. J., Mészáros, P., & Rees, M. J. 2007, ApJ, 664, L1
Pe'er, A., Zhang, B.-B., Ryde, F., et al. 2012, MNRAS, 420, 468
Penacchioni, A. V., Ruffini, R., Izzo, L., et al. 2012, A&A, 538, A58
Peng, Z. Y., Yin, Y., Bi, X. W., Bao, Y. Y., & Ma, L. 2011, Astron. Nachr., 332, 92
Piran, T. 1999, Phys. Rep., 314, 575
Piran, T. 2005, Rev. Mod. Phys., 76, 1143
Piran, T., Shemi, A., & Narayan, R. 1993, MNRAS, 263, 861
Piran, T., Sari, R., & Zou, Y. 2009, MNRAS, 393, 1107
Preece, R. D., Briggs, M. S., Giblin, T. W., et al. 2002, ApJ, 581, 1248
Qin, Y.-P. 2002, A&A, 396, 705
Ramirez-Ruiz, E., & Fenimore, E. E. 2000, ApJ, 539, 712
Rao, A. R., Malkar, J. P., Hingar, M. K., et al. 2011, ApJ, 728, 42
Rees, M. J., & Meszaros, P. 1992, MNRAS, 258, 41
Rees, M. J., & Meszaros, P. 1994, ApJ, 430, L93
Rees, M. J., & Meszaros, P. 1998, ApJ, 496, L1
Roming, P., Kennedy, T., Mason, K., et al. 2005, Space Sci. Rev., 120, 95
Ruffini, R. 1999, A&AS, 138, 513
Ruffini, R. J. 2001, Analogies, new paradigms and observational data as growing factors of Relativistic Astrophysics
Ruffini, R. 2011, ArXiv e-prints
Ruffini, R., Salmonson, J. D., Wilson, J. R., & Xue, S. 2000, A&A, 359, 855
Ruffini, R., Bianco, C. L., Fraschetti, F., Xue, S.-S., & Chardonnet, P. 2001a, ApJ, 555, L113
Ruffini, R., Bianco, C. L., Fraschetti, F., Xue, S.-S., & Chardonnet, P. 2001b, ApJ, 555, L107
Ruffini, R., Bianco, C. L., Chardonnet, P., Fraschetti, F., & Xue, S. 2002, ApJ, 581, L19
Ruffini, R., Bianco, C. L., Chardonnet, P., et al. 2003, in Cosmology and Gravitation, ed. M. Novello, & S. E. Perez Bergliaffa, AIP Conf. Ser., 668, 16
Ruffini, R., Bernardini, M. G., Bianco, C. L., et al. 2005, in XIth Brazilian School of Cosmology and Gravitation, ed. M. Novello, & S. E. Perez Bergliaffa, AIP Conf. Ser., 782, 42
Ruffini, R., Bernardini, M. G., Bianco, C. L., et al. 2007, in ESA SP, 622, 561
Ruffini, R., Chakrabarti, S. K., & Izzo, L. 2010a, Adv. Sp. Res., submitted
Ruffini, R., Vereshchagin, G., & Xue, S.-S. 2010b, Phys. Rep., 487, 1
Ruffini, R., Izzo, L., Penacchioni, A. V., et al. 2011, PoS(Texas2010), 101
Ryde, F. 2004, ApJ, 614, 827
Ryde, F., & Pe'er, A. 2009, ApJ, 702, 1211
Ryde, F., Björnsson, C.-I., Kaneko, Y., et al. 2006, ApJ, 652, 1400
Ryde, F., Axelsson, M., Zhang, B. B., et al. 2010, ApJ, 709, L172
Rykoff, E. S., Aharonian, F., Akerlof, C. W., et al. 2009, ApJ, 702, 489
Sakamoto, T., Ukwatta, T. N., & Barthelmy, S. D. 2009, GRB Coordinates Network, 9534, 1
Sari, R. 1997, ApJ, 489, L37
Sari, R. 1998, ApJ, 494, L49
Sari, R., & Piran, T. 1999, ApJ, 520, 641
Sari, R., Piran, T., & Halpern, J. P. 1999, ApJ, 519, L17
Schady, P. 2009, GRB Coordinates Network, 9527, 1
Schady, P., Baumgartner, W. H., Beardmore, A. P., et al. 2009, GRB Coordinates Network, 9512, 1
Schaefer, B. E. 2007, ApJ, 660, 16
Shara, M. M., Zurek, D. R., Williams, R. E., et al. 1997, AJ, 114, 258
Shemi, A. 1994, MNRAS, 269, 1112
Shemi, A., & Piran, T. 1990, ApJ, 365, L55
Spitkovsky, A. 2008, ApJ, 673, L39
Stern, B. E., & Poutanen, J. 2004, MNRAS, 352, L35
Strong, I. B. 1975, in Neutron Stars, Black Holes and Binary X-ray Sources, ed. H. Gursky, & R. Ruffini, Astrophys Space Sci. Lib., 48, 47
Strong, I. B., & Klebesadel, R. W. 1974, Nature, 251, 396
Strong, I. B., Klebesadel, R. W., & Olson, R. A. 1974, ApJ, 188, L1
Tavani, M. 1996, ApJ, 466, 768
Tavani, M. 1998, ApJ, 497, L21
van Paradijs, J., Groot, P. J., Galama, T., et al. 1997, Nature, 386, 686
van Paradijs, J., Kouveliotou, C., & Wijers, R. A. M. J. 2000, ARA&A, 38, 379
Waxman, E. 1997, ApJ, 491, L19
Zdziarski, A. A., Svensson, R., & Paczynski, B. 1991, ApJ, 366, 343
Zhang, B.-B., Zhang, B., Liang, E.-W., et al. 2011, ApJ, 730, 141

A&A 538, A58 (2012)
DOI: 10.1051/0004-6361/201118403

Astronomy & Astrophysics

Evidence for a proto-black hole and a double astrophysical component in GRB 101023

A. V. Penacchioni[1,3], R. Ruffini[1,2,3], L. Izzo[1], M. Muccino[1], C. L. Bianco[1,2], L. Caito[1,2], B. Patricelli[1], and L. Amati[4,2]

[1] Dip. di Fisica, Sapienza Università di Roma and ICRA, Piazzale Aldo Moro 5, 00185 Rome, Italy
e-mail: [ana.penacchioni;ruffini;luca.izzo;marco.muccino;bianco;letizia.caito]@icra.it
[2] ICRANet, Piazzale della Repubblica 10, 65122 Pescara, Italy
e-mail: barbara.patricelli@icranet.org
[3] Université de Nice Sophia Antipolis, Nice, Cedex 2, Grand Chateau Parc Valrose, France
[4] Italian National Institute for Astrophysics (INAF) – IASF Bologna, via P. Gobetti 101, 40129 Bologna, Italy
e-mail: amati@iasfbo.inaf.it

Received 4 November 2011 / Accepted 5 December 2011

ABSTRACT

Context. It has been recently shown that GRB 090618, observed by AGILE, Coronas Photon, *Fermi*, Konus, *Suzaku*, and *Swift*, is composed of two very different components: episode 1, lasting 50 s, shows a thermal plus power-law spectrum with a characteristic temperature evolving in time as a power law; episode 2 (the remaining 100 s) is a canonical long GRB. We have associated episode 1 to the progenitor of a collapsing bare core leading to the formation of a black hole: what was defined as a "proto black hole"
Aims. In precise analogy with GRB 090618 we aim to analyze the 89 s of the emission of GRB 101023, observed by *Fermi*, Gemini, Konus and *Swift*, to see if there are two different episodes: the first one presenting a characteristic black-body temperature evolving in time as a broken power law, and the second one consistent with a canonical GRB.
Methods. To obtain information on the spectra, we analyzed the data provided by the GBM detector onboard the *Fermi* satellite, and we used the heasoft package XSPEC and RMFIT to obtain their spectral distribution. We also used the numerical code GRBsim to simulate the emission in the context of the fireshell scenario for episode 2.
Results. We confirm that the first episode can be well fit by a black body plus power-law spectral model. The temperature changes with time following a broken power law, and the photon index of the power-law component presents a soft-to-hard evolution. We estimate that the radius of this source increases with time with a velocity of 1.5×10^4 km s^{-1}. The second episode appears to be a canonical GRB. By using the Amati and the Atteia relations, we determined the cosmological redshift, $z \sim 0.9 \pm 0.084(stat.) \pm 0.2(sys.)$. The results of GRB 090618 are compared and contrasted with the results of GRB 101023. Particularly striking is the scaling law of the soft X-ray component of the afterglow.
Conclusions. We identify GRB 090618 and GRB 101023 with a new family of GRBs related to a single core collapse and presenting two astrophysical components: a first one related to the proto-black hole prior to the process of gravitational collapse (episode 1), and a second one, which is the canonical GRB (episode 2) emitted during the formation of the black hole. For the first time we are witnessing the process of a black hole formation from the instants preceding the gravitational collapse up to the GRB emission. This analysis indicates progress towards developing a GRB distance indicator based on understanding the P-GRB and the prompt emission, as well as the soft X-ray behavior of the late afterglow.

Key words. black hole physics – gamma-ray burst: individual: GRB 101023

1. Introduction

Discovered at the end of the 60 s (Strong 1975), gamma-ray bursts (GRBs) are extremely intense flashes of hard X-radiation, coming from random directions in the sky at unpredictable times and typically lasting from a fraction of a second up to a few minutes. They are detected by satellites in low Earth orbit at a rate of ∼0.8 events/day. As outlined by breakthrough observations in the last ∼15 years, these phenomena are by far the most energetic sources in the Universe, observed in a range of cosmological redshift $0.0084 \leq z \lesssim 9$ (Salvaterra et al. 2009; Tanvir et al. 2009; Cucchiara et al. 2011), with isotropic equivalent radiated energy $E_{\rm iso}$ in the range 10^{49}–10^{55} erg and a theoretically predicted upper limit to their energies of 10^{55} erg (Ruffini 2011). Since the early observation by BATSE (Meegan et al. 1992), they have been divided into two classes: the short GRBs, with a characteristic duration of $T_{90} < 2$ s, and the long GRBs, with a characteristic $T_{90} > 2$ s (Dezalay et al. 1992; Klebesadel 1992; Kouveliotou et al. 1993).

Analysis of the GRBs within the fireshell model (see e.g. Ruffini et al. 2001, 2009, and references therein) has led to identifying a canonical GRB structure described by two parameters: the total energy $E^{e^\pm}_{\rm tot}$ of the initially optically thick electron-positron plasma and its baryon load $B = M_{\rm B}c^2/E^{e^\pm}_{\rm tot}$. To this information characterizing the source is added the information on the density and filamentary distribution of the circumburst medium (CBM) (Ruffini et al. 2004b, 2005; Patricelli et al. 2010, 2011).

Within this model the structure of a canonical GRB has been identified. It is composed by a proper-GRB (P-GRB), followed by an extended afterglow. The P-GRB originates at the moment of transparency of the relativistically expanding electron-positron plasma. The extended afterglow originates in the collision of the ultra-relativistic baryons with the filamentary

structure of the CBM. The acceleration process of the baryons occurs in the optically thick phase of the self-accelerating electron-positron plasma. This explains the spiky emission observed in the prompt radiation (Ruffini et al. 2002). The average density, the porosity, and the dimensions of the clouds in the CBM are in turn determined (see e.g. Ruffini et al. 2006; Bernardini et al. 2007; Dainotti et al. 2007; Caito et al. 2009).

This model has allowed the nature of long GRBs to be explained and two new classes of short bursts to be introduced. A first class contains the disguised short GRBs (Bernardini et al. 2007; Caito et al. 2009, 2010; De Barros et al. 2011): just long GRBs exploding in low density CBM ($n = 10^{-3}$ part/cm^3), and often referred to as short GRBs in the literature (see e.g. Gehrels et al. 2005). A second class contains the genuine short GRBs, theoretically foreseen in Ruffini et al. (2001) as canonical GRBs occurring in the limit of a very low baryon load, $B < 10^{-5}$. This new class of genuine short GRBs is expected to occur on a much shorter time scale, $T_{90} \leq 10^{-2}$–10^{-3} s.

With the observation of GRB 090618, a novel situation has occurred with respect to the above classification. It had been shown in the pioneering works of Felix Ryde and his collaborators (Ryde 2004) that, in the early emission of selected BATSE sources and also in some *Fermi* sources, a characteristic thermal component is present with temperature changing in time following a broken power law (Ryde 2004, 2005; Ryde & Pe'er 2009). They attempted to interpret this emission within the GRB fireball model (see e.g. Pe'er et al. 2007).

Ruffini et al. (2010a) showed that two very different episodes occur in GRB 090618: episodes 1 and 2. Episode 1 presents an emission "á la Ryde". There it was proposed that such an emission, alternatively to the Ryde interpretation, had to be interpreted as originating in a new kind of source in the late phase of a core collapse. The concept of proto-black hole was introduced there. Episode 2 was shown to be consistent with a canonical GRB.

Details of the data analysis showing the characteristic broken power law temporal variation of the temperature of the thermal component of episode 1 are presented in Izzo et al. (2011). The radius of the emitting region and its time variation have been determined as well, along with the details of the GRB emission of episode 2, including the P-GRB structure, the porosity of the interstellar medium, the baryon load B, and the total energy. Identifying these two components has been made possible by the extraordinary coincidence of three major factors for this GRB: 1) precise determination of the cosmological redshift of this source $z = 0.54$, implying the fortunate occurrence of a very close source with an energy $E_{\rm iso} = 2.7 \times 10^{53}$ erg; 2) joint observations by several X and gamma-ray telescopes; 3) the exceptional dataset on the instantaneous spectral distribution, light curve, and luminosity variation of this source (see Sect. 2).

There is a striking morphological analogy between GRB 101023 and GRB 090618 (see Figs. 2 and 1). Both light curves present a first emission that lasts ~50 s, followed by a spikier structure in the remaining part. We identify the first 45 s of GRB 101023 with episode 1 and the remaining 44 s with episode 2 (a canonical GRB). There is, however, a substantial difference between these two sources. In the present source, GRB 101023, the cosmological redshift is unknown. This has not been a drawback for us but a challenge that probes our understanding of the GRB phenomenon. It is interesting, as a rough estimate, that if one were to assume that the two sources, GRB 101023 and GRB 090618 had not only the same morphology but also the same energy $E_{\rm iso}$, one would infer $z = 1$ for the cosmological redshift of GRB 101023. A main result of this article is that, assuming the validity of the Amati relation (see Amati et al. 2009, and references therein) and Atteia criteria (Atteia 2003), it is possible to theoretically derive an expected cosmological redshift $z = 0.9 \pm 0.084(stat.) \pm 0.2(sys.)$ for episode 2.

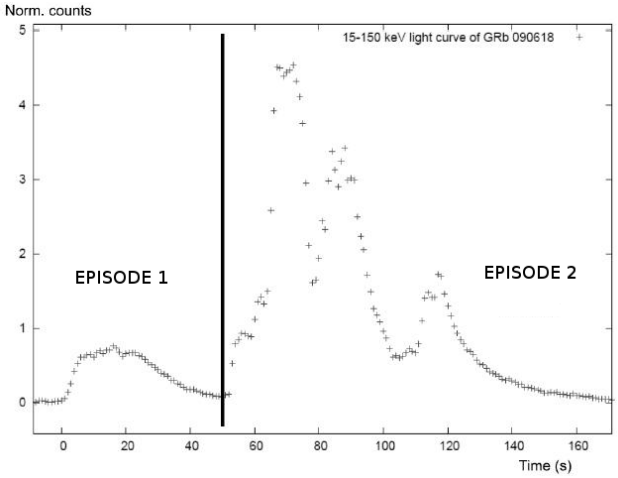

Fig. 1. Count light curve of GRB 090618 obtained from *Fermi* GBM detector, with a bin time of 1 s, and showing two-episode nature of the GRB.

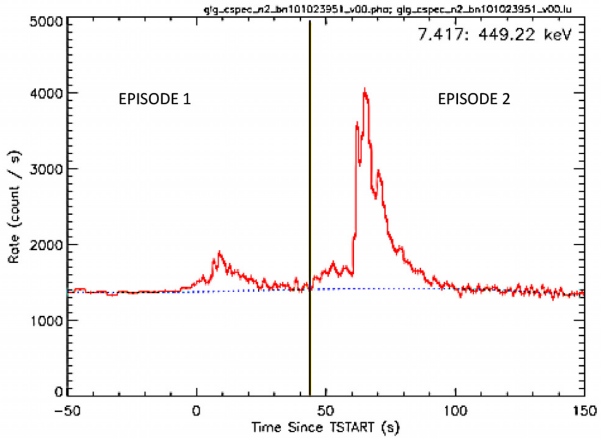

Fig. 2. Count light curve of GRB 101023 obtained from the *Fermi* GBM detector, with a bin time of 1 s. The time is given with respect to the GBM trigger time of 22:50:04.73 UT, 2010 October 23. The plot was obtained with the RMFIT program. The two-episode nature of the GRB is shown in analogy with GRB 090618.

What is most striking is that we can have an independent verification of this redshift by comparing the late part of the afterglows of the two sources. Since we have verified that both GRB 090618 and GRB 101023 have similar energetics, and under the hypothesis of the same progenitor mechanism, we compare and contrast the luminosities of both GRBs in the late X-ray afterglow emission. We know that the X-ray afterglow is related to the residual kinetic energy of the outflow, although we do not attempt here to present a theoretical model for this emission. We rescaled, in the observed time interval and energy range, the X-ray afterglow luminosity of GRB 090618 for different redshifts in an interval between $0.04 < z < 3$ (see Fig. 15). The striking coincidence for $z = 0.9$ is presented in Fig. 14.

In Sect. 2 we summarize the results of GRB 090618 and identify episode 1 and episode 2. In Sect. 3 we present the

observations of GRB 101023 by the different satellites. In Sect. 4 we give a brief summary of the fireshell scenario. In Sect. 5 we perform a spectral analysis of episodes 1 and 2 of this GRB. In Sect. 6 we try to identify the P-GRB of the gamma-ray burst, taking different time intervals into account along the entire emission. In Sect. 7 we present the methods we used to constrain the redshift. In Sect. 8, after interpreting the second episode as a canonical GRB within the fireshell model, we build its light curve and spectrum. In Sect. 9 we go into further detail in the analysis of the first episode, making clear the evolution of the thermal component and the radius of the outermost shell and establishing the complete correspondence with GRB 090618. Finally, in Sect. 10 we present the conclusions.

2. Brief summary of GRB 090618 analysis

We recall that GRB 0908618 is one of the most energetic among the nearest sources, with an isotropic energy of $E_{\rm iso} = 2.7 \times 10^{53}$ erg, at redshift $z = 0.54$. It has been observed in a wide energy range by many satellites, such as as *Fermi* GBM (Meegan et al. 2009), *Swift*-BAT (Gehrels et al. 2009), AGILE (Longo et al. 2009), Konus-WIND (Golenteskii et al. 2009), *Suzaku*-WAM (Kono et al. 2009), and CORONAS-PHOTON (Kotov et al. 2008), and by many onground telescopes. We have shown (see the work of Izzo et al. 2011) that the light curve is quite particular, as it consists of two different emissions, of 50 s and 100 s of duration. A time-resolved spectral analysis showed that the first part is well fit by a black body and an extra power-law component. The temperature decays with time following a broken power law, in agreement with the results found by Ryde and collaborators (Ryde & Pe'er 2009). The first power law has an index $a_{kT} = -0.33 \pm 0.07$, and the second one has an index $b_{kT} = -0.57 \pm 0.11$. The evolution of the radius $r_{\rm em}$ of the black body emitter has also been studied, finding an initial radius of 12 000 km, expanding in the early phase with a velocity of $\sim$4000 km s^{-1}. By analyzing it within the fireshell model, we concluded that the first episode cannot be either a GRB or part of a GRB. Indeed, we relate this episode to the phases just preceding the gravitational collapse and define it as a "proto-black hole": the latest phase of the collapsing bare core leading to the black hole formation and the simultaneous emission of the GRB (Ruffini et al. 2010a). In this interpretation, the radius $r_{\rm em}$ only depends on the observed energy flux of the black body component $\phi_{\rm obs}$, the temperature kT and the luminosity distance to the source D. Episode 2 was identified as a canonical GRB, which comes from the black hole formation process. The first 4 s were identified as the P-GRB, and its spectrum is well fit by a black body with an extra power-law component, the latter mainly caused by the early emission of the extended afterglow. We found a P-GRB temperature of $kT = 29.22 \pm 2.21$ keV and a dyadosphere energy of the whole second episode of $E^{\rm e^\pm}_{\rm tot} = 2.49 \times 10^{53}$ erg. We performed a numerical simulation with the numerical code GRBsim and found a baryon load $B = (1.98 \pm 0.15) \times 10^{-3}$ and a Lorentz Gamma factor at the transparency of $\Gamma = 495 \pm 40$. From this analysis we concluded that we are in the presence of a very interesting source, because for the first time we can witness the process of formation of a black hole from the phases just preceding the gravitational collapse to the GRB emission.

3. Observations of GRB 101023

On 23 October 2010 the *Fermi* GBM (GCN circular 2010) detector was triggered by a source quite similar to GRB 090618, with a trigger time of 309 567 006.726968 (in MET seconds). The burst was also detected by BAT (Saxton et al. 2010) (see Fig. 3), onboard the *Swift* satellite (Gehrels et al. 2004), with a trigger time of 436 981 (in MET seconds) and the following location coordinates: RA(J2000) = 21h11m49s, Dec(J2000) = $-65°23'37''$ with an uncertainty of 3 arcmin. The *Swift*-XRT detector (Page et al. 2010; Burrows et al. 2005) has also observed this source from 88 s to 6.0 ks after the BAT trigger. GRB 101023 was also detected by the Wind instrument onboard Konus satellite, in the energy range (10–770) keV (Golenetskii et al. 2010). The inferred location is in complete agreement with that determined by *Swift* and *Fermi*. Moreover, there have been detections in the optical band by the Gemini telescope (Levan et al. 2010).

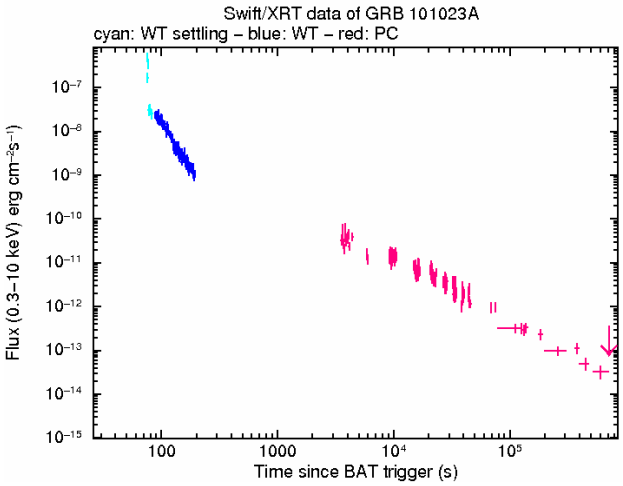

Fig. 3. Count light curve of GRB 101023 obtained from the *Swift* XRT detector.

The GBM light curve (Fig. 2) shows two major pulses.The first one starts at the trigger time and lasts 45 s. It consists of a small peak that lasts about 10 s, followed by a higher emission that decays slowly with time. The duration, as well as the topology of this curve, lead us to think that this may not be a canonical GRB, but its origin may lie on another kind of source, which remains unidentified. The second pulse starts at 45 s after the trigger time and lasts 44 s. It presents a peaky structure, composed of a short and weak peak at the beginning, followed by several bumps, big not only in magnitude but also in duration. This second emission, in contrast, does have all the characteristics that describe a canonical GRB (Ruffini et al. 2010c).

4. Theoretical model considered: fireshell scenario

In the fireshell scenario, the GRB emission comes from a process of vacuum polarization, resulting in pair creation in the so-called dyadosphere. In the process of gravitational collapse to a black hole (Ruffini et al. 2010b), an $e^\pm$ plasma is formed in thermal equilibrium, with total energy $E^{\rm e^\pm}_{\rm tot}$. The annihilation of these $e^\pm$ pairs occurs gradually and is confined in a shell, called "fireshell". This shell self-accelerates to relativistic velocities, engulfing the baryonic matter (of mass $M_{\rm B}$) left over in the process of collapse and reaching a thermal equilibrium with it (Ruffini et al. 2000). The baryon loading is measured by the dimensionless parameter $B = M_{\rm B}c^2/E^{\rm e^\pm}_{\rm tot}$. The fireshell continues to self-accelerate up to relativistic velocities (Ruffini 1999) until it reaches the transparency condition. At this time

Table 1. Time-resolved spectral analysis of GRB 101023.

Time [s]	α	β	$E_0^{\rm BAND}$[keV]	χ^2	Norm	kT[keV]	γ	χ^2	Norm $^{\rm po}$	Norm $^{\rm BB}$
0–44	-1.3 ± 0.8	-1.9 ± 0.2	87 ± 147	0.98	0.006 ± 0.01	14 ± 6	-1.7 ± 0.1	0.98	0.0003 ± 0.0004	$(4.1 \pm 7.4) \times 10^{-5}$
45–89	-0.9 ± 0.1	-2.02 ± 0.1	151 ± 24	1.09	0.043 ± 0.008	26 ± 1	-1.58 ± 0.03	1.12	0.0124 ± 0.0006	$(4.2 \pm 1.1) \times 10^{-5}$

we have a first flash of radiation, the P-GRB (Ruffini et al. 2001). The energy released in the P-GRB is a fraction of the initial energy of the dyadosphere $E_{\rm tot}^{\rm e^\pm}$. The residual plasma of leptons and baryons interacts with the circumburst medium (CBM) as it expands, giving rise to multi-wavelength emission: the "extended" afterglow. However, owing to these collisions, the plasma starts to slow down. We assume a fully-radiative condition in this model (Ruffini et al. 2003). The structures observed in the prompt emission of a GRB come from the inhomogeneities in this CBM, while in the standard fireball scenario (Meszaros 2006) they are caused by internal shocks. In this way we need few parameters for a complete description of a GRB: the dyadosphere energy $E_{\rm tot}^{\rm e^\pm}$, the baryon load B and the CBM density distribution, $n_{\rm CBM}$. In addition, we assume that there is spherical symmetry, and the energy released in the explosion $E_{\rm iso}$ is equal to the energy of the dyadosphere $E_{\rm tot}^{\rm e^\pm}$. From this approach, to sum up, the GRB bolometric light curve will be composed of two main parts: the P-GRB and the extended afterglow. Their relative energetics and their observed time separation are functions of the parameters $E_{\rm tot}^{\rm e\pm}$, B, and $n_{\rm CBM}$. We want to stress that the emission of the P-GRB does not always coincide with what is called "prompt emission" in the fireball scenario. Indeed, within the fireshell model, this prompt emission corresponds to the gamma-ray emission, which addresses not only the P-GRB, but also the peak of the extended afterglow.

Instead of making use of the typical thermal spectrum, we introduced a modified black body spectrum (Patricelli et al. 2010, 2011), given by

$$\frac{{\rm d}N_\gamma}{{\rm d}V{\rm d}\epsilon} = \left(\frac{8\pi}{h^3c^3}\right)\left(\frac{\epsilon}{k_{\rm B}T}\right)^\alpha \frac{\epsilon^2}{\exp\left(\frac{\epsilon}{k_{\rm B}T}\right)-1}. \quad (1)$$

This way we can also reach an agreement with the most energetic GRBs ($E_{\rm iso} \geq 10^{53}$ erg). Furthermore, within the fireshell scenario we can naturally explain the hard-to-soft spectral variation observed in the extended afterglow emission. As the Lorentz gamma factor Γ decreases with time, the observed effective temperature of the fireshell also decreases, making the peak of the emission take place at lower energies. This effect is amplified by the curvature effect of the EQTS (Bianco & Ruffini 2005), which produces the observed time lag in the majority of the GRBs.

We need to identify the P-GRB in the observed data so that we are able to determine the parameters $E_{\rm tot}^{\rm e^\pm}$ and B, via a trial and error procedure, and consequently the P-GRB energy $E_{\rm P\text{-}GRB}$, the Lorentz gamma factor at the transparency γ, the theoretically predicted temperature $kT_{\rm th}$, and the radius at the transparency (see Fig. 1 in Ruffini et al. 2009). The observed temperature $kT_{\rm obs}$ is related to the theoretically predicted temperature $kT_{\rm th}$ through

$$kT_{\rm obs} = \frac{kT_{\rm th}}{1+z}. \quad (2)$$

5. Analysis of data and results

To obtain the *Fermi* GBM light curve and spectrum in the band 8−440 keV (see Fig. 2), we used the RMFIT program. We downloaded the data from the gsfc website[1]. We used the lightcurves corresponding to the second and fifth NaI detectors and the b0 BGO detector. We subtracted the background by fitting a cubic function from the intervals before and after the GRB (from 400 s to 200 s before the GRB and from 180 s to 220 s after it), where we suppose there is no data. Then we proceeded with the time-resolved spectral analysis.

To proceed with the fitting of the spectra, we defined first of all the time intervals we wanted to analyze: the first interval starts at the trigger time $t_0 = 0$ and lasts 45 s, while the other starts at $t_0 + 45$ s and lasts 44 s. For convenience, from now on we will refer to the first emission as episode 1 and the second emission as episode 2. For this source we considered two models: the black body plus power-law model and the Band spectral model (Band et al. 2003). We first analyzed each of the events separately, as if they were two GRBs and then subdivided each of the two emissions in the light curve into two other parts: the one that we think would correspond to the P-GRB emission and the one that would correspond to the afterglow. The results from the spectral analysis are shown in Table 1. The fit of the spectrum of the first episode with both models is shown in Fig. 4, while Fig. 5 shows the same fit for the second episode.

6. Identification of the P-GRB

6.1. Attempt for a single GRB scenario: the whole emission as a single GRB

The first step in our analysis was to attempt to interpret the whole emission as a single GRB, with episode 1 as the P-GRB. We performed a time-integrated analysis of the whole emission of episode 1, using a black body plus power-law model and a Band model. The results of this spectral analysis are shown in Table 1. We found a black-body temperature of $kT = 14 \pm 6$ keV with normalization factor $norm_{\rm bbody} = (4.1 \pm 7.4) \times 10^{-5}$, a photon index of $\gamma = -1.7 \pm 0.1$ with normalization factor $norm_{\rm po} = (3 \pm 4) \times 10^{-4}$ and a $\chi^2 = 0.98$ for both spectral models. The P-GRB energy is $E_{\rm P\text{-}GRB} = 1.625 \times 10^{52}$ erg and the isotropic energy $E_{\rm iso} = 4.03 \times 10^{53}$ erg, which gives a ratio $E_{\rm P\text{-}GRB}/E_{\rm iso} = 0.04$. This value in our simulations would imply a theoretically predicted temperature of $kT_{\rm th} = 110.63$ keV, which is by far much bigger than the observed one. Consequently, the first episode cannot be the P-GRB of the whole emission.

6.2. The identification of the P-GRB of the first episode

Our second step in the analysis of this source was to attempt to interpret episodes 1 and 2 as two different GRBs. We first analyzed episode 1 by taking two different possibilities into account:

1. We considered a P-GRB that lasts 6 s and made the spectral analysis with XSPEC. We fitted a black body plus power-law model and found a black-body temperature of $kT = 25.4 \pm 6.9$ keV with normalization factor $norm_{\rm bbody} = 0.9 \pm 0.5$, a photon index of $\gamma = 2.2 \pm 0.5$ with $norm_{\rm po} = 30.9 \pm 35.3$

[1] ftp://legacy.gsfc.nasa.gov/fermi/data/gbm/bursts

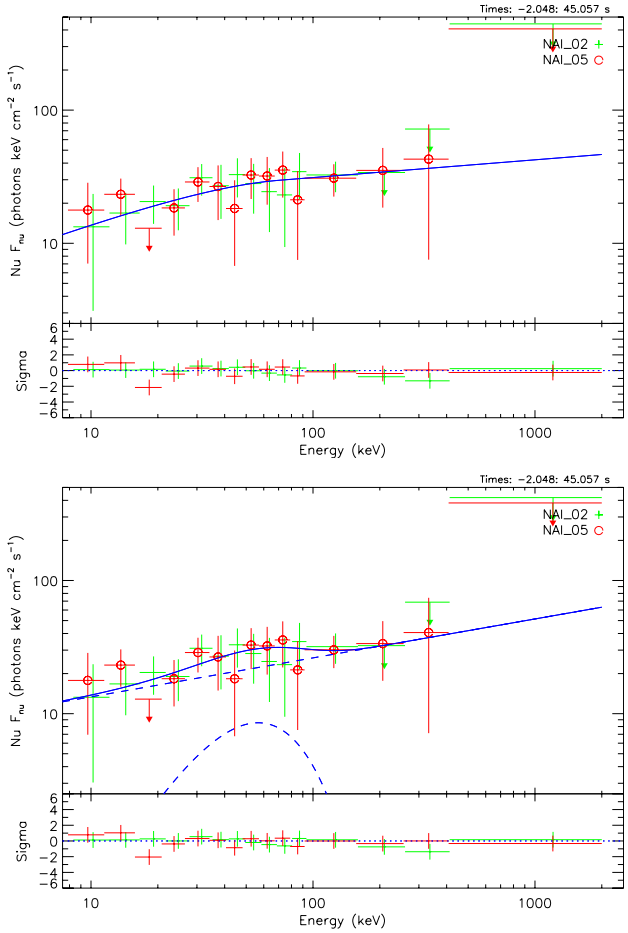

Fig. 4. Fit of the spectrum of episode 1, with a Band model (*upper panel*) and a black body plus power-law model (*lower panel*).

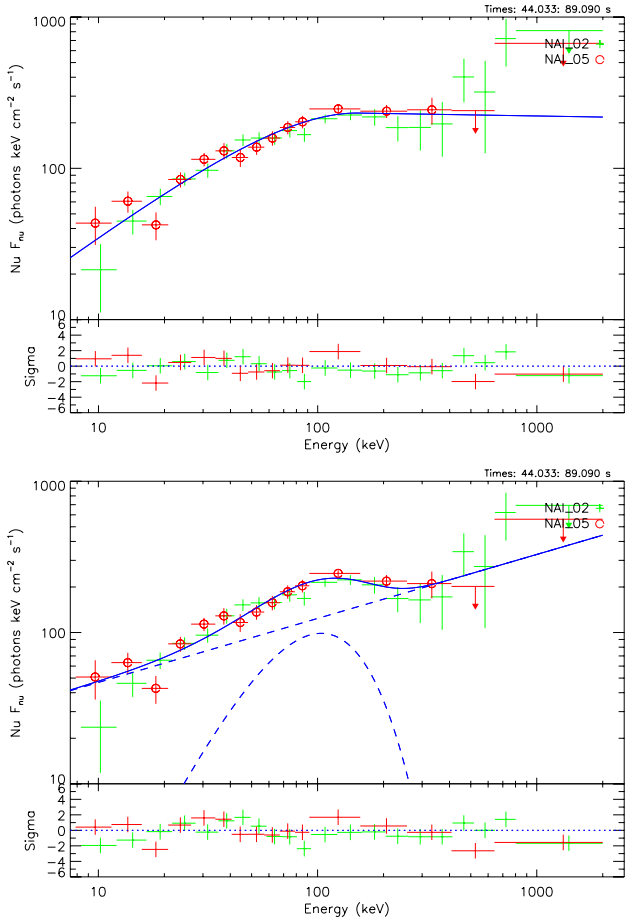

Fig. 5. Fit of the spectrum of episode 2, with a Band model (*upper panel*) and a black body plus a power-law model (*lower panel*). Both models fit the entire energy range well, with a chi squared of 0.79 and 0.84, respectively. The data points have been grouped according a signal-to-noise ratio of $N = 10$, and rebinned at higher energies in order to have better statistics and reduce the error bars.

and a reduced chi squared of $\chi^2 = 1.01$. Considering that the P-GRB is the thermal component of the GRB, by using XSPEC we found a flux of 7.25×10^{-8} erg/cm^2/s in the range (8−5000) keV. Then we followed the same procedure for the whole of episode 1, fitting a cutoffpl model, and found a photon index of $\gamma = 1.16 \pm 0.3$, a cutoff energy of $E_{\rm cutoff} = 73 \pm 27$ keV, a normalization factor of 2.9 ± 2.4, a reduced chi squared value of $\chi^2 = 1.08$, and a flux of 1.626×10^{-7} erg/cm^2/s. Using formula 4, we found a P-GRB energy of $E_{\rm P\text{-}GRB} = 9.56 \times 10^{50}$ erg and a total energy of $E^{\rm e^\pm}_{\rm tot} = 1.625 \times 10^{52}$ erg, which gives a ratio $E_{\rm P\text{-}GRB} = 5.9\%\, E^{\rm e^\pm}_{\rm tot}$. With these values we performed the simulation with the numerical code and found a baryon load $B = 8.5 \times 10^{-4}$ and a predicted temperature of $kT_{\rm th} = 128.82$ keV, which is much higher than the one observed. Therefore, we concluded that the first 6 s of emission cannot be the P-GRB of episode 1, at least in the fireshell scenario.

2. We considered the P-GRB under the threshold of the detector. We took the first 6 s before the trigger time as the P-GRB and supposed that it is well fitted by a Band model, with a flux of 10^{-8} erg/cm^2/s, which is comparable with the threshold of the detector. We derived a P-GRB energy of 10^{50} erg, which is the 0.9% of the total energy. For this ratio of the energies, we found with the numerical code a baryon load of $B = 10^{-2}$ and a predicted flux that is smaller than the detector threshold. This indicates that indeed this could be the P-GRB of the first emission, so that episode 1 could be a GRB, and we could be for the first time in the presence of a double GRB. However, in light of the results obtained from the analysis of GRB 090618 (Izzo et al. 2011) and taking into account that the value of the redshift has not been precisely determined, we decided to discard this result. Therefore, we conclude that episode 1 is not a GRB but another source whose origin is still unidentified. We come back to this interpretation later.

6.3. Analysis of the second episode

After the analysis of episode 1, we moved on to the analysis of episode 2. We followed the same steps taking the first 12 s of episode 2 as the possible P-GRB. We also fitted a black body plus power-law model to the whole P-GRB and found a black-body temperature of $kT = 15.5 \pm 1.6$ keV with normalization factor $norm_{\rm bbody} = 1.26 \pm 0.3$, a photon index of $\gamma = 2.5 \pm 0.4$ with normalization factor $norm_{\rm po} = 141.79$ and a $\chi^2 = 0.96$. We computed a flux in the band (260−5000) keV of 2.54×10^{-7} erg/cm^2/s and a P-GRB energy of $E_{\rm P\text{-}GRB} = 1.89 \times 10^{52}$ erg. By fitting a black body plus power-law model to the whole of episode 2 we found a flux in the band (8−5000) keV of 1.272×10^{-7} erg/cm^2/s and a total energy

Table 2. Detailed spectral analysis of the P-GRB of episode 2, of 12s of duration, using a BB+po model and performed every 1 s.

P-GRB of episode 2	(BB+po)			
Time int	kT(keV)	Norm factor	Flux 8–440 keV	χ^2
051–052	1.9 ± 1.7	0.9 ± 2	3.2525×10^{-8}	1.40
052–053	5 ± 1	1.3 ± 0.3	9.8254×10^{-8}	1.06
053–054	7 ± 1	1.2 ± 0.3	9.9689×10^{-8}	0.99
054–055	10 ± 2	1.2 ± 0.3	9.8285×10^{-8}	1.17
055–056	7 ± 1	1.6 ± 0.3	1.3217×10^{-7}	0.96
056–057	10 ± 1	2.1 ± 0.4	1.7721×10^{-7}	1.42
057–058	10 ± 1	1.7 ± 0.4	1.4245×10^{-7}	0.96
058–059	11 ± 1	2.1 ± 0.4	1.7738×10^{-7}	1.16
059–060	10 ± 1	2.6 ± 0.4	2.1844×10^{-7}	1.38
060–061	10 ± 1	1.8 ± 0.3	1.4976×10^{-7}	1.51
061–062	9 ± 1	1.8 ± 0.3	1.5193×10^{-7}	1.18
062–063	14 ± 2	1.6 ± 0.4	1.3462×10^{-7}	1.74

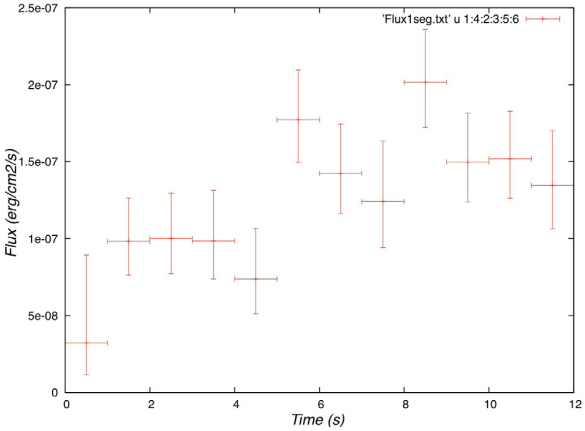

Fig. 6. Plot of the flux of the BB component vs time for the first 12 s of episode 2.

of $E^{e^\pm}_{tot} = 1.309 \times 10^{53}$ erg. The ratio is $E_{P\text{-}GRB} = 0.9\% E^{e^\pm}_{tot}$. This same value is reached with the numerical code for a baryon load $B = 7.6 \times 10^{-3}$ and a predicted temperature of $kT_{th} = 14.02$ keV, which after cosmological correction gives 7.38 keV (assuming $z = 0.9$, see next section), which is not in good agreement with the observed one, $kT_{obs} = 26$ keV. Thus we conclude that the first 12 s of emission cannot be the P-GRB.

To be more accurate, we performed the following procedure: as we know that the P-GRB consists of a black-body emission, we performed a detailed spectral analysis every 1 s with the Black body model to see the behavior of the black body component, i.e. where the black body component dominates. That will indicate more precisely the time range and duration of the P-GRB. Table 2 shows the results of this analysis and Fig. 6 shows the behavior of the black body component with time. We see that in fact only the first 5 s of emission have a marked black body component, with a typical pulse shape. The emission that follows seems not to be related to the P-GRB, but to the afterglow. So we conclude that episode 2 is indeed a GRB and the first 5 s of emission are the P-GRB (see Sect. 8).

7. Pseudo-redshift determination

The redshift of this source is unknown, owing to the lack of data in the optical band. However, to constrain it, we employed three different methods, mentioned below.

7.1. Method 1: nH column density

We first tried to estimate the redshift making use of the method developed in Grupe et al. (2007) work, where the authors comment on the possible relation between the absorption column density in excess of the galactic absorption column density $\Delta N_H = N_{H,fit} - N_{H,gal}$ and the redshift z. To do this, we considered the galactic absorption component taken from Kalberla et al. (2005), with the following values of the galactic coordinates of the GRB: $l = 328.88$, $b = -38.88$. We used the Lab Survey website[2] and obtained the value of $n_H = 2.59 \times 10^{20}$ cm^{-2} for the galactic H column density.

Then we took the values of some parameters, the spectrum, and response files from the XRT website[3], selected the part of interest and carried out an analysis making use of the program XSPEC. We fit the model wabs, which is the photoelectric absorption using Wisconsin cross sections (Morrison et al. 1983): $M(E) = \exp[-n_H \sigma(E)]$, where $\sigma(E)$ is the photoelectric cross section (not including Thomson scattering) and n_H is the equivalent hydrogen column density, in units of 10^{22} atoms/cm^2. Once we knew these parameters, we fit the data with a power-law model, considering a phabs component related to the intrinsic absorption. We obtained a value of $n_H^{intr} = 0.18 \pm 0.019 \times 10^{22}$ cm^{-2}. Wkth this result, we put them in formula (1) of Grupe et al. (2007) paper:

$$\log(1 + z) < 1.3 - 0.5[\log(1 + \Delta N_H)], \quad (3)$$

and we obtained an upper limit for the redshift of 3.8.

7.2. Method 2: Amati relation

We tried another method of constraining the redshift, making use of the Amati relation (Amati 2006), shown in Fig. 7. This relates the isotropic energy E_{iso} emitted by a GRB to the peak energy in the rest frame $E_{p,i}$ of its νF_ν electromagnetic spectrum (see Amati et al. 2009, and references therein). E_{iso} is the isotropic-equivalent radiated energy, while $E_{p,i}$ is the photon energy at which the time averaged νF_ν spectrum peaks. The analytical expression of E_{iso} is

$$E_{iso} = \frac{4\pi d_l^2}{(1+z)} S_{bol}, \quad (4)$$

[2] http://www.astro.uni-bonn.de/~webaiub/english/tools_labsurvey.php
[3] http://www.swift.ac.uk/xrt_curves/

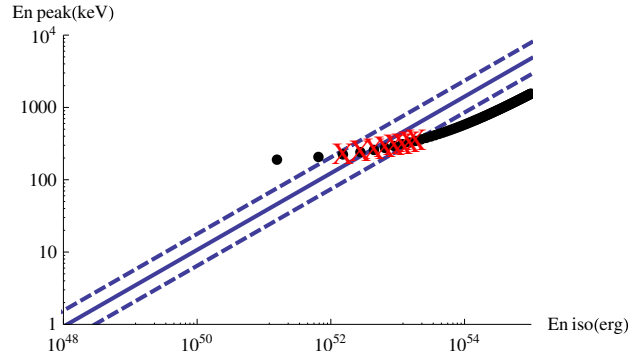

Fig. 7. Plot of the relation between $E_{p,i}$ and E_{iso} for the second episode of GRB 101023, considering different values of the redshift. It can be seen that the plot lies within 1σ for the range $z = 0.3-z = 1.0$.

where d_l^2 is the luminosity distance, z is the redshift and S_{bol} is the bolometric fluence, related to the observed fluence in a given detection band (E_{min}, E_{max}) by

$$S_{bol} = S_{obs} \frac{\int_{1/(1+z)}^{10^4/(1+z)} E\phi(E)\mathrm{d}E}{\int_{E^{min}}^{E^{max}} E\phi(E)\mathrm{d}E}, \quad (5)$$

with ϕ the spectral model considered for the spectral data fit. The value of $E_{p,i}$ is related to the peak energy E_p in the observer's frame by

$$E_{p,i} = E_p(1+z). \quad (6)$$

We started our analysis under the hypothesis that episode 2 is a long GRB. We computed the values of $E_{p,i}$ and E_{iso} for different given values of z and plotted them in Fig. 7. We found that the Amati relation is fulfilled by episode 2 for $0.3 < z < 1.0$. This interval has been calculated at 1σ from the best fit from the Amati relation, in order to obtain a tighter interval around the best fit than with the previous method.

7.3. Method 3: empirical method for the pseudo-redshift

We also tried an empirical method, following Atteia (2003) and Pelangeon et al. (2006), which can be used as a redshift indicator. This method consists in determining a pseudo-redshift from the GRB spectral properties. Using the parameters from the Band model, namely the index of the low-energy power-law α and the break energy E_0, we can compute the value of the peak energy of the νF_ν spectrum, as $E_p = E_0(2+\alpha)$. Then, we define the isotropic-equivalent number of photons in a GRB, N_γ, as the number of photons below the break, integrated from $E_p/100$ to $E_p/2$. If we also know the T_{90}, we define the redshift indicator

$$X = \frac{N_\gamma}{E_p \sqrt{T_{90}}}. \quad (7)$$

From a sample of 17 GRBs with known redshift reported in Atteia (2003) we compute the theoretical evolution of X with the redshift z, that is $X = f(z)$. Then we invert the relation to derive a pseudo-redshift from the value of X. That way we obtain the pseudo-redshift as $\hat{z} = f^{-1}(X)$, for the GRB of interest.

We applied this treatment to episode 2 of GRB 101023, introducing the spectral parameters from the Band model on the Cosmos website[4] and obtained a value for the redshift of $z = 0.9 \pm 0.084$. It is important to mention here that this error is a statistical one, while the systematic error is much bigger (Atteia 2003; Pelangeon et al. 2006; Pelangeon 2008), of a factor of ~1.5, i.e., $z = 0.9^{+0.45}_{-0.3}$.

This result agrees with the redshift range found from the Amati relation for episode 2 and is also consistent with the upper limit determined with method 1.

[4] http://cosmos.ast.obs-mip.fr/projet/v2/fast_computation.html

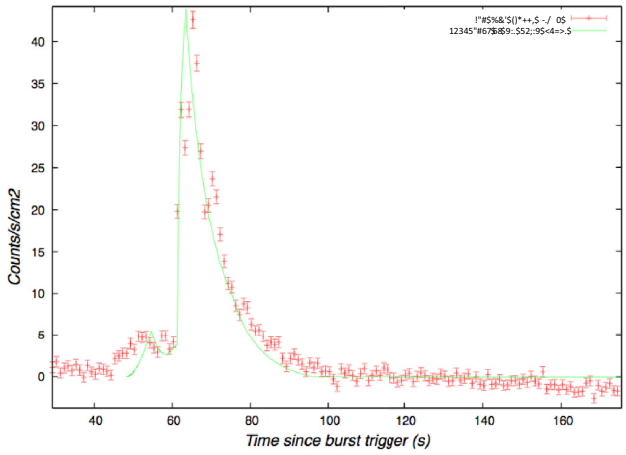

Fig. 8. Fit of the second major pulse of the light curve of GRB 101023.

8. Simulation of the light curve and spectrum

To simulate the light curve we made use of a numerical code called GRBsim. This numerical code simulates a GRB emission by solving the fireshell equations of motion, taking the effect of the EQuiTemporal Surfaces (EQTS, Bianco & Ruffini 2005) into account. We made the simulation for episode 2. We found, at the transparency point, a value of the laboratory radius of 1.34×10^{14} cm, a theoretically predicted temperature that after cosmological correction gives $kT_{th} = 13.26$ keV, a Lorentz Gamma factor of $\Gamma = 260.48$, a P-GRB laboratory energy of 2.51×10^{51} erg and a P-GRB observed temperature of 28.43 keV. We adopted a value for the dyadosphere energy of $E^{e^\pm}_{tot} = 1.8 \times 10^{53}$ erg and a baryon loading of $B = 3.8 \times 10^{-3}$. The simulated light curve and spectrum of episode 2 are shown in Figs. 8 and 9, respectively.

Figure 10 shows the fitted spectrum with different models. We took the data points from the NaI n2 and BGO b0 detectors together. We note there is a good agreement between both fits, in the low and medium energy range. At high energies, the spectrum follows a power-law behavior, which cannot be reproduced by the modified black body model due to the exponential cutoff.

9. Analysis of the first episode

To analyze episode 1 more into detail, in order to identify the nature of this phenomenon, we plotted the temperature of the black body component as a function of time, for the first 20 s of emission (see Fig. 11). We note a strong evolution in the first 20 s of emission which, according to Ryde (2004) can be reproduced by a broken power-law behavior, with $\alpha = -0.47 \pm 0.34$ and $\beta = -1.48 \pm 1.13$ being the indices of the first and second power law, respectively. We also plotted the radius of the most external shell with time (see Fig. 12). Following Izzo et al. (2011), the radius can be written as

$$r_{em} = \frac{\hat{R}D\Gamma}{(1+z)^2}, \quad (8)$$

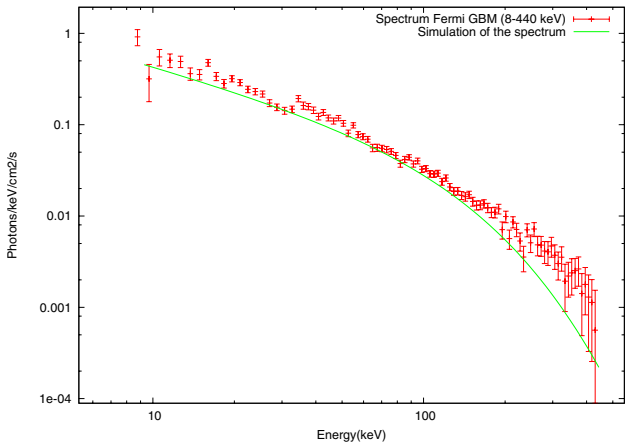

Fig. 9. Fit of the spectrum of episode 2.

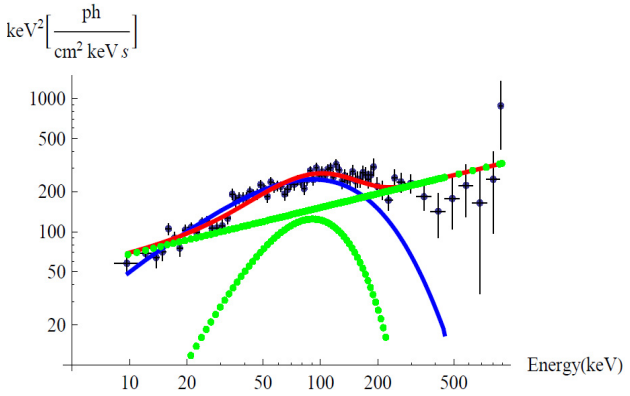

Fig. 10. Fit of the spectrum of episode 2. The green dotted lines represent the fit of a black body and a power-law components, separately. The red line is the sum of them, calculated with XSPEC (BB+po). The blue line is the fit with the modified black body spectrum given in Eq. (1), calculated with the GRBsim numerical code.

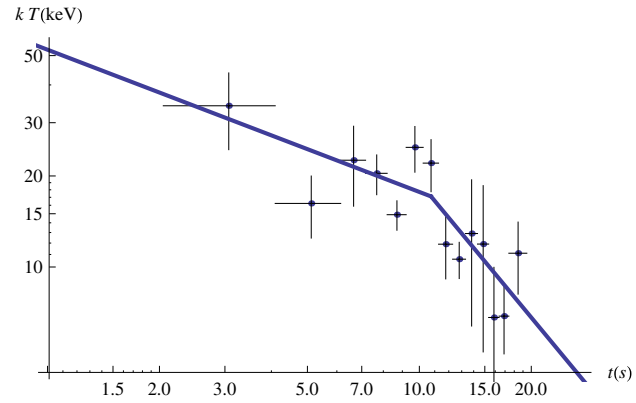

Fig. 11. Evolution of the observed temperature kT of the BB component. The blue line corresponds to a broken power-law fit. The indices of the first and second power laws are $\alpha = -0.47 \pm 0.34$ and $\beta = -1.48 \pm 1.13$, respectively. The break occurs at 11 s after the trigger time.

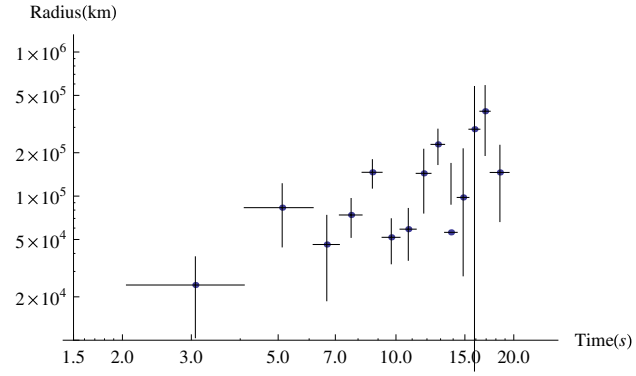

Fig. 12. Evolution of the radius of the first episode progenitor.

where $\hat{R}^2 = \phi_{\rm obs}/(4\pi\sigma T_{\rm obs}^4)$ is a parameter, D the luminosity distance, Γ the Lorentz factor, and $\phi_{\rm obs}$ the observed flux. We can see that the radius remains almost constant (in fact it increases, but only slightly). From this it is possible to see that the plasma is expanding at nonrelativistic velocities. According to the work of Arnett & Meakin (2011), there is an expansion phase of the boundary layers, while the iron core suffers a contraction. This is due to the presence of strong waves originated while the different shells of the progenitor mix during the collapse phase. This fact confirms the non-GRB nature for the first episode.

9.1. The X-ray afterglow as a possible redshift estimate?

We have seen that GRB 090618 and GRB 101023 share similar properties. They seem to be composed of two different emission episodes, the first being connected to a quasi-thermal process before the collapse of the core, while the second is the canonical GRB (see Ruffini et al. 2010a,d).

Anyway, if both GRBs were created originated by the same physical mechanism and since the energetics are very similar, considering the value $z = 0.9$ for GRB 101023, we can expect similar luminosity behavior for the X-ray afterglow. Although we have not yet developed a theory for this late afterglow emission, we attempted a simple test that compared the observed X-ray afterglow of both GRBs as if they were located at the same redshift. Since there are different spectral components in the GRB X-ray afterglow, we built the pseudo-redshift light curves for both these different emissions. Thanks to the *Swift*-XRT observations, we know that the early X-ray afterglow of both GRBs shows a canonical behavior, where the emission can be divided in three distinct parts (Nousek 2006): 1) a first very steep decay, associated with the late prompt emission; 2) a shallower decay, the plateau; 3) a final steeper decay. At first, we determined for GRB 090618 and GRB 101023 these three time intervals by using the phenomenological function introduced in the work of Willingale et al. (2007):

$$f(t) = \begin{cases} F_{\rm c} \exp\left(\alpha_{\rm c} - \frac{t\alpha_{\rm c}}{T_{\rm c}}\right) \exp\left(\frac{-t_{\rm c}}{t}\right), & t < T_{\rm c}; \\ F_{\rm c} \left(\frac{t}{T_{\rm c}}\right)^{-\alpha_{\rm c}} \exp\left(\frac{-t_{\rm c}}{t}\right), & t > T_{\rm c}, \end{cases} \quad (9)$$

which represents the transition from an exponential regime to a power law. This transition occurs at the point $(T_{\rm c}, F_{\rm c})$ where the two functional sections have the same value and gradient. The $\alpha_{\rm c}$ parameter determines both the time constant of the exponential decay and the temporal decay index of the power law, while the $t_{\rm c}$ parameter marks the initial rise. The maximum flux occurs at $t = (t_{\rm c} T_{\rm c}/\alpha_{\rm c})^{1/2}$. We fit the afterglow data of the two GRBs with this model, and the results of our fits are shown in Fig. 13.

After the determination of these three time intervals, we built the X-ray light curve of GRB 090618 as if it was observed at redshift $z = 0.9$, which is our estimate for the redshift of GRB 101023. The *Swift*-XRT (which operates in

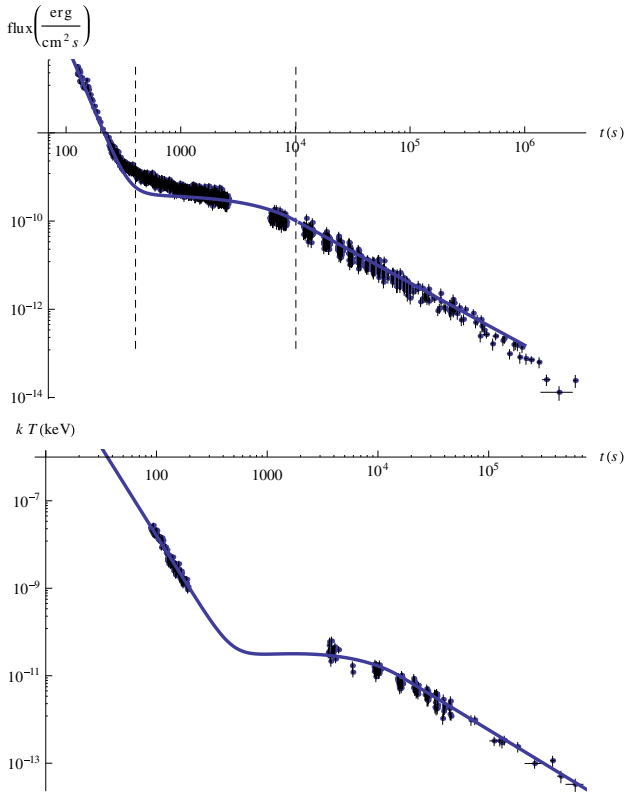

Fig. 13. The fit of the X-ray afterglow of GRB 090618 (*upper panel*) and GRB 101023 (*lower panel*) with the model of Willingale et al. (2007).

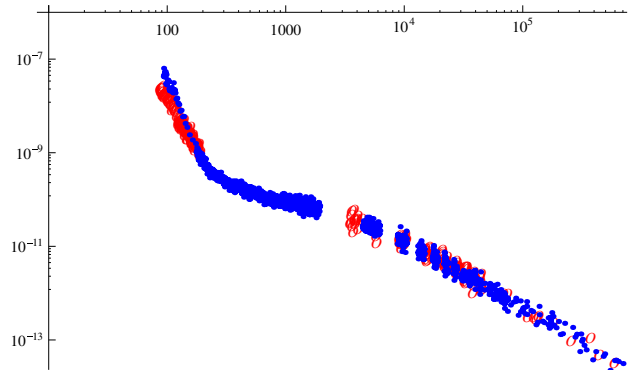

Fig. 14. The X-ray afterglow of GRB 090618 (blue data) as if it was observed at redshift $z = 0.9$ (see text). The X-ray afterglow of GRB 101023 is also shown as comparison (red data). Data on GRB 101023 are missing between ∼200 s and 3550 s. Where data are present, the superposition is striking.

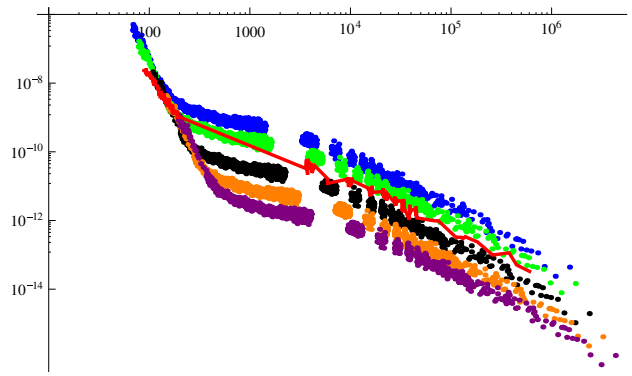

Fig. 15. The X-ray afterglow of GRB 090618 as if it was observed at different redshifts $z = (0.4, 0.6, 1.2, 2, 3)$, where each color corresponds to a different redshift. The X-ray afterglow of GRB 101023 is also shown for comparison (red data).

the (0.3−10) keV energy range) light curve of GRB 090618 (Evans et al. 2007, 2009) corresponds to the emission in the rest frame at $z = 0.54$ in the energy range (0.462−15.4) keV, while for GRB 101023 the XRT window corresponds to the range (0.57−19) keV. We must obtain the emission of GRB 090618 in this last energy range, in order to compare the two light curves. At first we made the assumption that the spectrum of each time interval is best fitted by a simple power-law model. This assumption is supported by the hypothesis that the X-ray afterglow comes from a synchrotron emission mechanism Sari et al. (1999), whose spectral emission is represented by a simple power law function. Then, we extrapolated the emission of the afterglow of GRB 090618 in the (0.57−19) keV energy range by considering the ratio between the number of photon counts in both energy ranges. This value corresponds to a conversion factor, which we consider for scaling the intensity of the light curve. We finally amplified, by a term $(1 + z_{101023})/(1 + z_{090618})$, the time interval of emission of GRB 090618, obtaining as a final result the afterglow light curve of GRB 090618 as if it was observed by XRT at redshift 0.9, see Fig. 14. It is, most remarkably, a perfect superposition of the light curve emission of both GRBs. This evidence delineates three important aspects:

– the X-ray afterglow of both GRBs clearly confirms a common physical mechanism for these GRBs;
– there is ample convergence and redundancy with different methods of determining a value of redshift $z = 0.9$ for GRB 101023. There has also been the unexpected result pointing to the late afterglow as a possibly independent redshift estimator;
– the redshift of GRB 101023 derived by the superposition of the two afterglow curves is consistent with the value of $z = 0.9$, which we have found before.

This last point led us to do another analysis consisting in the redshift-translation of the X-ray afterglow of GRB 090618 considering different values for the redshift. Following the same procedure and considering five different values for the redshift, $z = (0.4, 0.6, 1.2, 2, 3)$, we see that the X-ray emission of GRB 101023 is compatible with the X-ray afterglow of GRB 090618 as if it bursted between $z = 0.6$ and $z = 1.2$, see Fig. 15. Then we conclude that our estimate for the redshift of GRB 101023 of $z = 0.9$ is very reliable.

10. Conclusions

GRB 101023 is a very interesting source for the following reasons.

1. We find a striking similarity between GRB 101023 and GRB 090618, as can be seen from the light curves. Following the study of GRB 090618, we divided the emission into two episodes: episode 1, which lasts 45 s, presents a smooth emission without spikes that decays slowly with time. Episode 2, of 44 s of duration, presents a spiky structure, composed of a short and faint peak at the beginning,

followed by several intense bumps, after which there is a fast decay with time. Episode 2 has all the characteristics of a canonical long GRB.

2. We performed a time-resolved analysis of episode 1. We fitted a black body plus a power-law model and plotted the evolution of the black body component with time. The observed temperature decreases during the first 20 s following a broken power law: the first with index $\alpha = -0.47 \pm 0.34$ and the second with index $\beta = -1.48 \pm 1.13$, see Sect. 9. This behavior is very similar to GRB 090618.
3. In the absence of a direct measurement of the redshift to the source, we have inferred it from several empirical methods. First, following the work of Grupe et al. (2007), which considers the hydrogen equivalent column density in the direction of the source, we obtained an upper limit of $z < 3.8$. Then we performed a spectral analysis to episode 2, fitting a Band model. From the peak energy $E_{\rm peak}$ and using the Amati relation under the hypothesis that episode 2 is a canonical long GRB, we constrain the value of the redshift to be between 0.3 and 1.0. Finally, using the parameters of the Band model and following the work of Atteia (2003), we determine a value of the redshift of $z = 0.9 \pm 0.084(stat.) \pm 0.2(sys.)$. The three methods are consistent, so we assumed for the redshift of this source $z = 0.9$.
4. From the knowledge of the redshift of the source, we have analyzed episode 2 within the fireshell model. We determined a total energy $E_{\rm iso} = 1.79 \times 10^{53}$ erg and a P-GRB energy of 2.51×10^{51} erg, which we used to simulate the light curve and spectrum with the numerical code GRBsim. We find a baryon load $B = 3.8 \times 10^{-3}$ and, at the transparency point, a value of the laboratory radius of 1.34×10^{14} cm, a theoretically predicted temperature of $kT_{\rm th} = 13.26$ keV (after cosmological correction) and a Lorentz gamma factor of $\Gamma = 260.48$, confirming that episode 2 is indeed a canonical GRB.
5. From the knowledge of the redshift, we can also evaluate the flux emitted by episode 1, and from the observed black body temperature, infer the radius of the black body emitter and its variation with time, see Fig. 12. We saw that it increases during the first 20 s of emission, with a velocity $\sim 1.5 \times 10^4$ km s^{-1}. In analogy with GRB 090618, we concluded that episode 1 originates in the last phases of gravitational collapse of a stellar core, just prior to the collapse to a black hole. We call this core a "proto-black hole" (Ruffini et al. 2010a). Immediately afterwards, the collapse occurs and the GRB is emitted (episode 2).
6. Finally, we performed the following test. Owing to the similarities between GRB 101023 and GRB 090618 regarding morphology and energetics, we expect them to be created by the same physical mechanism, so we compared the late observed X-ray afterglow of both GRBs as if they were located at the same redshift; i.e, we built the light curve of GRB 090618 (of $z = 0.54$) as if it had redshift $z = 0.9$, extrapolating it to the XRT energy window of GRB 101023. We found a surprising perfect superposition of the light curves for $z = 0.9$, receiving a further confirmation of the correctness of the cosmological redshift determination. The same procedure for the redshift determination will be repeated for sources with a spectroscopical-determined redshift, as a further check of our proposal. This result points to a possible use of the late afterglow as a distance indicator.

We concluded that GRB 101023 and GRB 090618 have striking analogies and are members of a specific new family of GRBs developing out of a single core collapse. It is also appropriate to remark that this new kind of source does not present any GeV emission. The existence of precise scaling laws between these two sources opens a new window on the use of GRBs as distance indicators. We will go on to identify additional sources belonging to this family. This new paradigm is also being applied to sources at very high redshift to see how the absence of a signal under the threshold can affect the theoretical interpretation. We are also considering the possibility that proto-neutron stars in addition to proto-black holes may exist in the case of supernovae or hypernovae. Particularly interesting in this respect is the work of Soderberg et al. (2008) showing the X-ray emission prior to SN events, which may relate the observed X-ray emission prior to SN 2008D to episode 1 in GRB 090618 and GRB 101023. In this sense we are revisiting our considerations of GRB 980425 (see e.g. Fraschetti et al. 2004, 2005; Ruffini et al. 2004a, 2007; Bernardini et al. 2008), as well as of GRB 030329 (Bernardini et al. 2004, 2005b) and GRB 031203 (Bernardini et al. 2005a; Ruffini et al. 2007, 2008).

Acknowledgements. We thank the *Swift* and *Fermi* teams for their support. This work made use of data supplied by the UK *Swift* Data Centre at the University of Leicester. We are especially grateful to an anonymous referee for her/his important remarks which have improved the presentation of our results.

References

Amati, L. 2006, MNRAS, 372, 233
Amati, L., Frontera, F., & Guidorzi, C. 2009, A&A, 508, 173
Arnett, W. D., & Meakin, C. 2011, ApJ, 733, 78
Atteia, J.-L. 2003, A&A, 407, L1
Band, D., Matteson, J., Ford, L., et al. 1993, ApJ, 413, 281
Bernardini, M. G., Bianco, C. L., Chardonnet, P., et al. 2004, in Gamma-Ray Bursts: 30 Years of Discovery, ed. E. Fenimore, & M. Galassi, AIP Conf. Ser., 727, 312
Bernardini, M. G., Bianco, C. L., Chardonnet, P., et al. 2005a, ApJ, 634, L29
Bernardini, M. G., Bianco, C. L., Ruffini, R., et al. 2005b, in The Tenth Marcel Grossmann Meeting. On recent developments in theoretical and experimental general relativity, gravitation and relativistic field theories, ed. M. Novello, S. Perez Bergliaffa, & R. Ruffini (Singapore: World Scientific), 2459
Bernardini, M. G., Bianco, C. L., Caito, L., et al. 2007, A&A, 474, L13
Bernardini, M. G., Bianco, C. L., Caito, L., et al. 2008, in The Eleventh Marcel Grossmann Meeting, ed. R. T. Jantzen, H. Kleinert, & R. Ruffini (Singapore: World Scientific)
Bianco, C. L., & Ruffini, R. 2005a, ApJ, 633, L13
Briggs, M. S. 2010, GCN 11376
Burrows, D., Hill, J., Nousek, J., et al. 2005, Space Sci. Revi., 120, 165
Caito, L., Bernardini, M. G., Bianco, C. L., et al. 2009, A&A, 498, 501
Caito, L., Amati, L., Bernardini, M. G., et al. 2010, A&A, 521, A80
Cucchiara, A., Levan, A. J., Fox, D. B., et al. 2011, ApJ, 736, 7
Dainotti, M. G., Bernardini, M. G., Bianco, C. L., et al. 2007, A&A, 471, L29
De Barros, G., Amati, L., Bernardini, M. G., et al. 2011, A&A, 529, A130
Dezalay, J.-P., Barat, C., Talon, R., et al. 1992, in Gamma-ray bursts, ed. W. S. Paciesas, & G. J. Fishman, AIP Conf. Ser., 265, 304
Evans, P. A., Beardmore, A. P., Page, K. L., et al. 2007, A&A, 469, 379
Evans, P. A., Beardmore, A. P., Page, K. L., et al. 2009, MNRAS, 397, 1177
Fraschetti, F., Bernardini, M. G., Bianco, C., et al. 2004, in Gamma-Ray Bursts: 30 Years of Discovery, ed. E. Fenimore, & M. Galassi, AIP Conf. Ser., 727, 424
Fraschetti, F., Bernardini, M. G., Bianco, C. L., et al. 2005, in The Tenth Marcel Grossmann Meeting. On recent developments in theoretical and experimental general relativity, gravitation and relativistic field theories, ed. M. Novello, S. Perez Bergliaffa, & R. Ruffini (Singapore: World Scientific), 2451
Gehrels, N., Chincarini, G., Giommi, P., et al. 2004, ApJ, 611, 1005
Gehrels, N., Sarazin, C. L., O'Brien, P. T., et al. 2005, Nature, 437, 851
Gehrels, N., Ramirez-Ruiz, E., & Fox, D. B. 2009, ARA&A, 47, 567
Golenteskii, S., Aptekar, R., Mazets, E., et al. 2009, GCN, 9553
Golenetskii, S., Aptekar, R., Frederiks, D., et al. 2010, GCN, 11384
Grupe, D., Nousek, J. A., vanden Berk, D. E., et al. 2007, AJ, 133, 2216
Izzo, L., Ruffini, R., Penacchioni, A. V., et al. 2011, A&A, submitted
Kalberla, P. M. W., Burton, W. B., Hartmann, D., et al. 2005, A&A, 440, 775
Klebesadel, R. W. 1992, in Gamma-Ray Bursts – Observations, Analyses and Theories, ed. C. Ho, R. I. Epstein, & E. E. Fenimore (Cambridge University Press), 161

Kono, K., Daikyuji, A., Sonoda, E., et al. 2009, GCN, 9568
Kotov, Y., Kochemasov, A., Kuzin, S., et al. 2008, in COSPAR, Plenary Meeting, 37th COSPAR Scientific Assembly, 37, 1596
Kouveliotou, C., Meegan, C. A., Fishman, G. J., et al. 1993, ApJ, 413, L101
Levan, A. J., Perley, D., & D'Avanzo, P. 2010, GCN, 11366
Longo, F., Moretti, E., Barbiellini, G., et al. 2009, GCN, 9524
Meegan, C. A., Fishman, G. J., Wilson, R. B., et al. 1992, Nature, 355, 143
Meegan, C., Lichti, G., Bhat, P. N., et al. 2009, ApJ, 702, 791
Meszaros, P. 2006, Rep. Progress Phys., 69, 2259
Morrison, R., & Mc Cammon, D. 1983, ApJ, 270, 119
Nousek, J. A. 2006, Chin. J. Astron. Astrophys., 6, 357
Page, K. L., & Saxton, C. J. 2010, GCN, 11368
Patricelli, B., Bernardini, G., Bianco, C. L., et al. 2010, in The Shocking Universe, ed. G. Chincarini, P. DAvanzo, R. Margutti, & R. Salvaterra, SIF Conf. Proc., 102, 559
Patricelli, B., Bernardini, G., Bianco, C. L., et al. 2011, IJMPD, 20, 1983
Pe'er, A., Ryde, F., Wijers, R. A. M. J., Mészáros, P., & Rees, M. J. 2007, ApJ, 664, L1
Pelangeon, A., Atteia, J.-L., Lamb, D. Q., et al. 2006, in Gamma-Ray Bursts in the *Swift* Era, ed. S. S. Holt, N. Gehrels, & J. A. Nousek, AIP Conf. Ser., 836, 149
Pelangeon, A., Atteia, J.-L., Nakagawa, Y. E., et al. 2008, A&A, 491, 157
Ruffini, R. 1999, A&AS, 138, 513
Ruffini, R. 2011, Proceedings of the Twelfth Marcel Grossmann Meeting on General Relativity, World Scientific, Singapore
Ruffini, R., Salmonson, J. D., Wilson, J. R., & Xue, S.-S. 2000, A&A, 359, 855
Ruffini, R., Bianco, C. L., Fraschetti, F., Xue, S.-S., & Chardonnet, P. 2001, ApJ, 55, L113
Ruffini, R., Bianco, C. L., Chardonnet, P., et al. 2002, ApJ, 581, L19
Ruffini, R., Bianco, C. L., Chardonnet, P., et al. 2003, in Cosmology and Gravitation, ed. M. Novello, & S. E. Perez Bergliaffa, AIP Conf. Ser., 668, 16
Ruffini, R., Bernardini, M. G., Bianco, C. L., et al. 2004a, Adv. Space Res., 34, 2715
Ruffini, R., Bianco, C. L., Chardonnet, P., et al. 2004b, IJMPD, 13, 843
Ruffini, R., Bianco, C. L., Chardonnet, P., et al. 2005, IJMPD, 14, 97
Ruffini, R., Bernardini, M. G., Bianco, C. L., et al. 2006, ApJ, 645, L109
Ruffini, R., Bernardini, M. G., Bianco, C. L., et al. 2007, in ESA Special Publication, Vol. SP-622, The 6th Integral Workshop – The Obscured Universe, ed. S. Grebenev, R. Sunyaev, C. Winkler, A. Parmar, & L. Ouwehand, ESA SP, 622, 561
Ruffini, R., Bernardini, M. G., Bianco, C. L., et al. 2008, in Relativistic Astrophysics Legacy and Cosmology – Einstein's Legacy, ed. B. Aschenbach, V. Burwitz, G. Hasinger, & B. Leibundgut, 399
Ruffini, R., Aksenov, A., Bernardini, M. G., et al. 2009, in Cosmology and Gravitation, ed. M. Novello, & S. E. Perez Bergliaffa, AIP Conf. Ser., 1132, 199
Ruffini, R., Chakrabarti, S. K., & Izzo, L. 2010a, in COSPAR, Plenary Meeting, 38th COSPAR Scientific Assembly, 2593
Ruffini, R., Vereschagin, G., & Xue, S.-S. 2010b, Phys. Rep., 487, 1
Ruffini, R., Izzo, L., Penacchioni, A., et al. 2010c, GCN, 11459
Ruffini, R., Chakrabarti, S. K., & Izzo, L., 2010d, Adv. Sp. Res., submitted
Ryde, F. 2004, ApJ, 614, 827
Ryde, F. 2005, ApJ, 625, L95
Ryde, F., & Pe'er, A. 2009, ApJ, 702, 1211
Salvaterra, R., Della Valle, M., Campana, S., et al. 2009, Nature, 461, 1258
Sari, R., & Piran, T. 1999, ApJ, 520, 641
Saxton, C. J., Barthelmy, S. D., Baumgartner, W. H., et al. 2010, GCN, 11363
Soderberg, A. M., Berger, E., Page, K. L., et al. 2008, Nature, 453, 469
Strong, I. B. 1975, in Neutron Stars, Black Holes and Binary X-Ray Sources, ed. H. Gursky, & R. Ruffini, D. Reidel Publishing Co., 47
Tanvir, N. R., Fox, D. B., Levan, A. J., et al. 2009, Nature, 461, 1254
Willingale, R., O'Brien, P. T., Goad, M. R., et al. 2007, ApJ, 662, 109

"Great spirits have always
encountered violent opposition
from mediocre minds."
Albert Einstein

Chapter 5

The induced gravitational collapse model

5.1 Introduction

It is well known nowadays that SN associated with GRBs are of type Ib/c, but the physics behind the emission and their progenitors are still a mystery. The optical emission of a SN peaks about 10-15 days after its explosion (Arnett 1996), so it is very likely that the onset of the SN and the GRB explosion occur almost simultaneously. In fact, there are evidences of the association of some nearby GRBs with SN (Della Valle 2011), as we have already shown in Chapter 2. Following this argument, the concept of induced gravitational collapse (IGC) was initially proposed by Ruffini et al. (2001a). Some authors instead have assumed that GRBs originate from a specially violent SN process, a hypernova, or a collapsar (Woosley & Bloom 2006). However, both of these possibilities imply a very dense and strong wind-like CBM structure, and such a dense medium appears to be in contrast with the CBM density found in most GRBs, which is on the order of 1 particle cm^{-3} (Izzo et al. 2012c; Penacchioni et al. 2011). The concept of induced gravitational collapse was further developed in (Ruffini et al. 2008b) and later in (Rueda & Ruffini 2012). In the latest work the authors give a more detailed description of the assumed progenitor system by theoretically developing the basic equations describing this concept, and explain the physical processes that take place all the way up to the GRB emission.

5.2 The IGC model

The concept of IGC is essential to explain the GRB-SN connection. This model assumes a particularly close binary system composed of an evolved massive star in the latest phases of its thermonuclear evolution and a NS companion. There is a well-determined time sequence (see Fig.5.1):

1) the massive star undergoes a SN explosion; 2) part of the "early-SN" material is accreted onto the NS companion; 3) the NS companion reaches its critical mass and consequently it gravitationally collapses to form a BH; 4) a canonical GRB is emitted.

As an outcome, at the endpoint of the IGC scenario, a binary system represented by a NS (formed much later out of the SN explosion) and a BH (formed after the GRB explosion) should be expected.

From an observational point of view, we should be able to distinguish these episodes within the GRB emission, in the electromagnetic range from the gamma-rays to the radio band. We present in the following sections some examples of this observational evidence.

Let us turn now to the details of the accretion process onto the NS. The amount of material that reaches the NS gravitational capture region

$$R_{cap}(t) = \frac{2GM_{NS}(t)}{v^2_{ej,rel}(t)} \tag{5.1}$$

per unit time is given by

$$\dot{M}(t) = \pi \rho_{ej}(t) v_{ej,rel}(t) R^2_{cap}(t), \tag{5.2}$$

where R_{cap} is measured from the NS center.

In Eqs. (5.1) and (5.2), $\rho_{ej}(t) = 3M_{ej}(t)/(4\pi r^3_{ej}(t))$ is the density of the ejecta, M_{NS} is the NS mass (that increases with time due to the accretion until it reaches the critical value of $2.7M_{\odot}$),

$$M_{ej}(t) = M_{ej}(0) - M(t) \tag{5.3}$$

is the total available mass to be accreted by the NS, and

$$v_{ej,rel}(t) = \sqrt{v^2_{orb,NS}(t) + v^2_{ej}(t)} \tag{5.4}$$

is the velocity of the ejecta relative to the NS. $M_{ej}(0)$, given in Eq. (5.3), is the initial mass of the ejecta, just at the beginning of the accretion process. Finally, $M(t)$ is the mass of the ejecta that is lost because it passes through the capture region of the NS. In Eq.(5.4), $v_{orb.NS}(t) = \sqrt{G(M_{prog} + M_{NS}(t))/a}$ is the orbital velocity relative to the SN core progenitor, a is the separation distance between the NS and the SN core progenitor, and

$$v_{ej}(t) = \frac{dr_{ej}(t)}{dt} \tag{5.5}$$

is the expansion velocity of the early-SN material.

There is something to notice, though. Not all the mass that reaches the gravitational capture region of the NS is accreted. Actually, the mass accretion rate $\dot{M}_{accr}(t)$ onto the NS is a fraction $\eta_{accr} \leq 1$ of $\dot{M}(t)$, i.e.

$$\dot{M}_{accr}(t) = \eta_{accr} \dot{M}(t), \tag{5.6}$$

where η is the accretion efficiency onto the NS. Therefore, there is an amount of material per unit time that is not accreted by the NS, $\dot{M}_{out}(t) = (1-\eta_{accr})\dot{M}(t)$.

5.3 GRB 110709B in the IGC scenario

We turn now to the analysis of some sources within the IGC scenario. One of this sources is GRB 110709B, which is quite particular due to its double

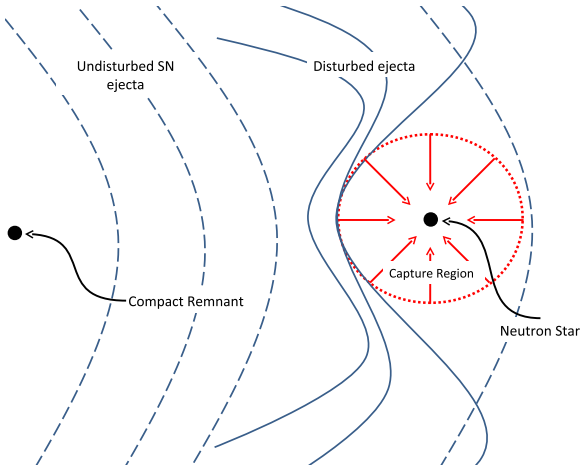

Figure 5.1: Sketch of the accretion induced collapse scenario. An evolved star in close binary with a NS explodes as a SN Ib/c. The NS rapidly accretes a part of the SN ejecta and reaches in a few seconds the critical mass undergoing gravitational collapse to a BH, emitting the GRB. Taken from Rueda & Ruffini (2012).

episode emission, with a separation of $\sim$ 10 minutes between the first and the second episode (see Fig.5.2a). The redshift of this source is unknown. It has been detected by *Suzaku* (Ohmori et al. 2011), *Konus* (Golenetskii et al. 2011) and *Swift* (Cummings et al. 2011) satellites, and by the on-ground telescopes GROND (Updike et al. 2011), APEX (de Ugarte Postigo et al. 2011), EVLA (Zauderer & Berger 2011) and *Gemini-South* (Berger 2011). There were no detections by the *Fermi* satellite. Fig.5.2b shows the XRT light curve of GRB 110709B. XRT was able to detect the whole episode 2, since it had already slewed to detect the emission of the first episode.

The BAT instrument onboard *Swift* was triggered a first time at 21:32:39 UT (trigger N° = 456967). The right ascension and declination of the source as measured by BAT are RA = 164.65 and DEC = -23.45. The light curve of the first trigger presents a spiky structure, and the emission goes from 40 s before the trigger time up to 60 s after it (see Fig.5.3a). The BAT instrument was triggered a second time at 21:43:25 UT (trigger N° = 456969), around 10 minutes after the first trigger time. The equatorial coordinates for this event are RA = 164.647, DEC = -23.464. The light curve shows a bump that begins 100 s before the second trigger time and lasts around 50 s, followed by several overlapping peaks with a total duration of about 40 s, and another isolated peak of 10 s of duration at 200 s after the second trigger time (see Fig.5.3b). There have not been detections in the optical band by the UVOT instrument onboard *Swift*, although it started to observe 70 s after BAT was triggered for the first time.

Zauderer and collaborators (Zauderer & Berger 2011) suggest that this source is an "optically dark" GRB due to the following possible reasons: 1) dust obscuration, 2) intrinsically dim event, and/or 3) high redshift source (optical emission suppressed by Lyα absorption at $\lambda_{obs} \leq 1216\mathring{A}\,(1+z)$). However, the

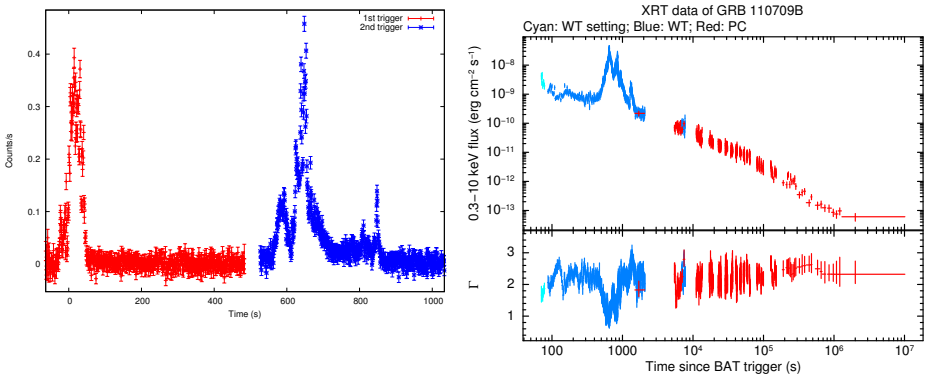

Figure 5.2: a) BAT light curve of GRB 110709B, including the first and second trigger times (red and blue, respectively). There is a separation of about 10 minutes between the first and the second trigger time. The light curve is in the (15-150 keV) energy band. The time is relative to the first trigger time, of 331939966 s (in MET seconds). The second trigger was at 331940612 s in MET seconds. b) XRT light curve in the range $(0.3 - 10$ keV).

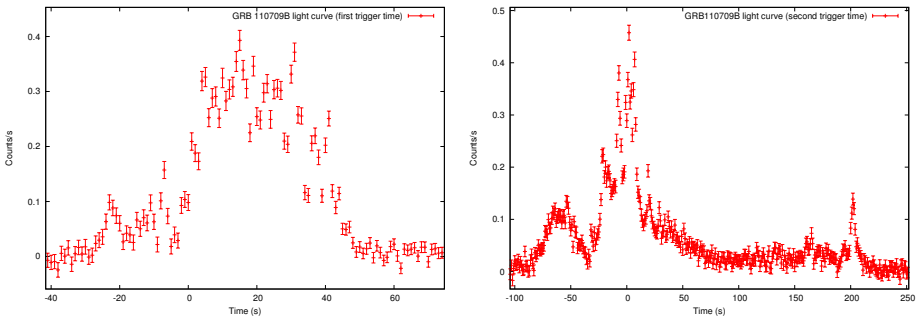

Figure 5.3: Count light curve of episode 1 (left) and episode 2 (right) of GRB 110709B obtained from the *Swift*-BAT detector, in the $(15 - 150$ keV) energy band. The times are relative to the first and second trigger times, of 331939966 s and 331940612 s, respectively (in MET seconds).

Table 5.1: Fit results of Episode 1 with five spectral models: BB, Band, BB+PL, PL and CutoffPL. The flux is in the energy band (15- 150) keV, in units of erg/cm^2/s.

BB	Band	BB+PL	PL	CutoffPL
kT=18.9±0.2	α=−1.2±0.1	kT=22±5	γ=1.37±0.02	γ=1.1±0.1
K_{BB}=0.95±0.01	β=unconstr.	K_{BB}=0.2±0.1	K_{PO}=2.0±0.2	E_0=196±68
	E_0=296±255	γ=1.4±0.1		K=0.8±0.2
		K_{PO}=2.2±0.8		
Redχ^2=7.3	1.031	1.049	1.14	0.99
DOF=56	54	54	56	55
Flux=7.52×10^{-8}	8.99×10^{-8}	8.96×10^{-8}	9.08×10^{-8}	8.93×10^{-8}

third possibility is ruled out, since a host galaxy has been detected in the optical band. Furthermore, they have inferred the optical brightness of the afterglow according to the standard afterglow synchrotron model (Sari et al. 1999; Granot & Sari 2002), and from the non-detection in the optical-NIR wavelengths they find a very large rest frame extinction for GRB 110709B . This can explain the lack of detections in the optical band.

Finally, there have been detections in the radio band on several occasions by EVLA (Zauderer & Berger 2011), revealing a single unresolved radio source within the XRT error circle, which re-brightened by a factor of 1.6 between 2.1 and 7 days after the burst. The location of the source is RA = 10:58:37.114, DEC= -23:27:16.760.

5.3.1 Data analysis

In order to perform a spectral analysis we made use of the *Swift*-BAT data. We call episode 1 the emission from 40 s before the first trigger time to 60 s after it, and episode 2 the emission from 35 s before the second trigger time to 100 s after it. To reduce the data, we used the BAT pipeline, and we used the program XSPEC to fit the spectra.

We fit five different spectral models to episode 1, namely BB, Band (Band et al. 1993), BB+PL, PL and CutoffPL. A statistical test shows that the best models are BB+PL (χ^2 = 56.65) and CutoffPL (χ^2 = 54.45). Since the difference in the χ^2 between these two models is 2.2, the two models are statistically equivalent. So we discriminate between them based on the physical grounds expected from the IGC scenario. As we expect a thermal emission from the expansion of the outer layers of the compact core SN progenitor, we have chosen the BB+PL model. Table 5.1 shows the parameters of the spectral fits with the five models and Fig. 5.4 shows the best spectral fit, with a BB+PL model.

As in the cases of GRB 090618 (Izzo et al. 2012c) and GRB 101023 (Penacchioni et al. 2012), when we perform a time-resolved analysis with a BB+PL model, we find that the temperature of the BB component decreases with time following a broken power-law (see Fig.5.5). As in the previous cases, the simultaneous presence of a BB and PL component is necessary in order to obtain an acceptable fit of the data.

For episode 2, we fit the spectrum with the same five spectral models. We easily discarded the BB and Band models because the χ^2 is too high and there is

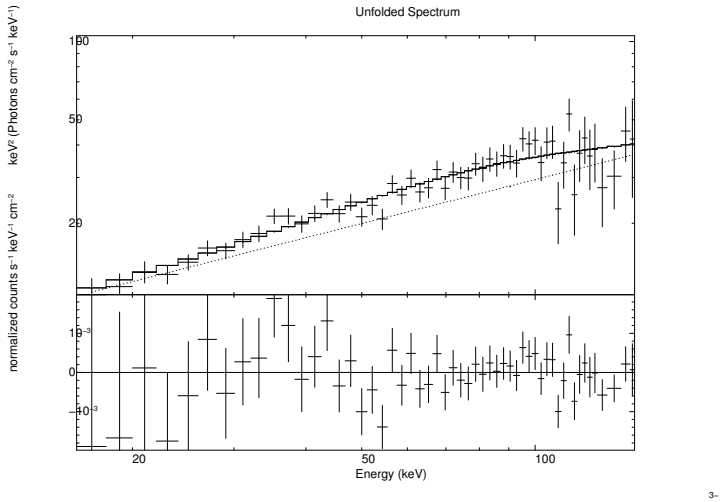

Figure 5.4: Fit of Episode 1 with a BB+PL model. The parameters of the fit are: $kT = (22 \pm 5)$ keV, BB Amp$= 0.2 \pm 0.1$, $\gamma = 1.4 \pm 0.1$, PL Amp$= 2.2 \pm 0.8$, Red-$\chi^2 = 1.049$ (54 DOF).

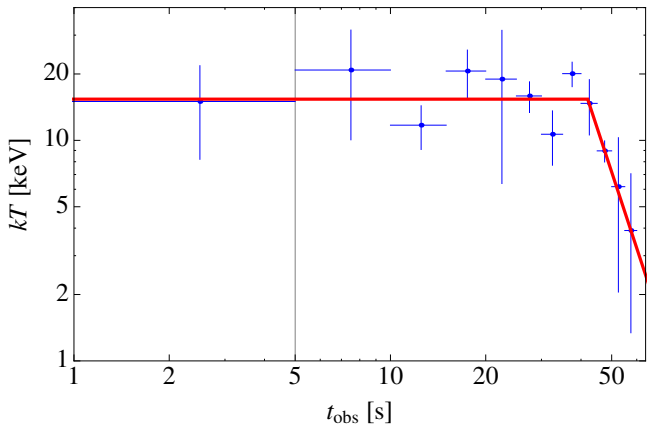

Figure 5.5: Evolution of the temperature of the thermal component in the BB+PL model during episode 1. The first data point corresponds to 5 s before the first BAT trigger. The vertical line corresponds to the trigger time. The time is in the observer frame. The temperature evolves with time following a broken power-law fit. There is a break at $t = 41.21$ s. The indices of the PL are $\alpha = 0$ and $\beta = -4 \pm 2$, respectively.

an unconstrained parameter. We performed a statistical test[1] to choose between the PL and the BB+PL models, as they are nested models.

We obtained a probability Prob=0.001 that the simpler model is better, so the BB+PL dominates over the PL. Then, between the CutoffPL and the BB+PL models, we chose the one with the lower value of the χ^2, which is the CutoffPL.

At a first glance, everything leads to claim that episode 2 is a canonical GRB, but in order to calculate its energy and perform a simulation of its light curve and spectrum we need to know the redshift.

5.3.2 Cosmological redshift estimation

Following the example of GRB 101023 (Penacchioni et al. 2012), which redshift is also unknown, we made use of some phenomenological methods to infer its value.

N_H column density

As already explained in section 4.3.6, we followed the method by Grupe et al. (2007) using the galactic coordinates of this source RA=164.64, DEC=-23.46. We obtained a value of the galactic column density of $N_{H,gal} = 10.5 \times 10^{20}$ cm^{-2} from the Lab Survey website[2]. Then we fit the XRT data from 2000 s to 10^6 s with a power-law corrected by the photoelectric absorption, *phabs*po*. By using the formula of the paper we obtained a value for the total hydrogen column density of $N_{H,fit} = 71.76 \times 10^{20}$ cm^{-2}, and an upper limit for the redshift, $z < 1.35$.

Amati relation

We then made use of the Amati relation, already explained into detail in section 4.3.6. We calculated E_{iso} and $E_{p,i}$ for different values of the redshift, and we found that the relation is satisfied within 1σ for values of the redshift $z \geq 0.4$ (see Fig. 5.6).

[1] F-test: Consider two models, 1 and 2, where model 1 is 'nested' within model 2. Model 1 is the Restricted model, and Model 2 is the Unrestricted one. That is, model 1 has p_1 parameters, and model 2 has p_2 parameters, where $p_2 > p_1$, and for any choice of parameters in model 1, the same regression curve can be achieved by some choice of the parameters of model 2. The model with more parameters will always be able to fit the data at least as well as the model with fewer parameters. Thus typically model 2 will give a better (i.e. lower error) fit to the data than model 1. But one often wants to determine whether model 2 gives a *significantly* better fit to the data. One approach to this problem is to use an F test.

If there are n data points to estimate parameters of both models from, then one can calculate the F statistic, given by

$$F = \frac{\left(\frac{\chi_1^2 - \chi_2^2}{p_2 - p_1}\right)}{\left(\frac{\chi_2^2}{n - p_2}\right)}, \tag{5.7}$$

where χ^2 is the weighted sum of squared residuals. Under the null hypothesis that model 2 does not provide a significantly better fit than model 1, F will have an F distribution, with $(p_2 - p_1, n - p_2)$ degrees of freedom. The null hypothesis is rejected if the F calculated from the data is greater than the critical value of the F-distribution for some desired false-rejection probability (e.g. 0.05).

[2] http://www.astro.uni-bonn.de/ webaiub/english/tools_labsurvey.php

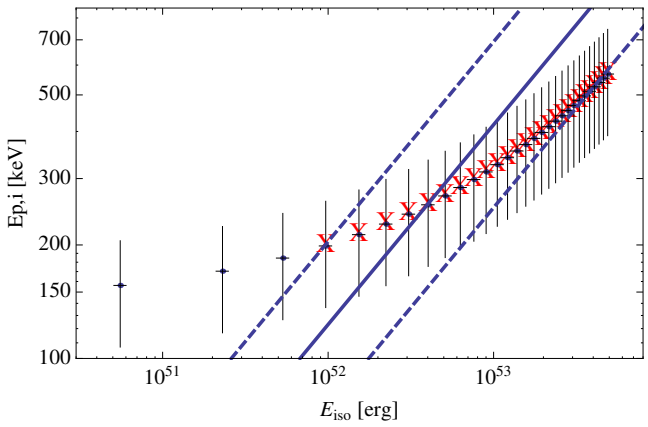

Figure 5.6: Amati relation (solid line) with its 1σ uncertainties (doted lines) and peak energy $E_{p.i}$ vs. E_{iso} for GRB 110709B, for different values of the redshift, from 0.1 to 3, at steps of 0.1. We can see that the data matches the theoretical function within 1σ for $z > 0.4$.

Yonetoku relation

We also made use of the Yonetoku relation (Yonetoku et al. 2004) to infer the redshift of GRB 110709B. The Yonetoku relation is also known as the Peak energy-Luminosity relation ($E_p - L$), as it connects the observed isotropic luminosity L in units of 10^{52} erg s^{-1} with the rest-frame peak energy $E_p(1+z)$. The relation holds for values of the energy between 50 and 2000 keV, and luminosities in the range $(10^{50} - 10^{54})$ erg s^{-1}.

The best fit function for the $E_p - L$ relation is

$$\frac{L}{10^{52}\mathrm{erg\,s^{-1}}} = (2.34^{+2.29}_{-1.76}) \times 10^{-5} \left[\frac{E_p(1+z)}{1\ \mathrm{keV}}\right]^{2.0\pm0.2}. \tag{5.8}$$

The peak luminosity and the peak energy are calculated by integrating within a 1 s interval around the most intense peak of the light curve. The peak luminosity is given by

$$L = 4\pi d_L^2 F_{bol}, \tag{5.9}$$

where F_{bol} is the bolometric fluence, given by

$$F_{bol} = P_{obs} \frac{\int_{1/(1+z)}^{10000/(1+z)} EN(E)dE}{\int_{E_{min}}^{E_{max}} N(E)dE} \tag{5.10}$$

and P_{obs} is the observed photon flux.

The Yonetoku relation is satisfied within 1σ for $z > 0.7$ (see Fig.5.7). This result is in agreement with the Amati relation. Moreover, if we take into account also the upper limit from the Grupe method we obtain a range of possible redshifts: $0.7 < z < 1.35$.

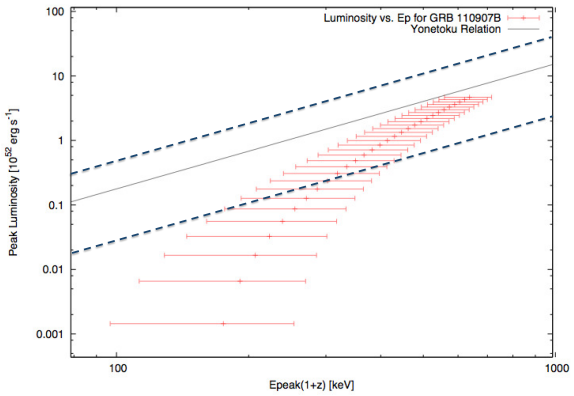

Figure 5.7: Yonetoku relation (solid line) with its 1σ uncertainties (dotted lines) and peak Luminosity vs. $E_{p,i}$ for GRB 110709B, for different values of the redshift, from 0.1 to 3, at steps of 0.1. The data match the theoretical function within 1σ for $z > 0.7$.

Analysis of the late X-ray light curve

Following the procedure presented in Sec. 4.3.6, we rescaled the X-ray light curve of the already known source GRB 090618 as if it were seen at different redshifts, and plotted it together with GRB 110709B observed light curve. To do this, we performed a spectral analysis of the late decay of GRB 090618 with an absorbed power-law spectral model. We extrapolated the spectrum to a common cosmological rest-frame energy range for a given value of the redshift. Then we corrected the arrival time for this given value of z, which implies a correction to the observed flux. In this way we compared directly both light curves. A more detailed description of this method is given in Pisani et al. (2013). Fig. 5.8a shows GRB 110709B observed light curve (red) together with GRB 090618 light curve as if the source were located at different redshifts: 0.2 (blue), 0.4 (green), 0.7 (gray), 1.0 (orange) and 2.0 (purple). A more accurate scaling of the X-ray late afterglow suggests a redshift $z = 0.75$ for GRB 110709B (see Fig. 5.8b).

We adopted the value of $z = 0.75$ as the redshift of GRB 110709B for the following analysis.

5.3.3 Radius of the emitting region

With the energy flux of the BB component ϕ_{BB} as a function of time from the time-resolved spectral analysis and the luminosity distance d_L, we can compute the value of the radius of the emitter in cm through the formula

$$r_{em} = \sqrt{\frac{\phi_{BB}}{\sigma T^4}} \frac{d_L}{(1+z)^2}, \tag{5.11}$$

where the BB flux is in units of $erg\ cm^{-2}\ s^{-1}$, $\sigma = 5.6704\ erg\ cm^2\ s^{-1}\ K^{-4}$ is the Stefan-Boltzmann constant and d_L is the luminosity distance in cm. The

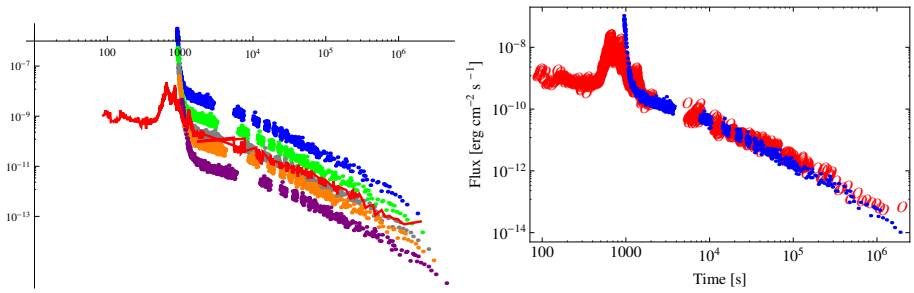

Figure 5.8: a) Plot of GRB 090618 seen as if it were at different redshifts: 0.2 (blue), 0.4 (green), 0.7 (gray), 1.0 (orange), and 2.0 (purple), together with GRB 110709B observed X-ray light curve (red). We can see that the red light curve lies between the green and the orange light curves, indicating that the redshift must be between 0.4 and 1.0. b) GRB 090618 light curve (blue) as if it were seen at z = 0.75 together with the GRB 110709B light curve (red). There is an excellent superposition in the late decay.

best fit for the expanding radius is $r(t) = at^b$, with $a = (1.5 \pm 1.2) \times 10^4$ km s^{-b} and $b = 0.32 \pm 0.27$ (see Fig. 5.9).

As we interpret form the IGC model, we associate the BB component to the expansion of the ejected material, while the power-law is associated with the accretion of part of this material onto the NS companion. We will come back to this discussion in Sec.5.3.5 .

5.3.4 Episode 2 in the Fireshell model

Once we fixed the value of the redshift of GRB 110709B to $z = 0.75$, we started the analysis of episode 2 in the fireshell model. We first looked for the P-GRB in the first bump (from 100 s to 40 s before the second trigger time), but the fits were poor or we needed a too big baryon load, $B > 10^{-2}$, which has no physical meaning. This led us to conclude that this bump should belong to episode 1. From a theoretical point of view, we found no thermal signatures here because episode 1 starts ~ 10 minutes before, and the temperature of the BB component decreases with time as a power-law. After such a long time we do not expect to see any thermal signature from episode 1.

We selected the P-GRB as the nine-second-interval from 35 to 26 s before the second trigger time, and the emission from -26 to 100 s as the extended afterglow. The parameters of the fit are shown in Table 5.2. Inserting these values into the numerical code allowed us to calculate the baryon load, $B = 5.7 \times 10^{-3}$. We then simulated the light curve and the spectrum (see Fig.5.10) obtaining, at the transparency point, a laboratory radius $r_{tr} = 6.04 \times 10^{13}$ cm, a gamma Lorentz factor $\Gamma = 1.73 \times 10^2$ and a P-GRB observed temperature (after cosmological correction) $kT = 12.36$ keV. The photon index of the XRT and BAT spectra are in agreement with that predicted by the simulation. It is important to mention that this is one of the few sources for which we have simultaneous gamma and X-ray data of the prompt emission, since by the time the BAT instrument was triggered for the second time, the XRT was already pointing at the source and was able to detect the whole emission of episode 2.

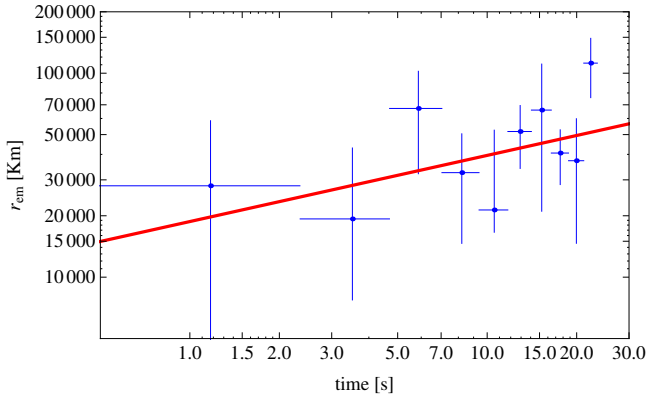

Figure 5.9: Radius of the emitting region as a function of time (in the cosmological rest frame), corresponding to episode 1. The radius increases with time following a power-law at^b, with $a = (1.5 \pm 1.2) \times 10^4$ km/s and $b = 0.32 \pm 0.27$.

Table 5.2: Fit of the P-GRB and the afterglow of GRB 110709B, Episode 2. The P-GRB is well fit with a BB model, while the whole Episode 2 is best fit by a CutoffPL model. From this fit and the value of the redshift we are able to calculate E_{iso} and E_{P-GRB}.

Parameter	P-GRB	P-GRB+Afterglow
kT [keV]	14 ± 1	
BB Amp	0.30 ± 0.02	
γ		1.03 ± 0.1
PL Amp		0.5 ± 0.1
Red χ^2	1.448 (56 DOF)	0.77 (55 DOF)
Energy Flux $(15 - 150$ keV) [erg cm^{-2} s^{-1}]	2.413×10^{-8}	6.34×10^{-8}
Energy [erg]	3.44×10^{50}	2.43×10^{52}

Finally, Fig.5.11 shows the simulated particle density of the ISM as a function of the radius. The mean density is 76 part/cm^3, which is quite high. This is in agreement with GRB 110709B being a "dark" GRB.

5.3.5 Nature of the progenitor

We suggest for the origin of GRB 110709B a binary system formed by a massive evolved star on the verge of an SN explosion and an NS. The early SN material expanding at non-relativistic velocities is then accreted by the NS companion at times longer than $t_{0,accr}$, when the material reaches the NS gravitational capture region. The emission observed in episode 1 is associated to this early SN evolution, which is identified with the thermal component, and the accretion process onto the NS, which is possibly related to the non-thermal component. The NS reaches the critical mass in a time $t_{0,accr} + t_{accr}$ and gravitationally collapses to a black hole, emitting the GRB seen in episode 2. We assume the

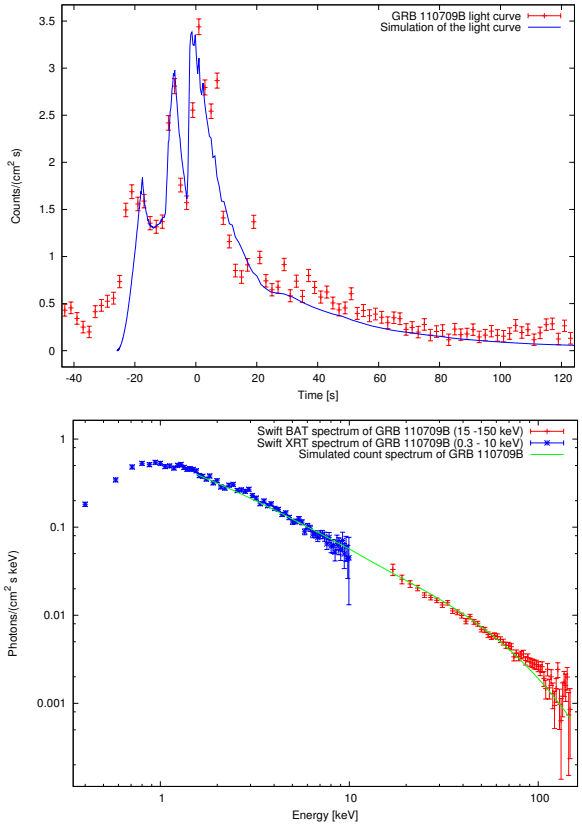

Figure 5.10: Simulation of the BAT light curve (up) and BAT+XRT spectrum (down) of episode 2. We included XRT data in the fit of the spectrum to show that the slope predicted in the fireshell model agrees with the slope of the X-ray spectrum, too.

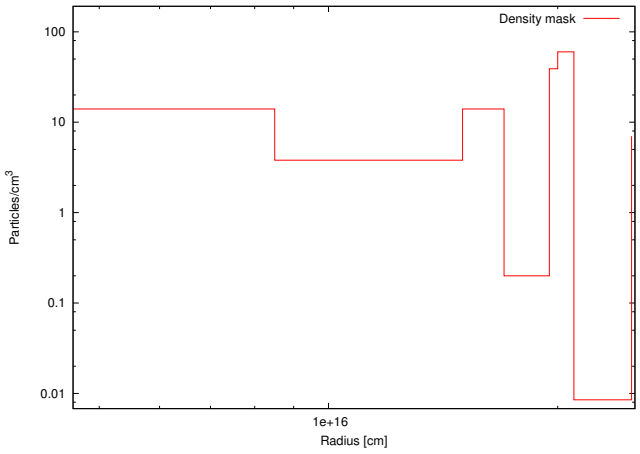

Figure 5.11: Particle density of the ISM clouds as a function of the distance. The mean density is 76 part/cm^3.

critical mass of a non-rotating NS $M_{crit} = 2.67 M_{\odot}$ as given by Belvedere et al. (2012).

Since the power-law component is present from the beginning of episode 1, we fixed the value of $t_{0,accr}$ to be equal to the starting time of episode 1. This constrains the separation distance a of the binary, which under these conditions is given by

$$a = r_0 + R_{cap}(0), \tag{5.12}$$

where $r_0 = r_{ej}(0)$ and $R_{cap}(0)$ are the radius of the early SN ejecta and the capture radius of the NS companion at the beginning of episode 1. In this case, $r_0 \approx 1.75 \times 10^9$ cm, as can be seen form Fig. 5.9. The separation a is a function of the initial mass of the NS and of the SN core progenitor mass, as well as of the orbital velocity, through R_{cap} (Eq.5.1). It has to be noticed that Eq.(5.12) is a lower limit for the value of the separation distance, since the accretion process onto the NS could have been triggered before, for example by layers at lower densities (e.g. He), which makes the separation a higher.

Moreover, we need to take into account that the NS companion must reach its critical mass M_{crit} exactly at the beginning of episode 2, since at that time the canonical GRB is produced. So, the NS must already have collapsed to a BH by that time. As the time interval between episode 1 and episode 2 is 611 s, we have that, in the rest frame,

$$\Delta t_{accr} \approx \frac{611}{(1+z)} \approx 349 s. \tag{5.13}$$

Table 5.3 shows the parameters of the binary system leading to the induced gravitational collapse of the NS in a time interval equal to the duration of episode 1. We adopted an initial mass for the NS, $M_{NS}(0) = 1.4 M_{\odot}$ and an NS radius of $R_{NS}(0) = 12.3$ km from the mass-radius relation of Belvedere et al. (2012). From the constraint given by Eq.(5.12), we fixed the binary separation a. We then proceeded with the numerical integration of the accretion rate equations by requiring that $M_{NS}(t) = M_{crit}$ at $t = \Delta t_{accr}$, given by Eq.(5.13), from which we obtained the efficiency μ_{accr} .

How can the NS accrete such a large mass, in some cases on the order of 47 % of the early SN material? During the accretion process, the NS is moving with a high orbital velocity relative to the core progenitor ($\sim 10^8$ cm/s), and consequently travels effective arc-lengths several times longer than the circumference of the orbit (see column $\Delta t_{\rm accr}/P$ of Table 5.3).

Which is the luminosity of the system? If we assume that the gain in gravitational energy of the accreted material onto the NS can be released from the system, we have an upper limit for the luminosity given by

$$|\dot{E}_b(t)| = \frac{G \dot{M}_{\rm accr}(t) M_{\rm NS}(t)}{R_{\rm NS}(t)}, \tag{5.14}$$

where we take into account the dependence of the NS radius with time, due to the increment of the NS mass by the accretion process. The self-consistent radius is computed at each time from the mass-radius relation of Belvedere et al. (2012).

The luminosity depends on the efficiency ν_{rad} in converting gravitational energy into electromagnetic energy by some process that we still do not know.

$M_{\rm prog}/M_\odot$	$M_{\rm ej}(0)/M_\odot$	$\rho_{\rm ej}(0)$ (g cm^{-3})	$\eta_{\rm accr}$	$\Delta M_{\rm accr}/M_{\rm ej}(0)$
4	2.7	2.39×10^5	0.92	0.47
5	3.7	3.27×10^5	0.88	0.34
6	4.7	4.16×10^5	0.88	0.27
7	5.7	5.04×10^5	0.89	0.22
8	6.7	5.93×10^5	0.91	0.19
9	7.7	6.81×10^5	0.94	0.16
10	8.7	7.69×10^5	0.96	0.15

$M_{\rm prog}/M_\odot$	P (min)	$v_{\rm orb,NS}(0)$ (km s^{-1})	$\Delta t_{\rm accr}/P$	$a/R_\odot$
4	0.52	5.24×10^3	11.14	0.037
5	0.45	5.84×10^3	12.96	0.036
6	0.39	6.39×10^3	14.71	0.035
7	0.35	6.91×10^3	16.39	0.034
8	0.32	7.40×10^3	18.00	0.033
9	0.30	7.87×10^3	19.55	0.032
10	0.27	8.32×10^3	21.04	0.031

Table 5.3: The massive star - neutron star binary progenitor of GRB 110709B. $M_{\rm prog}$ is the mass of the massive star (in solar masses), $M_{\rm ej}(0)$ is the mass of the ejected material in the early-SN phase (in solar masses), $\rho_{\rm ej}(0)$ is the density of the ejecta at the beginning of the expansion, $\eta_{\rm accr}$ is the efficiency of the accretion process onto the NS, $\Delta M_{\rm accr} = M_{\rm crit} - M_{\rm NS}(0)$ is the total mass accreted by the NS before the collapse, $P = 2\pi a/v_{\rm orb,NS}$ is the period of the binary, $v_{\rm orb,NS}(0)$ is the initial orbital velocity of the NS and $\Delta t_{\rm accr}/P$ is the arc-length travelled by the NS during the accretion process in units of the length of the whole orbit and $a/R_\odot$ is the binary separation (in units of solar radii). We suppose that the accretion process starts 5 s before the first trigger, i.e. $t_{0,\rm accr}$ coincides with the time corresponding to the first datapoint in Fig.5.5.

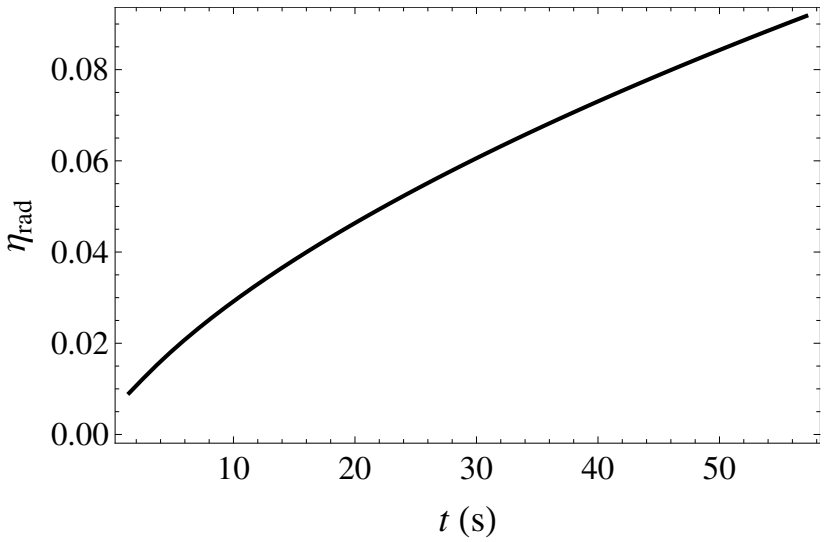

Figure 5.12: Theoretical estimation of the efficiency $\eta_{\rm rad}$ given by Eq. (5.15) of the process to convert gravitational energy in radiation as a function of time. For this plot, we have assumed a constant and isotropic power-law luminosity of Episode 1, $L_{\rm PL} \approx 1.8 \times 10^{50}$ erg s^{-1} $\approx 10^{-4}$ $M_\odot$ s^{-1}. We computed the values of the efficiency for the binary systems shown in Table 5.3. For all the cases, we obtain the same evolution of the efficiency with time, i.e. the curves overlap. The values of $\eta_{\rm rad}$ are always $< 10\%$.

We estimated the efficiency by assuming that $|\dot{E}_b|$ is responsible for the PL luminosity, since the BB luminosity is caused by the early SN expansion. We then have

$$\eta_{\rm rad}(t) = \frac{L_{\rm PL}}{|\dot{E}_b(t)|}. \tag{5.15}$$

The evolution of $\eta_{\rm rad}$ with time in the first seconds of emission is shown in Fig.5.12 for the binary systems considered in Table 5.3. We assumed a constant and isotropic power-law luminosity of episode 1, as found from the spectral analysis, $L_{PL} \approx 1.8 \times 10^{50}$ erg s^{-1} $\approx 10^{-4} M_\odot$ s^{-1}. For all the cases the curves overlap, namely, we obtain the same evolution of the efficiency with time. This is because we constrained all the systems to have the same initial NS mass and Δt_{accr}.

5.4 Conclusions

It is clear that GRB 110709B is a very peculiar source. It is the first source that has triggered the BAT detector twice and it presents two well-defined episodes. The total isotropic energy of episode 1 is $E^{(1)} = 1.42 \times 10^{53}$ erg. The total isotropic energy of episode 2 is $E^{(2)} = 2.43 \times 10^{52}$ erg.

There is no measured redshift for this source, so we inferred it by phenomenological methods, using the Amati relation (Amati 2006b), the Yonetoku relation (Yonetoku et al. 2004, 2010), the method developed by Grupe et al. (2007) and

our scaling of the X-ray afterglow light curve. We found a redshift $z = 0.75$. The four methods are consistent with this value.

We interpret this source as another member of the IGC family, together with GRB 101023 (Penacchioni et al. 2012), GRB 090618 (Izzo et al. 2012a,c) and GRB 970828 (Izzo et al. 2012b). The progenitor is a binary system formed by a massive evolved star on the verge of an SN explosion and an NS companion.

Episode 1 is fit by a BB+PL model. The temperature of the BB component evolves with time following a broken power-law. We calculated the radius of the emitting region and associated it to the evolution of the SN ejecta, while the power-law component is interpreted as due to the accretion of the ejecta onto the NS companion. Episode 2 is fit by a power-law model with an exponential cutoff. We interpret this episode as a canonical GRB. We simulated the light curve and spectrum within the fireshell model with the numerical code developed by the group and found at the transparency point the following parameters: Lorentz factor $\Gamma \sim 1.73\times10^2$, laboratory radius 6.04×10^{13} cm, P-GRB observed temperature $kT_{P-GRB} = 12.36$ keV, baryon load $B = 5.7\times10^{-3}$, P-GRB energy $E_{P-GRB} = 3.44 \times 10^{50}$ erg, and a CBM mean density of 76 part cm^{-3}. This value is consistent with a "dark GRB", as cited in Zauderer & Berger (2011). The lack of detection of an SN emission for this particular GRB could be due to obscuration by the circumstellar dust in the host galaxy.

There is the possibility that the accretion process also contributes thermally. The energy from just the thermal component is on the order of 10^{50} erg, which is reasonable for the expansion of the early SN ejecta. We performed all the necessary calculations to obtain the parameters of the binary system. For all our calculations we assumed a fixed NS mass of $1.4M_\odot$. We computed the rate at which the early SN material enters the capture region, for given values of the SN core progenitor mass. From this material, only a fraction will be accreted by the NS, therefore we introduced an efficiency factor μ_{accr}. Since the power-law component is present since the beginning of episode 1, we assumed that this episode starts at the same time $t_{0,accr}$ as the accretion process, namely, when the outermost shell of expanding ejecta reaches the capture radius R_{cap} of the NS (measured from the center of the NS). This puts a constraint on the separation distance a of the binary. In addition, the NS must reach its critical mass and collapse to a BH at the beginning of episode 2. This puts a constraint on the duration of the accretion process Δt_{accr}. By integrating the accretion rate equations with these boundary conditions we obtained the efficiency μ_{accr}. We summarized the results in Table 5.3 for different values of the core-progenitor mass and the density of the early SN ejecta. Assuming that the power-law radiation comes from the conversion of the binding energy of the accreted material onto the NS, we estimated the efficiency μ_{rad} of this conversion process, which we show in Fig.5.12 for an isotropic power-law luminosity $L_{PL} \approx 1.8 \times 10^{50}$ erg s^{-1} $\approx 10^{-4}M_\odot$ s^{-1} observed in episode 1. For the parameters of the binary system shown in Table 5.3, we obtained values of $\mu_{rad} < 10\%$. The efficiency of the radiation mechanism can be even lower if some beaming or boosting is present. However, we did not address any such possible mechanism in this work.

A&A 551, A133 (2013)
DOI: 10.1051/0004-6361/201220679

Astronomy & Astrophysics

GRB 110709B in the induced gravitational collapse paradigm

A. V. Penacchioni[1,3], R. Ruffini[1,2], C. L. Bianco[1,2], L. Izzo[1], M. Muccino[1], G. B. Pisani[1,3], and J. A. Rueda[1,2]

[1] Dip. di Fisica, Sapienza Università di Roma and ICRA, Piazzale Aldo Moro 5, 00185 Roma, Italy
e-mail: [ruffini;luca.izzo;marco.muccino;bianco;jorge.rueda]@icra.it
[2] ICRANet, Piazzale della Repubblica 10, 65122 Pescara, Italy
[3] Université de Nice Sophia Antipolis, Nice Cedex 2, Grand Chateau Parc Valrose, France
e-mail: ana.penacchioni@icra.it

Received 31 October 2012 / Accepted 20 January 2013

ABSTRACT

Context. Gamma-ray burst (GRB) 110709B is the first source for which *Swift*-BAT was triggered twice, with a time separation of ∼10 min. The first emission (called here episode 1) lasted from 40 s before the first trigger time until 60 s after it. The second emission (hereafter episode 2) lasted from 35 s before the second trigger time until 100 s after it. These features reproduce those of GRB 090618, which has recently been interpreted within the induced gravitational collapse (IGC) paradigm. In line with this paradigm, we assume the progenitor to be a close binary system composed of the core of an evolved star and a neutron star (NS). The evolved star explodes as a supernova (SN) and ejects material that is partially accreted by the NS. We identify this process with episode 1. The accretion process accumulates more than the critical mass of the NS, which gravitationally collapses into a black hole (BH). This process leads to the GRB emission, episode 2. The two trigger episodes have for the first time provided the possibility to cover the X-ray emission observed by XRT both prior to and during the prompt phase of GRB 110709B.
Aims. We analyze the spectra and time variability of episodes 1 and 2 and compute the relevant parameters of the binary progenitor, as well as the astrophysical parameters both in the SN and the GRB phase in the IGC paradigm.
Methods. We performed a time-resolved spectral analysis of episode 1 by fitting the spectrum with a blackbody (BB) plus a power-law (PL) spectral model. From the BB fluxes and temperatures of episode 1 and the luminosity distance $d_{\rm L}$, we evaluated the evolution with time of the radius of the BB emitter, associated here to the evolution of the SN ejecta. We analyzed episode 2 within the fireshell model, identifying the proper GRB (P-GRB) and simulating the light curve and spectrum. We established the redshift to be $z = 0.75$, following the phenomenological methods described in the literature, and our analysis of the late X-ray afterglow. It is most remarkable that the determination of the cosmological redshift on the basis of scaling the late X-ray afterglow, which was already verified in GRB 090618 and GRB 101023, is again verified by this analysis.
Results. We find for episode 1 a temperature of the BB component that evolves with time following a broken PL, with the slope of the PL at early times $\alpha = 0$ (constant function) and the slope of the PL at late times $\beta = -4 \pm 2$. The break occurs at $t = 41.21$ s. The total energy of episode 1 is $E^{(1)}_{\rm iso} = 1.42 \times 10^{53}$ erg. The total energy of episode 2 is $E^{(2)}_{\rm iso} = 2.43 \times 10^{52}$ erg. We find at transparency a Lorentz factor $\Gamma \sim 1.73 \times 10^2$, laboratory radius of 6.04×10^{13} cm, P-GRB observed temperature $kT_{\rm P-GRB} = 12.36$ keV, baryon load $B = 5.7 \times 10^{-3}$ and P-GRB energy of $E_{\rm P-GRB} = 3.44 \times 10^{50}$ erg. We find a remarkable coincidence of the cosmological redshift by scaling the XRT data and with three other phenomenological methods.
Conclusions. We interpret GRB 110709B as a member of the IGC sources, together with GRB 970828, GRB 090618, and GRB 101023. The existence of the XRT data during the prompt phase of the emission of GRB 110709B (episode 2) offers an unprecedented tool for improving the diagnostic of GRBs emission.

Key words. Gamma-ray burst: individual: GRB 110709B – black hole physics

1. Introduction

Of all the astrophysical processes that are currently being analyzed, few are more fundamental than the one presenting the coincidence of some gamma-ray bursts (GRBs) with the explosion of a supernova (SN). For this, the induced gravitational collapse (IGC) paradigm was first introduced by Ruffini et al. (2001b) and was subsequently analyzed in Ruffini et al. (2007, 2008); Rueda & Ruffini (2012), and Izzo et al. (2012b). Recently, it has been shown that this process can indeed explain the coincidence between the SN and GRB emission, both from an observational and a theoretical point of view (Izzo et al. 2012a; Penacchioni et al. 2012).

In the IGC paradigm (Ruffini et al. 2001b, 2007), a binary system formed by an evolved star and a neutron star (NS) companion is considered as the progenitor.

The IGC paradigm implies a well-determined time sequence. In a close binary system of a massive star in the latest phases of its thermonuclear evolution and an NS companion, the massive star undergoes an SN explosion. The accretion of the early SN material onto the NS companion leads the NS to its critical mass and consequently to its gravitational collapse to form a black hole (BH). The emission of a canonical GRB in the collapse to the BH takes place. A young NS is born out of the SN explosion. Finally, an SN emission is either observed or expected in association with the GRB, ∼10 days after the burst in the rest frame. We aim to find sources in which the data are of a sufficiently good quality to allow us to see this complete sequence.

The prototype for the IGC paradigm has recently been given in the analysis of GRB 090618 (Izzo et al. 2012a), following the works of Rueda & Ruffini (2012) and Izzo et al. (2012b). In this work we follow the same line and identify four different

episodes in GRB 110709B. Episode 1 starts 40 s before the first trigger time and lasts up to 60 s after it. It is well-fit by a blackbody (BB) plus power-law (PL) spectral model. It corresponds to the trigger of the SN explosion of the compact core and its accretion onto the NS companion. The BB temperature decays with time following a broken PL (Ryde 2004). Episode 2 starts 35 s before the second trigger time and lasts up to 100 s after it. It corresponds to the emission of the canonical GRB emitted in the formation of a BH. Episode 3 starts at 800 s all the way to 10^6 s. It consists of a standard X-ray emission identified in all systems following the IGC paradigm (Pisani et al., in prep.). Episode 4 corresponds to the observation of the optical SN emission, observable after $T_{\rm obs} = (1+z)T_{\rm SN}$. In the present case, there is no evidence of an associated SN in the optical band. An explanation for this is given by Zauderer et al. (2012), who classified GRB 110709B as dark and stated that its optical emission may have been absorbed by the host galaxy and/or the interstellar medium (ISM). The ensemble of these four episodes characterize the IGC scenario.

As an outcome, at the endpoint of the IGC scenario, a binary system represented by an NS (formed by the SN explosion) and a BH (formed after the GRB explosion) should be expected.

As in the case of GRB 101023, we do not know the cosmological redshift of GRB 110709B due to the lack of optical data. Therefore, we infer it from phenomenological methods: 1) the Amati relation (Amati 2006), 2) the Yonetoku relation (Yonetoku 2004, 2010), 3) the work of Grupe et al. (2007), and 4) the work by Penacchioni et al. (2012), Ruffini (2012), and Pisani et al. (in prep.), which describe a scaling of the late X-ray emission of GRB 090618. In the case of GRB 111228, which we are currently analyzing, we find a striking coincidence between the values of the cosmological redshift determined by these methods for GRB 110709B.

In Sect. 2 we report the observations of the two components of GRB 110709B by the different instruments, in space and on the ground. In Sect. 3 we reduce the *Swift* data and perform a detailed spectral analysis of both episodes 1 and 2. In Sect. 4 we infer the redshift of the source using the four phenomenological methods mentioned above. In Sect. 5 we determine the radius of the emitting region from the knowledge of the redshift and the BB flux of the first episode. In Sect. 6 we give a brief description of the fireshell model and perform a deeper analysis of episode 2 within this model, reproducing the light curve and the spectrum by a numerical simulation. In Sect. 7 we calculate the parameters of the binary progenitor leading to the IGC of the NS to a BH by the SN explosion. Details on the accretion rate onto the NS, total accreted mass, SN ejecta density, NS mass, and binary orbital period are obtained for selected values of the SN progenitor mass. In Sect. 8 we comment on the radio emission detected by EVLA (Zauderer & Berger 2012). In Sect. 9 we present the conclusions.

2. Observations of GRB 110709B

GRB 110709B has been detected by the *Suzaku* (Ohmori et al. 2011) and *Swift* (Cummings et al. 2011) satellites and by the ground-based telescopes GROND (Updike et al. 2011) and Gemini (Berger 2011).

The Burst Alert Telescope (BAT) onboard *Swift* was triggered a first time at 21:32:39 UT (trigger N° = 456 967). The location of this event is RA = 164.6552, Dec = –23.4550. The light curve is composed of multiple peaks, with the whole emission extending up to 60 s after the trigger (see Fig. 1). What is most interesting is that there was another trigger point at 21:43:25 UT

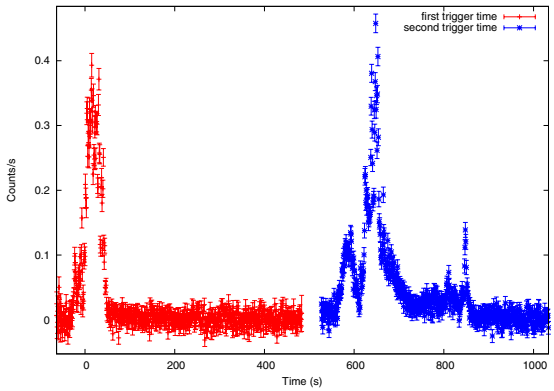

Fig. 1. BAT light curve of GRB 110709B, including the two trigger times. Here we can appreciate the time separation (about 10 min) between the first and the second trigger. The light curve is in the (15–150 keV) energy band. The time is relative to the first trigger time, of 331 939 966 s (in MET seconds). The second trigger time was at 331 940 612 s in MET seconds.

(trigger N° = 456 969), ~11 min after the first trigger time. The onboard calculated location is RA = 164.647, Dec = –23.464. This time *Swift* did not need to slew, because it was already pointing to that position. This second emission shows a bump that begins 100 s before the second trigger time and lasts around 50 s, followed by several overlapping peaks with a total duration of about 40 s, and another isolated peak of 10 s of duration, 200 s after the second trigger time. Figure 1 shows the complete BAT light curve and Fig. 2 shows the light curve taken by the X-Ray Telescope (XRT) in the 0.3–10 keV band.

There have been no detections in the optical band by *Swift*-UVOT, which started to observe 70 s after the first BAT trigger time (Holland 2011). The observations with GROND at the La Silla Observatory (Updike et al. 2011) simultaneously in the g' r' i' z' JHK, reveal two point sources within the 5".3 XRT error circle reported by Cummings et al. (2011). They suggest that one of them could be an afterglow candidate for GRB 110709B, although it is very faint.

It has been suggested by Zauderer et al. (2012) that this source is an "optically dark" GRB. The possible reasons for this are 1) dust obscuration; 2) an intrinsically dim event; and/or 3) high redshift (optical emission suppressed by Lyα absorption at $\lambda_{\rm obs} \leq 1216\,\text{Å}\,(1+z)$). However, they rule out the possibility of a high-redshift event due to the association with an optically detected host galaxy. Furthermore, they have inferred the optical brightness of the afterglow according to the standard afterglow synchrotron model (Granot & Sari 2002; Sari et al. 1999), and from the non-detection in the optical-near-infrared (NIR) wavelengths they find a very high rest-frame extinction for GRB 110709B. This can explain the lack of detections in the optical band.

There have been detections in the radio band on several occasions by EVLA (Zauderer & Berger 2012), revealing a single unresolved radio source within the XRT error circle, which rebrightened by a factor of 1.6 between 2.1 and 7 days after the burst. The location of the source is RA = 10:58:37.114, Dec = –23:27:16.760.

3. Data analysis

In the following we refer to the emission that lasted from 40 s before the first BAT trigger time to 60 s after it as episode 1 (see Fig. 3). We call the emission lasting from 35 s before the

Table 1. Fit results of episode 1 with five spectral models: BB, Band, BB+PL, PL and cutoffPL.

BB	Band	BB+PL	PL	cutoffPL
$kT = 18.9 \pm 0.2$	$\alpha = -1.2 \pm 0.1$	$kT = 22 \pm 5$	$\gamma = 1.37 \pm 0.02$	$\gamma = 1.1 \pm 0.1$
$K_{BB} = 0.95 \pm 0.01$	β = unconstr.	$K_{BB} = 0.2 \pm 0.1$	$K_{PO} = 2.0 \pm 0.2$	$E_0 = 196 \pm 68$
	$E_0 = 296 \pm 255$	$\gamma = 1.4 \pm 0.1$		$K = 0.8 \pm 0.2$
		$K_{PO} = 2.2 \pm 0.8$		
Red$\chi^2 = 7.3$	Red$\chi^2 = 1.031$	Red$\chi^2 = 1.049$	Red$\chi^2 = 1.14$	Red$\chi^2 = 0.99$
56 D.O.F.	54 D.O.F.	54 D.O.F.	56 D.O.F.	55 D.O.F.
Flux $= 7.52 \times 10^{-8}$	Flux $= 8.99 \times 10^{-8}$	Flux $= 8.96 \times 10^{-8}$	Flux $= 9.08 \times 10^{-8}$	Flux $= 8.93 \times 10^{-8}$

Notes. The flux is measured in the energy band (15–150) keV, in units of erg/cm^2/s.

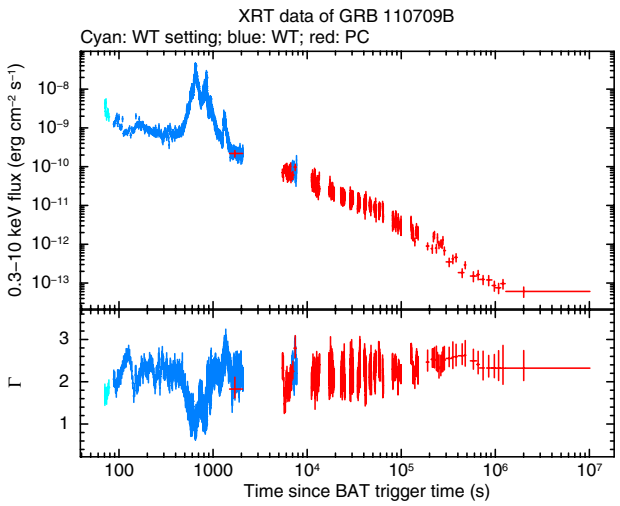

Fig. 2. Count light curve of GRB 110709B obtained from the *Swift*-XRT detector in the (0.3–10 keV) energy band. The time is relative to the first trigger time, of 331 939 966 s (in MET seconds). Picture taken from http://www.swift.ac.uk/xrt_curves/00456967/

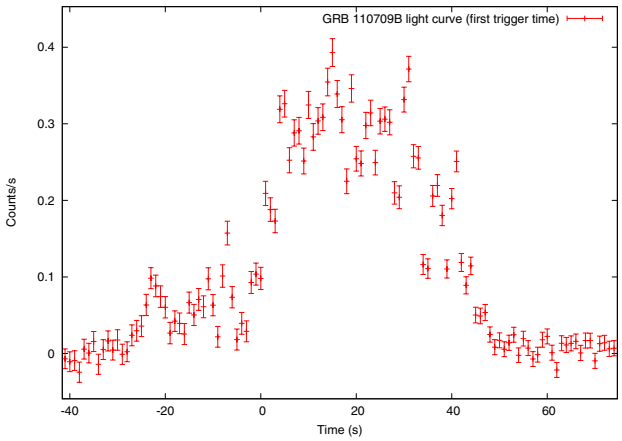

Fig. 3. Count light curve of episode 1 of GRB 110709B obtained from the *Swift*-BAT detector in the (15–150 keV) energy band. The time is relative to the first trigger time, of 331 939 966 s (in MET seconds).

second BAT trigger time to 100 s after it as episode 2. We used *Swift*-BAT data to perform the spectral analysis with XSPEC.

3.1. Episode 1

We performed a time-integrated analysis of the whole episode 1 using five different spectral models, BB, Band (Band et al. 1993),

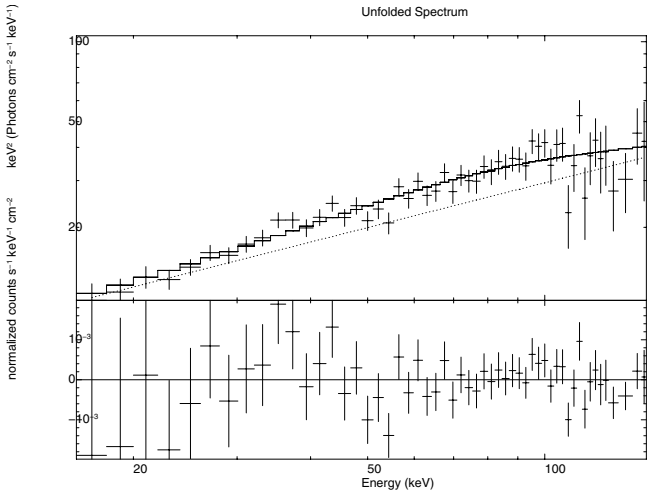

Fig. 4. Fit of episode 1 with a BB+PL model. The parameters of the fit are $kT = (22 \pm 5)$ keV, BB Amp $= 0.2 \pm 0.1$, $\gamma = 1.4 \pm 0.1$, PL Amp $= 2.2 \pm 0.8$, Red-$\chi^2 = 1.049$ (54 D.O.F.).

BB+PL, PL, and cutoffPL. The results of the fits are shown in Table 1 and in Fig. 4. The Band function is not well constrained, therefore we excluded it from the following analysis. A statistical test shows that the best models are BB+PL ($\chi^2 = 56.65$) and cutoffPL ($\chi^2 = 54.45$). Since the difference in the χ^2 between these two models is 2.2, the two models are statistically equivalent, therefore we distinguished between these two models based on the physical grounds expected from the IGC scenario. In this scenario, we expect a thermal emission from the expansion of the outer layers of the compact-core SN progenitor. Accordingly, we chose the BB+PL model. We obtain a BB temperature $kT = (22 \pm 5)$ keV, a PL index $\gamma = 1.4 \pm 0.1$ and a $\chi^2 = 56.65$ (54 D.O.F.). The flux of the BB component is ~12% of the total flux. The total energy of episode 1 is $E_{iso}^{Ep_1} = 1.42 \times 10^{53}$ erg. The results of the fit are shown in Table 1. Then we performed a time-resolved spectral analysis with a binning of 5 s fitting the same model and found that the temperature of the BB component follows a broken power-law, as mentioned in Ryde (2004), from 5 s before the trigger time to 55 s after it (see Fig. 5). The broken PL is indeed a constant function plus a simple power-law function. This is the same behavior as observed in the previously analyzed GRB 090618 (Izzo et al. 2012a) and GRB 101023 (Penacchioni et al. 2012). However, the temperatures for this GRB are lower. Nevertheless, the simultaneous presence of a BB and PL component is necessary to obtain an acceptable fit of the data (see Fig. 4).

Table 2. Spectral fit of the whole episode 2 with different models: BB, PL, BB+PL, cutoffPL, and Band.

BB	PL	BB+PL	CUTOFFPL	BAND
kT [keV] = 17.5 ± 0.2	γ = 1.46 ± 0.02	kT [keV] = 20 ± 3	γ = 1.0 ± 0.1	α = −1.0 ± 0.1
K_{BB} = 0.661 ± 0.009	K_{PO} = 2.1 ± 0.2	K_{BB} = 0.16 ± 0.06	E_0 = 132 ± 31	β = unc
		γ = 1.5 ± 0.1	K = 0.5 ± 0.1	E_0 = 142 ± 42
		K_{PO} = 2.3 ± 0.8		K = 0.0048 ± 0.0008
Red χ^2 = 7.16	Red χ^2 = 1.109	Red χ^2 = 0.78	Red χ^2 = 0.77	Red χ^2 = 0.79
D.O.F. = 56	D.O.F. = 56	D.O.F. = 54	D.O.F. = 55	D.O.F. = 54
Flux = 5.2×10^{-8}	Flux = 6.52×10^{-8}	Flux = 6.35×10^{-8}	Flux = 2.43×10^{-8}	Flux = 6.36×10^{-8}

Notes. The flux corresponds to the (15–150) keV energy range. The models with which we fit the data are those defined in the XSPEC manual: http://heasarc.nasa.gov/xanadu/xspec/xspec11/manual/manual.html

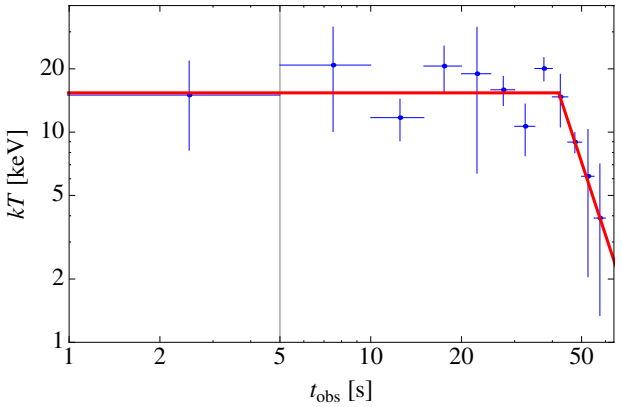

Fig. 5. Evolution of the kT component of the BB+PL model during episode 1. The first data point corresponds to 5 s before the first BAT trigger time. The vertical line corresponds to the trigger time. The time is given in the observer frame. The temperature evolves in time following a broken power-law fit. There is a break at t = 41.21 s. The indices of the PL are α = 0 (consistent with a constant function) and $\beta = -4 \pm 2$. The presence of the BB, although weaker than in previous cases, is essential to obtain an acceptable fit.

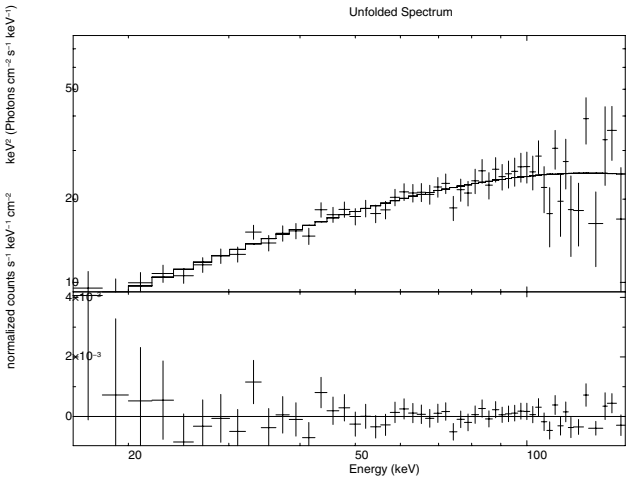

Fig. 6. Fit of episode 2 with a cutoffPL model. The photon index is $\gamma = 1.0 \pm 0.1$, the normalization constant is 0.5 ± 0.1, the cutoff energy is $E_0 = 132 \pm 31$ and the reduced chi squared of the fit is Red-χ^2 = 0.77 (55 D.O.F.).

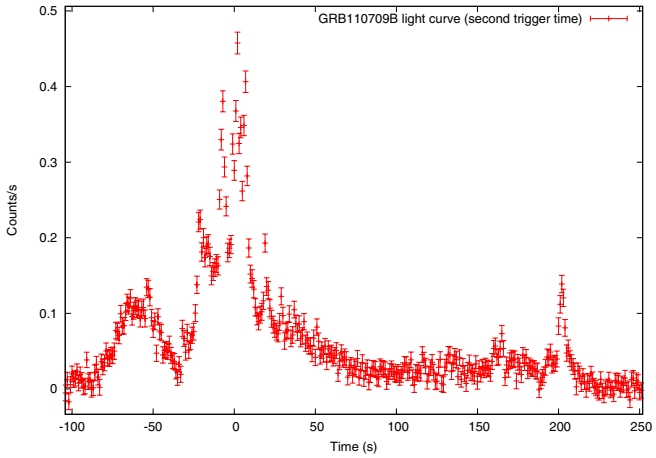

Fig. 7. Count light curve of episode 2 of GRB 110709B obtained from the *Swift*-BAT detector in the (15–150 keV) energy band. The time is given with respect to the second trigger time, of 331 940 612 s (in MET seconds).

3.2. Episode 2

We also performed a time-integrated spectral analysis of episode 2, whose light curve is shown in Fig. 7. This episode starts 35 s before the second trigger time and last 135 s, until 100 s after the second trigger time. We tried to fit the spectrum with the following spectral models: BB, PL, BB+PL, cutoffPL and Band (see Table 2). We could easily discard the BB and Band models because in one case the Red χ^2 is too high and in the other case there is an unconstrained parameter. Because the PL and the BB+PL are nested models, we performed a statistical test to see which one is the best. We obtained a probability Prob = 0.001 that the simpler model is better, therefore the BB+PL dominates over the PL. Then we compared the BB+PL and the cutoffPL models. Because they are not nested, we could not apply the same test. Therefore we chose the model that gives the lowest χ^2. We concluded that the model that best fits episode 2 is the cutoffPL model.

It is clear from the analogies with GRB 090618 and GRB 101023 that episode 2 has all the characteristics of a canonical GRB. A difference between GRB 110790B and the already analyzed ones is that the separation between episodes 1 and 2, ∼10 min, is much bigger than previously, ∼50 s. This remarkable time separation between the two episodes is an additional new fact to propose a different astrophysical origin of these two components.

We now turn to the crucial analysis of the cosmological redshift determination of episode 2.

4. Cosmological redshift determination

We used four phenomenological methods to constrain the redshift of the source, based on different relations that are detailed below.

4.1. $N_{\rm H}$ column density

We first tried to derive an upper limit for z following the work of Grupe et al. (2007). These authors considered a relation between the absorption column density in excess of the galactic column density, given by $\Delta N_{\rm H} = N_{\rm H,fit} - N_{\rm H,gal}$ and the redshift z, through the equation

$$\log(1+z) < 1.3 - 0.5[\log(1+\Delta N_{\rm H})]. \quad (1)$$

We calculated $N_{\rm H,gal}$ from the radio map of the galaxy in the Lab Survey website[1] by entering the coordinates of the GRB (RA = 164.64, Dec = –23.46). We obtained $N_{\rm H,gal} = 10.5 \times 10^{20}$ cm^{-2}.

To obtain the value of $N_{\rm H,fit}$ we took the XRT data from 2000 s to 10^6 s after the first BAT trigger time and fitted the model *phabs*po* using the program XSPEC. The XRT data were reduced by the xrtpipeline software, version 0.10.4, which is part of the HEASOFT package, version 6.12. We used the standard response matrix swxpc0to12s6_20010101v013.rmf for the PC mode data. The model *phabs* represents the photoelectric absorption

$$M(E) = \mathrm{e}^{-n_{\rm H}\sigma(E)}, \quad (2)$$

where $n_{\rm H}$ is the equivalent hydrogen column density (in units of 10^{22} cm^{-2}) and $\sigma(E)$ is the photoelectric cross section, not including Thompson scattering. We obtained a value of $N_{\rm H,fit} = 71.76 \times 10^{20}$ cm^{-2}. Using these values in (1) we obtained an upper limit for the redshift of $z < 1.35$.

4.2. Amati relation

We also tried to determine the redshift of episode 2 through the Amati relation (Amati 2006), which relates the isotropic energy $E_{\rm iso}$ of the GRB to the peak energy in the rest frame $E_{\rm p,i}$ of the νF_ν spectrum (Amati et al. 2009). The analytical expression of $E_{\rm iso}$ is

$$E_{\rm iso} = \frac{4\pi d_{\rm L}^2}{(1+z)} S_{\rm bol}, \quad (3)$$

where $d_{\rm L}^2$ is the luminosity distance, z is the redshift, and $S_{\rm bol}$ is the bolometric fluence, related to the observed fluence in a given detection band ($E_{\rm min}$, $E_{\rm max}$) by

$$S_{\rm bol} = S_{\rm obs} \frac{\int_{1/(1+z)}^{10^4/(1+z)} E\phi(E)\mathrm{d}E}{\int_{\rm E^{min}}^{\rm E^{max}} E\phi(E)\mathrm{d}E}. \quad (4)$$

Here, ϕ is the spectral model considered for the spectral data fit; in this case a Band model (Band et al. 1993), composed of two smoothly connected power-laws. $E_{\rm p,i}$ is related to the peak energy $E_{\rm p}$ in the observer frame by

$$E_{\rm p,i} = E_{\rm p}(1+z). \quad (5)$$

[1] http://www.astro.uni-bonn.de/~webaiub/english/tools_labsurvey.php

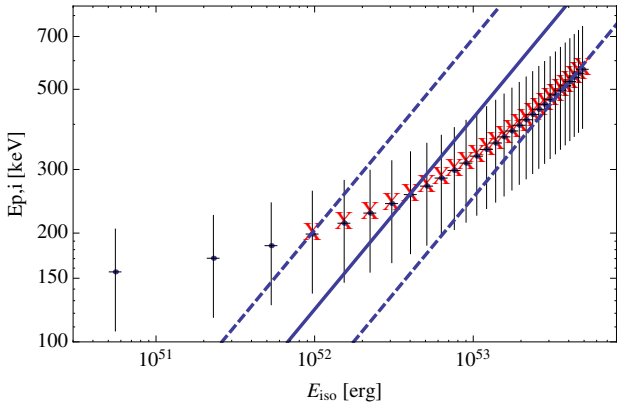

Fig. 8. Amati relation (solid line) with its $1-\sigma$ uncertainties (doted lines) and peak energy $E_{\rm p,i}$ vs. $E_{\rm iso}$ for GRB 110709B, for different values of the redshift, from 0.1 to 3, at steps of 0.1. We can see that the data match the theoretical function within $1-\sigma$ for $z > 0.4$.

The peak energy is the energy at the peak of the νF_ν spectrum. It can be written as

$$E_{\rm p} = E_0(2+\alpha),$$

where E_0 is the energy at which the two power-laws intersect and α is the slope of the low-energy power-law, according to the Band model.

We calculated the luminosity distance d_L as given by the standard cosmological model

$$d_{\rm L} = \frac{c}{H_0}(1+z)\int_0^z \frac{\mathrm{d}x}{\sqrt{\Omega_{\rm m}(1+x)^3+\Omega_\Lambda}}, \quad (6)$$

where the Hubble constant is $H_0 = 70$ km s^{-1} Mpc^{-1}, $\Omega_{\rm m} = 0.27$, $\Omega_\Lambda = 0.73$ and c is the speed of light.

Following the same procedure as described in Penacchioni et al. (2012), we calculated $E_{\rm iso}$ and $E_{\rm p,i}$ for different values of z, from 0.1 to 3, at steps of 0.1. Figure 8 shows that the relation is satisfied for values of $z > 0.4$. This puts a lower limit to the estimation of the redshift.

4.3. Yonetoku relation

We finally obtained a range of possible redshifts by using the Yonetoku relation (Yonetoku 2004). This relation, also known as the $E_{\rm p}$–luminosity relation ($E_{\rm p}$–L), connects the observed isotropic luminosity L in units of 10^{52} erg s^{-1} with the peak energy $E_{\rm p}(1+z)$ in the rest frame of the GRB. It is valid for values of $E_{\rm p}$ between 50 and 2000 keV, and a luminosity range of 10^{50}–10^{54} erg s^{-1}.

The best-fit function for the $E_{\rm p}$–L relation is

$$\frac{L}{10^{52}\ \mathrm{erg\,s^{-1}}} = (2.34^{+2.29}_{-1.76}) \times 10^{-5} \left[\frac{E_{\rm p}(1+z)}{1\ \mathrm{keV}}\right]^{2.0\pm0.2}. \quad (7)$$

The peak luminosity and the peak energy are calculated by integrating within a 1 s interval around the most intense peak of the light curve, because this is a better distance indicator than the burst average luminosity. However, we took a 10 s interval around the most intense peak to better constrain the value of the parameters (i.e., to increase the number of photons in the spectrum and obtain an error that is smaller than the value of the parameters). The peak luminosity in the rest frame (with the proper K-correction) can be calculated as

$$L = 4\pi d_{\rm L}^2 F_{\rm bol}, \quad (8)$$

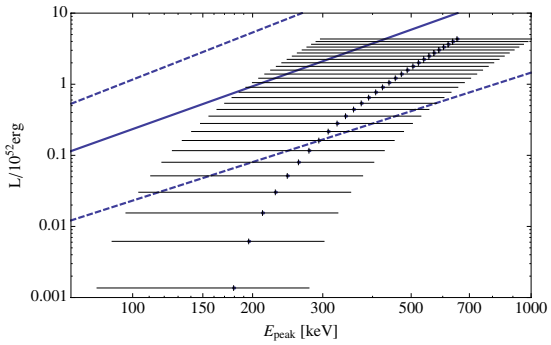

Fig. 9. Yonetoku relation (solid line) with its $1-\sigma$ uncertainties (doted lines) and peak luminosity vs. $E_{\rm p,i}$ for GRB 110709B, for different values of the redshift, from 0.1 to 3, at steps of 0.1. We can see that the data matches the theoretical function within $1-\sigma$ for $z > 0.6$.

where

$$F_{\rm bol} = P_{\rm obs} \frac{\int_{1/(1+z)}^{10000/(1+z)} EN(E){\rm d}E}{\int_{\rm E_{min}}^{\rm E_{max}} N(E){\rm d}E} \quad (9)$$

is the energy flux and $P_{\rm obs}$ is the photon flux.

Figure 9 shows the Yonetoku relation (solid line) with its uncertainties (dotted lines), and the values of L and $E_{\rm p,i}$ for each value of z, from 0.1 to 3, at steps of 0.1. We see that the Yonetoku relation is satisfied within 1σ for values of the redshift >0.7, consistent with the results obtained with the Amati relation.

In conclusion, if we put together the three methods, we have a range of possible redshifts of $0.7 < z < 1.35$.

4.4. Estimate of the redshift using the X-ray afterglow

We previously presented (Penacchioni et al. 2012) a method for estimating the redshift of GRB 101023 by comparing its X-ray light curve to that of GRB 090618, of known redshift ($z = 0.54$). Here we rescale the X-ray light curve of GRB 090618 as if it were seen at different redshifts and plot it together with GRB 110709B light curve, looking for the values of z for which these light curves overlap at late times. We find a remarkable consistency between this method and the phenomenological methods mentioned above.

To compare the two emissions from the GRBs in a common rest frame, we applied the following operations only to GRB 090618:

1) determination of the starting time $T_{\rm start}$ of the late decay emission,
2) spectral analysis of this emission with an absorbed power-law model,
3) extrapolation of this spectral model in a common cosmological rest-frame energy range and, consequently, rescaling of the GRB 090618 light curve for the different energy ranges,
4) cosmological correction for the arrival time by taking into account the different scaling due to cosmological redshift, and
5) correction of the observed flux by changing the redshift of GRB 090618.

A detailed description of the method will be given in a forthcoming publication (Pisani et al., in prep.).

In this way we directly compared the two light curves for different redshifts of GRB 090618. Figure 10 shows the GRB 090618 light curve seen as if the source were located at different redshifts: 0.2 (blue), 0.4 (green), 0.7 (gray), 1.0 (orange) and 2.0 (purple). The red light curve corresponds to GRB 110709B. We can see that it lies between the green and the orange curves. A more accurate scaling of the late X-ray afterglow suggests a redshift of $z = 0.75$ for this source.

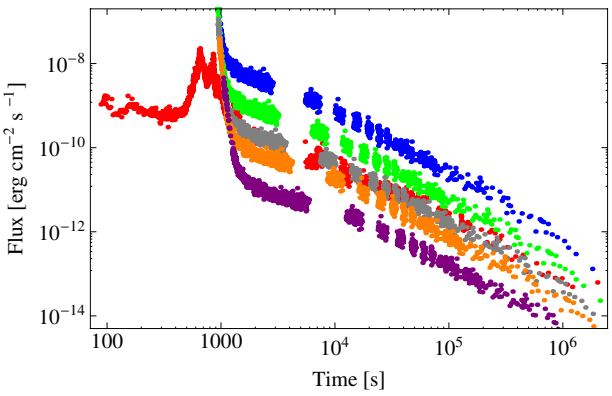

Fig. 10. Plot of GRB 090618 seen as if it were at different redshifts: 0.2 (blue), 0.4 (green), 0.7 (gray), 1.0 (orange), and 2.0 (purple). The red light curve corresponds to GRB 110709B. We can see that it lies between the green and the orange light curves, indicating that the redshift must be between 0.4 and 1.0.

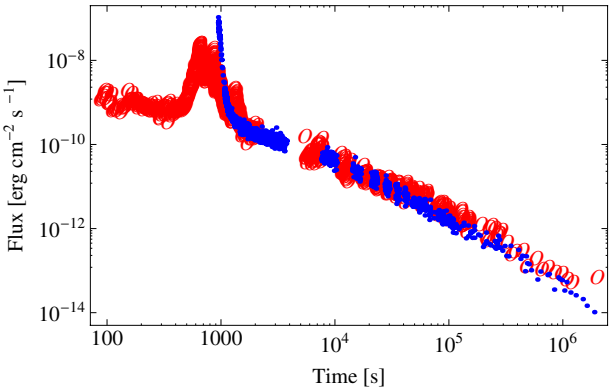

Fig. 11. GRB 090618 light curve (blue) as if it were seen at $z = 0.75$ together with the GRB 110709B light curve (red). There is an excellent superposition in the late decay assuming a temporal shift of GRB 090618 of $T_* = 800$ s to the right to align the steep decays of the light curves.

Figure 11 shows the superposition of the GRB 110709B and GRB 090618 light curves in the observer frame, as if they were located at a redshift $z = 0.75$.

There is a second aspect, however, which is due to the peculiarity of the turn-on T_0 of the XRT detector. At the time BAT was triggered for the second time, XRT was already pointing at the source and was able to detect the emission at very early times, making this GRB probably the first for which XRT has the earliest detection up to date. We shifted the GRB 110709B light curve to align the early steep decays (originating in the prompt in our interpretation). This was done by adding a time $T_* = +800$ s to the GRB 090618 light curve. The superposition is very good. In this way we also aligned the early decays. This factor is arbitrary, but we needed to include it because the GRB 110709B XRT light curve presents many spikes at the beginning, which according to our interpretation correspond not to the steep decay of the X-ray light curve, but to the prompt emission.

For GRB 110709B, because XRT was already active and collecting data at the time of the second BAT trigger time,

we were able to follow the behavior of the whole GRB emission of episode 2. This is a key point of our understanding of GRB 110709B, since only in very few cases XRT had a response during the early emission.

In the big flare at ~1000 s after the first BAT trigger time we notice a strong correlation between the emission in X-rays and in γ-rays. We identify this emission as the prompt emission of episode 2. After this prompt phase the traditional plateau phase is observed. After the plateau phase, there is the late decay phase in the X-ray light curve, following a power-law behavior that was also observed in other sources (i.e., GRB 101023, GRB 090618, and GRB 111228). We studied this decay in the IGC paradigm, and considered the possibility that it might be produced by the early emission of the newly born NS. It is interesting to notice that in GRB 110709B the typical flare in X-rays just preceding the plateau phase and following the prompt emission is not observed. This X-ray emission usually occurs without any associated γ-ray emission, since the data are usually below the BAT threshold. In the present case, it is conceivable that the flaring indeed occurred during some of the gaps of ~4000 s in which there are no data due to Earth occultation.

We can then distinguish two types of flares in the X-ray light curve. The first type occurs at early times, previous to the steep decay, and belongs to the prompt emission. These flares can be seen in X-rays only when XRT starts its detection at early enough times, e.g., when the satellite was already pointing at a region near the burst position and did not need much time to slew. The light curve in X-rays generally follows the trend of the light curve in γ-rays. The second type of flares occurs at later times, just preceding the plateau phase. These flares are seen only in X-rays since their photon flux is much lower than the BAT threshold. In the ICG paradigm, we interpret these flares as possible indicators of the breakout of the SN.

We are currently analyzing more sources in the catalog by Margutti et al. (2013) to look for these three very distinct phases, i.e., the flares in the prompt emission, the flares in the afterglow, and the late decay after the plateau, each of which has a different physical origin within the IGC paradigm.

5. Episode 1: radius of the emitting region

Knowing the redshift and parameters of the fit with a BB + PL model, we computed the isotropic energy of the whole episode 1, $E^{(1)}_{\rm iso} = 1.42 \times 10^{53}$ erg.

With the energy flux of the BB component $\phi_{\rm BB}$ as a function of time from the time-resolved spectral analysis and the luminosity distance $d_{\rm L}$, we can compute the value of the radius of the emitter in cm (we then express it in km in Fig. 12) through

$$r_{\rm em} = \sqrt{\frac{\phi_{\rm BB}}{\sigma T^4}}\frac{d_{\rm L}}{(1+z)^2}. \quad (10)$$

Here $\phi_{\rm BB}$ is the BB flux in units of erg cm^{-2} s^{-1}, $\sigma = 5.6704$ erg cm^{2}s^{-1}K^{-4} is the Stefan-Boltzmann constant and $d_{\rm L}$ is the luminosity distance in cm.

The best fit of the expanding radius is

$$r(t) = at^b, \quad (11)$$

where $a = (1.5 \pm 1.2) \times 10^4$ km s^{-b} and $b = 0.32 \pm 0.27$ (see Fig. 12).

We associate the BB component to the expansion of the ejected material, while the power-law is associated (because we interpret from the IGC paradigm) with the accretion of part of this material onto the NS companion.

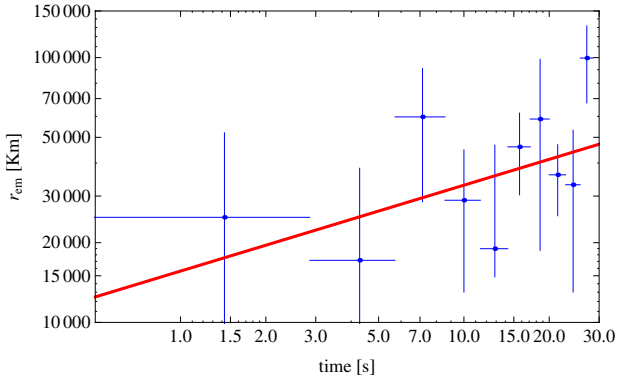

Fig. 12. Radius of the emitting region as a function of time (in the cosmological rest frame), corresponding to episode 1. The radius increases with time following a power-law at^b, with $a = (1.5 \pm 1.2) \times 10^4$ km s^{-1} and $b = 0.32 \pm 0.27$.

6. Analysis of episode 2 in the fireshell model

We recall that the fireshell model (Damour & Ruffini 1975; Ruffini et al. 2000, 2010; Ruffini 2001) is an alternative to the Fireball model, first proposed by Cavallo & Rees (1978), Goodman (1986) and Paczynsky (1986). We assume, within the fireshell model, that all GRBs originate from the gravitational collapse of a star approaching asymptotically the formation of a Kerr-Newmann BH (Wiltshire et al. 2009). An electric field E is created just outside the collapsing core and in between the expanding outer shells that act as a capacitor (Preparata et al. 1998). This electrical field grows until it reaches a critical value, $E_c = m^2c^3/\hbar e$. At this time, vacuum polarization occurs, leading to pair creation at the expenses of the gravitational energy. An optically thick $e^\pm$ plasma forms with total energy $E^{e^\pm}_{\rm tot}$ in the range 10^{49}–10^{54} erg. The $e^\pm$ plasma reaches thermal equilibrium on a timescale of 10^{-12} s (Aksenov et al. 2007). Because it is optically thick, the plasma self-accelerates due to its internal radiation pressure (Ruffini et al. 1999a,b). After an early expansion in vacuum, the $e^\pm$-photon plasma engulfs the baryonic matter M_B of the outer shells and reaches thermal equilibrium with it. The baryonic matter is described by the dimensionless parameter $B = M_Bc^2/E^{e^\pm}_{\rm tot}$. B must be less than 10^{-2}, otherwise there will not be any relativistic expansion (Ruffini et al. 2000). The optically thick fireshell composed of $e^\pm$-photon-baryon plasma self-accelerates to ultrarelativistic velocities, finally reaching the transparency condition. A flash of radiation is then emitted. This is the P-GRB (Ruffini et al. 2001a). The amount of energy radiated in the P-GRB is only a fraction of the initial energy $E^{e^\pm}_{\rm tot}$. The remaining energy is stored in the kinetic energy of the optically thin baryonic and leptonic matter fireshell that expands ballistically and starts to slow down through the inelastic collisions with the circumburst medium (CBM). This interaction gives rise to a multi-wavelength emission, the extended afterglow (Ruffini et al. 2001a). We can estimate the characteristic inhomogeneities of the CBM by fitting the luminosity of the X-ray source and imposing the fully radiative condition in the collision between the ultra relativistic baryonic shell and the clouds of the ISM. The complete analytic solution has been developed in Bianco & Ruffini (2004, 2005a,b), together with the analytic expression of the surfaces of equal arrival time of the photons at the detector (EQTS). The afterglow presents three different regimes: a rising part, a peak, and a decaying tail. We therefore define a "canonical GRB" light curve with two sharply different components: 1) the P-GRB and 2) the extended afterglow. What is usually

Table 3. Fit of the P-GRB and the afterglow of GRB 110709B, episode 2.

Parameter	P-GRB	P-GRB+afterglow
kT [keV]	14 ± 1	
BB Amp	0.30 ± 0.02	
γ		1.03 ± 0.1
PL Amp		0.5 ± 0.1
Red χ^2	1.448 (56 D.O.F.)	0.77 (55 D.O.F.)
Energy flux (15−150 keV) [erg cm^{-2} s^{-1}]	2.413×10^{-8}	6.34×10^{-8}
Energy [erg]	3.44×10^{50}	2.43×10^{52}

Notes. The P-GRB is well-fit with a BB model, while the whole episode 2 is best fit by a cutoffPL model. From this fit and the value of the redshift we are able to calculate $E_{\rm iso}$ and $E_{\rm P-GRB}$.

called prompt emission in the current GRB literature mixes the P-GRB with the raising part and the peak of the extended afterglow (Ruffini et al. 2003). The spectrum of the extended afterglow is initially assumed to be thermal in the comoving frame of the expanding shell. Recently, after the analysis of some highly energetic sources observed by *Swift* and *Fermi* satellites, this assumption of a pure comoving thermal spectrum has been relaxed and a phenomenological modification by a power-law of the low-energy spectral slope has been introduced (Patriceli et al. 2012). The observed nonthermal spectrum shape is due to a double convolution of thousands of instantaneous comoving spectra, with different temperatures and different Doppler factors, over both the EQTS and the observation time (Ruffini et al. 2004).

After fixing the value of the redshift to $z = 0.75$, we started the analysis of episode 2 within the fireshell model. We first looked for the P-GRB during the first bump of episode 2 (from 100 to 40 s before the second trigger time) by fitting the data with a BB + PL model. We selected several time intervals as the P-GRB during the first bump of episode 2, but in some cases the fits were poor. In some other cases, to reproduce the ratio between the P-GRB energy and the total energy we needed to consider a baryon load $B > 10^{-2}$ (which is unphysical within the fireshell model) and, in other cases, there was a discrepancy between the observed temperature and the one given by the simulation. Thus we concluded that this bump should belong to episode 1. The reason why we found no strong thermal signature in this bump is that episode 1 starts ∼10 min before the beginning of the bump and the temperature of the BB component decreases very rapidly following a power-law in the first seconds of emission. Consequently, after such a long time we do not expect to find any signature of a BB from episode 1.

We finally selected the P-GRB as the 9 s from 35 to 26 s before the second trigger, and the following emission from –26 to 100 s as the afterglow. Table 3 shows the parameters of the fit. We calculated a P-GRB energy of $E_{\rm P-GRB} = 3.44 \times 10^{50}$ erg and an isotropic energy of $E_{\rm iso} = 2.43 \times 10^{52}$ erg.

We inserted these energy values into our numerical code and calculated the value of the baryon load, $B = 5.7 \times 10^{-3}$. We simulated the light curve and the spectrum, obtaining, at the transparency point, a laboratory radius $r_{\rm tr} = 6.04 \times 10^{13}$ cm, a gamma Lorentz factor $\Gamma = 1.73 \times 10^2$ and a P-GRB observed temperature (after cosmological correction) $kT = 12.36$ keV.

Figures 13a, b show the simulation of the light curve and the spectrum of episode 2. The photon index of the XRT and BAT spectra agree with that predicted by the simulation. Details of this calculation will be given in a forthcoming letter

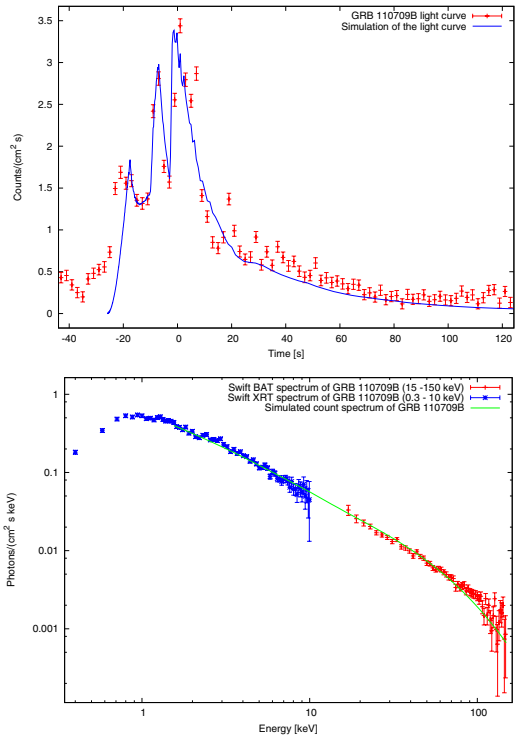

Fig. 13. Simulation of the BAT **a)** light curve and **b)** spectrum of episode 2. We included XRT data in the fit of the spectrum to show that the slope predicted in the fireshell model agrees with the slope of the X-ray spectrum.

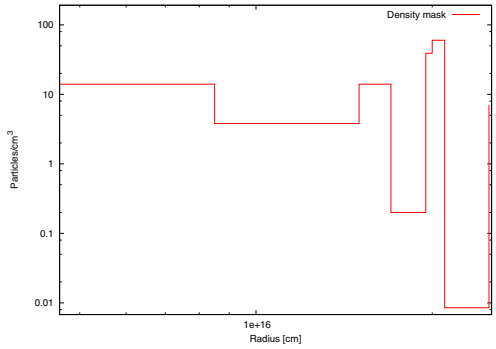

Fig. 14. Particle density of the ISM clouds as a function of the distance. The mean density is 76 part/cm^3.

(Penacchioni et al., in prep.). Figure 14 shows the density mask of the ISM, i.e., the density of particles of the interstellar clouds as a function of the distance to the center of the BH. This density has to be interpreted as an effective density because fragmentation may occur in the expanding shell (Ruffini et al. 2007; Dainotti et al. 2007).

7. Nature of the progenitor

Following the works of Rueda & Ruffini (2012) and Izzo et al. (2012b), we suggest for the origin of GRB 110709B a binary system formed by a massive evolved star on the verge of an SN explosion and an NS. The early SN material expanding at non-relativistic velocities is then accreted by the NS companion at times longer than $t_{0,\rm accr}$, when the material reaches the NS gravitational capture region. The emission observed in episode 1 is associated to this early SN evolution, which is identified with the thermal component, and the accretion process onto the NS,

which is possibly related to the nonthermal component. The NS reaches the critical mass in a time $t_{0,\rm accr} + \Delta t_{\rm accr}$ and gravitationally collapses to a black hole, emitting the GRB seen in episode 2. We assume the critical mass of a nonrotating NS $M_{\rm crit} = 2.67\,M_\odot$ as given by Belvedere et al. (2012).

The amount of material that reaches the NS gravitational capture region

$$R_{\rm cap}(t) = \frac{2GM_{\rm NS}(t)}{v^2_{\rm ej,rel}(t)} \tag{12}$$

per unit time is given by (see Rueda & Ruffini 2012; Izzo et al. 2012b)

$$\dot{M}(t) = \pi\rho_{\rm ej}(t)v_{\rm ej,rel}(t)R^2_{\rm cap}(t), \tag{13}$$

where $R_{\rm cap}$ is measured from the NS center.

In these expressions, $\rho_{\rm ej}(t) = 3M_{\rm ej}(t)/(4\pi r^3_{\rm ej}(t))$ is the density of the ejecta,

$$M_{\rm ej}(t) = M_{\rm ej}(0) - M(t) \tag{14}$$

is the total available mass to be accreted by the NS, $M_{\rm NS}(t)$ is the NS mass, and $v_{\rm ej,rel}(t)$ is the velocity of the ejecta relative to the NS

$$v_{\rm ej,rel}(t) = \sqrt{v^2_{\rm orb,NS}(t) + v^2_{\rm ej}(t)}. \tag{15}$$

In Eq. (14), $M_{\rm ej}(0)$ is the given initial mass of the ejecta (just at the beginning of the accretion process); we chose different values for it in Table 4. $M(t)$ is the mass of the ejecta that is lost because it passes through the capture region of the NS.

The actual mass accretion rate onto the NS, $\dot{M}_{\rm accr}(t)$, is a fraction $\eta_{\rm accr} \leq 1$ of Eq. (13), i.e.,

$$\dot{M}_{\rm accr}(t) = \eta_{\rm accr}\dot{M}(t), \tag{16}$$

where η is the accretion efficiency onto the NS. Accordingly, there is an amount of material per unit time $\dot{M}_{\rm out}(t) = (1 - \eta_{\rm accr})\dot{M}(t)$ not accreted by the NS.

In Eq. (15), $v_{\rm orb,NS}(t) = \sqrt{G(M_{\rm prog} + M_{\rm NS}(t))/a}$ is the orbital velocity relative to the SN core progenitor, a is the separation distance between the NS and the SN core progenitor, and

$$v_{\rm ej}(t) = \frac{{\rm d}r_{\rm ej}(t)}{{\rm d}t} = b\frac{r_{\rm ej}(t)}{t} \tag{17}$$

is the expansion velocity of the early SN material, where we have used $r_{\rm ej}(t) = r_{\rm em}(t)$, given by Eq. (11).

We already mentioned that the power-law component in the spectrum of episode 1 might be due to the accretion onto the NS companion. Because this power-law component is present since the beginning of episode 1, we fixed the value of $t_{0,\rm accr}$ to be equal to the starting time of episode 1. This constrains the separation distance a of the binary, which under these conditions is given by

$$a = r_0 + R_{\rm cap}(0), \tag{18}$$

where $r_0 = r_{\rm ej}(0)$ and $R_{\rm cap}(0)$ are the radius of the early SN ejecta and the capture radius of the NS companion at the beginning of episode 1. In this case, $r_0 \approx 1.75 \times 10^9$ cm, see Fig. 12. The separation a is a function of the initial mass of the NS and of the SN core progenitor mass, as well as of the orbital velocity, through $R_{\rm cap}$. Clearly, the constraint given by Eq. (18) is a lower limit, since the accretion process onto the NS could have been triggered before by layers at lower densities (e.g. He). In that case, the binary separation a could be higher.

In addition to this constraint, we must take into account that the NS must reach its critical mass $M_{\rm crit}$ at the beginning of episode 2, since by that time the NS must collapse to a BH and emit the canonical GRB. This implies that

$$\Delta t_{\rm accr} \approx \frac{611}{(1+z)} \approx 349 \text{ s}. \tag{19}$$

We show in Table 4 the parameters of the binary system leading to IGC of the NS in a time interval equal to the duration of episode 1. We adopted an initial mass for the NS, $M_{\rm NS}(0) = 1.4\,M_\odot$ and, correspondingly, an NS radius of $R_{\rm NS}(0) = 12.3$ km from the mass-radius relation of Belvedere et al. (2012). From the constraint given by Eq. (18), we fixed the binary separation a. We then proceeded with the numerical integration of the accretion rate equations by requiring that $M_{\rm NS}(t) = M_{\rm crit}$ at $t = \Delta t_{\rm accr}$, given by Eq. (19), from which we obtained the efficiency $\eta_{\rm accr}$.

It is interesting to analyze how the NS can accrete such a large mass, in some cases on the order of 47% of the early SN material (see Col. 5 of Table 4), since one might assume that solid angles of ~50% between the early SN material and the accreting NS are hard to obtain. Indeed, during the accretion process the NS is moving with high orbital velocities on the order of 10^8 cm s^{-1} relative to the core progenitor (see Col. 7 of Table 4), and consequently travels effective arc-lengths several times longer than the circumference of the orbit (see Col. 8 of Table 4).

Assuming that the gain in gravitational energy of the accreted material onto the NS can be released from the system leads to an upper limit of the luminosity

$$|\dot{E}_b(t)| = \frac{G\dot{M}_{\rm accr}(t)M_{\rm NS}(t)}{R_{\rm NS}(t)}, \tag{20}$$

where we take into account the dependence of the NS radius with time, due to the increment of the NS mass by the accretion process. The self-consistent radius is computed at each time from the mass-radius relation of Belvedere et al. (2012).

The actual luminosity depends on the efficiency $\eta_{\rm rad}$ in converting gravitational energy into electromagnetic energy by some still unknown process. Since in our model we assume that the BB component of episode 1 is caused by the early SN expansion, we estimate the efficiency $\eta_{\rm rad}$ from the assumption that $|\dot{E}_b|$ is responsible for the power-law luminosity $L_{\rm PL}$, namely

$$\eta_{\rm rad}(t) = \frac{L_{\rm PL}}{|\dot{E}_b(t)|}. \tag{21}$$

In Fig. 15 we show the evolution of the efficiency $\eta_{\rm rad}$ in the first seconds of emission for the binary systems shown in Table 4. We assumed a constant and isotropic power-law luminosity of episode 1, $L_{\rm PL} \approx 1.8 \times 10^{50}$ erg s^{-1} $\approx 10^{-4}\,M_\odot$ s^{-1}, as found from the spectral analysis. For all cases, we obtain the same evolution of the efficiency with time, i.e., the curves overlap. This is because we constrained all systems to have the same initial NS mass and $\Delta t_{\rm accr}$.

8. Radio observations

Zauderer & Berger (2012) reported observations with the EVLA radio telescopes on several occasions between 11 and 16 July 2011, at a frequency of 5.8 GHz. They found a radio source that brightened by about a factor of 1.6 between 2.1 and 7 days after

Table 4. Massive star – neutron star binary progenitor of GRB 110709B.

$M_{\rm prog}/M_\odot$	$M_{\rm ej}(0)/M_\odot$	$\rho_{\rm ej}(0)$ (g cm^{-3})	$\eta_{\rm accr}$	$\Delta M_{\rm accr}/M_{\rm ej}(0)$	P (min)	$v_{\rm orb,NS}(0)$ (km s^{-1})	$\Delta t_{\rm accr}/P$	$a/R_\odot$
4	2.7	2.39×10^5	0.92	0.47	0.52	5.24×10^3	11.14	0.037
5	3.7	3.27×10^5	0.88	0.34	0.45	5.84×10^3	12.96	0.036
6	4.7	4.16×10^5	0.88	0.27	0.39	6.39×10^3	14.71	0.035
7	5.7	5.04×10^5	0.89	0.22	0.35	6.91×10^3	16.39	0.034
8	6.7	5.93×10^5	0.91	0.19	0.32	7.40×10^3	18.00	0.033
9	7.7	6.81×10^5	0.94	0.16	0.30	7.87×10^3	19.55	0.032
10	8.7	7.69×10^5	0.96	0.15	0.27	8.32×10^3	21.04	0.031

Notes. $M_{\rm prog}$ is the mass of the massive star (in solar masses), $M_{\rm ej}(0)$ is the mass of the ejected material in the early SN phase (in solar masses), $\rho_{\rm ej}(0)$ is the density of the ejecta at the beginning of the expansion, $\eta_{\rm accr}$ is the efficiency of the accretion process onto the NS, $\Delta M_{\rm accr} = M_{\rm crit} - M_{\rm NS}(0)$ is the total mass accreted by the NS before the collapse, $P = 2\pi a/v_{\rm orb,NS}$ is the period of the binary, $v_{\rm orb,NS}(0)$ is the initial orbital velocity of the NS and $\Delta t_{\rm accr}/P$ is the arc-length traveled by the NS during the accretion process in units of the length of the whole orbit and $a/R_\odot$ is the binary separation (in units of solar radii). We assume that the accretion process starts 5 s before the first trigger time, i.e. $t_{0,\rm accr}$ coincides with the time corresponding to the first datapoint in Fig. 5.

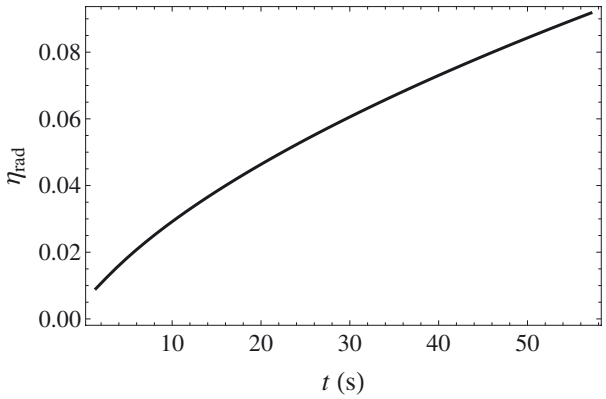

Fig. 15. Theoretical estimation of the efficiency $\eta_{\rm rad}$ given by Eq. (21) of the process to convert gravitational energy into radiation as a function of time. For this plot, we assumed a constant and isotropic power-law luminosity of episode 1, $L_{\rm PL} \approx 1.8 \times 10^{50}$ erg s^{-1} $\approx 10^{-4}$ $M_\odot$ s^{-1}. We computed the values of the efficiency for the binary systems shown in Table 4. For all cases, we obtain the same evolution of the efficiency with time, i.e., the curves overlap. The values of $\eta_{\rm rad}$ are always <10%.

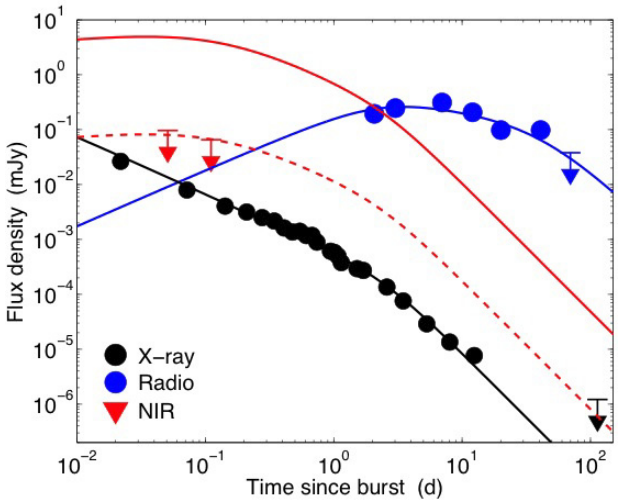

Fig. 16. X-ray (black), radio (blue) and NIR (red, upper limits) light curves of GRB 110709B. Taken from Zauderer et al. (2012) with kind permission.

the burst. The coincidence with the XRT position and the rising flux indicate that this is the radio afterglow of GRB 110709B. The position of the source is RA = 10:58:37.114, Dec = –23:27:16.760. We show in Fig. 16 the 5.8 GHz light curve presented in Zauderer et al. (2012), which shows evidence of a radio bump. Following the work of Chevalier & Soderberg (2010), we reproduced the plot of the peak spectral radio luminosity per unit frequency as a function of time (days) at which the peak is produced for different SN associated with GRBs, including GRB 110709B (see Fig. 17). We find that the radio emission of this source is higher than those associated with typical SN.

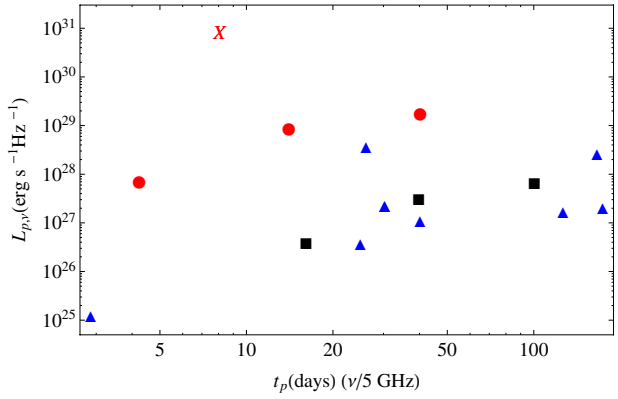

Fig. 17. Plot of the peak spectral radio Luminosity per unit frequency versus the time at which the peak occurs, for different SN associated to GRBs. The circles represent the SN emission associated to SN 2006aj (GRB 060218), SN 1998bw (GRB 980425) and SN 2003lw (GRB 031203). The triangles represent the SN Ib/c for which there are radio observations, namely SN 2002ap, SN 1990B, SN 2008D, SN 1994I, SN 2009bb and SN 2003L. The squares represent the SN IIb: SN 2008ax, SN 2001ig, SN 1993J, SN 2001gd and SN 2003bg. The red cross is the luminosity related to GRB 110709B afterglow. It is higher than the emissions of the other SN, considered "standard".

9. Conclusions

GRB 110709B is a very peculiar source, since it is the first for which *Swift*-BAT was triggered twice. Its *Swift*-BAT light curve presents two well-defined episodes, episode 1 and episode 2. Episode 1 lasts 100 s and episode 2 lasts 135 s. Particularly interesting is the fact that the X-ray observations started well before the second trigger time. The light curve and spectrum of this source share characteristics with GRB 090618 (Izzo et al. 2012b), GRB 101023 (Penacchioni et al. 2012), and GRB 970828 (Izzo et al. 2012c). It has recently been shown

that GRBs that show such distinct emissions, episodes 1 and 2, form a new family of GRBs, which are described by the IGC paradigm (Rueda & Ruffini 2012; Izzo et al. 2012b). Within this scenario, the GRB originates in a binary system formed by a massive star on the verge of an SN and an NS close to its critical mass for the gravitational collapse to a BH. The compact-core SN progenitor ejects material in the very early phases of the SN explosion, which is then accreted by the NS; this process is identified with episode 1. The accretion process onto the NS brings it to the critical mass, which in turn leads to its gravitational collapse to a BH and to emitting the GRB, identified with episode 2. Later on, we see a standard emission in X-rays, which we called episode 3. Several days after the burst, when it is present, we see an optical emission, associated to the SN (episode 4). Following the recent works on GRB 090618 (Izzo et al. 2012b) and GRB 970828 (Izzo et al. 2012c), we here applied the IGC paradigm to GRB 110709B.

The redshift of GRB 110709B is unknown, therefore we used in Sect. 4 four phenomenological methods to constrain it; i.e., Grupe (Grupe et al. 2007), Amati (Amati 2006), Yonetoku (Yonetoku 2004) and the scaling of the X-ray afterglow (Izzo et al. 2012a; Penacchioni et al. 2012). The first method gives an upper limit of $z < 1.35$. The second and third methods give a lower limit of $z > 0.6$ and $z > 0.7$, respectively. The last method gives a precise value of $z = 0.75$, which lies within the range determined by three of the above mentioned methods. We then decided on this last value as the redshift of GRB 110709B.

The spectral analysis of episode 1 was given in Sects. 3.1 and 5. We found a value of the isotropic energy for episode 1 of $E^{(1)}_{\rm iso} = 1.42 \times 10^{53}$ erg (see Table 1). We fit the spectrum with a BB+PL model. The temperature of the BB component evolves with time following a broken power-law (see Fig. 5). The corresponding radius of the BB emitter evolves in time following a power-law given in Eq. (11) and shown in Fig. 12. We associated this radius and the BB component to the evolution of the SN ejecta, while the power-law is associated to the accretion of the ejected material onto the NS companion.

Episode 2 was analyzed in Sects. 3.2 and 6. We found an isotropic energy of $E^{(2)}_{\rm iso} = 2.43 \times 10^{52}$ erg (see Table 3). We interpreted this episode as a canonical GRB and simulated its light curve and spectrum within the fireshell model. We found at transparency a Lorentz factor $\Gamma \sim 1.73 \times 10^2$, laboratory radius of 6.04×10^{13} cm, P-GRB observed temperature $kT_{\rm P-GRB} = 12.36$ keV, baryon load $B = 5.7 \times 10^{-3}$, P-GRB energy of $E_{\rm P-GRB} = 3.44 \times 10^{50}$ erg, and a CBM mean density 76 part cm^{-3}. This value is consistent with a "dark GRB", as cited in Zauderer et al. (2012). The lack of detection of an SN emission for this particular GRB could be due to obscuration by the circumstellar dust in the host galaxy.

The nature of the progenitor was discussed in Sect. 7. We indicated that it is a binary system formed by a massive evolved star on the verge of an SN explosion and an NS. We associated the thermal component of episode 1 mainly with the early SN evolution and the power-law component to the accretion process onto the NS. There is the possibility that the accretion process also contributes thermally. The energy from just the thermal component is on the order of 10^{50} erg, which is reasonable for the expansion of the early SN ejecta. We performed all necessary calculations to obtain the parameters of the binary system. For all our calculations we assumed a fixed NS mass of $1.4\,M_\odot$. We computed the rate at which the early SN material enters the capture region, for given values of the SN core progenitor mass. From this material, only a fraction will be accreted by the NS, therefore we introduced an efficiency factor $\eta_{\rm accr}$. Because the power-law component is present since the beginning of episode 1, we assumed that this episode starts at the same time $t_{0,\rm accr}$ as the accretion process, namely, when the outermost shell of expanding ejecta reaches the capture radius $R_{\rm cap}$ of the NS (measured from the center of the NS). This puts a constraint on the separation distance a of the binary. In addition, the NS must reach its critical mass and collapse to a BH at the beginning of episode 2. This puts a constraint on the duration of the accretion process $\Delta t_{\rm accr}$. By integrating the accretion rate equations with these boundary conditions we obtained the efficiency $\eta_{\rm accr}$. We summarized the results in Table 4 for different values of the core-progenitor mass and the density of the early SN ejecta. Assuming that the power-law radiation comes from the conversion of the binding energy of the accreted material onto the NS, we estimated the efficiency $\eta_{\rm rad}$ of this conversion process, which we show in Fig. 15 for an isotropic power-law luminosity $L_{\rm PL} \approx 1.8 \times 10^{50}$ erg s^{-1} $\approx 10^{-4}\,M_\odot$ s^{-1} observed in episode 1. For the parameters of the binary system shown in Table 4, we obtained values of $\eta_{\rm rad} < 10\%$. The efficiency of the radiation mechanism can be even lower if some beaming or boosting is present. However, we did not address any such possible mechanism in this work.

In Sect. 8 we presented the radio observations of GRB 110709B with the EVLA radio telescopes and the X-ray, radio and NIR light curves taken from Zauderer et al. (2012). We remarked on the presence of a bump in the radio afterglow, at ≈10 days after the burst. Because GRB 110709B has been classified as an optically dark burst, we plotted the peak spectral radio luminosity per unit frequency as a function of time and compared it with the luminosities of typical SNe, to see if it was possible to find any coincidences that might indicate the presence of the SN in the radio band. However, the luminosity we found is much higher than those of standard SNe.

We interpreted, within the IGC paradigm, that GRB 110709B is a new member of the IGC family, in addition to GRB 090618, GRB 101023, and GRB 970828.

A remarkable support for the above IGC paradigm comes from the observations of the X-ray afterglow emission of these systems. The X-ray light curve is composed of an early steep decay, a plateau, and a late decay. The analysis of the late decay of the afterglow luminosity has been identified with the cooling of the newly born NS, left by the SN explosion (Negreiros et al. 2012).

Acknowledgements. We are very grateful to the anonymous referee for his/her comments and suggestions that helped to improve the presentation of our results. We thank the *Swift* team for the support. This work made use of data supplied by the UK *Swift* Data Centre at the University of Leicester. A.V.P. is supported by the Erasmus Mundus Joint Doctorate Program by Grant Number 2010-1816 from the EACEA of the European Commission. G.B.P. is supported by the Erasmus Mundus Joint Doctorate Program by Grant Number 2011-1640 from the EACEA of the European Commission.

References

Aksenov, A. G., Ruffini, R., & Vereshchagin, G. V. 2007, Phys. Rev. Lett., 99, 125003
Amati, L. 2006, MNRAS, 372, 233
Amati, L., Frontera, F., & Guidorzi, C. 2009, A&A, 508, 173.
Band, D., Matteson, J., Ford, L., et al. 1993, ApJ, 413, 281
Belvedere, R., Pugliese, D., Rueda, J. A., et al. 2012, Nucl. Phys. A, 883, 1
Berger, E. 2011, GCN 12128
Berger, E., Fox, D. B., Kulkarni, S. R., et al. 2007, ApJ, 660, 504
Bianco, C. L., & Ruffini, R. 2004, ApJ, 605, L1
Bianco, C. L., & Ruffini, R. 2005a, ApJ, 633, L13
Bianco, C. L., & Ruffini, R. 2005b, ApJ, 620, L23

Bloom, J. S., Frail, D. A., & Sari, R. 2001, ApJ, 121, 2879
Cavallo, G., & Rees, M. J. 1978, MNRAS, 183, 359
Chevalier, R. A., & Soderberg, A. M. 2010, ApJ, 711, L40
Cummings, J. R., Barthelmy, S. D., Burrows, D. N., et al. 2011, GCN 12122
D'avanzo, P., Melandri, A., Palazzi, E., et al. 2012, GCN 13069
Damour, T., & Ruffini, R. 1975, Phys. Rev. Lett., 35, 463
Dainotti, M. G., Bernardini, M. G., Bianco, C. L., et al. 2007, A&A, 471, L29
Goodman, J. 1986, ApJ, 308, L47
Granot, J., & Sari, R. 2002, ApJ, 568, 820
Grupe, D., Nousek, J. A., vanden Berk, D. E., et al. 2007, AJ, 133, 2216
Holland, S. 2011, GCN 12157
Izzo L., Ruffini, R., Penacchioni A. V., et al. 2012a, A&A, 543, A10
Izzo, L., Rueda, J. A., & Ruffini, R. 2012b, A&A, 548, L5
Izzo, L., Rueda, J. A., Bianco, C. L., et al. 2012c, ApJ, submitted [arXiv:1205.6651]
Krühler, T., Greiner, J., Schady, P., et al. 2011, A&A, 534, A108
Levesque, E. M., Kewley, L. J., Graham, J. F., et al. 2010, ApJ, 712, L26
Margutti, R., Zainoni, E., Bernardini, M. G., et al. 2013, MNRAS, 428, 729
Negreiros, R., Ruffini, R., Bianco, C. L., et al. 2012, A&A, 540, A12
Nomoto, K., & Hashimoto, M. 1998, Phys. Rep., 163, 13
Nomoto, K., Yamakoa, H., Pols, O. R., et al. 1994, Nature, 371, 227
Ohmori, N., Akiyama, M., Yamauchi, M., et al. 2011, GCN 12172
Paczynsky, B. 1986, ApJ, 308, L43
Patricelli, B., Bernardini, M. G., Bianco, C. L., et al. 2012, ApJ, 756, 16
Penacchioni, A. V., Ruffini, R., Izzo, L., et al. 2012, A&A, 538, A58
Perley, D. A., Cenko, S. B., Bloom, J. S., et al. 2009, AJ, 138, 1690
Perley, D. A., Morgan, A. N., Updike, A., et al. 2011, AJ, 141, 36
Preparata, G., Ruffini, R., & Xue, S.-S. 1998, A&A, 338, L87
Ryde, F. 2004, ApJ, 614, 827
Rueda, J. A., & Ruffini, R. 2012, ApJ, 758, L7
Ruffini, R. 2001, in Fluctuating Paths and Fields, eds. W. Janke, A. Pelster, H.-J. Schmidt, & M. Bachmann (Singapore: World Scientific), 771
Ruffini, R. 2012, Plenary Talk at the Thirteenth MG Meet., Stockholm, Sweden
Ruffini, R., Salmonson, J. D., Wilson, J. R., & Xue, S.-S. 1999a, A&A, 350, 334
Ruffini, R., Salmonson, J. D., Wilson, J. R., & Xue, S.-S. 1999b, A&AS, 138, 511
Ruffini, R., Salmonson, J. D., Wilson, J. R., et al. 2000, A&A, 359, 855
Ruffini, R., Bianco, C. L., Fraschetti, F., et al. 2001a, ApJ, 555, L113
Ruffini, R., Bianco, C. L., Fraschetti, F., et al. 2001b, ApJ, 555, L117
Ruffini, R., Bianco, C. L., Chardonnet, P., et al. 2003, in XIth Brazilian School of Cosmology and Gravitation, eds. M. Novello, & S. E. Perez Bergliaffa, AIP Conf. Ser., 782, 16
Ruffini, R., Bianco, C. L., Chardonnet, P., et al. 2004, IJMPD, 13, 843
Ruffini, R., Bernardini, M. G., Bianco, C. L., et al. 2007, ESA-SP, 622, 561
Ruffini, R., Bernardini, M. G., Bianco, C. L., et al. 2008, in Proc. 11th Marcel Grosmann Meet. on General Relativity, eds. H. Kleinert, & R. T. Jantzen (World Scientific Publishing), 368
Ruffini, R., Vereshchagin, G., & Xue, S.-S. 2010, Phys. Rep., 487, 1
Sari, R., Piran, T., & Halpern, J. P. 1999, ApJ, 519, L17
Updike, A. C., Olivares, F., Greiner, J., et al. 2011, GCN 12129
Wiltshire, D. L., Visser, M., & Scott, S. M. 2009, The Kerr Spacetime: Rotating Black Holes in General Relativity (Cambridge University Press)
Xu, D., Fynbo, J. P. O., McCormac, J., et al. 2012, GCN 12764
Yonetoku, D., Murakami, T., Nakamura, R., et al. 2004, ApJ, 609, 935
Yonetoku, D., Murakami, T., Tsutsui, R., et al. 2010, PASJ, 62, 1495
Zauderer, B. A., Berger, E., Margutti, R., et al. 2012 [arXiv:1209.4654v1]
Zauderer, B. A., & Berger, E. 2012, GCN 12190
Zhang, B.-B., Burrows, D., Zhang, B., et al. 2012, ApJ, 748, 132

"If you can't explain it simply, you
don't understand it well enough."
Albert Einstein

Chapter 6

The scaling law for GRBs

As explained in Chapter 5, the concept of IGC explains the temporal coincidence of a GRB and a Type Ib/c SN. Recently, this concept has been extended, including a precise description of the progenitor system (Rueda & Ruffini 2012). The first members of the IGC family were GRB 090618 (Izzo et al. 2012c), with redshift $z = 0.54$, and GRB 101023 and GRB 110709B, of unknown redshift. We noticed in all these sources a standard behavior in the late part of the X-ray luminosity light curves, and used it to estimate the redshift in the cases of GRB 101023 and GRB 110709B. The results we found are consistent with other possible redshift indicators.

6.1 The sample

GRB 090618 is considered the prototype of the sample. Four different episodes have been identified:

- Episode 1 presents a thermal emission, sometimes accompanied by a power-law. The thermal emission evolves in time following a broken power-law (see Fig.4.12). This emission corresponds to the onset of the SN (from the evolved core) within the IGC scenario.
- Episode 2 is a canonical GRB, coincident with the formation of a BH from the NS companion. Both episodes are detected in the γ-ray emission.
- Episode 3 can be seen in the X-ray emission, from 10^2 s to 10^6 s after the BAT trigger time. It is usually characterized by a shallow phase or plateau (although for some sources the plateau is missing) and a final steeper decay. This emission is associated with the cooling of the NS generated in the SN explosion.
- Episode 4 takes place after ~ 10 days from the burst in the cosmological rest frame. It is observed as a bump in the optical band and it corresponds to the SN emission due to the Ni decay.

Following this argument, we selected a sample of eight *Swift* GRBs which had an isotropic energy $E_{iso} > 10^{52}$ erg and which satisfied at least one of the following requirements:

Table 6.1: Sample of GRBs belonging to the IGC family. The redshifts marked with an (*) were estimated by using the method described in this chapter, and the corresponding energies were calculated assuming these redshifts.

GRB	z	E_{iso} (erg)
060729	0.54	1.6×10^{52}
061007	1.261	1.0×10^{54}
080319B	0.937	1.3×10^{54}
090618	0.54	2.9×10^{53}
091127	0.49	1.1×10^{52}
111228	0.713	2.4×10^{52}
101023	0.9*	1.8×10^{53}
110709B	0.75*	1.7×10^{53}

- they need to present Episodes 1, 2, 3 and 4, with the characteristics described above,
- they need to have a measured cosmological redshift,
- they have to present evidence of an associated SN.

The cosmological redshifts of the GRBs of the sample lie in the range $0.49 \leq z \leq 1.261$. Table 6.1 shows the GRBs from the sample, with their respective redshifts and isotropic energies. We give a brief description of each source below.

GRB 060729 presents a small precursor and a main event in the γ-ray light curve. A SN bump was observed in the optical afterglow.

GRB 061007 presents a precursor with a clear evolving thermal emission (Larsson et al. 2011). No SN was observed for this source, due to its high redshift, $z = 1.261$.

GRB 080319B is known as the "naked-eye" GRB. Its prompt emission shows a possible double emission. A tentative SN associated to this source was reported (Kann et al. 2008). The X-ray light curve does not present a plateau and is well fit by a simple power-law.

GRB 090618 is the prototype of the IGC GRB-SN subclass. There is a clear optical bump, about ten days in the rest frame after the GRB trigger time, which is associated with a SN emission.

GRB 091127 has a redshift $z = 0.49$ and is associated with SN 2009nz (Cobb et al. 2010).

GRB 111228 shows several peaks in the prompt light curve. The detection of an SN is debated, since the subsequent optical bump has the same flux as the host galaxy, but a transient component not related to the afterglow was detected.

GRB 101023 presents two clear episodes in the prompt light curve, but no SN has been detected. The redshift is unknown because of the lack of optical observations at late times. We estimated a redshift $z \sim 0.9$ by comparing its light curve to the one of GRB 090618 in a common rest frame (Penacchioni et al. 2012).

GRB 110709B is the first GRB for which the BAT detector onboard the *Swift* satellite was triggered twice. The prompt emission is composed of two clear episodes of 50 s and 100 s of duration, separated by ~ 10 minutes. Like in

the case of GRB 101023, there is no detection of a SN nor measured redshift. Zauderer et al. (2013) classified this source as a "dark" GRB, as the CBM density is quite large and the emission must be strongly influenced by absorption. We estimated a redshift $z = 0.75$ using the same method described above.

6.2 Data analysis

To compare the XRT luminosity light curves of the six GRBs from the sample with measured redshift in the common rest frame energy range $0.3 - 10$ keV, we first converted the observed XRT flux f_{obs} to the rest frame energy range. In the detector frame, the $0.3 - 10$ keV rest-frame energy range becomes $\frac{0.3}{(1+z)} - \frac{10}{(1+z)}$ keV, where z is the redshift of each GRB.

On the one hand, we assume that the late decay of the X-ray light curve is best fit by a simple power-law

$$\frac{dN}{dAdtdE} \propto E^{-\gamma}, \tag{6.1}$$

so the flux in the $0.3 - 10$ keV rest-frame energy range, f_{rf}, can be written as a function of the observed flux f_{obs}

$$f_{rf} = f_{obs} \frac{\int_{0.3keV/(1+z)}^{10keV/(1+z)} E^{-\gamma} dE}{\int_{0.3keV}^{10keV} E^{-\gamma} dE} = f_{obs}(1+z)^{\gamma-1}. \tag{6.2}$$

To derive the luminosity in the rest frame L_{rf}, we just need to know the luminosity distance d_l (see Eq.(4.4))

$$L_{rf} = 4\pi d_l^2(z) f_{rf}. \tag{6.3}$$

On the other hand, we need to convert the time to the rest-frame. This is done by dividing the observed time by (1+z)

$$t_{rf} = \frac{t_{obs}}{(1+z)}. \tag{6.4}$$

Fig.6.1 shows the light curves of the six GRBs of the sample. Although the shape at early times (prompt emission and early X-ray light curve) varies from burst to burst, there is a remarkable common behavior at late times (i.e, the overlapping of the Episodes 3). This common behavior starts between $10^4 - 10^5$ after the trigger and continues until the the emission falls below the XRT energy threshold.

6.3 Conclusions

We presented a sample of IGC GRB-SN systems with a standard late time X-ray luminosity light curve in the $0.3 - 10$ keV energy band. This standard behavior points to a common physical origin of this emission, possibly related to a newly born NS out of the SN event (Negreiros et al. 2012), and not by the GRB itself. This scaling law offers a powerful tool to estimate the redshift of the GRBs that belong to this subclass. Another important point to note is that

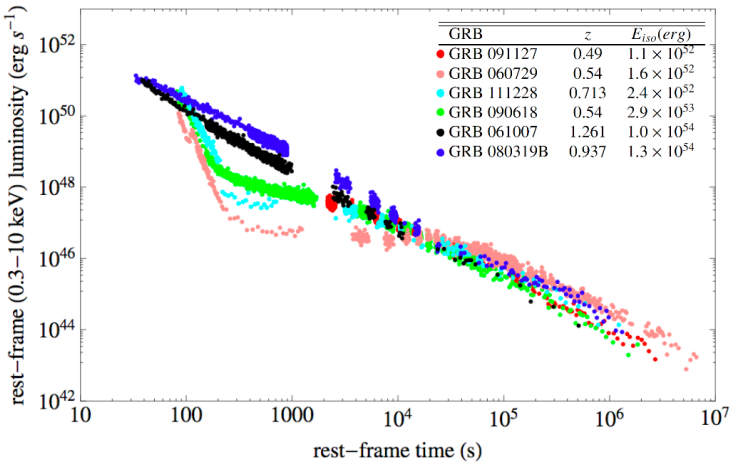

Figure 6.1: X-ray luminosity light curves in the rest frame of the six GRBs of the sample.

the binary systems giving rise to this subclass are very different from the binary systems giving rise to the short or disguised short GRBs. It is thought that the progenitor of short GRBs is a binary NS system, while for the disguised short, the progenitor might be a binary system which drifted to the galactic halo. Another proof of this is that the X-ray luminosity light curve is quite different for each of these classes. For example, the X-ray light curves of the disguised short GRB 090510 and GRB 060614 are very different from the one of GRB 090618 (see Fig.6.2). In addition, the less energetic sources like GRB 980425 (Pian et al. 2000) also show an even different behavior form the previous mentioned sources.

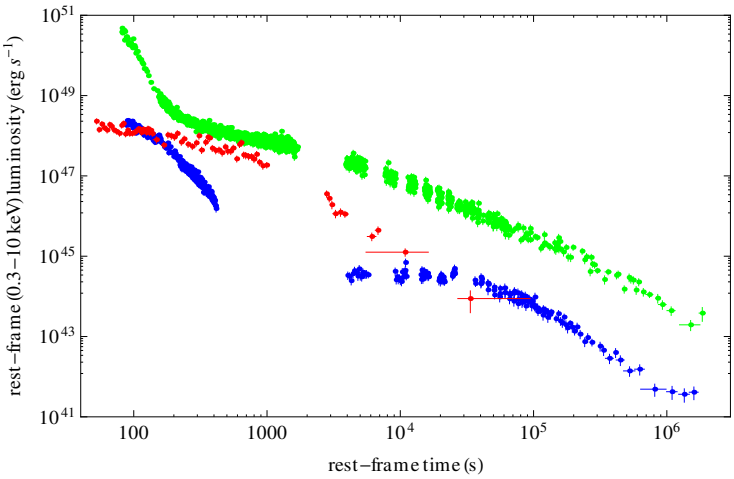

Figure 6.2: X-ray luminosity light curves in the $0.3 - 10$ keV rest frame energy range of GRB 090510 (red), GRB 060614 (blue) and GRB 090618 (green).

A&A 552, L5 (2013)
DOI: 10.1051/0004-6361/201220829

Astronomy & Astrophysics

L E

Novel distance indicator for gamma-ray bursts associated with supernovae

G. B. Pisani[1,3], L. Izzo[1,2], R. Ruffini[1,2], C. L. Bianco[1,2], M. Muccino[1], A. V. Penacchioni[1,3], J. A. Rueda[1,2], and Y. Wang[1]

[1] Dipartimento di Fisica, Sapienza Universitá di Roma and ICRA, Piazzale Aldo Moro 5, 00185 Roma, Italy
e-mail: gb.pisani@icranet.org
[2] ICRANet, Piazza della Repubblica 10, 65122 Pescara, Italy
[3] Université de Nice Sophia Antipolis, Grand Chateau Parc Valrose, 06103 Nice Cedex 2, France

Received 30 November 2012 / Accepted 4 March 2013

ABSTRACT

Context. It has been proposed that the temporal coincidence of a gamma-ray burst (GRB) and a type Ib/c supernova (SN) can be explained with the concept of induced gravitational collapse (IGC), induced by the matter ejected from an SN Ib/c accreting onto a neutron star (NS). The NS is expected to reach the critical mass necessary for it to collapse to a black hole (BH) and emit a GRB. We found a standard luminosity light curve behavior in the late-time X-ray emission of this subclass of GRBs.
Aims. We test if this standard behavior in the luminosity found in this subclass of GRBs can become a redshift estimator of these sources.
Methods. We selected a sample of GRBs that belong to this subclass of IGC GRBs associated to an SN (IGC GRB-SN sources). These sources have an isotropic energy $E_{\rm iso} > 10^{52}$ erg and their cosmological redshifts are in the range of $z = 0.49-1.261$. We focused on the corresponding X-ray luminosity light curves.
Results. We find that all GRBs of the sample with measured redshift present a standard luminosity late-time light curve in the 0.3−10 keV rest-frame energy range. We used these results to estimate the GRB redshift of the sample without a measured redshift and found results consistent with other possible redshift indicators.
Conclusions. The standard late-time X-ray luminosity light curve of all GRBs of the sample shows a common physical mechanism in this particular phase of the X-ray emission, possibly related to the creation of the NS from the SN process. This scaling law moreover represents strong evidence of very low or even absent beaming in this late phase of the X-ray afterglow emission process. This could be a fundamental tool for estimating the redshift of GRBs that belong to this subclass of events. We are currently expanding this subclass of GRBs to further verify the universal validity of this new redshift estimation method.

Key words. supernovae: general – binaries: general – gamma-ray burst: general – distance scale

Recently, Ruffini et al. (2001, 2007) proposed that the temporal coincidence of some gamma-ray bursts (GRBs) and a type Ib/c supernovae (SNe) can be explained with the concept of induced gravitational collapse (IGC) of a neutron star (NS) to a black hole (BH) induced by accretion of matter ejected by the SN Ib/c. More recently, this concept has been extended, including a precise description of the progenitor system of such GRB-SN systems (Rueda & Ruffini 2012).

The main new result presented here is that the IGC GRB-SN class shows a standard late X-ray luminosity light curve in the common energy range 0.3−10 keV (Ruffini 2013).

The prototype is GRB 090618 (Ruffini et al. 2011; Izzo et al. 2012b,a) at redshift $z = 0.54$, where four different emission episodes have been identified.

Episode 1, corresponding to the SN onset, has been observed to have thermal as well as power-law emission. The thermal emission changes in time following a precise power-law behavior (Izzo et al. 2012b; Penacchioni et al. 2012, 2013).

Episode 2 follows and in the IGC model corresponds to the GRB emission coincident with the BH formation. The characteristic parameters of the GRB, including baryon load, the Lorentz factor, and the nature of the circumburst medium (CBM), have been computed (Izzo et al. 2012b; Penacchioni et al. 2012, 2013).

Episode 3 is characterized in the X-ray light curve by a shallow phase (a plateau) followed by a final steeper decay. Typically, it is observed in the range 10^2-10^6 s after the GRB trigger.

Episode 4 occurs after a time of about ten days in the cosmological rest-frame, corresponding to the SN emission due to the Ni decay (see Arnett 1996, for a complete review). This emission is clearly observed in GRB 090618 during the late optical GRB afterglow emission.

Here we analyze the X-ray emission of a sample of eight GRBs with $E_{\rm iso} \geq 10^{52}$ erg that satisfy at least one of the following three requirements:

- there is a double emission episode in the prompt emission: Episode 1, with a decaying thermal feature, and Episode 2, a canonical GRB, as in GRB 090618 (Izzo et al. 2012b), GRB 101023 (Penacchioni et al. 2012), and in GRB 110709B (Penacchioni et al. 2013);
- there is a shallow phase followed by a final steeper decay in the X-ray light curve: Episode 3;

Table 1. GRB sample considered in this work.

GRB	z	$E_{\rm iso}$ (erg)
GRB 060729	0.54	1.6×10^{52}
GRB 061007	1.261	1.0×10^{54}
GRB 080319B	0.937	1.3×10^{54}
GRB 090618	0.54	2.9×10^{53}
GRB 091127	0.49	1.1×10^{52}
GRB 111228	0.713	2.4×10^{52}
GRB 101023	0.9*	1.8×10^{53}
GRB 110709B	0.75*	1.7×10^{53}

Notes. The redshifts of GRB 101023 and GRB 110709B, which are marked with an asterisk, were deduced theoretically by using the method outlined here (Penacchioni et al. 2012) and the corresponding isotropic energy computed by assuming these redshifts.

– an SN is detected after about ten days from the GRB trigger in the rest-frame: Episode 4.

We found eight GRBs that satisfy our requirements (see Table 1).

GRB 060729. In this source an SN bump was observed in the optical GRB afterglow (Cano et al. 2011). It is at the same redshift $z = 0.54$ as GRB 090618 and shows a small precursor plus a main event in the prompt light curve and a peculiar prolonged duration for the X-ray afterglow. The isotropic energy emitted in this burst is $E_{\rm iso} = 1.6 \times 10^{52}$ erg (Grupe et al. 2007).

GRB 061007. This GRB has no associated SN but is characterized by a precursor with a clear evolving thermal emission (Larsson et al. 2011). With an energetic $E_{\rm iso}$ of 1.0×10^{54} erg (Golenetskii et al. 2006) at $z = 1.261$, it is the farthest GRB in our sample. The large distance makes the detection of an SN from this GRB difficult.

GRB 080319B. A tentative SN was reported also for GRB 080319B, well-known as the naked-eye GRB, whose prompt emission also shows a possible double-emission episode (Kann et al. 2008). Its measured redshift is $z = 0.937$. This is one of the most energetic GRB, with $E_{\rm iso} = 1.3 \times 10^{54}$ erg (Golenetskii et al. 2008), and its X-ray light curve is well fit by a simple decaying power-law.

GRB 090618. This GRB is the prototype of the IGC GRB-SN subclass. Its prompt emission shows a clear Episode 1 plus Episode 2 structure in light curve and spectrum. The measured redshift is $z = 0.54$ and the $E_{\rm iso} = 2.9 \times 10^{53}$ erg (Izzo et al. 2012b). There is a clear optical bump, about ten days of rest-frame time after the GRB trigger, in the afterglow light curve of GRB 090618 that is associated with the SN emission (Cano et al. 2011). The characteristic parameters of this GRB, including the baryon load ($B = 1.98 \times 10^{-3}$), the Lorentz factor at the transparency ($\Gamma_{\rm tr} = 495$), and the nature of the CBM ($\langle n_{\rm CBM} \rangle = 0.6\,{\rm part/cm^3}$), have been estimated previously (Izzo et al. 2012b).

GRB 091127. GRB 091127 is associated with SN 2009nz at a redshift of $z = 0.49$ (Cobb et al. 2010). The $E_{\rm iso}$ for this burst is 1.1×10^{52} erg (Wilson-Hodge & Preece 2009).

GRB 111228. An SN feature was also reported in the literature for GRB 111228 (D'Avanzo et al. 2012), which shows a multiply peaked prompt light curve in the Fermi-GBM data. The measured redshift of this GRB is $z = 0.713$, its $E_{\rm iso} = 2.4 \times 10^{52}$ erg (Briggs & Younes 2011), and a dedicated analysis of this GRB will be presented elsewhere. The detection of an SN in GRB 111228 is debated, since the subsequent optical bump has the same flux as the host galaxy of the source, but SN features were observed in the differential photometry between the last epochs of observations, where a transient component was detected that was unrelated to the afterglow, and was consequently attributed to the SN.

GRB 101023. This GRB shows clear Episode 1 and Episode 2 emissions in the prompt light curve and spectrum, but there is no detection of an SN and no measured redshift because of the lack of optical observations at late times. We estimated the redshift of this source at $z = 0.9$ by analogy to the late X-ray afterglow decay observed in the six GRBs with a measured redshift. This leads to an estimate of $E_{\rm iso} = 1.8 \times 10^{53}$ erg, a baryon load of $B = 3.8 \times 10^{-3}$, a Lorentz factor at transparency of $\Gamma_{\rm tr} = 260$, and an average density for the CBM of ($\langle n_{\rm CBM} \rangle \approx 16\,{\rm part/cm^3}$ (Penacchioni et al. 2012).

GRB 110709B. Like GRB 101023, this GRB shows clear Episode 1 plus Episode 2 emission in the prompt light curve and spectrum, but there is no detection of an SN. This can be explained by the fact that it is a dark GRB, whose emission is strongly influenced by absorption. Particularly interesting is the detection of clear radio emission (Zauderer et al. 2012). There is no measurement for the redshift but, as for GRB 101023, we estimated it to be $z = 0.75$ by analogy to the late X-ray afterglow decay observed in the six GRBs with measured redshifts. This leads to an estimate of an isotropic energy of $E_{\rm iso} = 1.7 \times 10^{53}$ erg, a baryon load of $B = 5.7 \times 10^{-3}$, a Lorentz factor at the transparency of $\Gamma_{\rm tr} = 174$, and an average density of the CBM of $\langle n_{\rm CBM} \rangle \approx 76\,{\rm part/cm^3}$ (Penacchioni et al. 2013).

We focused the analysis of all available XRT data of these sources. Characteristically, XRT follow-up starts only about 100 seconds after the BAT trigger (typical repointing time of *Swift* after the BAT trigger). Because the behavior was similar in all sources, we compared the analyzed XRT luminosity light curve $L_{\rm rf}$ for the six GRBs with measured redshifts in the common rest-frame energy range 0.3–10 keV. As a first step we converted the observed XRT flux $f_{\rm obs}$ to one in the 0.3–10 keV rest-frame energy range. In the detector frame, the 0.3–10 keV rest-frame energy range becomes $[0.3/(1+z)] - [10/(1+z)]$ keV, where z is the redshift of the GRB. We assumed a simple power-law function as the best fit for the spectral energy distribution of the XRT data[1]:

$$\frac{{\rm d}N}{{\rm d}A\,{\rm d}t\,{\rm d}E} \propto E^{-\gamma}. \tag{1}$$

We can then write the flux light curve, $f_{\rm rf}$, in the 0.3–10 keV rest-frame energy range as

$$f_{\rm rf} = f_{\rm obs} \frac{\int_{\frac{0.3\ {\rm keV}}{1+z}}^{\frac{10\ {\rm keV}}{1+z}} E^{-\gamma}{\rm d}E}{\int_{0.3\ {\rm keV}}^{10\ {\rm keV}} E^{-\gamma}{\rm d}E} = f_{\rm obs}(1+z)^{\gamma-1}. \tag{2}$$

Then, we have to multiply $f_{\rm rf}$ by the luminosity distance to derive $L_{\rm rf}$:

$$L_{\rm rf} = 4\,\pi\,d_l^2(z) f_{\rm rf}, \tag{3}$$

where we assume a standard cosmological ΛCDM model with $\Omega_{\rm m} = 0.27$ and $\Omega_\Lambda = 0.73$. Clearly, this luminosity must be plotted as a function of the rest-frame time $t_{\rm rf}$, namely

$$t_{\rm rf} = \frac{t_{\rm obs}}{1+z}. \tag{4}$$

The X-ray luminosity light curves of the six GRBs with measured redshifts in the 0.3–10 keV rest-frame energy band are

[1] http://www.swift.ac.uk/

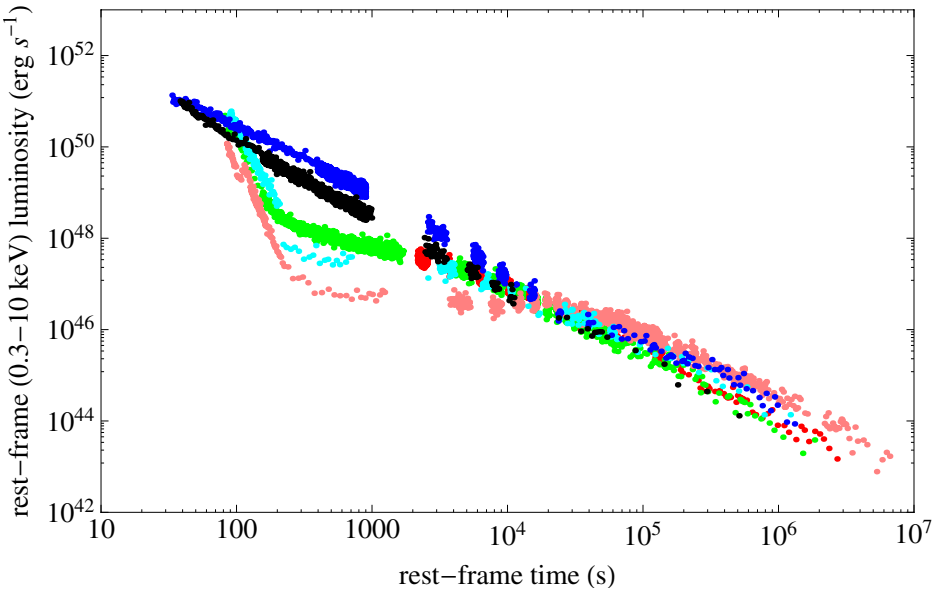

Fig. 1. X-ray luminosity light curves of the six GRBs with measured redshift in the 0.3−10 keV rest-frame energy range: in pink GRB 060729, $z = 0.54$; black GRB 061007, $z = 1.261$; blue GRB 080319B, $z = 0.937$; green GRB 090618, $z = 0.54$, red GRB 091127, $z = 0.49$, and in cyan GRB 111228, $z = 0.713$.

plotted in Fig. 1. What is most striking is that these six GRBs, with redshifts in the range 0.49−1.261, show a remarkably common behavior of the late X-ray afterglow luminosity light curves (Episode 3), despite their very different prompt emissions (Episode 1 and 2) and energetics spanning more than two orders of magnitude. The common behavior starts between 10^4−10^5 s after the trigger and continues until the emission falls below the XRT threshold. This standard behavior of Episode 3 represents a strong evidence of very low or even absent beaming in this particular phase of the X-ray afterglow emission process. We have proposed that this late-time X-ray emission in Episode 3 is related to the process of the SN explosion within the IGC scenario, possibly emitted by the newly born NS, and not by the GRB itself (Negreiros et al. 2012). This scaling law, when confirmed in sources with Episode 1 plus Episode 2 emissions, offers a powerful tool for estimating the redshift of GRBs that belong to this subclass of events. As an example, Fig. 2 plots the rest-frame X-ray luminosity (0.3−10 keV) light curve of GRB 090618 (considered the prototype of the common behavior shown in Fig. 1) with the rest-frame X-ray luminosity light curves of GRB 110709B estimated for selected values of its redshifts $z = 0.4, 0.6, 0.8, 1.0$, and 1.2, and similarly the corresponding analysis for GRB 101023 for redshifts $z = 0.6, 0.8, 1.0, 1.2$, and 1.5. This shows that GRB 101023 should have been located at $z \sim 0.9$ and GRB 110709B at $z \sim 0.75$. These redshift estimates are within the range expected using the Amati relation as shown in Penacchioni et al. (2012, 2013). This is an important independent validity confirmation for this new redshift estimator we are proposing for the family of IGC GRB-SN systems. We stress, however, that the redshift was determined assuming the validity of the standard ΛCDM cosmological model for sources with redshift in the range $z = 0.49$−1.216. We are currently testing the validity of this assumption for sources at higher cosmological redshifts.

Before concluding, it is appropriate to recall once again that we assumed that these binary systems give rise to the IGC GRB-SN sources, which are a subclass of all GRBs. Their special binary nature is very different from that corresponding to the genuine short GRBs, for instance. For these the progenitors are thought by many to be binary neutron stars and there is no expected observable afterglow emission (see e.g. the case of GRB 090227B presented in Muccino et al. 2013). They are also different from disguised short GRBs, which again may originate from binary systems drifting to the galactic halo (Bernardini et al. 2007; Caito et al. 2009, 2010; de Barros et al. 2011). In particular, they may differ from GRB 060614, where there is strong evidence that it has no associated SN (Della Valle et al. 2006; Gal-Yam et al. 2006; Gehrels et al. 2006). We were also able to show explicitly that the X-ray luminosity light curve of the IGC GRB-SN prototype, GRB 090618, is drastically different both from that of GRB 060614 and that of GRB 090510, which may be an example of a disguised short GRB that may have instead exploded in a very high density region (Muccino et al. 2013), see Fig. 3. In all the above examples we have considered very energetic sources ($E_{\rm iso} \geq 10^{52}$ erg). Less energetic GRB-SN sources, e.g. GRB 980425 (Pian et al. 2000), also show a late X-ray emission different from the typical emission of the IGC GRB-SN sources, and we will discuss this matter elsewhere.

We presented a sample of IGC GRB-SN systems with a standard late-time (10^4−10^5 s after the trigger) X-ray luminosity light curve in the 0.3−10 keV rest-frame energy band. This standard behavior points to a common physical origin of this emission, possibly related to a newly born NS out of the SN event (Negreiros et al. 2012). This scaling law can provide a new distance indicator for this subclass of GRBs, allowing one to predict the redshift of the source as well as the presence of an associated SN.

We are currently testing the predictive power of our results on three different observational scenarios for sources of the IGC GRB-SN subclass:

– GRBs at high redshift. We are able to predict the existence of an SN in these systems, which is expected to emerge after $t \sim 10\,(1 + z)$ days, the canonical time sequence of an SN explosion. This offers a new challenge to detect SNe at high redshift, e.g., by observing radio emission (Penacchioni et al. 2013);

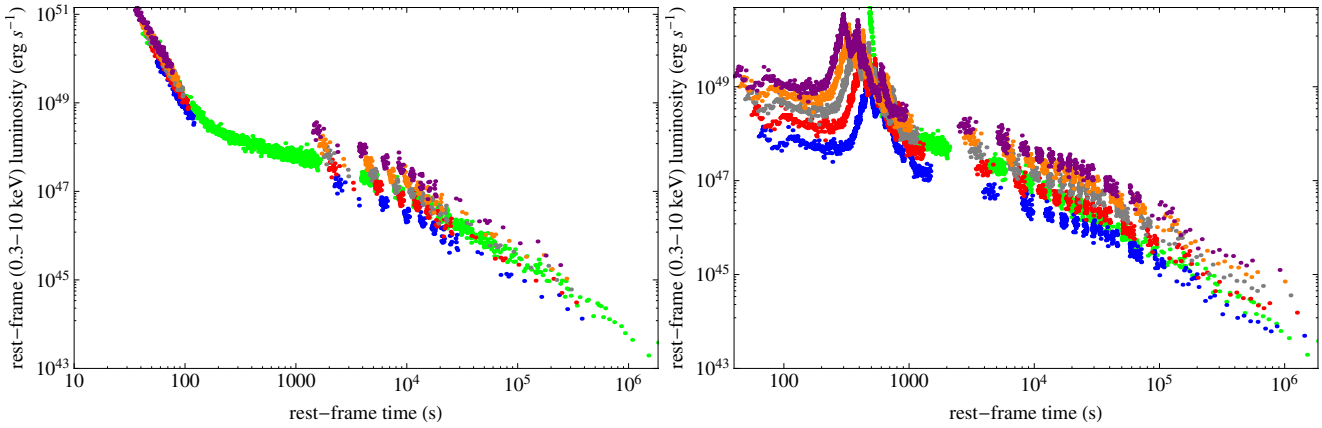

Fig. 2. In green we show the rest-frame X-ray luminosity light curve of GRB 090618 in the 0.3−10 keV energy range in comparison with the one of GRB 101023 (*left*) and GRB 110709B (*right*), computed for different hypothetical redshifts: respectively, from blue to purple: z = 0.6, 0.8, 1.0, 1.2, 1.5 (*left*) and z = 0.4, 0.6, 0.8, 1.0, 1.2 (*right*). The overlapping at late time of the two X-ray luminosity light curves is obtained for a redshift of z = 0.9 (*left*) and z = 0.75 (*right*). For further details see Penacchioni et al. (2012, 2013).

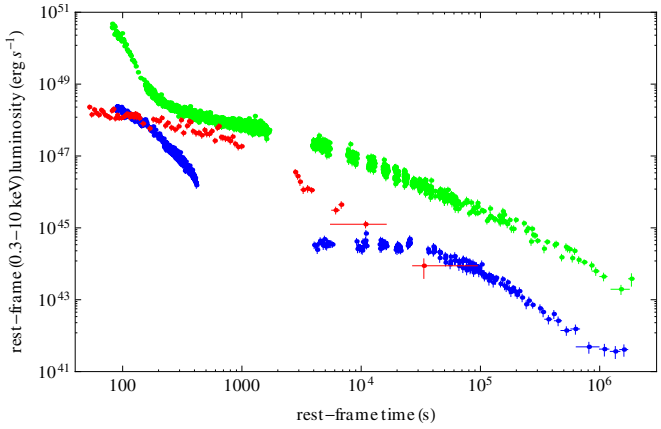

Fig. 3. X-ray luminosity light curves of GRB 090618 (green), GRB 060614 (blue), and GRB 090510 (red) in the 0.3−10 keV rest-frame energy range.

- for GRBs with $z \leq 1$ we can indicate in advance from the X-ray luminosity light curve observed by XRT the expected time for the observations of an SN and alert direct observations from ground- and space-based telescopes;
- as we showed here, we can infer the redshift of GRBs in the same way we did for GRB 110709B and GRB 101023A.

We are currently expanding the sample to increase the statistical validity of our approach and its cosmological implications.

Acknowledgements. We are grateful to the anonymous referee for important remarks that have improved the presentation of our paper. We also thank the *Swift* team for the support. This work made use of data supplied by the UK *Swift* Data Center at the University of Leicester. G.B. Pisani and A.V. Penacchioni are supported by the Erasmus Mundus Joint Doctorate Program by Grant Numbers 2011-1640 and 2010-1816, respectively, from the EACEA of the European Commission.

References

Arnett, D. 1996, Supernovae and Nucleosynthesis (Princeton University Press)
Bernardini, M. G., Bianco, C. L., Caito, L., et al. 2007, A&A, 474, L13
Briggs, M. S., & Younes, G. 2011, GRB Coordinates Network, 12744, 1
Caito, L., Bernardini, M. G., Bianco, C. L., et al. 2009, A&A, 498, 501
Caito, L., Amati, L., Bernardini, M. G., et al. 2010, A&A, 521, A80
Cano, Z., Bersier, D., Guidorzi, C., et al. 2011, MNRAS, 413, 669
Cobb, B. E., Bloom, J. S., Perley, D. A., et al. 2010, ApJ, 718, L150
D'Avanzo, P., Melandri, A., Palazzi, E., et al. 2012, GRB Coordinates Network, 13069, 1
de Barros, G., Amati, L., Bernardini, M. G., et al. 2011, A&A, 529, A130
Della Valle, M., Chincarini, G., Panagia, N., et al. 2006, Nature, 444, 1050
Gal-Yam, A., Fox, D. B., Price, P. A., et al. 2006, Nature, 444, 1053
Gehrels, N., Norris, J. P., Barthelmy, S. D., et al. 2006, Nature, 444, 1044
Golenetskii, S., Aptekar, R., Mazets, E., et al. 2006, GRB Coordinates Network, 5722, 1
Golenetskii, S., Aptekar, R., Mazets, E., et al. 2008, GRB Coordinates Network, 7482, 1
Grupe, D., Gronwall, C., Wang, X.-Y., et al. 2007, ApJ, 662, 443
Izzo, L., Rueda, J. A., & Ruffini, R. 2012a, A&A, 548, L5
Izzo, L., Ruffini, R., Penacchioni, A. V., et al. 2012b, A&A, 543, A10
Kann, D. A., Schulze, S., & Updike, A. C. 2008, GRB Coordinates Network, 7627, 1
Larsson, J., Ryde, F., Lundman, C., et al. 2011, MNRAS, 414, 2642
Muccino, M., Ruffini, R., Bianco, C. L., Izzo, L., & Penacchioni, A. V. 2013, ApJ, 763, 125
Negreiros, R., Ruffini, R., Bianco, C. L., & Rueda, J. A. 2012, A&A, 540, A12
Penacchioni, A. V., Ruffini, R., Izzo, L., et al. 2012, A&A, 538, A58
Penacchioni, A. V., Ruffini, R., Bianco, C. L., et al. 2013, A&A, 551, A133
Pian, E., Amati, L., Antonelli, L. A., et al. 2000, ApJ, 536, 778
Rueda, J. A., & Ruffini, R. 2012, ApJ, 758, L7
Ruffini, R. 2013, in The Thirteenth Marcel Grossmann Meeting On Recent Developments in Theoretical and Experimental General Relativity, Gravitation and Relativistic Field Theories, in press
Ruffini, R., Bianco, C. L., Fraschetti, F., Xue, S., & Chardonnet, P. 2001, ApJ, 555, L117
Ruffini, R., Bernardini, M. G., Bianco, C. L., et al. 2007, in ESA SP, 622, 561
Ruffini, R., Izzo, L., Penacchioni, A. V., et al. 2011, PoS(Texas2010), 101
Wilson-Hodge, C. A., & Preece, R. D. 2009, GRB Coordinates Network, 10204, 1
Zauderer, B. A., Berger, E., Margutti, R., et al. 2012 [arXiv:1209.4654]

"We cannot solve our problems with
the same thinking we used when we
created them."
Albert Einstein

Chapter 7

Future prospects

7.1 Observational predictions based on the IGC paradigm

After applying the IGC model to the members of the sample presented in Pisani et al. (2013), we continued searching for new members to enlarge the sample. A particular case is the one of GRB 130427A, since it is one of the brightest sources ever seen. It was observed by the three detectors onboard *Swift* satellite. The BAT detector was triggered at 07:47:57 UT, with a calculated location RA=173.139, DEC=27.692 (Maselli et al. 2013). The XRT detector started to observe 140.2 s after the BAT trigger. The UVOT made a follow-up observation of the optical afterglow (Pritchard et al. 2013). It appears to be a blurred bright source near the XRT position. This extremely bright source was also detected by *Fermi*-GBM (von Kienlin 2013) and *Fermi*-LAT (Zhu et al. 2013b,a). There have been observations also by *Konus*-Wind (Golenetskii et al. 2013). Soon after that, ground-based telescopes like Keck (Perley & Tang 2013), Gemini-north (Levan et al. 2013a), GMG (Zhao et al. 2013), NOT (Xu et al. 2013b) and VLT (Melandri et al. 2013), among others, started to follow the optical afterglow. NOT detected absorption and emission lines at a common redshift of $z = 0.338 \pm 0.002$, consistent with the one detected by the Gemini-North telescope (Levan et al. 2013a) and further confirmed by the VLT/X-shooter (Flores et al. 2013).

The main characteristic of GRB 130427A is that it presents the typical pattern of the IGC family in its X-ray afterglow light curve. The overlapping of this light curve with one GRB from the sample presented in Pisani et al. (2013) (GRB 060729) is shown in Fig.7.1. From this overlapping we could estimate a redshift $z \approx 0.3$, in full agreement with the measured value. Besides, the prompt light curve shows a double emission, as detected by *Fermi*-GBM (see Fig.7.2).

7.1.1 Predictions of a SN

We proceeded to the prediction of the possible observation of an SN associated to this source. We first assumed that the luminosity of the SN associated to GRB 130427A would be the same as the one of SN 1998bw, as found in the IGC sample. Then, for the intergalactic absorption in the I-band (which corresponds

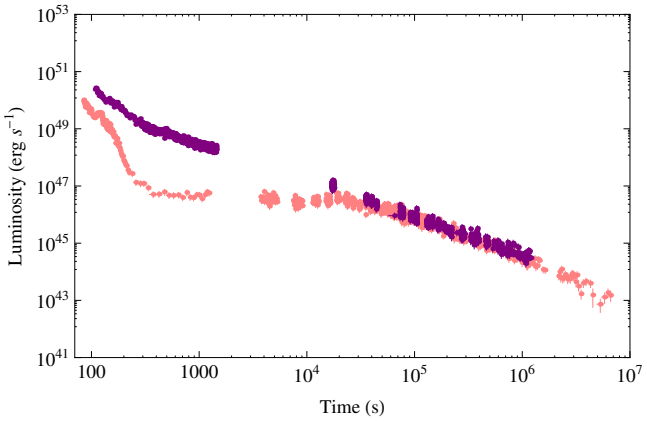

Figure 7.1: X-ray luminosity light curves of GRB 060729 (pink) and GRB 130427A (purple) in the rest frame energy band $0.3 - 10$ keV. The light curves overlap also with all the ones from the sample presented in Pisani et al. (2013) in the late decay phase, after 2×10^4 s, but we show just one source for clearness.

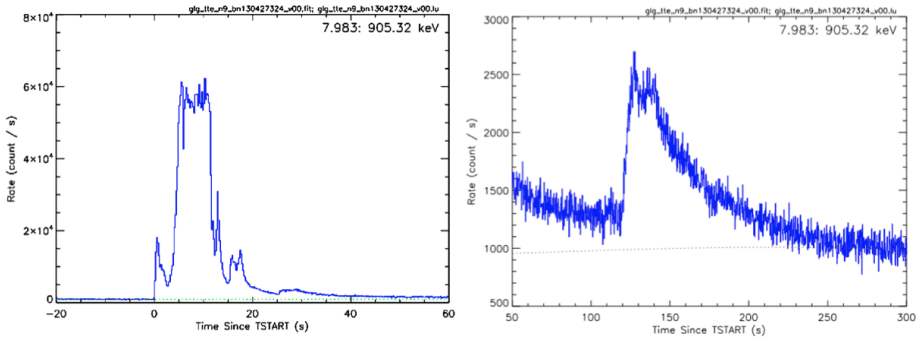

Figure 7.2: *Fermi*-GBM (NaI 81000 keV) light curve of GRB 130427A, with episodes 1 (left) and 2 (right) explicitly indicated.

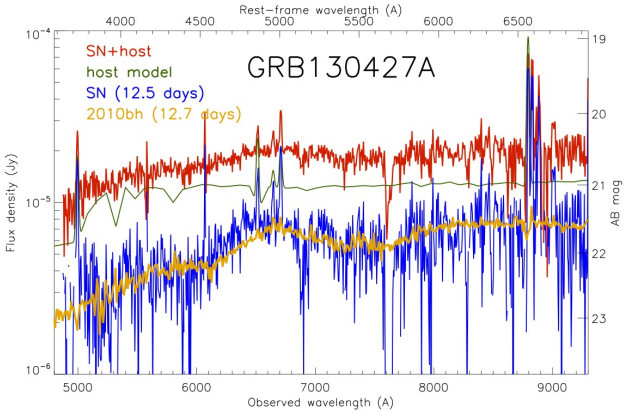

Figure 7.3: Preliminary analysis of the GTC observations, showing the presence of a SN. Taken from de Ugarte Postigo et al. (2013).

to the R-band in the rest-frame) and the intrinsic one, and assuming a Milky Way type for the host galaxy, we obtained a magnitude expected for the peak of the SN of $I = 22 - 23$ to be observed $t \approx 13 - 15$ days after the GRB trigger, namely between May, 10 and 12, 2013. We sent a GCN circular with the estimates of our model (Ruffini et al. 2013), encouraging further optical and radio observations that could confirm our prediction.

On May, 7 the first circular appeared about the presence of a SN (Xu et al. 2013a). The NOT telescope observed the optical counterpart, starting 12.85 hr after the GRB trigger. The light curve between ~ 1 and 5 days after the trigger (observer frame) is well fit by a power law with decay index 1.3, but after day 5, however, the light curve gradually flattens. The flattening, albeit reduced, is still evident after subtracting the (known) flux contribution of the host galaxy. The flattening in the decay, summed to the change of the spectral shape, and the overall flux level are all consistent with the emergence of a SN.

The GTC telescope (de Ugarte Postigo et al. 2013) observed the optical counterpart 16.7 days after the GRB onset. Since the spectrum has a strong contribution from the host galaxy, they built a synthetic host galaxy spectrum based on the SDSS (DR9) photometry. They then subtracted this host galaxy template from the GTC spectrum to obtain a "clean" spectrum of the counterpart associated to GRB 130427A. The resulting spectrum was that of a broad-lined Ic SN, with a prominent bump at $\sim 6800A$ observer frame. In particular, they obtained an excellent match with the spectrum of SN 2010bh (see Fig.7.3).

Skynet observed the source after 17.8 days. There is a rebrightening in the V, R and I bands, which may be the onset of the classical SN (Trotter et al. 2013). Finally, on May, 20, the Hubble Space Telescope measured the preliminary magnitude of the source in the UV, optical and NIR bands (Levan et al. 2013b). They discovered a significant curvature in the optical band, likely due to the underlying supernova SN 2013cq. This way, our predictions were confirmed.

Figure 7.4: Geographical distribution of the LOFT community.

7.1.2 Conclusions

The prediction of the occurrence of an SN associated with GRB 130427A has been a huge step forward. Not only have we been able to understand the nature of the progenitors of this kind of sources (IGC family), but also to predict many days in advance the occurrence of a SN. It is important to note, though, that this has been a lucky strike, since the source is one of the brightest ones ever seen, it satisfies all the requirements to be a member of the IGC sources, there is a good coverage in all its electromagnetic spectrum from the sky and from the Earth, and the redshift is low ($z \sim 0.3$). We are currently searching for more sources that could be members of this special class of GRBs. We strongly encourage the development of new space missions, which could provide light curves and spectra in a wider energy band, covering also the prompt emission in X-rays.

7.2 The LOFT mission

The Large Observatory for X-ray Timing (LOFT) is a satellite mission currently in assessment phase for the ESA M3 selection. It was selected in 2011 as one of the four Cosmic Vision M3 candidate missions to compete for a launch opportunity between 2022 and 2024. The current schedule foresees the end of the assessment study by the end of 2013 and the final selection in the first months of 2014 (Amati et al. 2013). System aspects are currently being studied by ESA and its industrial contractors. The scientific payload is being studied by a consortium of European scientific institutes (including teams from the Czech Republic, Denmark, Finland, France, Germany, Italy, the Netherlands, Poland, Spain, Switzerland and the United Kingdom), with support form international partners in Brazil, Japan and the United States. An even wider science support community (see Fig.7.4) is contributing by providing scientific inputs to help focus and refine the science case and the scientific requirements (Feroci et al. 2012).

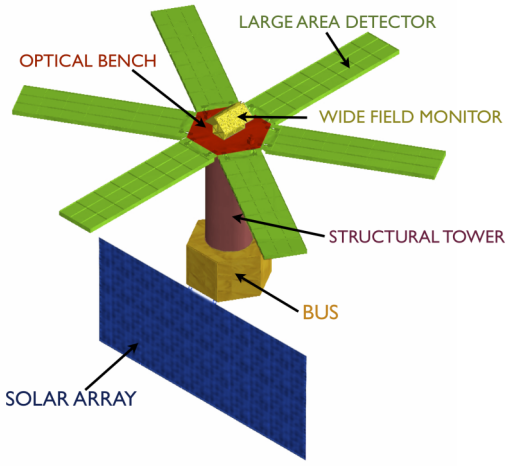

Figure 7.5: Conceptual scheme of the LOFT satellite.

7.2.1 LOFT payload

The LOFT payload is an extensive array of X-ray detectors with a total geometric area of ~ 18 m^2. The satellite will operate in a low equatorial Earth orbit (~ 600 km, $< 5°$ deg inclination) in order to reduce the background and the radiation damage effect of the South Atlantic Anomaly. It will carry two instruments onboard, the Large Area Detector (LAD) and the Wide Field Monitor (WFM), see Fig.7.5.

- The LAD has an effective area of ~ 10 m^2 at 8 keV (see Fig.7.6), which will provide a total of ~ 280000 cts/s for a 1Crab source (about 3000 cts/s are expected from the background) and a spectral resolution of ~ 260 keV in the energy band $2 - 30$ keV. With these characteristics, the LAD will be able to exploit the diagnostics of very rapid X-ray flux and spectral variability that directly probe the motion of matter down to distances very close to BH and NS.

  The basic setup of the instrument is a set of 6 Detector Panels (see Fig.7.7) tiled with ~ 2000 Silicon Drift Detectors (SSD), which operate in the energy range $2 - 30$ keV and have an energy resolution of ~ 260 eV (energy coverage in the $30 - 80$ keV band will be also provided but only with a coarse energy resolution). The modular structure ensures a high level of redundancy and the robustness of the instrument against single unit failures. The field of view of the LAD is limited to $\leq 1°$ by X-ray collimators. These are developed by using the technique of micro capillary plates, the same used for the micro-channel plates: a 6 mm thick sheet of lead glass is perforated by a huge number of micro-pores. The stopping peer of Pb in the glass over the large number of walls that off-axis photons need to cross is effective in collimating X-rays below 50 keV. The required stability of the instrument response is ensured by a combination of the collimator response and the attitude and orbital control system parameters. This will avoid any significant spurious modulation of the detected source flux.

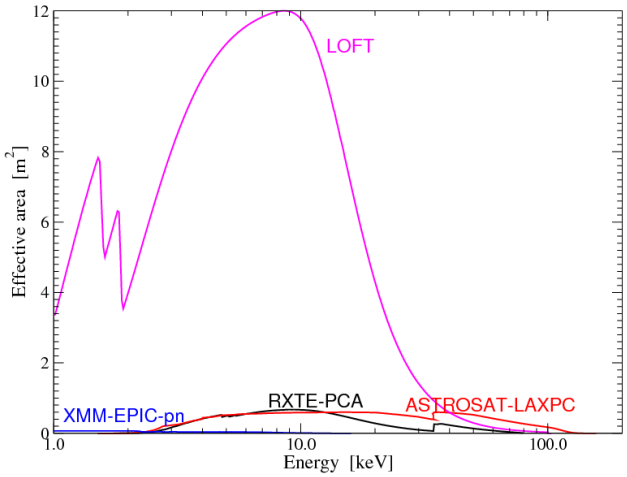

Figure 7.6: LOFT-LAD effective area compared with that of other existing and planned X-ray missions.

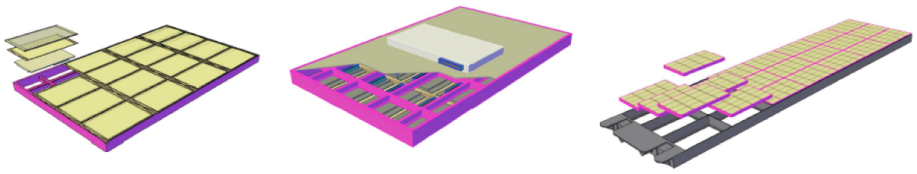

Figure 7.7: **Left**: front-side view of a module of the Large Area Detector, showing the mounting of the collimator, SDD and the front end electronics. **Center**: back side view of the module, showing the radiative surface and the module back end electronics. **Right**: one of the LOFT detector panels with all the assembled modules and the interfaces to the deployment system. Each panel comprises 21 modules and each module includes 16 SDD. Taken from http://www.isdc.unige.ch/loft/index.php/instruments-on-board-loft.

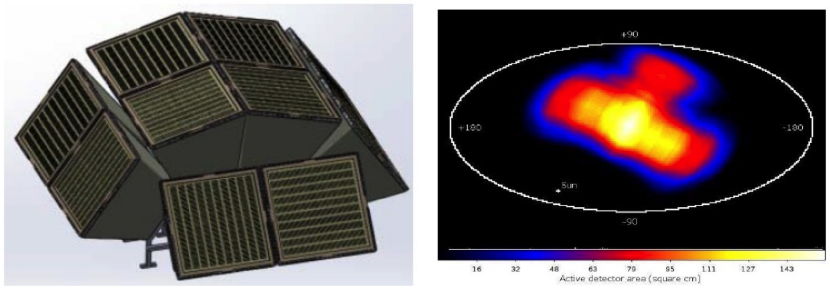

Figure 7.8: The Wide Field Monitor (left) and its field of view (right).

- The WFM (see Fig.7.8) is based on the classical coded mask integrated technique. The specific LOFT design is an evolution of the design adopted in the SuperAGILE experiment, with a noticeable improvement provided by the low energy threshold, better energy resolution and the (asymmetric) 2D imaging capabilities of the SDDs. The same SDDs used in the LAD can be used for imaging purposes in the WFM, by adopting a proper anode pitch (145μm). The main science requirement for the WFM is to monitor and image the sky accessible to the LAD, to trigger its observations of the most interesting source states. Its large field of view will allow to observe about 50% of the sky available to the LAD in the same energy band at any time. The WFM is designed also to catch transient/bursting events down to a few mCrab fluxes and provide for them the position and trigger time within $\sim$ 30 seconds from the event. For triggered events, data with fine spectral (up to $\sim$ 300 eV in the $2-50$ keV energy range) and temporal resolution (up to 10μsec) will be made available to the ground within a few hours.

Fig. 7.9 summarizes the properties of the WFM and the LAD instruments.

7.2.2 Science Objectives

The WFM will achieve scientific goals of fundamental importance and not fulfilled by GRB experiments presently flying, nor future missions. These are the following:

- Measurement of the GRBs spectral shape and its evolution down to $\sim$ 2 keV in photon energy, which is crucial for testing models of GRB prompt emission (see Fig.7.10),

-Detection and study of transient X-ray absorption column/features for tens of medium/bright GRBs per year. These measurements are important for understanding the properties of the CBM and hence the nature of GRB progenitors. In addition, the detection of transient features can allow the determination of the GRB redshift to be compared with that determined with the optical/NIR lines,

-To provide a substantial increase (with respect to past and and current missions) in the detection rate of XRFs,

-To extend the GRB detection up to very high redshift ($z > 8$),

-To provide fast and accurate location of the detected GRBs to allow their prompt multi-wavelength follow-up with ground and space telescopes, thus lead-

Current WFM performance specification

Parameter	Value (WFM)
Energy Range	2-50 keV (50-80 keV extended)
Geometric Area (10 cameras)	1820 cm^2
Peak Effective Area (on-axis)	>80 cm^2
Energy Resolution FWHM@6 keV	< 500 eV (EOL at -30°C)
Field of View at Zero Response	180° x 90° + 90°x90° toward night hemisphere
Angular Resolution	5′
Point Source Location Accuracy (10σ)	1′
On-axis sensitivity at 5σ in 3 s (Galactic Center)	270 mCrab
On-axis sensitivity at 5σ in 58 ks (1 day observation of the Galactic Center)	2.1 mCrab

Current LAD performance specification

Parameter	Value (LAD)
Energy range	2-30 keV (30-80 keV larger energy binning)
Effective Area	10 m^2 (@8 keV)
Field of View	≤1°
Energy resolution	≤260 eV at 6 keV (EOL)
Time resolution	~7μs
Dead-time	≤1% for 1 Crab source
Background	~10 mCrab
Maximum average source flux	500 mCrab
Maximum peak source flux	15 Crab

Figure 7.9: Properties of the WFM and the LAD.

ing to the identification of the optical counterparts and/or host galaxies, and to estimate the redshift.

The GRB science that could be done with LAD is strongly dependent on the time that will be required to start a ToO observation. Possible GRB science that could be performed by the LAD include:

-Investigating the plateau phase of the early afterglow and its transition to the "normal decay",

-Searching for emission lines, expected by theoretical models in the case of highly metal enriched circum-burst environment (detected in a few cases by BeppoSaX, Chandra and XMM, but not by Swift/XRT),

-Complementing the observations of the prompt emission by the WFM, by exploiting the transparency of the collimator at energies $> 30 - 40$ MeV.

7.3 GRB science with LOFT

Among all the improvements that LOFT can offer to science, I am going to concentrate on its contribution to the physics of GRBs. It is well known that most time-integrated spectra of the prompt emission of long GRBs are well fit by a Band model in the energy ranges provided by the instruments onboard the currently flying satellites (Swift, Fermi, Konus Wind, etc). But at lower energies, the low-energy index can be very different from the one predicted by the Band model. Fig.7.11 shows the Fermi-GBM spectrum of the prompt emission (first 50 s) of GRB 090618 (blue), fitted with a blackbody plus a power-law model (solid line). In the Fermi-GBM energy range, also a Band model fit is acceptable. We have performed a simulation of the same spectra as would have been seen by the LOFT-WFM in the range 2-50 keV, assuming that the

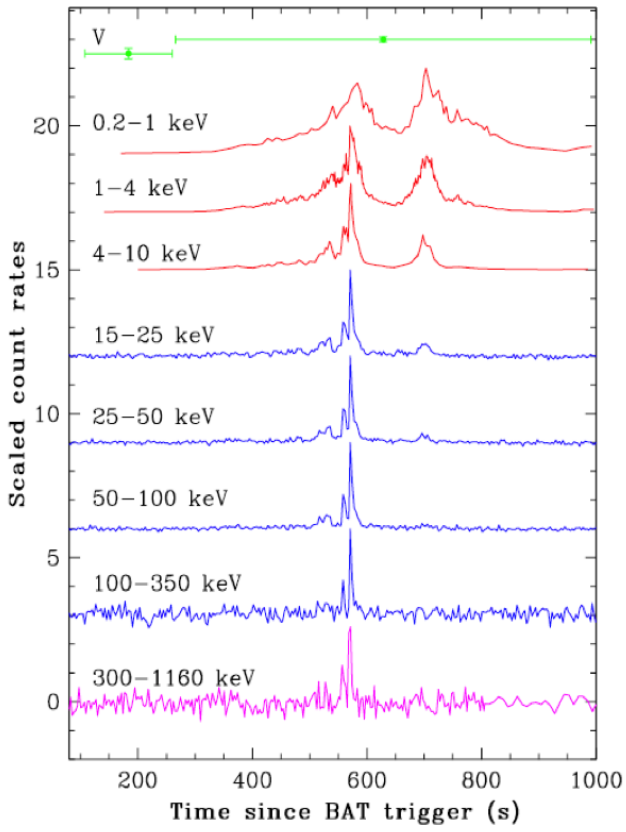

Figure 7.10: Example of the importance to have data of the prompt emission at low energies: GRB 060124 light curves as detected by UVOT (green, V band), XRT (red, $0.2 - 10$ keV), BAT (blue, $15 - 350$ keV) and Konus Wind (pink, $300 - 1160$ keV). GRB 060124, at a redshift $z \sim 2.2$, is the first event for which both the prompt and the afterglow emission could be observed simultaneously and in their entirety by the three *Swift* instruments and by *Konus*-Wind. It can be noticed the structure present after 600 s at lower energies, while at higher energies the signal is almost negligible. The count rates are normalized to the peak of each light curve. Taken from Romano et al. (2006).

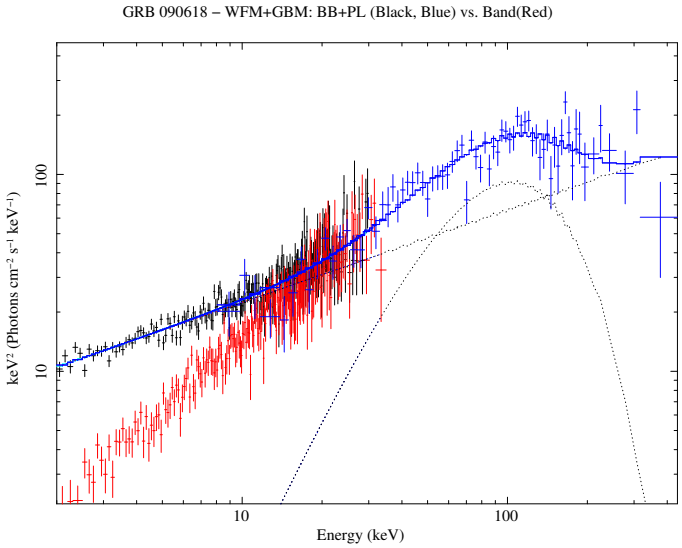

Figure 7.11: Fermi-GBM time-integrated spectrum of the first 50 s of emission of GRB 090618 (blue data), fitted with a BB+PL model (blue solid line). The data is equally well fitted by a Band model. The black (red) data is the same spectra as seen by the LOFT-WFM in the energy range 2-50 keV, assuming the the best fit is the BB+PL (Band) model. We can appreciate the difference in the low-energy slope. This shows the importance of having low energy data of the prompt emission, since this can change enormously the physical interpretation.

best model is either Band (red) or BB+PL (black). We see that the slope of the spectrum at lower energies varies considerably, while it is unnoticeable in the range provided by the current missions. Thus, the possibility to obtain data at low energies becomes fundamental for the study of the physical processes involved in GRBs.

Another contribution from the WFM to GRB science regards the prompt light curve. As already mentioned above, the structure at low energies sometimes is not discriminated at all by the current missions. The WFM would be able to put in evidence the soft emission, which can be very useful when compared to the harder one. Fig.7.12 shows GRB 090618 Fermi-GBM light curve (green) together with the one simulated by the WFM (red). The hard to soft behavior is evidenced in the last spike.

Following always this hard to soft behavior, in the case there is a thermal component that evolves with time during the prompt emission, the WFM will be able to measure the temperature down to 2 keV, which is currently impossible (the lower limit nowadays is 8 keV, as given by Fermi-GBM).

In cases where there is a hard-to-soft evolution that takes place very slowly, it is possible to follow and study into detail all the soft part below 10 keV. An example of these sources is GRB 060218, with a prompt emission that lasts ~ 3000 s.

While the WFM will detect the prompt emission of the GRB sources, the LAD will measure the late afterglow emission, after $\sim$ 6 hours, which is the time needed to repoint to the position given by the WFM. This procedure will

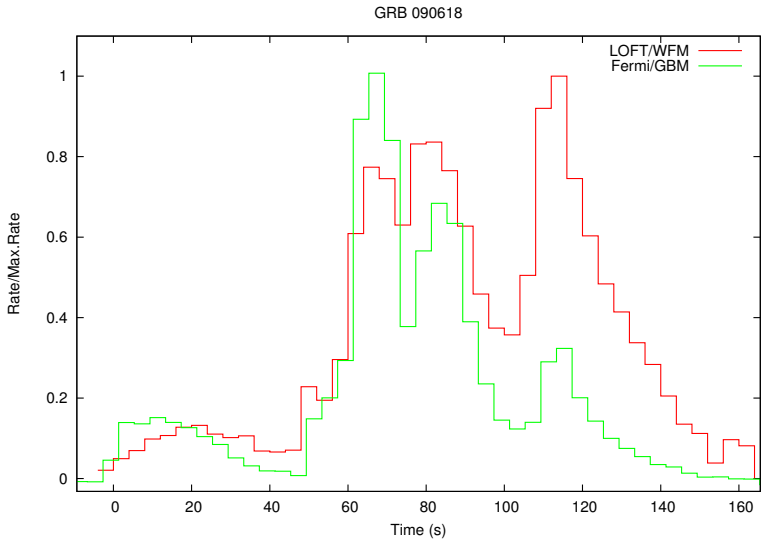

Figure 7.12: Fermi-GBM (green) and LOFT-WFM (red) light curve of GRB 090618. The hard-to-soft evolution is evidenced in the last peak, as the number of counts is higher in the low-energy band.

be applied only to 3 or 4 GRBs per year, and also the brightest ones, since the significance of the detections is much better in those cases. Moreover, apart from providing data in the low energy band (as XRT already does), there will be the possibility to analyze the data in the (10-30) keV band, which up to now has never been explored. An example of how the LAD would detect an X-ray afterglow is given in Fig.7.13, applied to the cases of GRB 130427A and GRB 060124. The left panels show the rate light curve. As the LAD energy band includes and is larger than the one of XRT, a larger number of counts is expected. With regard to the flux light curve, in the cases there is a harder emission, the LAD will be able to detect it. In these examples the flux light curve is quite similar to that of XRT, indicating that there is no emission at higher energies.

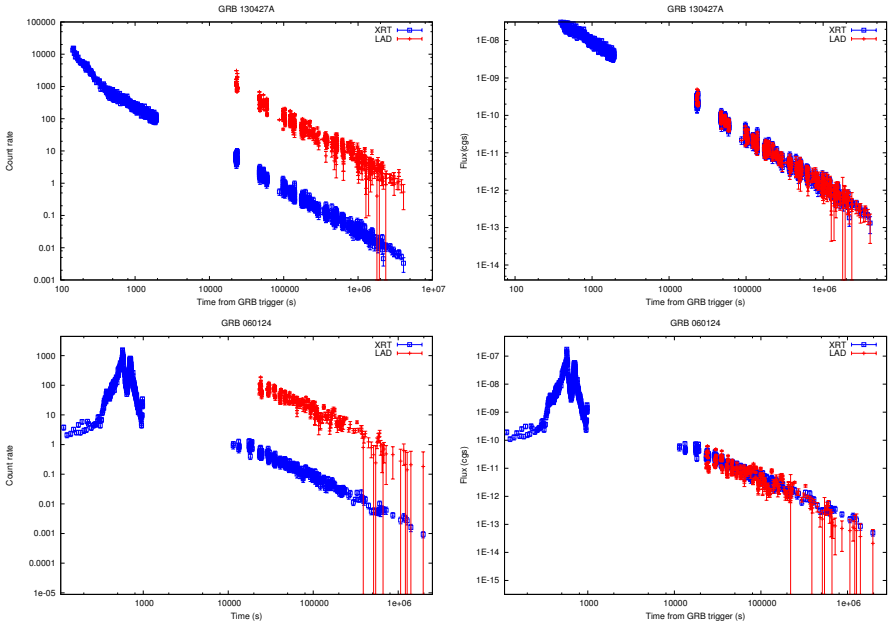

Figure 7.13: GRB 130427A (upper panels) and GRB 060124 (lower panels) rate (left) and flux (right) light curves, as detected by Swift-XRT (red) and would be detected by LOFT-LAD (blue). The time is measured from the BAT trigger.

Conclusions

The work carried out during my PhD consisted in studying the theoretical explanation of GRBs. It implied the analysis of a large sample of GRBs, from the reduction of the raw data all the way to their theoretical analysis and interpretation. In this work, we applied the Fireshell model, developed by Ruffini and collaborators (see e.g. Ruffini et al. 2009, and references therein), based on an idea first advanced by Damour & Ruffini (1975) just a few months after the official announcement of GRB discovery. This model allows to simulate the light curves and spectra of GRBs under the assumption that the emission is spherically symmetric and coming from the collapse of an extragalactic object onto a BH. According to this model, GRBs are classified in long, short and disguised short. The differences lie on the density of the ISM and the baryon load.

During the work, more and more peculiar features were discovered, that led us to further develop the theory in order to explain better the GRB nature. One of the special features we noticed in a sub-sample of GRBs is that they present a common behavior in their late X-ray light curves. In a common rest frame, the late decays overlap. Besides, some of these sources presented also a double emission in their prompt light curves. This led us to think that they may originate in a close binary system formed by an evolved core (probably a CO core) and a NS companion. As the evolved core undergoes a SN Ib/c explosion, the material ejected in this early-SN phase expands at a velocity of $\sim 0.1c$. This will induce an accretion process onto the NS companion. The NS reaches the critical mass value, undergoing a gravitational collapse to a BH. The process of gravitational collapse to a BH leads to the emission of the GRB. As a result, we end up with a binary system formed by a newly-born NS (left after the SN explosion) and a BH (left after the GRB emission). These phases are evidenced in the prompt light curve (in gamma-rays) and part of the X-ray light curve. The separation between the first and the second episode depends on the binary separation and the amount of mass to be accreted by the NS companion. The common decay we observe in the late X-ray light curves of this sub-class of GRBs may be related to the cooling of the newly-born NS. This is the Induced Gravitational Collapse (IGC) model, first introduced by Ruffini et al. (2001a) and later revised in Ruffini et al. (2007, 2008b). We developed it further, evaluating the accretion rate onto the NS and giving the explicit expression of the accreted mass as a function of the nature of the components and the binary parameters.

The method we found, consisting in overlapping the X-ray light curves after 10^4 s in a common rest frame, is also useful to estimate the redshift for the sources which satisfy all the other requirements to be members of the IGC family but do not have a measured redshift. That is the case for GRB 101023

and GRB 110709B. They presented two well defined episodes in the prompt light curve and their energetics were $> 10^{52}$ erg, but the absence or poor quality of the optical data made impossible to measure the redshift and to look for SN features. However, we have strong indications that they belong to the IGC family and that there must be an associated SN. We determined a redshift of $z = 0.9$ and $z = 0.75$ for GRB 101023 and GRB 110709B, respectively.

The concept of induced gravitational collapse is essential to explain the GRB-SN connection, as it enables us to predict, from the first thousands of seconds of GRB emission, the occurrence of a SN after ~ 10 days from the burst in the rest frame. This is how we predicted the occurrence of SN 2013cq, associated to GRB 130427A, and sent a GCN circular to alert the observatories in order to perform a follow-up of the optical afterglow. This was indeed confirmed, spectroscopically and photometrically, and many GCN circulars were sent reporting the observations.

There is no doubt that a huge step forward has been made in these years regarding the physics of GRBs. However, there is still a lot of work to do. We strongly encourage more observations with the current instrumentation and hope that the future space missions will be able to cover the gaps in the observed energy range. The most important thing would be to have data of the prompt emission (since the trigger time) in the band $< 1\ keV$, since that would let us choose the right model between the different spectral models that seem to be equivalent at higher energies, and thus find a physical explanation, hopefully to discover the real nature of the GRB progenitors.

Appendix

Publications leading to the elaboration of this thesis:

- Penacchioni, A.V., Ruffini, R., Izzo, L., Muccino, M., Bianco, C.L., Caito, L., Patricelli, B., Amati, L.; "Evidence for a proto-black hole and a double astrophysical component in GRB 101023"; Astronomy & Astrophysics, 538, A58 (2012). ¡http://adsabs.harvard.edu/abs/2012A%26A...538A..58P¿ ¡http://dx.doi.org/10.1051/0004-6361/201118403¿
- Izzo, L.; Ruffini, R.; Penacchioni, A.V.; Bianco, C.L.; Caito, L.; Chakrabarti, S.K.; Rueda, J.A.; Nandi, A.; Patricelli, B., "A double component in GRB 090618: a proto-black hole and a genuinely long gamma-ray burst", 2012b, A&A, 543, A10
- Izzo, L.; Ruffini, R.; Bianco, C.L.; Dereli, H.; Muccino, M.; Penacchioni, A.V.; Pisani, G.; Rueda, J.A., "On the thermal and double episode emissions in GRB 970828", 2012a, ApJ, submitted (arXiv:1205.6651)
- Muccino, M.; Ruffini, R.; Bianco, C.L.; Izzo, L.; Penacchioni, A.V., "GRB 090227B: the missing link between the genuine short and disguised short GRBs", 2012, ApJ, 763, 125M
- Penacchioni, A.V., Ruffini, R., Bianco, C.L., Izzo, L., Muccino, M., Pisani, G.B., Rueda, J.A., "GRB 110709B in the induced gravitational collapse (IGC) paradigm", 2013, A&A, 551, A133
- Pisani, G.B, Izzo, L., Ruffini, R., Bianco, C.L., Muccino, M., Penacchoni, A.V., Rueda, J.A., Wang, Y., "Novel distance indicator for Gamma-Ray Bursts associated with Supernovae", 2013, A&A Letters, 552L, 5P.
- Muccino, M.; Ruffini, R.; Bianco, C.L.; Izzo, L.; Penacchioni, A. V.; Pisani, G. B.; "GRB 090510: A Disguised Short Gamma-Ray Burst with the Highest Lorentz Factor and Circumburst Medium", 2013, ApJ, 772, 62M.

Bibliography

Achterberg, A., Gallant, Y. A., Kirk, J. G., & Guthmann, A. W. 2001, MNRAS, 328, 393

Aksenov, A. G., Ruffini, R., & Vereshchagin, G. V. 2007, Physical Review Letters, 99, 125003

Aksenov, A. G., Ruffini, R., & Vereshchagin, G. V. 2010, in American Institute of Physics Conference Series, Vol. 1205, American Institute of Physics Conference Series, ed. R. Ruffini & G. Vereshchagin, 11–16

Amati, L. 2006a, Nuovo Cimento B Serie, 121, 1081

Amati, L. 2006b, MNRAS, 372, 233

Amati, L., Del Monte, E., D'Elia, V., et al. 2013, ArXiv e-prints

Amati, L., Frontera, F., & Guidorzi, C. 2009, A&A, 508, 173

Anupama, G. C., Gurugubelli, U. K., & Sahu, D. K. 2009, GRB Coordinates Network, 9576, 1

Arnett, D. 1996, Space Sci. Rev., 78, 559

Atteia, J.-L. 2003, A&A, 407, L1

Band, D., Matteson, J., Ford, L., et al. 1993, ApJ, 413, 281

Band, D. L., Norris, J. P., & Bonnell, J. T. 2004, ApJ, 613, 484

Barthelmy, S. D., Barbier, L. M., Cummings, J. R., et al. 2005, Space Sci. Rev., 120, 143

Battersby, S. J. R., Quenby, J. J., Dyer, C. S., et al. 1993, in American Institute of Physics Conference Series, Vol. 280, American Institute of Physics Conference Series, ed. M. Friedlander, N. Gehrels, & D. J. Macomb, 1107–1111

Beardmore, A. P. & Schady, P. 2009, GRB Coordinates Network, 9528, 1

Beloborodov, A. M. 2003, ApJ, 588, 931

Belvedere, R., Pugliese, D., Rueda, J. A., Ruffini, R., & Xue, S.-S. 2012, Nuclear Physics A, 883, 1

Berezhiani, Z., Bombaci, I., Drago, A., Frontera, F., & Lavagno, A. 2003, ApJ, 586, 1250

Berezinsky, V., Gazizov, A. Z., & Grigorieva, S. I. 2005, Physics Letters B, 612, 147

Berger, E. 2011, GRB Coordinates Network, 12128, 1

Berger, E., Kulkarni, S. R., Fox, D. B., et al. 2005, ApJ, 634, 501

Berger, E., Kulkarni, S. R., & Frail, D. A. 2003, ApJ, 590, 379

Bernardini, M. G., Bianco, C. L., Caito, L., et al. 2007, A&A, 474, L13

Bernardini, M. G., Bianco, C. L., Caito, L., et al. 2008, in American Institute of Physics Conference Series, Vol. 966, Relativistic Astrophysics, ed. C. L. Bianco & S.-S. Xue, 7–11

Bernardini, M. G., Bianco, C. L., Chardonnet, P., et al. 2005, ApJ, 634, L29

Bhat, P. N., Meegan, C. A., Lichti, G. G., et al. 2009, in American Institute of Physics Conference Series, Vol. 1133, American Institute of Physics Conference Series, ed. C. Meegan, C. Kouveliotou, & N. Gehrels, 34–36

Bianco, C. L., Bernardini, M. G., Caito, L., et al. 2008a, in American Institute of Physics Conference Series, Vol. 1000, American Institute of Physics Conference Series, ed. M. Galassi, D. Palmer, & E. Fenimore, 305–308

Bianco, C. L., Bernardini, M. G., Caito, L., et al. 2008b, in American Institute of Physics Conference Series, Vol. 1065, American Institute of Physics Conference Series, ed. Y.-F. Huang, Z.-G. Dai, & B. Zhang, 223–226

Bianco, C. L. & Ruffini, R. 2004, ApJ, 605, L1

Bianco, C. L. & Ruffini, R. 2005a, ApJ, 633, L13

Bianco, C. L. & Ruffini, R. 2005b, ApJ, 620, L23

Blandford, R. & Eichler, D. 1987, Phys. Rep., 154, 1

Blinnikov, S. I., Kozyreva, A. V., & Panchenko, I. E. 1999, Astronomy Reports, 43, 739

Bloom, J. S. 2011, What Are Gamma-Ray Bursts?

Bloom, J. S., Kulkarni, S. R., Djorgovski, S. G., et al. 1999, Nature, 401, 453

Bloom, J. S., Kulkarni, S. R., Price, P. A., et al. 2002, ApJ, 572, L45

Briggs, M. S. 2010, GRB Coordinates Network, 11376, 1

Briggs, M. S., Band, D. L., Kippen, R. M., et al. 1999, ApJ, 524, 82

Briggs, M. S., Paciesas, W. S., Brock, M. N., et al. 1993, in American Institute of Physics Conference Series, Vol. 280, American Institute of Physics Conference Series, ed. M. Friedlander, N. Gehrels, & D. J. Macomb, 691–693

Brock, M. N., Meegan, C. A., Fishman, G. J., et al. 1992, in American Institute of Physics Conference Series, Vol. 265, American Institute of Physics Conference Series, ed. W. S. Paciesas & G. J. Fishman, 399–403

Burrows, D. N., Hill, J. E., Nousek, J. A., et al. 2005, Space Sci. Rev., 120, 165

Burrows, D. N., Hill, J. E., Nousek, J. A., et al. 2004, in Society of Photo-Optical Instrumentation Engineers (SPIE) Conference Series, Vol. 5165, Society of Photo-Optical Instrumentation Engineers (SPIE) Conference Series, ed. K. A. Flanagan & O. H. W. Siegmund, 201–216

Caito, L., Amati, L., Bernardini, M. G., et al. 2010, A&A, 521, A80

Caito, L., Bernardini, M. G., Bianco, C. L., et al. 2009, A&A, 498, 501

Cano, Z., Bersier, D., Guidorzi, C., et al. 2011, ApJ, 740, 41

Cenko, S. B., Perley, D. A., Junkkarinen, V., et al. 2009, GRB Coordinates Network, 9518, 1

Chandra, P. & Frail, D. A. 2009, GRB Coordinates Network, 9533, 1

Chornock, R., Berger, E., Levesque, E. M., et al. 2010, ArXiv e-prints

Cobb, B. E., Bailyn, C. D., van Dokkum, P. G., Buxton, M. M., & Bloom, J. S. 2004, ApJ, 608, L93

Cobb, B. E., Bloom, J. S., Perley, D. A., et al. 2010, ApJ, 718, L150

Cohen-Tanugi, J. 2008, in International Cosmic Ray Conference, Vol. 3, International Cosmic Ray Conference, 1575–1578

Colgate, S. A. 1968, Canadian Journal of Physics Supplement, 46, 476

Costa, E. & Frontera, F. 2011, ArXiv e-prints

Costa, E., Frontera, F., Heise, J., et al. 1997, Nature, 387, 783

Covino, S., Malesani, D., Tagliaferri, G., et al. 2004, Memorie della Societa Astronomica Italiana Supplementi, 5, 160

Crider, A., Liang, E. P., Smith, I. A., et al. 1997, ApJ, 479, L39

Cummings, J. R., Barthelmy, S. D., Burrows, D. N., et al. 2011, GCN Circular, 12122, 1

Dainotti, M. G., Bernardini, M. G., Bianco, C. L., et al. 2007, A&A, 471, L29

Damour, T. & Ruffini, R. 1975, Physical Review Letters, 35, 463

de Barros, G., Amati, L., Bernardini, M. G., et al. 2011, A&A, 529, A130

de Ugarte Postigo, A., Lundgren, A., De Breuck, C., et al. 2011, GRB Coordinates Network, 12151, 1

de Ugarte Postigo, A., Xu, D., Leloudas, G., et al. 2013, GRB Coordinates Network, 14646, 1

Della Valle, M. 2011, International Journal of Modern Physics D, 20, 1745

Diehl, R. 1988, Space Sci. Rev., 49, 85

Djorgovski, S. G., Kulkarni, S. R., Bloom, J. S., & Frail, D. A. 1999, GRB Coordinates Network, 289, 1

Ellison, D. C. & Double, G. P. 2002, Astroparticle Physics, 18, 213

Feroci, M., den Herder, J. W., Bozzo, E., et al. 2012, in Society of Photo-Optical Instrumentation Engineers (SPIE) Conference Series, Vol. 8443, Society of Photo-Optical Instrumentation Engineers (SPIE) Conference Series

Ferrero, P., Kann, D. A., Zeh, A., et al. 2006, A&A, 457, 857

Fishman, G. J. 1988, in American Institute of Physics Conference Series, Vol. 170, Nuclear Spectroscopy of Astrophysical Sources, ed. N. Gehrels & G. H. Share, 378–388

Fishman, G. J. & Meegan, C. A. 1995, ARA&A, 33, 415

Fishman, G. J., Meegan, C. A., Wilson, R. B., et al. 1991a, in American Institute of Physics Conference Series, Vol. 265, American Institute of Physics Conference Series, 13–21

Fishman, G. J., Meegan, C. A., Wilson, R. B., Paciesas, W. S., & Pendleton, G. N. 1991b, in Bulletin of the American Astronomical Society, Vol. 23, Bulletin of the American Astronomical Society, 901

Flores, H., Covino, S., Xu, D., et al. 2013, GRB Coordinates Network, 14491, 1

Frail, D. A., Kulkarni, S. R., Nicastro, L., Feroci, M., & Taylor, G. B. 1997, Nature, 389, 261

Frail, D. A., Kulkarni, S. R., Sari, R., et al. 2001, ApJ, 562, L55

Frontera, F., Amati, L., Costa, E., et al. 2000, ApJS, 127, 59

Gal-Yam, A., Moon, D.-S., Fox, D. B., et al. 2004, ApJ, 609, L59

Galama, T. J., Tanvir, N., Vreeswijk, P. M., et al. 2000, ApJ, 536, 185

Galama, T. J., Vreeswijk, P. M., van Paradijs, J., et al. 1998, Nature, 395, 670

Garnavich, P. M., Stanek, K. Z., Wyrzykowski, L., et al. 2003, ApJ, 582, 924

Gehrels, N., Chincarini, G., Giommi, P., et al. 2004, ApJ, 611, 1005

Gehrels, N., Fichtel, C. E., Fishman, G. J., Kurfess, J. D., & Schonfelder, V. 1993, Scientific American, 269, 68

Gehrels, N., Ramirez-Ruiz, E., & Fox, D. B. 2009, ARA&A, 47, 567

Gehrels, N., Shrader, C., & Kniffen, D. A. 1994, in New Horizon of X-Ray Astronomy. First Results from ASCA, ed. F. Makino & T. Ohashi, 227

Ghirlanda, G., Celotti, A., & Ghisellini, G. 2002, A&A, 393, 409

Ghirlanda, G., Celotti, A., & Ghisellini, G. 2003, A&A, 406, 879

Golenetskii, S., Aptekar, R., Frederiks, D., et al. 2010, GRB Coordinates Network, 11384, 1

Golenetskii, S., Aptekar, R., Frederiks, D., et al. 2011, GRB Coordinates Network, 12135, 1

Golenetskii, S., Aptekar, R., Frederiks, D., et al. 2013, GRB Coordinates Network, 14487, 1

Golenetskii, S., Aptekar, R., Mazets, E., et al. 2009a, GRB Coordinates Network, 9553, 1

Golenetskii, S., Aptekar, R., Mazets, E., et al. 2009b, GRB Coordinates Network, 8926, 1

Golenetskii, S., Aptekar, R., Mazets, E., et al. 2009c, GRB Coordinates Network, 9344, 1

Goodman, J. 1986, ApJ, 308, L47

Granot, J. & Sari, R. 2002, ApJ, 568, 820

Greiner, J., Peimbert, M., Esteban, C., et al. 2003, GRB Coordinates Network, 2020, 1

Grupe, D., Nousek, J. A., vanden Berk, D. E., et al. 2007, AJ, 133, 2216

Guiriec, S. 2009, GRB Coordinates Network, 8921, 1

Guiriec, S., Connaughton, V., & Briggs, M. 2009, GRB Coordinates Network, 9336, 1

Gursky, H. & Ruffini, R., eds. 1975, Astrophysics and Space Science Library, Vol. 48, Neutron stars, black holes and binary X-ray sources; Proceedings of the Annual Meeting, San Francisco, Calif., February 28, 1974

Hanlon, L. O., Bennett, K., Williams, O. R., Winkler, C., & Preece, R. D. 1995, Ap&SS, 231, 157

Hartman, R. C., Bertsch, D. L., Fichtel, C. E., et al. 1992, in NASA Conference Publication, Vol. 3137, NASA Conference Publication, ed. C. R. Shrader, N. Gehrels, & B. Dennis, 116–125

Hjorth, J. & Bloom, J. S. 2012, in Cambridge Astrophysics Series, Vol. 51, Gamma-Ray Bursts, ed. C. Kouveliotou, R. A. M. J. Wijers, & S. Woosley (Cambridge University Press (Cambridge)), 169–190

Hjorth, J., Sollerman, J., Møller, P., et al. 2003, Nature, 423, 847

Horváth, I. 2002, A&A, 392, 791

Hoversten, E. A., Krimm, H. A., Grupe, D., et al. 2009, GCN Report, 218, 1

Iwamoto, K., Mazzali, P. A., Nomoto, K., et al. 1998, Nature, 395, 672

Izzo, L., Rueda, J. A., & Ruffini, R. 2012a, A&A, 548, L5

Izzo, L., Ruffini, R., Bianco, C. L., et al. 2012b, ArXiv e-prints

Izzo, L., Ruffini, R., Penacchioni, A. V., et al. 2012c, A&A, 543, A10

Johnson, W. N., Kurfess, J. D., Kinzer, R. L., Purcell, W. R., & Strickman, M. S. 1989, NASA STI/Recon Technical Report N, 91, 27516

Kalberla, P. M. W., Burton, W. B., Hartmann, D., et al. 2005, A&A, 440, 775

Kann, D. A., Schulze, S., & Updike, A. C. 2008, GRB Coordinates Network, 7627, 1

Kippen, R. M., Ryan, J., Connors, A., et al. 1995, in Bulletin of the American Astronomical Society, Vol. 27, American Astronomical Society Meeting Abstracts, 1295

Klebesadel, R. W., Strong, I. B., & Olson, R. A. 1973, in Bulletin of the American Astronomical Society, Vol. 5, Bulletin of the American Astronomical Society, 322

Kobayashi, S., Piran, T., & Sari, R. 1997, ApJ, 490, 92

Kono, K., Daikyuji, A., Sonoda, E., et al. 2009, GRB Coordinates Network, 9568, 1

Kotov, Y., Kochemasov, A., Kuzin, S., et al. 2008, in COSPAR Meeting, Vol. 37, 37th COSPAR Scientific Assembly, 1596

Kouveliotou, C., Wijers, R. A. M. J., & Woosley, S. 2012, Gamma-ray Bursts

Kouveliotou, C., Woosley, S. E., Patel, S. K., et al. 2004, ApJ, 608, 872

Kulkarni, S. R., Frail, D. A., Wieringa, M. H., et al. 1998, Nature, 395, 663

Kumar, P. & McMahon, E. 2008, MNRAS, 384, 33

Kurfess, J. D., Johnson, W. N., Kinzer, R. L., Leising, M. D., & Share, G. H. 1989, NASA STI/Recon Technical Report N, 91, 27517

Larsson, J., Ryde, F., Lundman, C., et al. 2011, MNRAS, 414, 2642

Lemoine, M. & Pelletier, G. 2003, ApJ, 589, L73

Levan, A. J., Cenko, S. B., Perley, D. A., & Tanvir, N. R. 2013a, GRB Coordinates Network, 14455, 1

Levan, A. J., Fruchter, A. S., Graham, J., et al. 2013b, GRB Coordinates Network, 14686, 1

Levan, A. J., Warwick, U., Perley, D., & D'Avanzo, P. 2010, GRB Coordinates Network, 11366, 1

Lipkin, Y. M., Ofek, E. O., Gal-Yam, A., et al. 2004, ApJ, 606, 381

Longo, F., Moretti, E., Barbiellini, G., et al. 2009a, GRB Coordinates Network, 9343, 1

Longo, F., Moretti, E., Barbiellini, G., et al. 2009b, GRB Coordinates Network, 9524, 1

Lu, T. & Shi, T.-Y. 1990, Scientia Sinica Series Mathematical Physical Technical Sciences, 33, 1230

MacFadyen, A. I. & Woosley, S. E. 1999, ApJ, 524, 262

Malesani, D., Tagliaferri, G., Chincarini, G., et al. 2004, ApJ, 609, L5

Mallozzi, R. S., Paciesas, W. S., Pendleton, G. N., et al. 1995, ApJ, 454, 597

Maselli, A., Beardmore, A. P., Lien, A. Y., et al. 2013, GRB Coordinates Network, 14448, 1

Mason, K. O., Breeveld, A., Hunsberger, S. D., et al. 2004, in Society of Photo-Optical Instrumentation Engineers (SPIE) Conference Series, Vol. 5165, Society of Photo-Optical Instrumentation Engineers (SPIE) Conference Series, ed. K. A. Flanagan & O. H. W. Siegmund, 277–286

McBreen, S. 2009, GRB Coordinates Network, 9535, 1

Meegan, C. 2008, in COSPAR Meeting, Vol. 37, 37th COSPAR Scientific Assembly, 1988

Meegan, C., Lichti, G., Bhat, P. N., et al. 2009, ApJ, 702, 791

Meegan, C. A., Fishman, G. J., Wilson, R. B., et al. 1992, Nature, 355, 143

Melandri, A., D'Elia, V., D'Avanzo, P., et al. 2013, GRB Coordinates Network, 14673, 1

Mészáros, P. 2006, Reports on Progress in Physics, 69, 2259

Meszaros, P. & Rees, M. J. 1997, ApJ, 476, 232

Michelson, P. 2008, in COSPAR Meeting, Vol. 37, 37th COSPAR Scientific Assembly, 2028

Mirabal, N., Halpern, J. P., An, D., Thorstensen, J. R., & Terndrup, D. M. 2006, ApJ, 643, L99

Morrison, R. & McCammon, D. 1983, ApJ, 270, 119

Muccino, M., Ruffini, R., Bianco, C. L., Izzo, L., & Penacchioni, A. V. 2013, ApJ, 763, 125

Murdin, P., ed. 2000, Compton Gamma Ray Observatory (CGRO)

Narayan, R., Paczynski, B., & Piran, T. 1992, ApJ, 395, L83

Negreiros, R., Ruffini, R., Bianco, C. L., & Rueda, J. A. 2012, A&A, 540, A12

Nolan, P. L., Bertsch, D. L., Fichtel, C. E., et al. 1992, IEEE Transactions on Nuclear Science, 39, 993

Norris, J. P. & Bonnell, J. T. 2006, ApJ, 643, 266

Ohmori, N., Akiyama, M., Yamauchi, M., et al. 2011, GRB Coordinates Network, 12732, 1

Ohmori, N., Noda, K., Sonoda, E., et al. 2009, GRB Coordinates Network, 9355, 1

Ohno, M. & Pelassa, V. 2009, GRB Coordinates Network, 9334, 1

Paciesas, W. S., Pendleton, G. N., Lestrade, J. P., et al. 1989, in Society of Photo-Optical Instrumentation Engineers (SPIE) Conference Series, Vol. 1159, Society of Photo-Optical Instrumentation Engineers (SPIE) Conference Series, ed. C. J. Hailey & O. H. W. Siegmund, 156–164

Paczynski, B. 1986, ApJ, 308, L43

Paczyński, B. 1998, in American Institute of Physics Conference Series, Vol. 428, Gamma-Ray Bursts, 4th Hunstville Symposium, ed. C. A. Meegan, R. D. Preece, & T. M. Koshut, 783–787

Paczynski, B. 2001, in Supernovae and Gamma-Ray Bursts: the Greatest Explosions since the Big Bang, ed. M. Livio, N. Panagia, & K. Sahu, 1–8

Paczynski, B. & Xu, G. 1994, ApJ, 427, 708

Page, K. L. & Saxton, C. J. 2010, GRB Coordinates Network, 11368, 1

Panaitescu, A. & Mészáros, P. 1999, ApJ, 526, 707

Patricelli, B., Bernardini, M. G., Bianco, C. L., et al. 2012, ApJ, 756, 16

Pélangeon, A., Atteia, J.-L., Lamb, D. Q., & HETE-2 Science Team. 2006, in American Institute of Physics Conference Series, Vol. 836, Gamma-Ray Bursts in the Swift Era, ed. S. S. Holt, N. Gehrels, & J. A. Nousek, 149–152

Pélangeon, A., Atteia, J.-L., Nakagawa, Y. E., et al. 2008, A&A, 491, 157

Penacchioni, A. V., Ruffini, R., Izzo, L., et al. 2012, A&A, 538, A58

Penacchioni, A. V., Ruffini, R., Izzo, L., et al. 2011, ArXiv e-prints

Perley, D. A. 2009, GRB Coordinates Network, 9514, 1

Perley, D. A. & Tang, S. 2013, GRB Coordinates Network, 14615, 1

Pian, E., Amati, L., Antonelli, L. A., et al. 2000, ApJ, 536, 778

Pian, E., Mazzali, P. A., Masetti, N., et al. 2006, Nature, 442, 1011

Piran, T. 1999, Phys. Rep., 314, 575

Piran, T. 2004, Reviews of Modern Physics, 76, 1143

Piran, T., Sari, R., & Zou, Y.-C. 2009, MNRAS, 393, 1107

Pisani, G. B., Izzo, L., Ruffini, R., et al. 2013, A&A, 552, L5

Pozdnyakov, L. A., Sobol, I. M., & Syunyaev, R. A. 1983, Astrophysics and Space Physics Reviews, 2, 189

Preece, R. D. 2000, in American Institute of Physics Conference Series, Vol. 526, Gamma-ray Bursts, 5th Huntsville Symposium, ed. R. M. Kippen, R. S. Mallozzi, & G. J. Fishman, 115–124

Preparata, G., Ruffini, R., & Xue, S.-S. 1998, A&A, 338, L87

Pritchard, T., Maselli, A., Kuin, N. P. M., et al. 2013, GRB Coordinates Network, 14472, 1

Rau, A., McBreen, S., & Kruehler, T. 2009, GRB Coordinates Network, 9353, 1

Rees, M. J. & Meszaros, P. 1992, MNRAS, 258, 41P

Rees, M. J. & Meszaros, P. 1994, ApJ, 430, L93

Romano, P., Campana, S., Chincarini, G., et al. 2006, Nuovo Cimento B Serie, 121, 1067

Roming, P. W. A., Kennedy, T. E., Mason, K. O., et al. 2005, Space Sci. Rev., 120, 95

Rueda, J. A. & Ruffini, R. 2012, ApJ, 758, L7

Ruffini, R., Aksenov, A. G., Bernardini, M. G., et al. 2009, in American Institute of Physics Conference Series, Vol. 1132, American Institute of Physics Conference Series, ed. M. Novello & S. Perez, 199–266

Ruffini, R., Aksenov, A. G., Bernardini, M. G., et al. 2008a, in American Institute of Physics Conference Series, Vol. 1065, American Institute of Physics Conference Series, ed. Y.-F. Huang, Z.-G. Dai, & B. Zhang, 219–222

Ruffini, R., Bernardini, M. G., Bianco, C. L., et al. 2008b, in The Eleventh Marcel Grossmann Meeting On Recent Developments in Theoretical and Experimental General Relativity, Gravitation and Relativistic Field Theories, ed. H. Kleinert, R. T. Jantzen, & R. Ruffini, 368–505

Ruffini, R., Bernardini, M. G., Bianco, C. L., et al. 2007, in ESA Special Publication, Vol. 622, ESA Special Publication, 561

Ruffini, R., Bianco, C. L., Chardonnet, P., et al. 2003a, in American Institute of Physics Conference Series, Vol. 668, Cosmology and Gravitation, ed. M. Novello & S. E. Perez Bergliaffa, 16–107

Ruffini, R., Bianco, C. L., Chardonnet, P., Fraschetti, F., & Xue, S.-S. 2002, ApJ, 581, L19

Ruffini, R., Bianco, C. L., Enderli, M., et al. 2013, GRB Coordinates Network, 14526, 1

Ruffini, R., Bianco, C. L., Fraschetti, F., Xue, S.-S., & Chardonnet, P. 2001a, ApJ, 555, L117

Ruffini, R., Bianco, C. L., Fraschetti, F., Xue, S.-S., & Chardonnet, P. 2001b, ApJ, 555, L113

Ruffini, R., Bianco, C. L., Fraschetti, F., Xue, S.-S., & Chardonnet, P. 2001c, ApJ, 555, L107

Ruffini, R., Bianco, C. L., Xue, S.-S., Chardonnet, P., & Fraschetti, F. 2003b, International Journal of Modern Physics D, 12, 173

Ruffini, R., Bianco, C. L., Xue, S.-S., et al. 2004, International Journal of Modern Physics D, 13, 843

Ruffini, R., Bianco, C. L., Xue, S.-S., et al. 2005, International Journal of Modern Physics D, 14, 97

Ruffini, R., Izzo, L., Penacchione, A., & Chakrabarti, S. K. 2010a, GRB Coordinates Network, 11459, 1

Ruffini, R., Vereshchagin, G., & Xue, S.-S. 2010b, Phys. Rep., 487, 1

Ruffini, R. J. 2001, ArXiv Astrophysics e-prints

Ryan, J. M. 1989, Nuclear Physics B Proceedings Supplements, 10, 121

Ryde, F. 2004, ApJ, 614, 827

Sakamoto, T., Ukwatta, T. N., & Barthelmy, S. D. 2009, GRB Coordinates Network, 9534, 1

Sari, R. & Piran, T. 1997, ApJ, 485, 270

Sari, R., Piran, T., & Halpern, J. P. 1999, ApJ, 519, L17

Saxton, C. J., Barthelmy, S. D., Baumgartner, W. H., et al. 2010, GRB Coordinates Network, 11363, 1

Sazonov, S. Y., Lutovinov, A. A., & Sunyaev, R. A. 2004, Nature, 430, 646

Schady, P. 2009, GRB Coordinates Network, 9527, 1

Schady, P., Baumgartner, W. H., Beardmore, A. P., et al. 2009, GRB Coordinates Network, 9512, 1

Schoenfelder, V. 1991, Advances in Space Research, 11, 313

Share, G. H., Johnson, W. N., Kinzer, R. L., et al. 1992, in American Institute of Physics Conference Series, Vol. 265, American Institute of Physics Conference Series, ed. W. S. Paciesas & G. J. Fishman, 32–37

Shemi, A. & Piran, T. 1990, ApJ, 365, L55

Soderberg, A. M. 2006, in American Institute of Physics Conference Series, Vol. 836, Gamma-Ray Bursts in the Swift Era, ed. S. S. Holt, N. Gehrels, & J. A. Nousek, 380–385

Sokolov, I. V., Roussev, I. I., Fisk, L. A., et al. 2006, ApJ, 642, L81

Strickman, M. S., Grabelsky, D., Matz, S., Pendleton, J., & Cameron, R. 1990, NASA STI/Recon Technical Report N, 91, 27515

Strickman, M. S., Grove, J. E., Johnson, W. N., et al. 1992, in Data Analysis in Astronomy, ed. V. di Gesu, L. Scarsi, R. Buccheri, & P. Crane, 283–294

Strong, I. B. 1975, in Astrophysics and Space Science Library, Vol. 48, Neutron Stars, Black Holes and Binary X-ray Sources, ed. H. Gursky & R. Ruffini, 47–58

Trotter, A., Reichart, D., Haislip, J., et al. 2013, GRB Coordinates Network, 14662, 1

Updike, A. C., Olivares, F. E., Greiner, J., & Kann, D. A. 2011, GRB Coordinates Network, 12129, 1

van Paradijs, J., Groot, P. J., Galama, T., et al. 1997, Nature, 386, 686

Vaughan, S., Willingale, R., O'Brien, P. T., et al. 2004, ApJ, 603, L5

von Kienlin, A. 2013, GRB Coordinates Network, 14473, 1

Willis, D. R., Barlow, E. J., Bird, A. J., et al. 2005, A&A, 439, 245

Winstein, B. & Zurek, K. M. 2009, Physics, 2, 37

Woosley, S. E. 1993, ApJ, 405, 273

Woosley, S. E. 1996, in American Institute of Physics Conference Series, Vol. 384, American Institute of Physics Conference Series, ed. C. Kouveliotou, M. F. Briggs, & G. J. Fishman, 709–718

Woosley, S. E. & Bloom, J. S. 2006, ARA&A, 44, 507

Woosley, S. E. & Weaver, T. A. 1982, in NATO ASIC Proc. 90: Supernovae: A Survey of Current Research, ed. M. J. Rees & R. J. Stoneham, 79

Xu, D., de Ugarte Postigo, A., Kruehler, T., et al. 2013a, GRB Coordinates Network, 14597, 1

Xu, D., de Ugarte Postigo, A., Schulze, S., et al. 2013b, GRB Coordinates Network, 14478, 1

Yonetoku, D., Murakami, T., Nakamura, T., et al. 2004, ApJ, 609, 935

Yonetoku, D., Murakami, T., Tsutsui, R., et al. 2010, PASJ, 62, 1495

Yu, W., Li, T., & Wu, M. 2000, Nuclear Physics B Proceedings Supplements, 80, C627

Zauderer, A. & Berger, E. 2011, GRB Coordinates Network, 12190, 1

Zauderer, B. A., Berger, E., Margutti, R., et al. 2013, ApJ, 767, 161

Zeh, A., Klose, S., & Hartmann, D. H. 2004, ApJ, 609, 952

Zhao, X.-H., Mao, J., Xin, Y. X., & Bai, J.-M. 2013, GRB Coordinates Network, 14466, 1

Zhu, S., Racusin, J., Chiang, J., & Vianello, G. 2013a, GRB Coordinates Network, 14508, 1

Zhu, S., Racusin, J., Kocevski, D., et al. 2013b, GRB Coordinates Network, 14471, 1